

RICE UNIVERSITY

**On-Orbit Transfer Trajectory Methods**

**Using High Fidelity Dynamic Models**

by

**Danielle Burke**

A THESIS SUBMITTED

IN PARTIAL FULFILLMENT OF THE

REQUIREMENTS FOR THE DEGREE

**Master of Science**

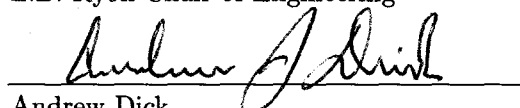
APPROVED, THESIS COMMITTEE:



---

Paul Spanos


L.B. Ryon Chair of Engineering



---

Andrew Dick

Mechanical Engineering & Materials  
Science



---

Andrew Meade

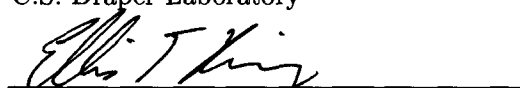
Mechanical Engineering & Materials  
Science



---

Naz Bedrossian

C.S. Draper Laboratory



---

Ellis King

C.S. Draper Laboratory

HOUSTON, TEXAS

APRIL, 2010

UMI Number: 1486020

All rights reserved

**INFORMATION TO ALL USERS**

The quality of this reproduction is dependent upon the quality of the copy submitted.

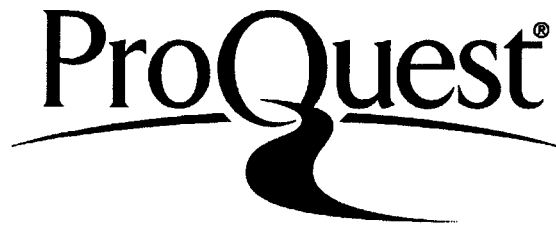
In the unlikely event that the author did not send a complete manuscript and there are missing pages, these will be noted. Also, if material had to be removed, a note will indicate the deletion.



UMI 1486020

Copyright 2010 by ProQuest LLC.

All rights reserved. This edition of the work is protected against unauthorized copying under Title 17, United States Code.



ProQuest LLC  
789 East Eisenhower Parkway  
P.O. Box 1346  
Ann Arbor, MI 48106-1346

The views expressed in this thesis are those of the author and do not reflect the official policy or position of the United States Air Force, Department of Defense, or the U.S. Government.

## Abstract

On-Orbit Transfer Trajectory Generation Methods Using High Fidelity Dynamic  
Models

by

Danielle Burke

A high fidelity trajectory propagator for use in targeting and reference trajectory generation is developed for aerospace applications in low Earth and translunar orbits. The dominant perturbing effects necessary to accurately model vehicle motion in these dynamic environments are incorporated into a numerical predictor-corrector scheme to converge on a realistic trajectory incorporating multi-body gravitation, high order gravity, atmospheric drag, and solar radiation pressure. The predictor-corrector algorithm is shown to reliably produce accurate required velocities to meet constraints on the final position for the dominant perturbation effects modeled. Low fidelity conic state propagation techniques such as Lambert's method and multiconic pseudostate theory are developed to provide a suitable initial guess. Feasibility of the method is demonstrated through sensitivity analysis to the initial guess for a bounding set of cases.

## Acknowledgments

The journey to completion of this thesis has been a long and arduous process that could not have been made possible without the help of a number of individuals. I would like to thank my Rice University advisor, Professor Pol Spanos, for supporting my research and coursework at Rice. I additionally would like to thank Nazareth Bedrossian of the C.S. Draper Laboratory who gave me the opportunity to come to Houston and work on this research. I would like to thank my advisor at Draper, Ellis King, for all of his guidance and support. Special thanks to my thesis committee, Pol Spanos, Andrew Dick, Andrew Meade, Nazareth Bedrossian, and Ellis King for valuable input and feedback on this research. Furthermore, Stan Sheppherd for taking the time to review my thesis and provide insightful inputs. Additionally, Zoran Milenkovic who was there to help when it seemed that the obstacles were insurmountable. Thanks to my colleagues with whom I shared an office for two years, they made this journey an unforgettable adventure: John who kept the room entertained with his ridiculous music, Eric who will forever be the MATLAB Graph Master, and Adam who will one day eat Chinese food and enjoy it. I would like to thank my husband who pushed me to see the final goal, never accepting my complaints. Finally, thanks to my mom who realized that not talking about the thesis was sometimes the best advice of all.

# Contents

<b>Abstract</b>	<b>ii</b>
<b>Acknowledgements</b>	<b>iii</b>
<b>List of Figures</b>	<b>xvi</b>
<b>List of Tables</b>	<b>xviii</b>
<b>1 Introduction</b>	<b>1</b>
<b>2 Special Perturbation Techniques</b>	<b>6</b>
2.1 Orbital Elements . . . . .	6
2.2 Two-body Equations of Motion . . . . .	9
2.3 Kepler’s Equation . . . . .	11
2.4 Equations of Motion with Perturbations . . . . .	15
2.5 Cowell’s Method . . . . .	17
2.6 Encke’s Method . . . . .	19
2.6.1 Rectification . . . . .	21
2.7 Variation of Parameters . . . . .	23
2.8 Numerical Integration Methods . . . . .	24
2.8.1 Integration Errors . . . . .	24
2.8.2 Euler’s Method . . . . .	27

2.8.3	Runge-Kutta Method . . . . .	28
2.8.4	Nystrom Integration Method . . . . .	31
2.8.5	MATLAB Solvers . . . . .	32
<b>3</b>	<b>Development of Propagator</b>	<b>37</b>
3.1	System Overview . . . . .	37
3.2	Three Body Motion . . . . .	38
3.2.1	SPICE . . . . .	39
3.3	High Order Gravity . . . . .	42
3.3.1	Formulation . . . . .	43
3.3.2	High Order Gravity Moon . . . . .	50
3.3.3	Validation of Higher Order Gravity Model . . . . .	51
3.3.4	Model Configuration . . . . .	59
3.4	Atmospheric Drag . . . . .	60
3.5	Solar Radiation . . . . .	63
<b>4</b>	<b>State Transition Matrix</b>	<b>68</b>
4.1	N-Body Partial . . . . .	71
4.2	Gravity Potential Partial . . . . .	73
4.3	Atmospheric Drag Partial . . . . .	77
4.4	Accuracy of Error State Transition Matrix . . . . .	79
4.4.1	Low Earth Orbit Transfer Test Results . . . . .	82
4.4.2	Translunar Transfer Test Results . . . . .	85
4.5	Shooting Method . . . . .	90
<b>5</b>	<b>Translunar Application</b>	<b>93</b>
5.1	Pseudostate Theory for Approximating Three-Body Trajectories . . . . .	94
5.1.1	Conic Approximations . . . . .	95
5.1.2	Overlapped Conic Approximation . . . . .	100

5.1.3	Pseudostate Theory . . . . .	105
5.1.4	Translunar Targeting . . . . .	107
5.2	EXLX Configuration . . . . .	111
5.2.1	Parameter Selection User Interface . . . . .	111
5.2.2	EXLX Multi-Conic Propagator . . . . .	114
5.3	Test Case Selection . . . . .	116
5.4	Results and Analysis . . . . .	121
5.4.1	Translunar Shooting Method Sensitivity . . . . .	124
5.5	Conclusion . . . . .	135
5.5.1	Method Limitations . . . . .	135
5.5.2	Summary of Test Results . . . . .	136
<b>6</b>	<b>Low Earth Orbit Application</b>	<b>138</b>
6.1	Lambert's Method . . . . .	138
6.1.1	Lagrange's Equations . . . . .	139
6.1.2	Gauss's Formulation . . . . .	142
6.1.3	Battin's Combined Equation . . . . .	144
6.2	Test Case Selection . . . . .	146
6.3	Results and Analysis . . . . .	150
6.4	Conclusions . . . . .	162
6.4.1	Method Limitations . . . . .	162
6.4.2	Summary of Test Results . . . . .	167
<b>7</b>	<b>Closure</b>	<b>170</b>
<b>A</b>	<b>Feasible Translunar Trajectories</b>	<b>177</b>
<b>B</b>	<b>Monte Carlo Sample Size</b>	<b>182</b>
<b>C</b>	<b>List of Test Cases</b>	<b>184</b>



**D LEO Contour Maps**

# List of Figures

1.1	Illustration of a generalized Hohmann transfer between two low Earth orbits . . . . .	2
1.2	Illustration of a generalized translunar transfer . . . . .	4
2.1	Illustration of the classic orbital elements: inclination ( $i$ ), right ascension of ascending node ( $\Omega$ ), argument of perigee ( $\omega$ ), and true anomaly ( $\nu$ ) [49] . . . . .	7
2.2	Elliptical orbit conic section illustrating the two foci, $F$ and $F'$ , as well as the semimajor axis, ( $a$ ) [49] . . . . .	8
2.3	Geometry of Kepler's equation [49] . . . . .	12
2.4	A representation of a spherical coordinate system [53] . . . . .	18
2.5	Vector definition for Encke's method [43] . . . . .	20
2.6	Boxplot comparison of the magnitude difference in final position of Cowell/Encke propagation and Kepler's analytical solution for 7,000 low Earth orbits over one orbit period . . . . .	23
2.7	Comparison of Euler's Method, second-order Runge Kutta method, and fourth-order Runge-Kutta method where the black dots represent the estimated values and the red dots are the intermediate points . . . . .	30
2.8	Comparison of computation time between MATLAB's ODE solvers . . . . .	34
2.9	Comparison of required number of steps between MATLAB ODE solvers . . . . .	35

2.10	Comparison of magnitude difference in final position between the integrated value and Kepler's analytical solution for MATLAB's ODE solvers . . . . .	36
3.1	Configuration of the Cowell propagator . . . . .	38
3.2	Illustration of the Earth's zonal harmonics with shaded regions representing additional mass [49] . . . . .	43
3.3	Illustration of the Earth's tesseral harmonics with shaded regions representing additional mass [49] . . . . .	43
3.4	Three body configuration of position vectors between the Earth, Moon, and satellite . . . . .	51
3.5	Radial component of the gravitational perturbation, $\mathbf{a}_{J_{3-9}} \left( \frac{m}{s^2} \right)$ , due to higher order gravity up to degree 9 excluding $J_2$ with respect to latitude/longitude . . . . .	53
3.6	Earth's gravity field anomalies (mGal) as determined by GRACE [2] .	54
3.7	The gravitational pull of the Earth's equatorial bulge causes the orbital plane of an eastbound satellite to regress westward . . . . .	55
3.8	Deviation in final position (km) due to $J_{2-9}$ for circular orbits with varying altitudes and inclinations propagated over one period . . . . .	56
3.9	Deviation in final position (km) due to $J_{3-9}$ for circular orbits with varying inclinations and ascending nodes at $a = 100$ km propagated over one period . . . . .	57
3.10	Deviation in final position (km) due to $J_{3-9}$ for circular orbits with varying ascending nodes and inclinations at $a = 100$ km propagated over one period . . . . .	58
3.11	General illustration of the Earth's atmosphere with the bands representing areas of similar properties [49] . . . . .	62

3.12	Geometry used by the program <i>Shadow</i> to calculate the regions of penumbra and umbra experienced by the vehicle [49] . . . . .	65
4.1	Illustration of 180° low Earth orbit transfer between two orbits with $i = 0^\circ$ and $e = 0.1$ . . . . .	83
4.2	Individual perturbation magnitudes for 180° low Earth orbit transfer between two orbits with $i = 0^\circ$ and $e = 0.1$ . . . . .	84
4.3	Magnitude difference in predicted position error between Cowell and the state transition matrix for a LEO transfer over varying transfer times	85
4.4	Magnitude difference in predicted position error between Cowell and the state transition matrix for a LEO transfer over varying initial perturbation percentages . . . . .	86
4.5	Illustration of a 5 day translunar transfer with conditions $i_\oplus = 16^\circ$ $\Omega_\oplus = 71^\circ$ and $i_\ominus = 15^\circ$ $\Omega_\ominus = 100^\circ$ . . . . .	87
4.6	Individual perturbation magnitudes for translunar transfer between a low Earth orbit with $i = 16^\circ$ $\Omega = 71^\circ$ and a low lunar orbit with $i = 15^\circ$ $\Omega = 100^\circ$ . . . . .	88
4.7	Magnitude difference in predicted position error between Cowell and the state transition matrix for a translunar transfer over varying times	89
4.8	Magnitude difference in predicted position error between Cowell and the state transition matrix for a translunar transfer over varying initial perturbation percentages . . . . .	89
4.9	Illustration of Lambert shooting method . . . . .	91
4.10	Flow chart summary of the higher order Lambert method formulation	92
5.1	General illustration of translunar transfer between TLI and LOI . . .	94
5.2	Summary of translunar transfer velocity computation and shooting method application . . . . .	95

5.3	Definition of interior and exterior points for overlapped conic approximation . . . . .	101
5.4	Pseudostate terminals for a short segment of a translunar trajectory .	108
5.5	Pseudostate terminals for a circumlunar segment of a translunar trajectory . . . . .	109
5.6	Pseudostate terminal geometry for translunar targeting problem . . .	110
5.7	Example of EXLX Excel lunar parking orbit accessibility scan matrix	113
5.8	Example of EXLX Excel timetable scan matrix . . . . .	114
5.9	Perturbation dynamics applied in each flight phase for the EXLX and Cowell propagators over a translunar trajectory . . . . .	115
5.10	Tilt of the Earth and Moon with respect to the ecliptic plane . . . . .	116
5.11	Contour plot of lunar orbit insertion $\Delta V$ for an initial Earth orbit with $i_{\oplus} = 0^{\circ}$ and $\Omega_{\oplus} = 0^{\circ}$ . The white lines represent lunar orbit parameter regions that meet the constraint of $\Delta V_{max} = 840$ km/s . . . . .	118
5.12	Contour plot of feasible lunar orbit parameters for varying initial Earth orbit parameters . . . . .	119
5.13	Distribution of Earth and lunar orbital elements for 110 test cases . .	121
5.14	Histogram of the iteration number for the 110 translunar test cases .	122
5.15	Convergence rate for a range of translunar cases with iteration numbers within 1.5IQR as well as the rate for the three outlier cases . . . . .	123
5.16	Translunar trajectories at LOI1 for a variety of test cases . . . . .	123
5.17	Example of a translunar transfer into a lunar prograde orbit (Test Case #77) . . . . .	124
5.18	Example of a translunar transfer into a lunar retrograde orbit (Test Case #71) . . . . .	125
5.19	Histogram of the change in $ \Delta V $ required for the translunar test cases	125
5.20	Stem plot of $ \Delta V $ based on the final lunar orbit inclination . . . . .	126

5.21	Number of iterations based on initial position perturbation percentage for the translunar test cases . . . . .	127
5.22	Number of iterations based on initial velocity perturbation percentage for the translunar test cases . . . . .	128
5.23	Inclinations of lunar orbits that resulted in non-convergent solutions for varying initial velocity perturbation percentages . . . . .	129
5.24	Radial component of the gravitational perturbation, $\mathbf{a}_{J_{3-9}} \left( \frac{m}{s^2} \right)$ , due to lunar higher order gravity up to degree 9 excluding $J_2$ with respect to latitude/longitude . . . . .	130
5.25	Radial gravity field (mGal) of the Moon expanded to degree 150 with the $J_2$ term removed [51] . . . . .	131
5.26	Convergence of translunar test Case #98 , $i = 359^\circ$ , at LOI1 with 31 iterations . . . . .	132
5.27	Convergence of translunar test Case #99 , $i = 360^\circ$ , at LOI1 with 34 iterations . . . . .	132
5.28	Convergence of translunar test Case #98 , $i = 359^\circ$ , at LOI1 with 20 iterations after lunar higher order gravity is removed . . . . .	134
5.29	Convergence of translunar test Case #99 , $i = 360^\circ$ , at LOI1 with 18 iterations after lunar higher order gravity is removed . . . . .	134
5.30	Histogram comparing iteration number for test cases with lunar incli- nations $\pm 25^\circ$ with and without higher order lunar gravity coefficients applied . . . . .	135
6.1	Transfer time as a function of $x$ using Lagrange's equations for the Lambert problem solution [7] . . . . .	142
6.2	Transfer time as a function of $-S_1$ using Gauss's equations for the Lambert problem solution [7] . . . . .	144
6.3	Flow chart summary of Lambert 2-body dynamic formulation . . . . .	146

6.4	Example of low Earth initial and final orbits for a variety of eccentricities and inclinations . . . . .	148
6.5	Example of the range of transfer angles tested for low Earth orbit trajectories . . . . .	149
6.6	Histogram of the iteration number for the 1050 low Earth orbit test cases	151
6.7	Convergence rate for a range of LEO cases with iteration numbers within 1.5IQR as well as the range of the outlier cases . . . . .	152
6.8	Histogram of iteration numbers based on final low Earth orbit altitude	153
6.9	Histogram of iteration numbers based on initial/final low Earth orbit eccentricity . . . . .	154
6.10	Histogram of iteration numbers based on initial/final low Earth orbit inclinations . . . . .	154
6.11	Histogram of iteration numbers based on initial low Earth orbit true anomalies . . . . .	155
6.12	Histogram of the change in $ \Delta V $ required for the low Earth orbit test cases . . . . .	157
6.13	Histogram of LEO cases comparing change in transfer velocity from two-body Lambert initial guess based on final orbit altitude . . . . .	158
6.14	Histogram of LEO cases comparing change in transfer velocity from two-body Lambert initial guess based on initial/final orbit eccentricity	159
6.15	Histogram of LEO cases comparing change in transfer velocity from two-body Lambert initial guess based on initial/final orbit inclination	159
6.16	Histogram of LEO cases comparing change in transfer velocity from two-body Lambert initial guess based on initial orbit true anomaly . .	160
6.17	Number of iterations based on initial position perturbation percentage for the LEO test cases . . . . .	161

6.18	Number of iterations based on initial velocity perturbation percentage for the LEO test cases . . . . .	161
6.19	Convergence failure for a LEO trajectory between two circular orbits with a transfer angle of $180^\circ$ and an inclination of $30^\circ$ . . . . .	163
6.20	Illustration of Rosenbrock's function plotted over two variables [52] .	164
6.21	Contour plot illustrating the position error (km) in the y-z plane due to an initial velocity perturbation (km/s) for an orbit with $\nu = 180^\circ$ and $i = 45^\circ$ . . . . .	165
6.22	Contour plot illustrating position error (km) less than 200 km in the y-z plane due to an initial velocity perturbation (km/s) for an orbit with $\nu = 180^\circ$ and $i = 45^\circ$ . . . . .	165
6.23	Contour plot illustrating the position error (km) in the y-z plane due to an initial velocity perturbation (km/s) for an orbit with $\nu = 160^\circ$ and $i = 45^\circ$ . . . . .	166
6.24	Contour plot illustrating position error (km) less than 200 km in the y-z plane due to an initial velocity perturbation (km/s) for an orbit with $\nu = 160^\circ$ and $i = 45^\circ$ . . . . .	167
7.1	Spheres of influence for the Sun, Mercury, Venus, Earth, Moon, and Mars. . . . .	174
A.1	Feasible lunar orbit parameters for an initial Earth orbit with varying inclinations and $\Omega_\oplus = 0^\circ$ . . . . .	178
A.2	Feasible lunar orbit parameters for an initial Earth orbit with varying inclinations and $\Omega_\oplus = 45^\circ$ . . . . .	178
A.3	Feasible lunar orbit parameters for an initial Earth orbit with varying inclinations and $\Omega_\oplus = 90^\circ$ . . . . .	179



A.4	Feasible lunar orbit parameters for an initial Earth orbit with varying inclinations and $\Omega_{\oplus} = 135^{\circ}$ . . . . .	179
A.5	Feasible lunar orbit parameters for an initial Earth orbit with varying inclinations and $\Omega_{\oplus} = 180^{\circ}$ . . . . .	180
A.6	Feasible lunar orbit parameters for an initial Earth orbit with varying inclinations and $\Omega_{\oplus} = 225^{\circ}$ . . . . .	180
A.7	Feasible lunar orbit parameters for an initial Earth orbit with varying inclinations and $\Omega_{\oplus} = 270^{\circ}$ . . . . .	181
A.8	Feasible lunar orbit parameters for an initial Earth orbit with varying inclinations and $\Omega_{\oplus} = 315^{\circ}$ . . . . .	181
D.1	Contour plot illustrating the position error (km) in the x-z plane due to an initial velocity perturbation (km/s) for an orbit with $\nu = 180^{\circ}$ and $i = 45^{\circ}$ . . . . .	189
D.2	Contour plot illustrating position error (km) less than 200 km in the x-z plane due to an initial velocity perturbation (km/s) for an orbit with $\nu = 180^{\circ}$ and $i = 45^{\circ}$ . . . . .	189
D.3	Contour plot illustrating the position error (km) in the x-y plane due to an initial velocity perturbation (km/s) for an orbit with $\nu = 180^{\circ}$ and $i = 45^{\circ}$ . . . . .	190
D.4	Contour plot illustrating position error (km) less than 200 km in the x-y plane due to an initial velocity perturbation (km/s) for an orbit with $\nu = 180^{\circ}$ and $i = 45^{\circ}$ . . . . .	190
D.5	Contour plot illustrating the position error (km) in the x-z plane due to an initial velocity perturbation (km/s) for an orbit with $\nu = 160^{\circ}$ and $i = 45^{\circ}$ . . . . .	191

D.6	Contour plot illustrating position error (km) less than 200 km in the x-z plane due to an initial velocity perturbation (km/s) for an orbit with $\nu = 160^\circ$ and $i = 45^\circ$ . . . . .	191
D.7	Contour plot illustrating the position error (km) in the x-y plane due to an initial velocity perturbation (km/s) for an orbit with $\nu = 160^\circ$ and $i = 45^\circ$ . . . . .	192
D.8	Contour plot illustrating position error (km) less than 200 km in the x-y plane due to an initial velocity perturbation (km/s) for an orbit with $\nu = 160^\circ$ and $i = 45^\circ$ . . . . .	192

# List of Tables

2.1	Characteristics of orbital parameters for specific orbit type . . . . .	9
2.2	MATLAB fixed-step continuous solvers . . . . .	33
3.1	Comparison of NASA and High Order Gravity model prediction position deviation . . . . .	59
3.2	Summary of effects for setting different parameters in the Higher Order Gravity model . . . . .	60
3.3	Required parameter definitions for higher order gravity model initialization . . . . .	60
3.4	Value of the solar radiation parameter $\nu$ based on the shadow type . . . . .	66
4.1	List of varying fidelity state transition matrices tested for selection purposes . . . . .	79
4.2	Initial conditions for low Earth orbit state transition matrix time accuracy test . . . . .	82
4.3	Initial conditions for translunar state transition matrix time accuracy test . . . . .	85
5.1	User selected parameters for EXLX Excel interface for three-burn sequence . . . . .	112
5.2	Selected parameter values for translunar test cases . . . . .	117

6.1	Variation in initial and final orbit parameters for testing LEO cases .	147
6.2	List of time of flights used for Lambert routine based on orbital elements	150
C.1	List of parameters for translunar test cases . . . . .	187

# Chapter 1

## Introduction

In the field of astrodynamics well-known tools exist to determine the initial and final conditions required to transfer a spacecraft from one orbit to another. Lambert's method is one general example that determines the orbit between two position vectors and a known time of flight [31]. Another option is the Hohmann transfer, which provides a quick solution for required transfer velocities between coplanar circular orbits, and it has the added advantage of calculating the necessary time of flight [14]. Figure 1.1 illustrates a simple example of this method of transfer. The disadvantage of these generalized methods is that they usually assume simplified planar two-body motion, and thus their results provide good initial guesses but not actual feasible solutions when applied to real situations. By neglecting higher order perturbations such as the gravity potential or three-body acceleration, these nominal transfer models fail to consider how the states will change outside of conic motion over the period of flight. It is of interest to expand these basic models to add accuracy and realism to predicted transfer trajectories.

Applications requiring increased complexity in trajectory propagation are abundant. They include problems such as determining probable Space Shuttle launch

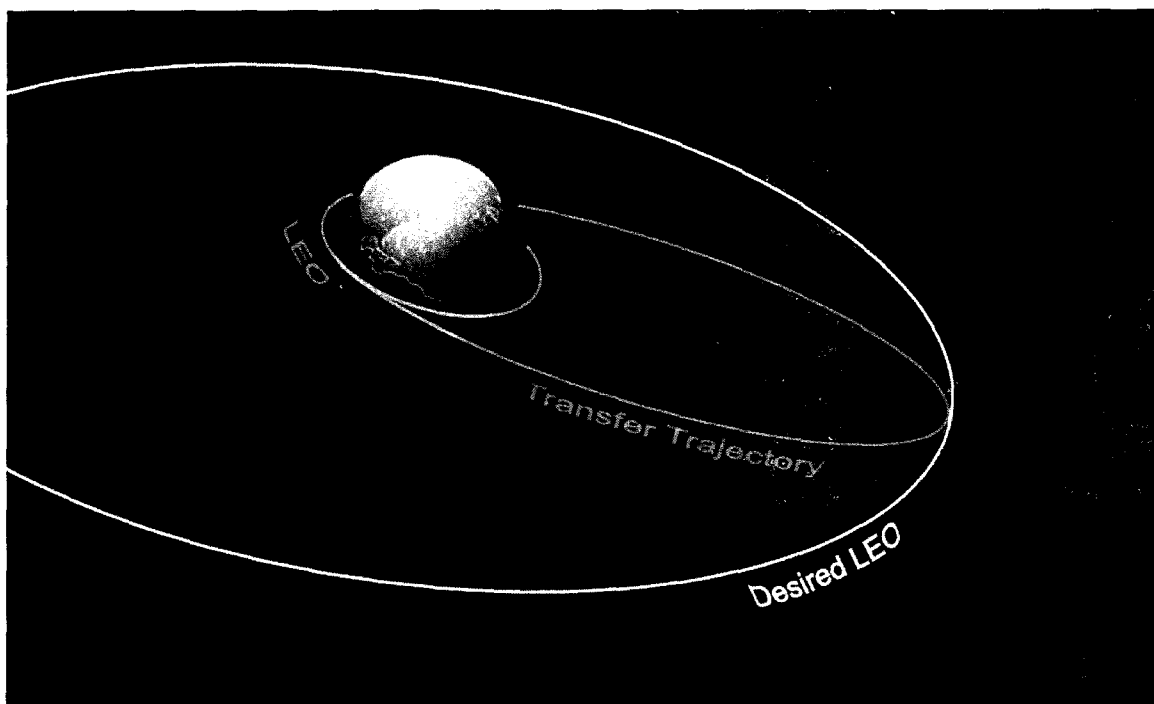


Figure 1.1: Illustration of a generalized Hohmann transfer between two low Earth orbits

windows based on the location of the International Space Station (ISS), assessing the degradation of satellites in low Earth orbit, and calculating target accuracy for ballistic missiles. When exploratory probes or robotics are sent on interplanetary missions, such as those to Mars and Pluto, a high level of landing accuracy is imperative when entering various atmospheric domains. Even more important is to realistically model costly manned flights. From low Earth orbit missions needing precise knowledge of both the target and chaser states for transfers to the ISS to missions to the Moon which call for distinct orbit insertion conditions, a high degree of accuracy results in less navigation correction and an overall less expensive flight.

To achieve the level of accuracy necessary to model realistic low Earth orbit and translunar trajectories, the complexity of the system must increase beyond planar two-body motion. This is accomplished by developing a propagator that includes at a minimum the following higher order perturbations:  $n$ -body acceleration, non-conic gravity, atmospheric drag, and solar radiation pressure. Numerical integration

techniques can be utilized to account for these perturbations, however resolving the trajectory of the vehicle to arrive at a specified target becomes a complicated task as the motion becomes non-Keplerian.

When a high order propagator is used to determine the final states of a trajectory based on initial conditions calculated from simplistic models, the predicted final position will not match the actual propagated one. Assuming the initial position and departure time cannot change, the transfer velocity must then be updated to fly out a more accurate trajectory to intersect the desired final position. Utilizing linear assumptions, the state transition matrix provides sensitivity information about the transfer trajectory which can be used to assist in correcting the initial velocity guess based on the error between the propagated and desired final position. Once the velocity is updated the trajectory is flown out again and the position error is recalculated. This process, known as a shooting method [8], continues until the error is within a predefined tolerance. The transfer velocity that results from a “converged” solution is the most accurate velocity for the fidelity level of perturbations included in the model. The multi-functionality of this predictor-corrector method is demonstrated by applying it to low Earth orbit and translunar cases.

The objective of this thesis is to develop an efficient, high fidelity propagator for use in targeting and prediction applications with the capability to handle low Earth orbit and translunar trajectories. In conjunction with low fidelity targeting tools such as Lambert’s method for low Earth orbits and Johnson Space Center’s “EXLX” for translunar trajectories (see Figure 1.2) [15], the propagator will adjust the initial velocities predicted by the tools utilizing the correcting capabilities of a state transition matrix. Applying a shooting method to converge on a more accurate solution, the propagator acting as the predictor and the state transition matrix acting as the corrector, produce a more accurate initial velocity required to reach a set final position. The increased accuracy is based upon the higher order perturbation

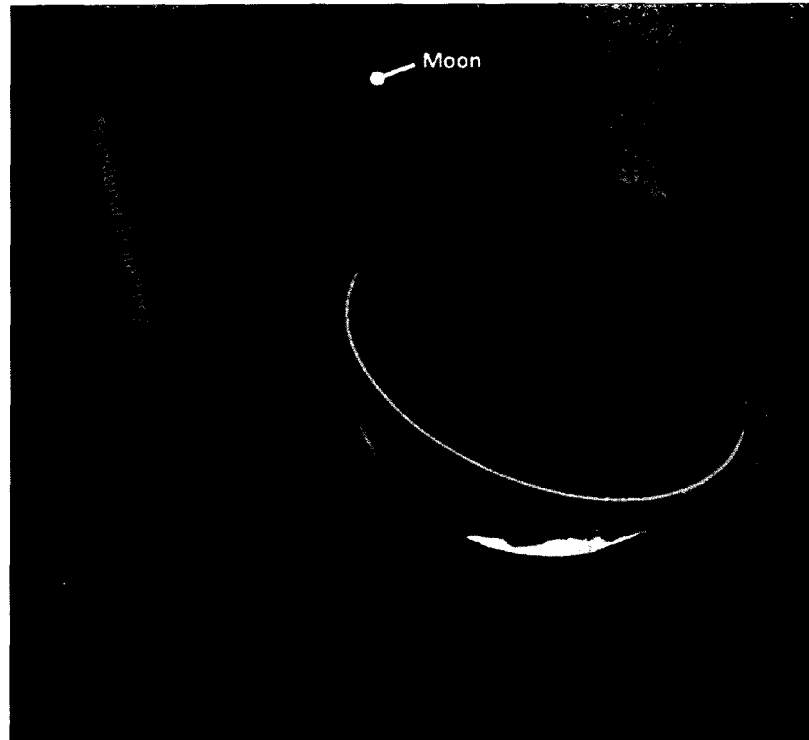


Figure 1.2: Illustration of a generalized translunar transfer

models utilized by the Keplerian propagator which are not taken into consideration by the low fidelity targeting schemes. The maximum error handling of the predictor-corrector will be demonstrated to quantify the accuracy of the initial guess to produce a converged solution. An additional key capability of the tool includes the output of the trajectory states over the transfer period. These values are relevant to applications such as navigation performance, velocity trade studies, or mission planning. Since the output frequency of the states is configurable, the generated trajectories are beneficial as reference trajectories in dynamic simulations as well.

The purpose of this thesis is to develop a high order propagator that can be utilized in conjunction with an error state transition matrix to predict feasible initial states for low Earth orbit and translunar trajectories. Chapter 2 begins with an introduction of the classical orbital elements and Kepler's problem. It continues with an overview of special perturbation techniques. The section covers the various perturbation methods utilized as well as the numerical integrators chosen for this research. Chapter 2 also



identifies the errors that are inherent in utilizing any form of numerical integration.

Chapter 3 discusses the development of the propagator model in MATLAB to include the perturbation models for n-body motion, higher order gravity, drag, and solar pressure.

Chapter 4 introduces the formulation of the state transition matrix to include the calculation of the partial derivatives for the perturbations. The accuracy of the state transition matrix over varying times of flight and initial perturbation percentages is demonstrated. The shooting method is also introduced.

The following two chapters demonstrate the capability of the predictor-corrector for translunar (Chapter 5) and low Earth orbit transfers (Chapter 6). Each chapter tests a variety of transfers as well as the sensitivity of the algorithm to initial perturbations.

Finally, Chapter 7 summarizes the findings of this research and makes recommendations for future work to include implementing a higher order propagator, utilizing a more accurate state transition matrix, and modeling finite burn effects through the use of two level targeting.

# Chapter 2

## Special Perturbation Techniques

Defining the state of a space vehicle is the first step to understanding orbital motion. At a minimum, six quantities are required to define the state. The two most popular representations of these quantities are the state vector which includes a position,  $\mathbf{r}$ , and velocity vector,  $\mathbf{v}$ ,

$$\mathbf{X} = \begin{bmatrix} \mathbf{r} \\ \mathbf{v} \end{bmatrix} \quad (2.1)$$

and the classical orbital element set which uses the scalar magnitude and angular representations of the orbital elements to describe the motion. Here and for the remainder of all equations in this paper, vectors are distinguished from scalar values with the use of bold text. Matrices are indicated by capitalized bold text.

### 2.1 Orbital Elements

The six classical orbital elements are semimajor axis ( $a$ ), eccentricity ( $e$ ), inclination ( $i$ ), right ascension of ascending node ( $\Omega$ ), argument of perigee ( $\omega$ ), and true anomaly ( $\nu$ ) [49]. The elements, excluding  $a$  and  $e$ , are illustrated in Figure 2.1.

To understand the semimajor axis, one must look at the geometry of a conic section. A conic section is the curve generated by the intersection of a plane and a

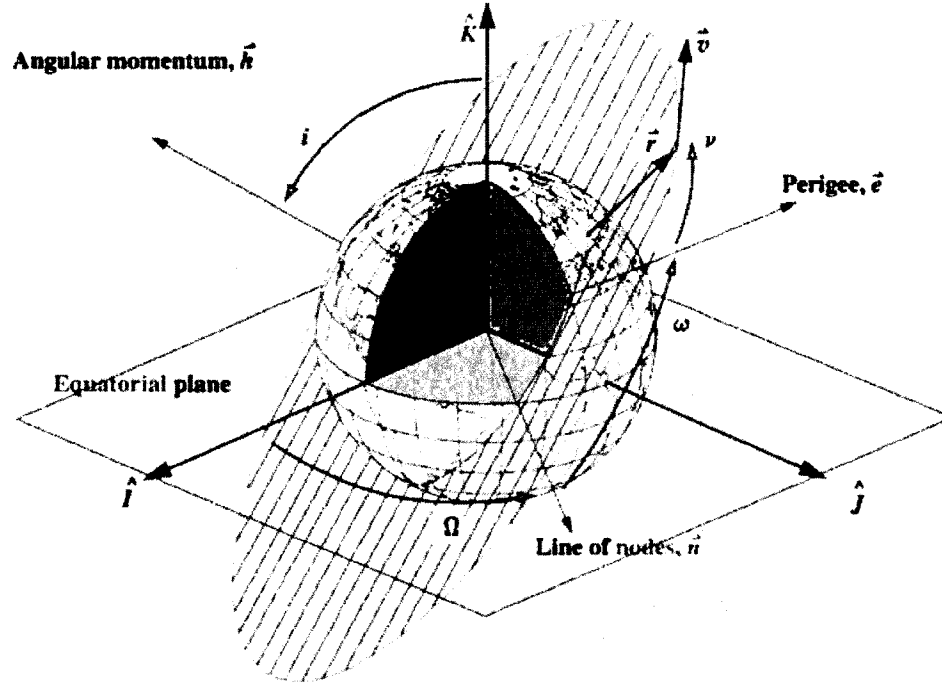


Figure 2.1: Illustration of the classic orbital elements: inclination ( $i$ ), right ascension of ascending node ( $\Omega$ ), argument of perigee ( $\omega$ ), and true anomaly ( $\nu$ ) [49]

right circular cone. Based on where the plane intersects the cone, four unique conic sections are created which represent all possible conics. These four sections make up circular, elliptical, parabolic, and hyperbolic orbits. Every conic section has two foci, illustrated as  $F$  and  $F'$  in the elliptical conic in Figure 2.2. In the field of astrodynamics, the gravitational center of attraction is located at the primary focus,  $F$ , and thus is illustrated as the center of the Earth in Figure 2.2. The semimajor axis is half the distance of the major axis, and is used to describe the size of the orbit. The directrix is the distance from each focus to a fixed line. The ratio of the distance of the focus from the orbit to the distance from the directrix is the eccentricity. The eccentricity of an orbit describes its shape and from Figure 2.2 is

$$e = \frac{c}{a} \quad (2.2)$$

where  $c$  is the half distance between the foci.

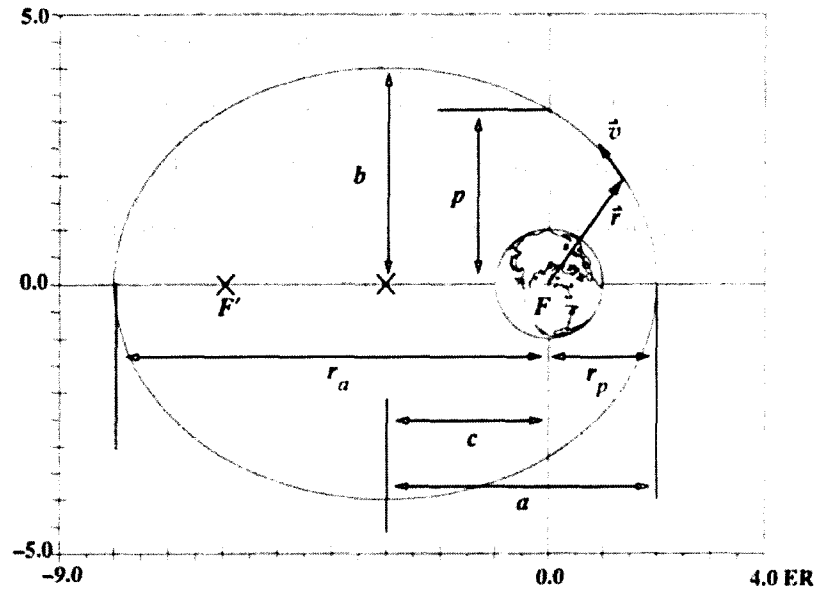


Figure 2.2: Elliptical orbit conic section illustrating the two foci,  $F$  and  $F'$ , as well as the semimajor axis,  $(a)$  [49]

The distance from the primary focus to the extreme points of an elliptical orbit are known as the radius of apoapsis,  $r_a$ , and radius of periapsis,  $r_p$ , which represent the distance from farthest and nearest points respectively. The inclination,  $i$ , refers to the tilt of the orbit plane and is the angle measured from the unit vector  $\hat{K}$  and the specific angular momentum vector,  $\mathbf{h}$

$$\mathbf{h} = \mathbf{r} \times \mathbf{v}. \quad (2.3)$$

The right ascension of the ascending node,  $\Omega$ , is the angle measured from the Earth's equatorial plane to the ascending node. The ascending node is the point on the equatorial plane at which the satellite crosses from the south to the north. For equatorial orbits the node does not exist and thus the right ascension of ascending node is undefined. The argument of perigee,  $\omega$ , is the angle from the ascending node to the periapsis. For circular orbits in which the periapsis is undefined and for equatorial orbits in which there is no ascending node, the argument of perigee

is undefined. Finally, the true anomaly,  $\nu$ , is the angle between the periapsis and the position vector of the satellite in the direction of motion. For circular orbits this element is undefined. Table 2.1 illustrates the possible values for the semimajor axis, eccentricity, and true anomaly for the four types of possible orbits.

Orbit	a	e	$\nu$
Circle	$a = r$	$e = 0$	Undefined
Ellipse	$r_p \leq a \leq r_a$	$0 < e < 1$	$0^\circ \leq \nu \leq 360^\circ$
Parabola	$a \rightarrow \infty$	$e = 1$	Limited
Hyperbola	$a < 0$	$e > 1$	Limited

Table 2.1: Characteristics of orbital parameters for specific orbit type

## 2.2 Two-body Equations of Motion

An elementary knowledge of two-body motion must be understood before analyzing the forces that alter it. The foundation of the problem is Newton's second law which states that the time rate of change of linear momentum is proportional to the force applied [49]. Thus, for a system whose mass is unchanging, Newton's law is

$$\sum \mathbf{F} = \frac{d(m\mathbf{v})}{dt} = m\mathbf{a}. \quad (2.4)$$

Newton's law of universal gravitation determines the components of the force vector if the system is only acted upon by gravity. Assuming an inertial system with two bodies, the Earth with mass,  $m_\oplus$ , and the satellite with mass,  $m_{sat}$ , the force of gravity acting on the satellite due to the Earth is written as

$$\mathbf{F}_g = -\frac{Gm_\oplus m_{sat}}{r_{\oplus sat}^3} \mathbf{r}_{\oplus sat} \quad (2.5)$$

where  $G$  is the universal gravitation constant. The position vectors of the Earth and satellite from the origin of the coordinate system are  $\mathbf{r}_\oplus$  and  $\mathbf{r}_{sat}$  respectively, thus

the position vector of the satellite with respect to the Earth can be written as

$$\mathbf{r}_{\oplus sat} = \mathbf{r}_{sat} - \mathbf{r}_{\oplus}. \quad (2.6)$$

Utilizing an inertial coordinate system, the second derivative of Equation 2.6 produces the acceleration of the satellite relative to the Earth

$$\ddot{\mathbf{r}}_{\oplus sat} = \ddot{\mathbf{r}}_{sat} - \ddot{\mathbf{r}}_{\oplus}. \quad (2.7)$$

Plugging the accelerations into Equation 2.4 and setting the results equal to Equation 2.5 gives

$$\mathbf{F}_{g_{sat}} = m_{sat} \ddot{\mathbf{r}}_{sat} = -\frac{Gm_{\oplus}m_{sat}}{r_{sat}^3} \mathbf{r}_{sat} \quad (2.8)$$

$$\mathbf{F}_{g_{\oplus}} = m_{\oplus} \ddot{\mathbf{r}}_{\oplus} = -\frac{Gm_{\oplus}m_{sat}}{r_{\oplus}^3} \mathbf{r}_{\oplus}.$$

Solving for the individual accelerations in Equation 2.8 and substituting these values into Equation 2.7, the relative acceleration

$$\ddot{\mathbf{r}}_{\oplus sat} = -\frac{G(m_{\oplus} + m_{sat})}{r_{\oplus sat}^3} \mathbf{r}_{\oplus sat} \quad (2.9)$$

is found. Assuming the mass of the satellite is significantly smaller than the mass of the Earth,  $m_{sat}$  can be neglected. Furthermore, the quantity  $Gm_{\oplus}$  can be replaced by the gravitational constant  $\mu$ , resulting in the relative form of the two-body equation of motion,

$$\ddot{\mathbf{r}}_{\oplus sat} = -\frac{\mu}{r_{\oplus sat}^3} \mathbf{r}_{\oplus sat}. \quad (2.10)$$

Equation 2.10 assumes no other forces act on the system except for gravitational forces between the Earth and satellite. Kepler's laws, which form the foundation for Kepler's equation, provide the necessary conditions for all two-body motion.

## 2.3 Kepler's Equation

Kepler's equation determines the relation between time and angular displacement within an orbit. To calculate the unknown area swept out by a satellite in an elliptical orbit, Kepler applied his second law that states equal areas are swept out in equal times, that is

$$\frac{\Delta t}{A_1} = \frac{P}{\pi ab} \quad (2.11)$$

where  $P$  is the orbit period

$$P = 2\pi \sqrt{\frac{a^3}{\mu}}, \quad (2.12)$$

with  $a$  and  $b$  being the semimajor and semiminor axes of the ellipse, and  $A_1$  denoting the unknown area. Figure 2.3 depicts the geometry of Kepler's equation used to solve for  $A_1$ . The circle drawn around the ellipse is an auxiliary circle and the new angle,  $E$ , is the eccentric anomaly which is specified with respect to the true anomaly,  $\nu$ , as illustrated. Using geometric and trigonometric relations as well as the definition of the period of a satellite, Kepler's equation is recast in the form [49]

$$\sqrt{\frac{a^3}{\mu}} = \frac{\Delta t}{E - e \sin(E)}. \quad (2.13)$$

Here the mean anomaly,  $M$ ,

$$M = E - e \sin(E) = \sqrt{\frac{\mu}{a^3}} \Delta t \quad (2.14)$$

is introduced, which is a transcendental function that must be solved numerically. Equation 2.14 establishes the mean motion,  $n$ , as the mean angular rate of orbital motion,

$$n = \sqrt{\frac{\mu}{a^3}}. \quad (2.15)$$

From Kepler's equation arises the classical orbital dynamics two-body problem:

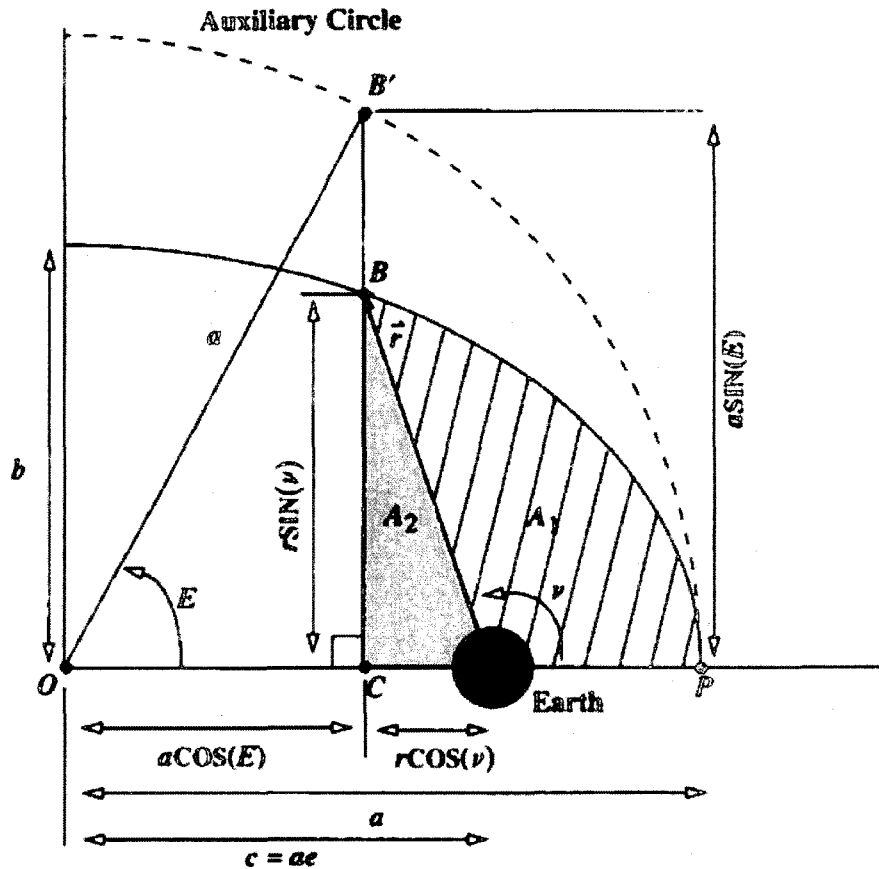


Figure 2.3: Geometry of Kepler's equation [49]

given initial states,  $\mathbf{r}_0$  and  $\mathbf{v}_0$ , find the states  $\mathbf{r}$  and  $\mathbf{v}$  after an arbitrary transfer time,  $\Delta t$ . For two-body motion there exist many analytical solutions to Kepler's problem including using orbital elements or the  $f$  and  $g$  functions [49]. The disadvantage of these two methods is that they are limited to specific orbit types. Following Bate Mueller and White [6] as well as Battin [7], Vallado [49] uses elements from both methods to present a universal formulation that is valid for all orbit types.

Vallado begins with the specific mechanical energy,

$$\xi = \frac{\mathbf{v}_0^2}{2} - \frac{\mu}{r_0} \quad (2.16)$$



and defines the variable  $\alpha$  as

$$\alpha = \frac{-\mathbf{v}_0^2}{\mu} + \frac{2}{r_0}. \quad (2.17)$$

Here  $\alpha$  is used to avoid calculating the eccentricity to determine the orbit kind in the initial guess. Depending on the value of  $\alpha$ , different algorithms are used to calculate the universal variable,  $\chi$ . If the orbit is circular or elliptical ( $\alpha > 0.000001$ ), the variable is approximated as

$$\chi_0 \approx \sqrt{\mu}(\Delta t)\alpha. \quad (2.18)$$

For parabolic orbits ( $\alpha < 0.000001$ ) the specific angular momentum  $\mathbf{h} = \mathbf{r}_0 \times \mathbf{v}_0$  is calculated to find the semiparameter,  $p$ ,

$$p = \frac{h^2}{\mu}. \quad (2.19)$$

The values are needed to solve for the angles  $w$  and  $s$  in Barker's equation

$$\cot(2s) = 3\sqrt{\frac{\mu}{p^3}}(\Delta t) \quad (2.20)$$

$$\tan^3(w) = \tan(s) \quad (2.21)$$

and are used to approximate the universal variable

$$\chi \approx \sqrt{p} 2 \cot(2w). \quad (2.22)$$

Finally, if the orbit is hyperbolic ( $\alpha < -0.000001$ ), the semimajor axis is defined as  $a = \frac{1}{\alpha}$  and

$$\chi_0 = \text{sign}(\Delta t)\sqrt{-a} \ln \left\{ \frac{-2\mu\alpha(\Delta t)}{r_0 \cdot \mathbf{v}_0 + \text{sign}(\Delta t)\sqrt{-\mu a}(1 - r_0\alpha)} \right\}. \quad (2.23)$$

Next the variable  $\psi$  is defined as

$$\psi = \chi_n^2 \alpha \quad (2.24)$$

and used to calculate a family of functions,  $c_2$  and  $c_3$ ; if  $\psi > 1 \times 10^{-6}$ ,

$$c_2 = \frac{1 - \cos(\sqrt{\psi})}{\psi} \quad c_3 = \frac{\sqrt{\psi} - \sin(\sqrt{\psi})}{\sqrt{\psi^3}}, \quad (2.25)$$

if  $\psi < -1 \times 10^{-6}$ ,

$$c_2 = \frac{1 - \cosh(\sqrt{-\psi})}{\psi} \quad c_3 = \frac{\sinh(\sqrt{-\psi}) - \sqrt{-\psi}}{\sqrt{(-\psi)^3}}, \quad (2.26)$$

and in all other cases  $c_2 = \frac{1}{2}$  and  $c_3 = \frac{1}{6}$ . The function values are used in the position equation

$$r = \chi_n^2 c_2 + \frac{\mathbf{r}_0 \cdot \mathbf{v}_0}{\sqrt{\mu}} \chi_n (1 - \psi c_3) + r_0 (1 - \psi c_2) \quad (2.27)$$

which updates the universal variable

$$\chi_{n+1} = \chi_n + \frac{\sqrt{\mu} \Delta t - \chi_n^3 c_3 - \frac{r_0 v_0}{\sqrt{\mu}} \chi_n^2 c_2 - r_0 \chi_n (1 - \psi c_3)}{r}. \quad (2.28)$$

The value of  $\chi_{n+1}$  replaces the previous value of  $\chi_n$  and Equations 2.24-2.28 are iterated until  $|\chi_n - \chi_{n+1}| < 1 \times 10^{-6}$ . Defining the  $f$  and  $g$  functions as

$$f = 1 - \frac{\chi_n^2}{r_0} c_2, \quad (2.29)$$

with

$$\dot{f} = \frac{\sqrt{\mu}}{r r_0} \chi_n (\psi c_3 - 1); \quad (2.30)$$

and

$$g = \Delta t - \frac{\chi_n^3}{\sqrt{\mu}} c_3, \quad (2.31)$$

with

$$\dot{g} = 1 - \frac{\chi_n^2}{r} c_2 \quad (2.32)$$

the final position and velocity vectors are calculated using the equations

$$\mathbf{r} = f\mathbf{r}_0 + g\mathbf{v}_0 \quad (2.33)$$

$$\mathbf{v} = \dot{f}\mathbf{r}_0 + \dot{g}\mathbf{v}_0. \quad (2.34)$$

This general formulation analytically predicts orbital states for any satellite motion about a central body. However, in actual spaceflight additional forces act causing significant perturbations from the Keplerian trajectory. Unfortunately no closed form solutions to these perturbed equations of motion are known to exist and as a result they must be solved numerically. The following section will discuss the development of equations of motion that include dominant perturbations and the numerical methods that are commonly used to find solutions for the general problem.

## 2.4 Equations of Motion with Perturbations

Disturbing accelerations from non-Keplerian effects such as the gravitational attraction of other planets, the non-spherical shape of the Earth, atmospheric drag, and even solar radiation cause deviations from the conic two-body trajectory presented in Section 2.3. As a consequence of these deviations, the two-body equations of motion are insufficient to accurately solve trajectory problems. The magnitude of a perturbation does not need to be large to greatly affect a trajectory. For example, over time the trajectory of a satellite in low Earth orbit will drift due to the oblateness of the Earth. If the effects of this uneven mass distribution were ignored in planning the initial trajectory, the satellite's orbit could degrade until the vehicle burned up in the Earth's atmosphere.

Perturbation analysis has played an important role throughout history in the study of celestial bodies. In 1619, Johannes Kepler theorized that comet tails were pushed outwards from the Sun due to pressure from sunlight; a theory that is qualitatively the same as our current view of solar radiation pressure [32]. At the end of the 18th century Pierre-Simon Laplace made significant developments to the modeling of Earth's gravitational field with his contribution to the potential function. Additional progress into the gravitational-potential problem was made in 1783 when Adrain Marie Legendre published his solutions to differential equations arising from his studies on the attraction of spheroids. In 1849, Sir George Gabriel Stokes published a formula which determined the shape of a geoid based on the known local gravity anomalies [49]. E.M. Brown's papers of 1897-1908 explained the perturbative effect of the oblateness of the Earth and Moon on the Moon's orbit. In the mid-19th century the English astronomer John Couch Adams and the French astronomer Urbain-Jean-Joseph Le Verrier separately used the method of variation of parameters to study the irregularities of the motion of Uranus. Their observations and calculations eventually led to the discovery of the new planet Neptune which was the cause of the deviations in Uranus's orbit. Calculating the perturbations caused by Jupiter and Saturn, Alexis Clairault made the first accurate prediction of the return of Halley's Comet in 1759 [6]. These few examples underline the necessity of including perturbations in targeting and prediction analysis.

There are two approaches to solving equations of motion with perturbations: the "general perturbation" approach and the "special perturbation" approach. The general perturbation technique is an analytical expansion and integration of the equations of variations of orbit parameters. The special perturbation process is a step-by-step numerical integration. Though the general perturbation approach will be briefly reviewed, the research of this thesis relies upon a basic special perturbation process known as Cowell's method.

## 2.5 Cowell's Method

Cowell's method is a step-by-step numerical integration of the two-body equations of motion, including a general disturbing acceleration term [17]. The equation of motion to include the disturbing "perturbing" accelerations is

$$\ddot{\mathbf{r}} + \frac{\mu}{r^3}\mathbf{r} = \mathbf{a}_p, \quad (2.35)$$

where  $\mu$  is the gravitational constant of the central body and  $\mathbf{a}_p$  is a linear combination of all the perturbation accelerations. For numerical integration Equation 2.35 is reduced to the first-order system of differential equations

$$\dot{\mathbf{r}} = \mathbf{v} \quad (2.36)$$

and

$$\dot{\mathbf{v}} = -\frac{\mu}{r^3}\mathbf{r} + \mathbf{a}_p. \quad (2.37)$$

Cowell's method has many advantages, the foremost being its simplicity of formulation and implementation. The method is most efficient if  $\mathbf{a}_p$  is of the same order of magnitude or higher than the dominant gravitational acceleration. If  $\mathbf{a}_p$  is small the method becomes inefficient as smaller integration steps must be taken to maintain accuracy which results in an increase in computation time and accumulative error due to roundoff [7]. Roundoff and truncation error will be discussed in further detail in Section 2.8.1. One way to slightly mitigate the error is to apply Cowell's method with polar or spherical coordinates instead of the classically implemented Cartesian coordinates [6]. With these coordinate systems, the radius from the Earth to the vehicle,  $r$ , tends to vary slowly and the angle change is always monotonic. This allows larger integration steps, and thus less computational time, for the same truncation

error. The equations of motion in spherical coordinates  $(r, \theta, \phi)$  are:

$$\begin{aligned} \ddot{r} - r(\dot{\theta}^2 \cos^2 \phi + \dot{\phi}^2) &= -\frac{\mu}{r^2} \\ r\ddot{\theta} \cos \phi + 2\dot{r}\dot{\theta} \cos \phi - 2r\dot{\theta}\dot{\phi} \sin \phi &= 0, \end{aligned} \quad (2.38)$$

where the angles  $\theta$  and  $\phi$  are defined in Figure 2.4.

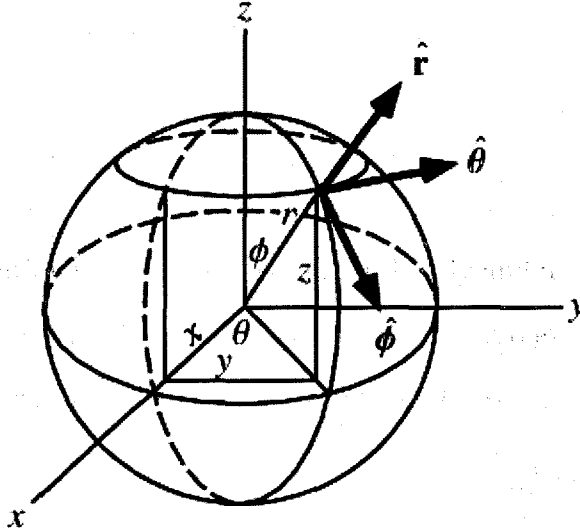


Figure 2.4: A representation of a spherical coordinate system [53]

Depending on the trajectory,  $\mathbf{a}_p$  can be orders of magnitude smaller than the dominant gravitational force. This occurs in low Earth orbit where the effect of Earth's oblateness is three orders of magnitude smaller than the spherical gravity acceleration [43]. In other words, looking at Equation 2.37, the two-body term,  $-\frac{\mu}{r^3}$ , has a much larger value than  $\mathbf{a}_p$ . Though Cowell's method will accurately integrate the effects of all the accelerations, it does not consider the benefit of integrating the perturbation separately from the two-body term. Since the two-body term dominates, most of the computational time will be spent integrating this piece. However, since an analytical solution exists for the two-body equations the expensive numerical integration of the dominating term can be avoided. Encke's method, which is another basic scheme in the special perturbation category, takes advantage of this benefit. As a result, Encke's

method requires fewer integration steps over a specified  $\Delta t$  to get the same accuracy as Cowell.

## 2.6 Encke's Method

Whereas Cowell's method integrates the sum of all the accelerations, Encke's method integrates the difference between the primary gravitational acceleration and all perturbing accelerations. Encke's method begins with an "osculating orbit" which is the conic path the orbit would make if no disturbing acceleration exerted an influence on the vehicle (see Section 2.2). However, the true motion of the vehicle will not take place along the osculating orbit, but will differ from the associated position in the conic orbit by an amount corresponding to the central body force. This concept is utilized to calculate the perturbed orbit [42].

At time  $t_0$ , the perturbed orbit is equal to the osculating orbit,

$$\mathbf{r} = \mathbf{r}_{osc} \quad \mathbf{v} = \mathbf{v}_{osc}. \quad (2.39)$$

At some time later,  $t = t_0 + \Delta t$ , the perturbed orbit has moved away some distance,  $\delta\mathbf{r}$ , and velocity,  $\delta\mathbf{v}$ , from the osculating orbit. See Figure 2.5 for clarification, where  $\delta\mathbf{r} = \boldsymbol{\delta}(t)$ . Thus at any time, the position and velocity vectors of the true orbit are given by the vector sum of the two-body and perturbed components. Specifically,

$$\mathbf{r} = \mathbf{r}_{osc} + \delta\mathbf{r} \quad \mathbf{v} = \mathbf{v}_{osc} + \delta\mathbf{v}. \quad (2.40)$$

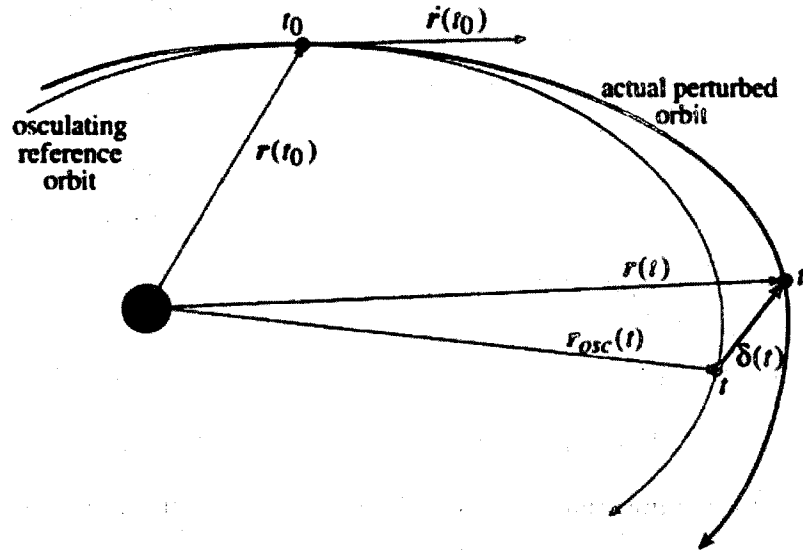


Figure 2.5: Vector definition for Encke's method [43]

To calculate  $\delta \mathbf{r}$ , start with the two-body and perturbed accelerations

$$\ddot{\mathbf{r}}_{osc} = -\frac{\mu}{r_{osc}^3} \mathbf{r}_{osc} \quad \ddot{\mathbf{r}} = -\frac{\mu}{r^3} \mathbf{r} + \mathbf{a}_p \quad (2.41)$$

where once again  $\mathbf{a}_p$  denotes the perturbation acceleration vector. The difference between the two types of orbital motion satisfies the differential equation

$$\delta \ddot{\mathbf{r}} = \mathbf{a}_p + \frac{\mu}{r_{osc}^3} \left\{ \left( 1 - \frac{r_{osc}^3}{r^3} \right) \mathbf{r} - \delta \mathbf{r} \right\}. \quad (2.42)$$

It is difficult to accurately calculate the coefficient of  $\mathbf{r}$  because Equation 2.42 essentially takes the difference of two nearly identical numbers resulting in roundoff error. This obstacle is circumvented by employing the approximate technique set forth by Battin [7]. Specifically,

$$\mathbf{r} = \mathbf{r}_{osc} + \delta \mathbf{r} \quad (2.43)$$

thus one can write that

$$1 - \frac{r_{osc}^3}{r^3} = -f(q) = 1 - (1 + q)^{\frac{3}{2}}, \quad (2.44)$$



where

$$q = \frac{\delta \mathbf{r} \cdot (\delta \mathbf{r} - 2\mathbf{r})}{\mathbf{r} \cdot \mathbf{r}}. \quad (2.45)$$

The function  $f(q)$  can be written as

$$f(q) = q \frac{3 + 3q + q^2}{1 + (1 + q)^{\frac{3}{2}}}, \quad (2.46)$$

thus, the deviations from the osculating orbit are calculated in the equation

$$\delta \ddot{\mathbf{r}} = \mathbf{a}_p - \frac{\mu}{r_{osc}^3} (f(q)\mathbf{r} + \delta \mathbf{r}). \quad (2.47)$$

Integrating the value produced from Equation 2.47 once results in  $\delta \mathbf{v}$ , integrating a second time produces  $\delta \mathbf{r}$ , both values which are needed in Equation 2.40 at each propagation interval.

### 2.6.1 Rectification

The terms in Equation 2.47 must remain small in order for Encke's method to remain accurate. As the deviation vector,  $\delta \mathbf{r}$ , grows in magnitude, the acceleration term increases as well. To maintain efficiency, the osculating orbit must be re-initialized, a process known as rectification. At rectification the osculating orbit is set equal to the true position and velocity vectors and the initial conditions for Equation 2.47 are set to zero so that the only acceleration felt by the vehicle is  $\mathbf{a}_p$ . The rectification point is set to occur at every pass or a set tolerance depending on the desired algorithm.

Rectification ensures the control of numerical errors. Calculation of the conic orbit results in only roundoff errors and is independent of the numerical technique utilized to perform the integration. However, calculation of the deviations from the osculating orbit result in both roundoff and truncation error due to the finite number of steps performed by a particular numerical algorithm. As the orbit is propagated,

truncation errors will increase for each step. To prevent these errors from growing large enough to have a detrimental effect, rectification resets the osculating orbit [7].

To compare the relative accuracy of Cowell's method to Encke's method, 7,000 low Earth orbits with various orbital elements were propagated over one period assuming two-body motion. The final position vectors were compared against the analytical solution to Kepler's problem as discussed in Section 2.3. The statistical information of the magnitude error for both methods is represented by a boxplot in Figure 2.6. For all boxplots in this research, the bottom and the top of the box represent the 25th and 75th percentile, or the lower and upper quartiles respectively. The red band near the middle of each box is the 50th percentile, or the median. The middle 50% of all the information collected falls within the boundaries of the box. The whiskers represent the lowest datum within 1.5 interquartile range of the lower quartile and the highest datum within 1.5 interquartile range of the upper quartile. Data outside of the whiskers is plotted as an outlier with a small circle.

For this comparison, Encke's method utilized a variable step Nystrom integration scheme whereas Cowell applied a variable step Runge-Kutta method. The integration schemes were selected based on tool availability. Both of these integration techniques are discussed in Section 2.8. The difference in integration methods will produce slightly different results in the final propagated states. The purpose of the comparison, however, is not to illustrate the benefit of one method over the other but to show how both produce relatively similar errors. From Figure 2.6 the similarity in median error between Cowell's and Encke's method is apparent, with 0.02 km and 0.09 km respectively. Outlier points for Cowell's method are indicative of highly elliptical orbits which have much longer periods. The trend of increased error over longer propagation times is an expected behavior of numerical integration and is discussed in Section 2.8.1. Errors in Encke's method are a result of the different algorithms used by the integration scheme and the truth value to compute the Keplerian solution. If

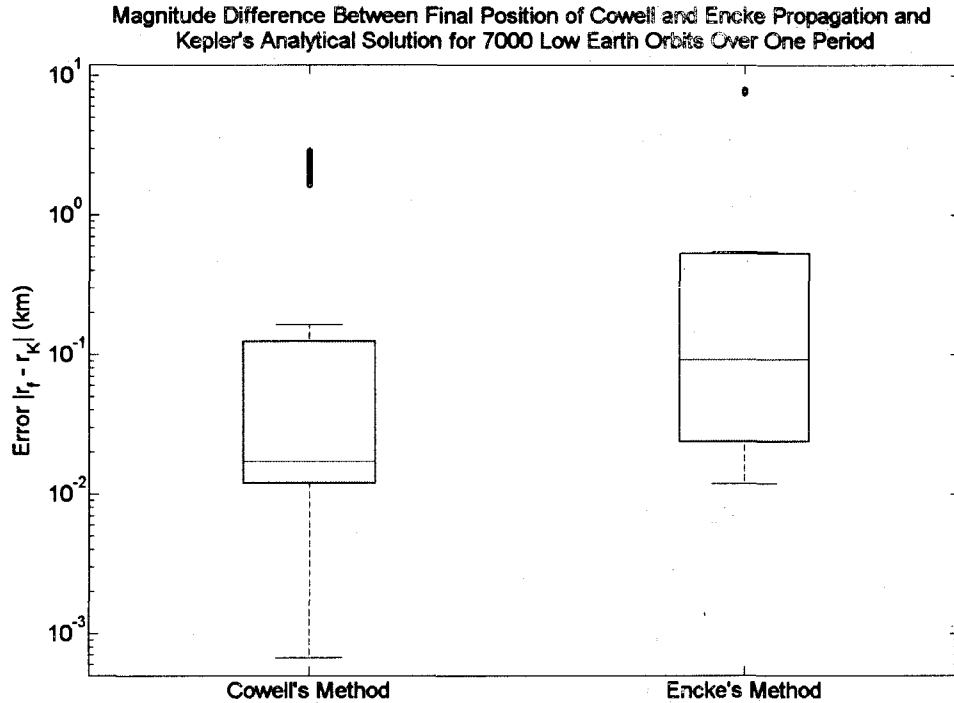


Figure 2.6: Boxplot comparison of the magnitude difference in final position of Cowell/Encke propagation and Kepler's analytical solution for 7,000 low Earth orbits over one orbit period

the same analytical algorithm was applied to both Encke's method and the truth case, Encke's method would produce zero error. From the 7,000 cases tested, depending on the orbit type, Encke's method took 2-3 times fewer steps than Cowell's method. Similar results are found in Reference [4]. Though Encke's method has the advantage of accuracy and computational time, Cowell's method is relatively simple to code and performs comparably to Encke's method. For this reason, Cowell's method was selected as the perturbation method used in this research.

## 2.7 Variation of Parameters

The method of variations of parameters was developed by Euler in 1748 and improved by Lagrange in 1873. It was the only successful method of perturbations until the development of Cowell's and Encke's method in the early 20th century. In terms of

the process of rectification as discussed in Encke’s method, the variation of parameter method can be viewed as a continuous rectification of the osculating orbit at each instant of time. Thus the “reference” orbit is constantly changing. Any two-body orbit can be completely described by a set of six orbital elements, however in the perturbed problem these elements become time varying parameters. The purpose of the variation of parameters method is then to determine how the parameters change with time as a result of some perturbing force [14]. Analytically integrating the expressions for the time changing orbital elements is the method of general perturbations. Due to the fact that the elements will change much more slowly than their position and velocity counterparts, larger integration steps may be taken.

From a coding stand point, the variation of parameters method is the most difficult to implement of the methods discussed thus far. For this reason, again Cowell was chosen as the preferred method to use.

## 2.8 Numerical Integration Methods

Special perturbations require a form of numerical integration in their implementation. No matter how complex the analytical foundation of a special perturbation technique may be, the results are worthless after integration if an appropriate integration scheme is not selected. The following is a discussion on the errors inherent in numerical integration as well as the numerical methods utilized in this research.

### 2.8.1 Integration Errors

In numerical integration there are two main types of errors involved: roundoff errors and truncation errors. Roundoff error is due to the finite precision, or floating point arithmetic implemented by computers. Computers are only accurate up to a certain number of digits. This number,  $\eta$ , is the smallest number which when added to a

number of order unity gives rise to a new number. Every floating-point calculation incurs a roundoff error of order  $\eta$ . For instance, if a computer could only carry up to five digits and the following numbers were added together:  $123.456 + 789.012 = 912.468$ , the computer would round the answer to 912.47. Where the actual answer has a 6 in the fifth digit, the rounding error has resulted in a 7. Over time, this accumulation of roundoff error will result in a much larger error. Brouwer and Clemence developed the formula

$$\log \left( .1124n^{\frac{3}{2}} \right) \quad (2.48)$$

to illustrate the probable error in terms of number of decimal places after  $n$  steps have been taken [9]. Thus, for an integration scheme that took 500 steps the error would be around 3.1 decimal places. If 6 places of accuracy are required then  $6 + 3.1 \approx 10$  places are required to carry out the calculations. Though modern computers have a value of  $\eta = 2.2 \times 10^{-16}$  for double precision floating point numbers, it is clear that integration schemes that require less steps will inherently incur less roundoff error. Where roundoff error is typically a result of the machine used to handle the calculations, truncation error is a function of the numerical integration method selected. Truncation error results from the inexact solution of the differential equations. As discussed in the following section, numerical methods are derived from some form of the Taylor series expansion. Since not all of the series are utilized, the methods are forced to truncate or exclude higher order terms, and a truncation error develops. Thus, the larger the step size the larger the truncation error.

Truncation error can be assessed from two points of view: local and global. Local error is the error that would occur in one step if the values from the previous step were exact and there was no roundoff error [33]. Assume  $u_n(t)$  is the solution of a differential equation calculated from the value of the computed solution at some time  $t_n$  and not from the original initial conditions at  $t_0$ . Thus  $u_n(t)$  is a function of  $t$

defined by the equations

$$\begin{aligned} \dot{u}_n &= f(t, u_n) \\ u_n(t_n) &= y_n. \end{aligned} \tag{2.49}$$

The local error,  $d_n$ , is the difference between the theoretical solution and the computed solution calculated using the same information at  $t_n$ . That is,

$$d_n = y_{n+1} - u_n(t_{n+1}). \tag{2.50}$$

Global error, on the other hand, is the difference between the computed solution and the true solution determined from the original conditions at time  $t_0$ ,

$$e_n = y_n - y(t_n). \tag{2.51}$$

For the case where a function  $f(t, y)$  does not depend on  $y$ , the global error becomes the sum of the local errors. In most cases, however,  $f(t, y)$  does depend on  $y$  and thus the relationship between global error and local error is related to the stability of the differential equation. For a single scalar equation, if the sign of the partial derivative is positive, the solution  $y(t)$  grows as  $t$  increases and the global error will be greater than the sum of the local errors. The opposite trend is true as well: a negative partial derivative will result in a larger local error than global error. All of the MATLAB solvers used in this research only attempt to control the local error. Solvers that try to control global errors are much more complicated and rarely successful.

A measure of accuracy of a numerical method is its order. The order represents the local error that would occur if the numerical method were applied to problems with smooth solutions. A method is of order  $p$  if there is a number  $C$  such that

$$|d_n| \leq Ch^{p+1} \tag{2.52}$$

where  $n$  is the step number and  $h$  is the step size. The value of  $C$  can depend on the derivatives of the differential equation and on the length of the interval but it is independent of  $n$  and  $h$ . A popular abbreviation of Equation 2.52 is the notation

$$d_n = O(h^{p+1}), \quad (2.53)$$

which will be used to discuss the accuracy of various numerical methods in the following section.

### 2.8.2 Euler's Method

There exist many numerical methods to approximate the equations of motion used in astrodynamics. For the purpose of this thesis the focus will remain on single-step methods for numerical integration problems. Single-step methods take the state at one time with the rates at several other times, based on the single-state value at time,  $t_0$ . The rates are obtained from the equations of motion and are used to determine the state at succeeding times,  $t_0 + h$ . Most numerical integrators are based on the integration of the Taylor series

$$y(t) = y(t_0) + \dot{y}(t_0)(t - t_0) + \frac{\ddot{y}(t_0)(t - t_0)^2}{2!} + \frac{\dddot{y}(t_0)(t - t_0)^3}{3!} + \dots \quad (2.54)$$

However, in this format two major issues arise. The first is after which order should the series be truncated. The second issue is how to calculate the higher order derivatives. Taking the most basic approach to both these issues results in the Euler integrator which approximates the Taylor series to the first order [28]

$$y(t) \approx y(t_0) + f(t_0, y_0)(t - t_0). \quad (2.55)$$

This method is simplistic in that it only requires knowledge of the first derivative but it is unsymmetrical in that it attempts to determine the slope only at the starting point. The major disadvantage of Euler's method is its sensitivity to step size, defined here as  $h = t - t_0$ . The method assumes the domain is linear, and the chosen step size is small enough to handle variations caused by the neglected higher-order derivatives. However situations can arise where the states change drastically between step sizes in which case the Euler method will provide very inaccurate solutions. The error associated with Euler's method is illustrated by Taylor expanding  $y(t)$  about  $t = t_0$ ,

$$y(t_0 + h) = y(t_0) + h\dot{y}(t_0) + \frac{h^2}{2}\ddot{y}(t_0) + \dots \quad (2.56)$$

$$y(t_0 + h) = y(t_0) + hf(t_0, y_0) + \frac{h^2}{2}\ddot{y}(t_0) + \dots \quad (2.57)$$

A comparison of Equations 2.56 and 2.57 illustrates

$$y(t) = y(t_0) + hf(t_0, y_0) + O(h^2). \quad (2.58)$$

Thus, each step using Euler's method incurs a local truncation error on the order of  $O(h^2)$ . Additionally, from Equation 2.53 it is clear that  $p = 1$ , so Euler's method is first order. The Runge-Kutta methods provide a more accurate scheme to handle complex problems.

### 2.8.3 Runge-Kutta Method

The Runge-Kutta method also derives from the Taylor series. However, instead of having to derive formulas for the higher order derivatives, the values are approximated by integrating the slope at different points within the desired interval. One option is to take a similar approach as Euler's method by obtaining the initial derivative at each step, but this time the derivative is used to find a point halfway across the



interval. The value of both  $t$  and  $y$  at the midpoint are then used to compute the actual step across the whole interval. This is the second-order Runge-Kutta method, also known as Heun's method,

$$\begin{aligned}\dot{y}_1 &= f(t_0, y_0) \\ \dot{y}_2 &= f\left(t_0 + \frac{h}{2}, y_0 + \frac{h}{2}\dot{y}_1\right) \\ y(t) &= y(t_0) + \frac{h}{2}(\dot{y}_1 + \dot{y}_2) + O(h^3).\end{aligned}\tag{2.59}$$

As evident from the error term, the symmetrization of the second-order Runge-Kutta method is accurate up to the second-order with a truncation error of the third order. The most often used variation of the Runge-Kutta methods is the classical fourth-order Runge-Kutta method,

$$\begin{aligned}\dot{y}_1 &= f(t_0, y_0) \\ \dot{y}_2 &= f\left(t_0 + \frac{h}{2}, y_0 + \frac{h}{2}\dot{y}_1\right) \\ \dot{y}_3 &= f\left(t_0 + \frac{h}{2}, y_0 + \frac{h}{2}\dot{y}_2\right) \\ \dot{y}_4 &= f(t_0 + h, y_0 + h\dot{y}_3) \\ y(t) &= y(t_0) + \frac{h}{6}(\dot{y}_1 + 2\dot{y}_2 + 2\dot{y}_3 + \dot{y}_4) + O(h^5).\end{aligned}\tag{2.60}$$

The method is derived from a fourth-order Taylor series expansion about the initial value  $y(t_0)$ . Equation 2.60 negates the need for higher order time derivatives by relating them to first derivatives at different times. The fourth-order Runge-Kutta uses the weighted averages of four slopes to then determine the next step. The method has fifth-order local truncation error and fourth-order global truncation error. A comparison of the three methods discussed is shown in Figure 2.7.

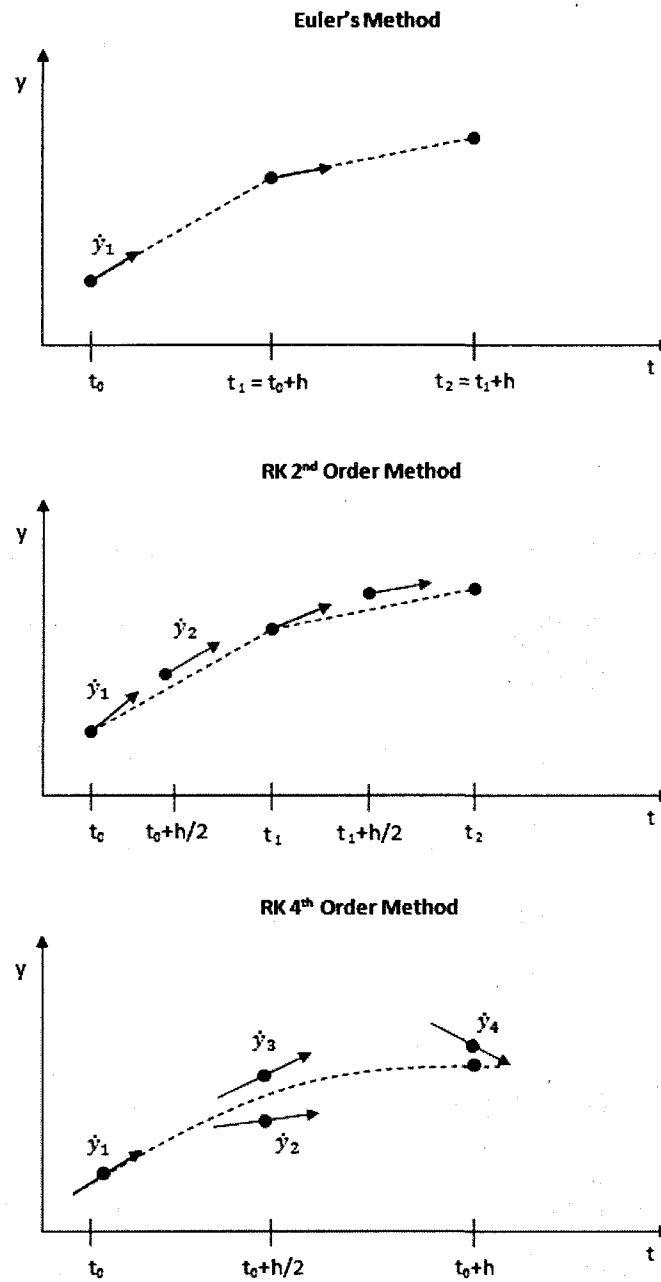


Figure 2.7: Comparison of Euler's Method, second-order Runge Kutta method, and fourth-order Runge-Kutta method where the black dots represent the estimated values and the red dots are the intermediate points

### 2.8.4 Nystrom Integration Method

Where the Runge-Kutta integration methods utilize the first order form of the equations of motion,  $\dot{y} = f(t, y)$ , the Nystrom method requires the second order form

$$\ddot{y} = f(t, y). \quad (2.61)$$

The method gives fourth-order accuracy while requiring only three derivative computations per time step. This is an advantage over the Runge-Kutta method which requires four derivative computations. Thus, in situations where the equations of motion can be expressed in second order form, the Nystrom method will be more accurate and efficient than Runge-Kutta. The second order system is written as

$$\begin{aligned} \dot{y} &= v \\ \ddot{y} &= \dot{v} = f(t, y). \end{aligned} \quad (2.62)$$

Where the formulas are of the form

$$\begin{aligned} \dot{y}_1 &= f(t_0, y_0) \\ \dot{y}_2 &= f\left(t_0 + \frac{h}{2}, y_0 + \frac{h}{2}v_0 + \frac{h^2}{8}\dot{y}_1\right) \\ \dot{y}_3 &= f\left(t_0 + h, y_0 + hv_0 + \frac{h^2}{2}\dot{y}_2\right) \\ y(t) &= y(t_0) + hv(t_0) + \frac{h^2}{6}(\dot{y}_1 + 2\dot{y}_2) + O(h^5) \\ v(t) &= v(t_0) + \frac{h}{6}(\dot{y}_1 + 4\dot{y}_2 + \dot{y}_3) + O(h^5). \end{aligned} \quad (2.63)$$

As previously mentioned, the Nystrom method requires equations of motion in the second order form. If the equations include velocity, the second derivative of velocity, known as jerk, must be calculated. In order to avoid this complexity, the Nystrom formulation assumes the equations of motion are independent of velocity, thus the

acceleration due to drag is not included in the traditional Nystrom formulation,

$$\ddot{y} = f(t, y) \neq f(t, y, \dot{y}). \quad (2.64)$$

D'Souza developed a modified Nystrom formulation that can handle the velocity term [20],

$$\begin{aligned} \dot{y}_1 &= f(t_0, y_0, v_0) \\ \dot{y}_2 &= \left( t_0 + \frac{h}{2}, y_0 + \frac{h}{2}v_0 + \frac{h^2}{8}\dot{y}_1, v_0 + \frac{h}{2}\dot{y}_1 \right) \\ \dot{y}_3 &= f \left( t_0 + h, y_0 + hv_0 + \frac{h^2}{2}\dot{y}_2, v_0 + h\dot{y}_2 \right) \\ y(t) &= y(t_0) + hv(t_0) + \frac{h^2}{6}(\dot{y}_1 + 2\dot{y}_2) + O(h^5) \\ v(t) &= v(t_0) + \frac{h}{6}(\dot{y}_1 + 4\dot{y}_2 + \dot{y}_3) + O(h^5). \end{aligned} \quad (2.65)$$

Analysis done on this modified formulation illustrates it is as accurate as the Runge-Kutta algorithm for fewer function evaluations.

### 2.8.5 MATLAB Solvers

All numerical integration for this thesis is performed using MATLAB's built in solvers. The available variable-step solvers for non-stiff systems with their specific integration techniques are listed in Table 2.2. Unlike a fixed-step solver which maintains a constant step size, a variable-step solver varies the step size depending on the dynamics of the model and the error tolerances specified by the user. This ability enables the solver to increase the step size where necessary and thus reduce the total number of steps needed. Minimum and maximum step sizes can be set as well if constraints are required. The `ode23` scheme implements the Bogacki-Shampine method which uses a Runge-Kutta formula of order three with four stages with the first-same-as-last (FSAL) property. As a result, it uses approximately three function evaluations per step. This method is a single-step method because only information from the previous point is needed to compute the successive point. The `ode45` scheme is an

explicit Runge-Kutta(4,5) formula that uses the Dormand-Prince method of applying six function evaluations to calculate the fourth and fifth order accurate solutions. The difference between the solutions is the error of the fourth order solution. Like `ode23`, `ode45` is a single-step solver. The `ode113` scheme is a variable order Adams-Bashforth-Moulton multi-step PECE solver. PECE is a technique of handling ordinary differential equation approximation by taking a prediction step and single correction step. The “E” in the acronym refers to the evaluations of the derivative function. Unlike `ode45`, `ode113` is not self starting and thus requires solutions from four preceding time points to compute the current solution [1].

Solver	Integration Technique
<code>ode23</code>	Explicit Runge-Kutta (2,3) pair of Bogacki and Shampine One-step solver
<code>ode45</code>	Explicit Runge-Kutta (4,5) pair of Dormand-Prince One-step solver
<code>ode113</code>	Variable order Adams-Bashforth-Moulton Multi-step PECE solver

Table 2.2: MATLAB fixed-step continuous solvers

To illustrate the performance of MATLAB’s numerical integrators, a circular equatorial orbit was propagated for one period using a variety of tolerances. In MATLAB, the relative tolerance is a measure of the error relative to the size of each solution component. It controls the number of correct digits in all solution components [1]. The default value is  $1 \times 10^{-3}$ , corresponding to 0.1% accuracy. The measures of performance used to compare the integrators were computation time, number of steps taken, and error. The computation time was calculated using MATLAB’s “tic toc” functions placed before and after each solver integration. The number of steps each solver took was determined by the length of the output vector. The error of the integrators was based off the magnitude difference of the final position vector after propagation and the analytical two-body Kepler solution. The results are plotted in Figures 2.8-2.10.

Figure 2.8 highlights the relative similar performance of all three solvers at very low tolerances. As the tolerances increase however, the lower order solvers require much more computational time. At a tolerance of  $1 \times 10^{-13}$ , `ode23` takes more than 37 times the amount of time as required by `ode113`. In comparing the number of steps the solver takes to maintain the specified tolerance as depicted in Figure 2.9, it is clear the advantage `ode45` and `ode113` have over the lower order `ode23`. Even at a tolerance as low as  $1 \times 10^{-4}$ , `ode23` takes three times the number of steps as `ode45`. Figure 2.10 depicts a relatively similar error performance for all the solvers across all tolerances. More importantly, the figure illustrates the importance of selecting sensitive tolerances ( $> 1 \times 10^{-6}$ ) for even the highest order solvers in order to achieve a level of accuracy. As a result of the performance demonstrated in Figures 2.8-2.10, only MATLAB's `ode45` and `ode113` were utilized in this research.

With the background of perturbation techniques and numerical methods just discussed, the next chapter develops the propagation model used as the “predictor” for the predictor-corrector algorithm applied in this study.

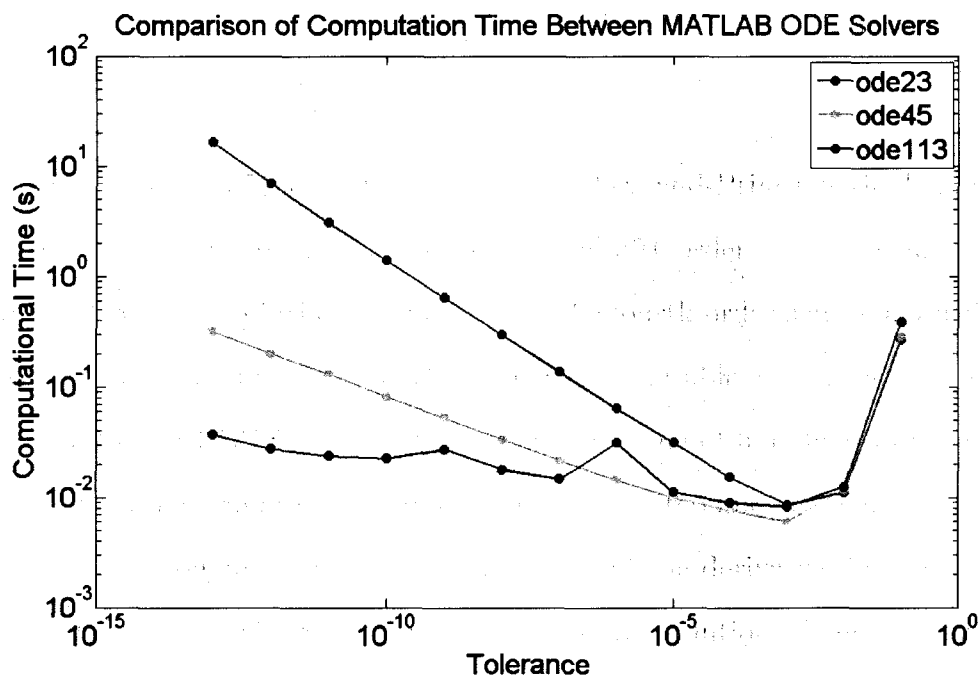


Figure 2.8: Comparison of computation time between MATLAB's ODE solvers

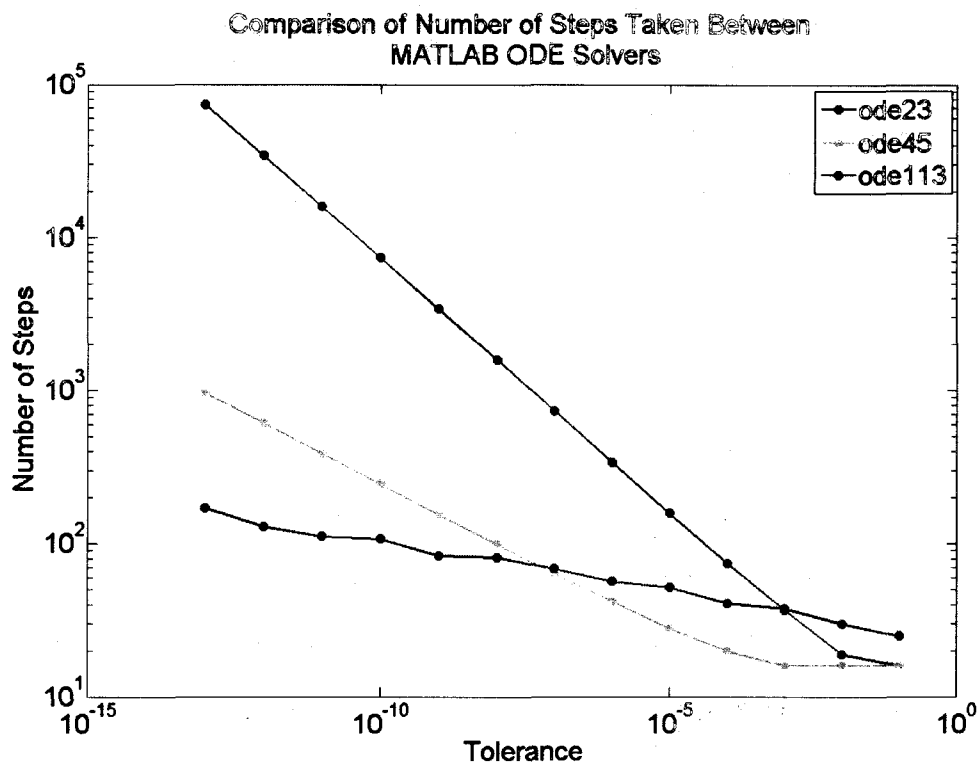


Figure 2.9: Comparison of required number of steps between MATLAB ODE solvers

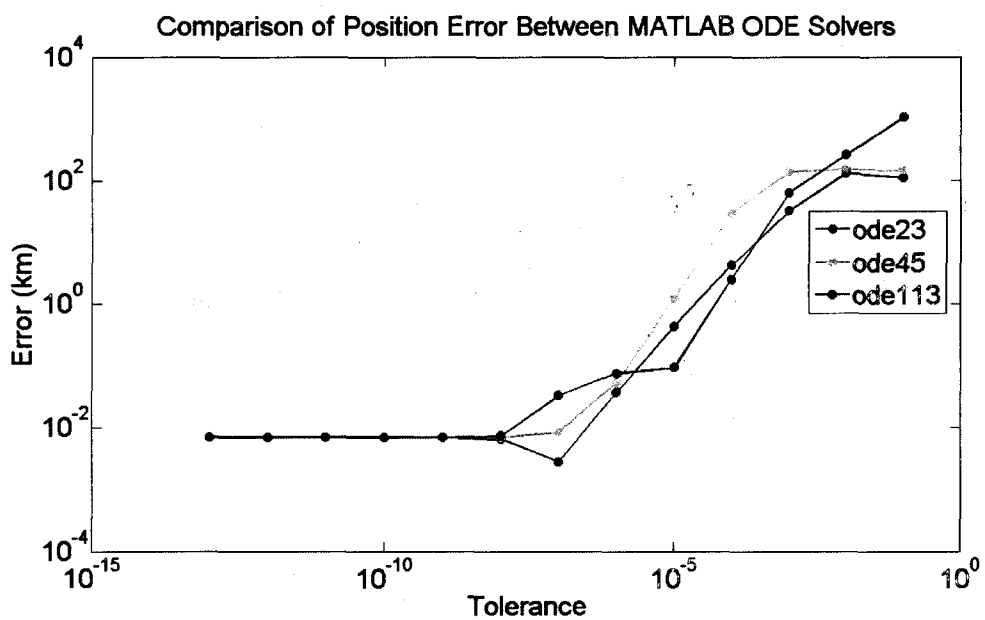


Figure 2.10: Comparison of magnitude difference in final position between the integrated value and Kepler's analytical solution for MATLAB's ODE solvers

**Comparison of Number of Steps Taken Between  
MATLAB ODE Solvers**

ode23  
ode45  
ode113



# Chapter 3

## Development of Propagator

### 3.1 System Overview

At initialization, the Cowell propagator requires the epoch state of the vehicle. Using the position and velocity of the spacecraft, the propagator calculates the total perturbation acceleration,  $\mathbf{a}_p$  from Equation 2.35, in five main blocks of code. **Three Body Motion** computes the perturbations due to n-bodies, **High Order Gravity** calculates the affects of non-conic gravity due to the Earth, **High Order Gravity Moon** calculates the affects of non-conic gravity due to the Moon, **Atmospheric Drag** determines the acceleration due to drag, and **Solar Pressure** measures the affects of solar radiation pressure. All the perturbations are summed and added to the 2-body equation of motion as defined in Equation 2.10 to produce the final acceleration for integration. Figure 3.1 portrays this configuration of the Cowell propagator and highlights which section in the following chapter each perturbation acceleration is examined.

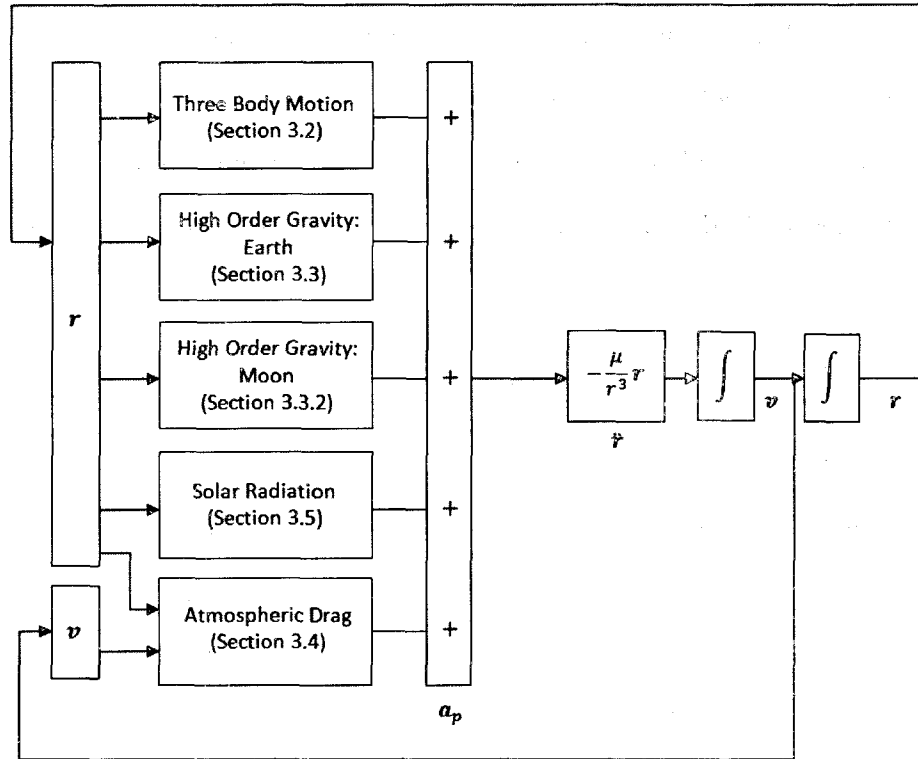


Figure 3.1: Configuration of the Cowell propagator

## 3.2 Three Body Motion

Using Newton's second law and the law of gravitation the acceleration of n-bodies acting on a spacecraft is calculated as [49],

$$\ddot{\mathbf{r}}_{1sat} = G \sum_{j=3}^n m_j \left( \frac{\mathbf{r}_{satj}}{r_{satj}^3} - \frac{\mathbf{r}_{1j}}{r_{1j}^3} \right). \quad (3.1)$$

Here the subscript, 1, represents the primary body which is the celestial body whose sphere of influence is acting on the spacecraft at any one time. The index,  $j$ , references the additional bodies included. The variable  $m_j$  is the mass of each respective planet. The left-hand term of Equation 3.1 represents the direct-effect of the acceleration of the third body on the vehicle. The right-hand term is called the indirect-effect because it is the force of the third body on the Earth. Note the two-body acceleration term of

the Earth acting on the vehicle,  $-\frac{\mu}{r^3}\mathbf{r}$ , is not included because the Cowell propagator handles the term separately (see Figure 3.1).

At high altitudes, lunisolar perturbations induce secular variations in eccentricity, inclination, ascending node, and argument of perigee. The Sun induces a gyroscopic precession of the orbit about the ecliptic pole, specifically a regression of the nodes along the ecliptic. The Moon causes a regression of the orbit about an axis normal to the Moon's orbit plane, which has a  $5^\circ$  inclination with respect to the ecliptic plane with a node rate of one rotation in 18.6 years [14]. The equation of nodal regression due to lunisolar perturbations is

$$\dot{\Omega}_{3Body} = -\frac{3 n_3^2 [1 + (3/2) e^2]}{8 n \sqrt{1 - e^2}} \cos i (3 \cos^2 i_3 - 1) \quad (3.2)$$

and for argument of perigee is

$$\dot{\omega}_{3Body} = \frac{3 n_3^2 [1 - (3/2) \sin^2 i_3]}{4 n \sqrt{1 - e^2}} \left( 2 - \frac{5}{2} \sin^2 i_3 + \frac{e^2}{2} \right) \quad (3.3)$$

where  $n_3$  and  $i_3$  are the mean motion and inclination with respect to the Earth equatorial plane. In order to calculate the perturbation effects of additional celestial bodies, the planet positions at specific times with respect to a single reference frame are required. For this research, all ephemeris data was collected from the SPICE program.

### 3.2.1 SPICE

SPICE is an information system built by the Navigation and Ancillary Information Facility under the direction of NASA's Planetary Science Division to assist engineers in the design of planetary exploration missions. The SPICE system produces data sets known as kernels which contain navigation and ancillary information such as planet ephemerides. The acronym SPICE loosely stands for the kernel file con-

tent: Spacecraft ephemeris, Planet location, Instrument Description, C-matrix, and Events. In order to utilize the n-body equations of motion for this research, SPICE returns the necessary states of the target body. The ephemeris program handles up to 11 bodies to include the Sun, nine planets, and the Moon. The output can be expressed in several reference frames to include planet-centered and barycentric. Documentation on the specifics of the program can be found in Reference [3]. All ephemeris data is time specific, thus, the correct time scheme must be utilized. The following section details the method to convert to the time reference used by SPICE.

### Time Conversion

Given the Gregorian calendar date for a desired epoch time, SPICE requires a time conversion to seconds since J2000. This calculation first requires determining the Julian Date based on the Roman calendar. The Roman calendar starts with March as month 1, April as month 2 and continues through February as month 12. The equation

$$M_R = 1 + (\text{mod}((M_G - 3), 12)), \quad (3.4)$$

converts the Gregorian month into the Roman month, where  $M_R$  refers to the Roman month,  $M_G$  is the Gregorian month, and  $\text{mod}$  is the modulus after division. If the Roman month is greater than 10 (either January or February), the Gregorian year is set to one less than the entered year due to the fact that January and February are the start of a new year. Next the number of Julian Days until March 1 of the year of interest is calculated, taking into account leap years. The three criteria that determine leap years are:

1. Every year that is divisible by four is a leap year;
2. of those years, if it can be divided by 100, it is NOT a leap year unless
3. the year is divisible by 400.

The third criterion refers to the Gregorian 400 year cycle, which occurs when the same weekdays for every year are repeated. The Julian Day is computed using the following algorithm:

First, consider the 400 year cycle. During this period there are 146,000 days and 97 leap years hence the coefficient  $146,000 + 97 = 146,097$ ,

$$\begin{aligned} JD &= JD + 146,097(\text{fix}(Years/400)) \\ Years &= \text{mod}(Years, 400), \end{aligned} \tag{3.5}$$

where the *fix* command rounds towards zero. Next consider the 100 year period which includes 36,500 days and 24 leap years,

$$\begin{aligned} JD &= JD + 36,524(\text{fix}(Years/100)) \\ Years &= \text{mod}(Years, 100). \end{aligned} \tag{3.6}$$

The 4 year period has 1,460 days and 1 leap year,

$$\begin{aligned} JD &= JD + 1,461(\text{fix}(Years/4)) \\ Years &= \text{mod}(Years, 4). \end{aligned} \tag{3.7}$$

Finally, the one year period has 365 days and no leap years,

$$JD = JD + 365(Years). \tag{3.8}$$

Next the number of days until the month of interest is calculated, adding this value to the days found in Equation 3.8. These two values are added to produce the final Julian Day value. The Gregorian hour, minute, and seconds are all converted to seconds, added together, then converted back into days to complete the Julian Date.

Since SPICE utilizes a J2000 epoch, the Julian Date is converted as follows

$$JD_{J2000} = (JD - 2,451,545)86,400, \quad (3.9)$$

where 2,451,545.0 is the Julian Date of January 1, 2000 at noon and 86,400 is the number of seconds in a day.

### 3.3 High Order Gravity

The High Order Gravity model computes the gravitational perturbation acceleration vector due to a rotating non-spherical body whose mass coefficients are given in terms of the zonal and tesseral harmonics. Gravity harmonics are derived from the gravity potential which will be explained in the following section. Zonal harmonics occur where the dependence of the gravity potential on longitude disappears and the field is symmetrical around the pole. These harmonics reflect the Earth's oblateness as seen in the shaded regions of Figure 3.2. The gray areas highlight additional mass, thus the central band of  $J_2$ , seen as degree 2 order 0 in the figure, clearly captures the bulge of the Earth. Tesseral harmonics on the other-hand take into account the latitudinal and longitudinal effects of the mass distribution dividing the Earth into a checkerboard (see Figure 3.3). The High Order Gravity function allows the user to specify the order of perturbation from spherical (no perturbation due to a non-spherical Earth), the “zeroth” order terms  $J_2$ ,  $J_2J_3J_4$ , or higher order of gravity which includes the tesseral harmonics. The mathematical formulation discussion in the follow section assumes that the primary body of interest is the Earth.

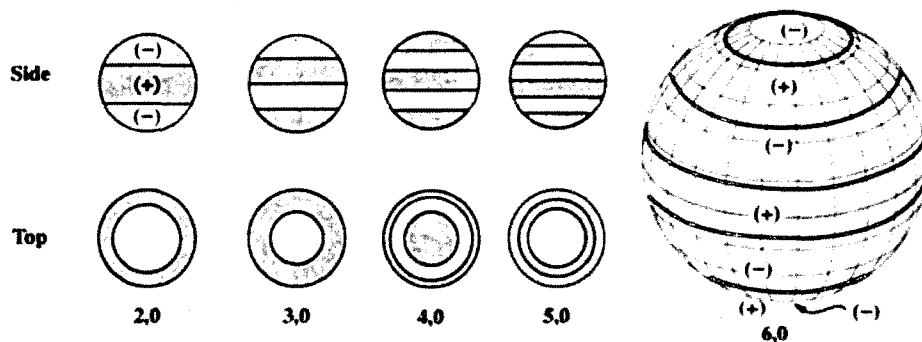


Figure 3.2: Illustration of the Earth's zonal harmonics with shaded regions representing additional mass [49]

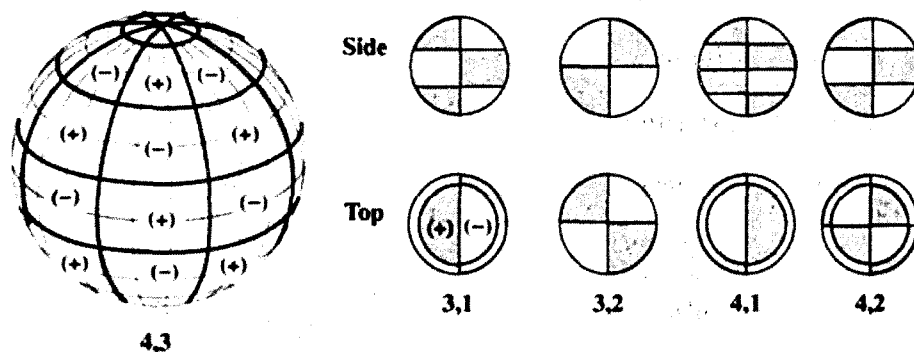


Figure 3.3: Illustration of the Earth's tesseral harmonics with shaded regions representing additional mass [49]

### 3.3.1 Formulation

#### Spherical

When the simplified gravitation potential of the Earth is utilized it assumes a spherically symmetric mass body which results in Keplerian motion. For this case, no perturbations are calculated. However, the Earth is not a spherically symmetric body but is bulged at the equator, flattened at the poles and is generally asymmetric. These are modeled in the following sections.

## $J_2$

The most commonly encountered gravity harmonic is  $J_2$  which is the largest magnitude term of the zonal harmonics. As the coefficient of the second harmonic,  $J_2$  is related to the Earth's equatorial oblateness. The estimated difference between the polar radius and the equatorial radius due to the bulge is 22 km [14]. The accelerations due to the second harmonic are determined using the equations

$$\begin{aligned} a_{J_2,x} &= -\frac{3J_2\mu R_\oplus^2 r_x}{2r^5} \left(1 - \frac{5r_z^2}{r^2}\right) \\ a_{J_2,y} &= -\frac{3J_2\mu R_\oplus^2 r_y}{2r^5} \left(1 - \frac{5r_z^2}{r^2}\right) \end{aligned} \quad (3.10)$$

and

$$a_{J_2,z} = -\frac{3J_2\mu R_\oplus^2 r_z}{2r^5} \left(3 - \frac{5r_z^2}{r^2}\right).$$

Where for the Earth,  $J_2$  has the coefficient value

$$J_2 = -1.08262668355 \times 10^{-3}, \quad (3.11)$$

$\mu$  is the gravitational parameter,  $R_\oplus$  is the equatorial radius of the Earth,  $\mathbf{r} = [r_x \ r_y \ r_z]$  are the position vector components, and  $r = |\mathbf{r}|$  is the magnitude of the position vector. It is assumed  $\mathbf{r}$  is in an Earth-Centered Earth-Fixed coordinate frame where  $\mathbf{z}$  is the North Pole and  $\mathbf{x}$  is at the zero longitude.

## $J_2J_3J_4$

Though the  $J_2$  coefficient is almost 1000 times larger than the next largest coefficient,  $J_3$ , multiplying  $J_2$  by  $J_3$  and  $J_4$  increases the accuracy of the predicted perturbation. The accelerations due to the second, third, and fourth harmonic utilizes Equation



3.10 added to the equations

$$\begin{aligned} a_{J_3,x} &= -\frac{5J_3\mu R_{\oplus}^3 r_x}{2r^7} \left( 3r_z - \frac{7r_z^3}{r^2} \right), \\ a_{J_3,y} &= -\frac{5J_3\mu R_{\oplus}^3 r_y}{2r^7} \left( 3r_z - \frac{7r_z^3}{r^2} \right), \end{aligned} \quad (3.12)$$

and

$$a_{J_3,z} = -\frac{5J_3\mu R_{\oplus}^3 r_z}{2r^7} \left( 6r_z - \frac{7r_z^3}{r^2} - \frac{3r^2}{5r_z} \right),$$

for the third harmonic and to the equations

$$\begin{aligned} a_{J_4,x} &= -\frac{15J_4\mu R_{\oplus}^4 r_x}{8r^7} \left( 1 - \frac{14r_z^2}{r^2} + \frac{21r_z^4}{r^4} \right), \\ a_{J_4,y} &= -\frac{15J_4\mu R_{\oplus}^4 r_y}{8r^7} \left( 1 - \frac{14r_z^2}{r^2} + \frac{21r_z^4}{r^4} \right), \end{aligned} \quad (3.13)$$

and

$$a_{J_4,z} = -\frac{15J_4\mu R_{\oplus}^4 r_x}{8r^7} \left( 5 - \frac{70r_z^2}{3r^2} + \frac{21r_z^4}{r^4} \right),$$

for the fourth harmonic. Here  $J_3$  and  $J_4$  have the respective coefficient values

$$J_3 = 2.53265648533 \times 10^{-6} \quad (3.14)$$

$$J_4 = 1.61962159137 \times 10^{-6}. \quad (3.15)$$

## Gravity Potential

To more clearly understand gravity harmonics, the concept of gravity potential is introduced. Similar to potential theory in fluid mechanics, the gravity field of a celestial body with finite mass can be represented by a potential function. If the mass of a celestial body is assumed to be a point mass or uniformly distributed in a sphere, the potential takes the simple form of [14]

$$\phi = \frac{\mu}{r}. \quad (3.16)$$

From potential theory, the gravitational force or the perturbing accelerations along a given direction are found by taking the partial derivatives with respect to the components of the position vector. Consequently, the two-body equations of motion become

$$\begin{aligned}\ddot{\mathbf{r}}_x &= \frac{\partial\phi}{\partial r_x} = -\frac{\mu}{r^3}\mathbf{r}_x, \\ \ddot{\mathbf{r}}_y &= \frac{\partial\phi}{\partial r_y} = -\frac{\mu}{r^3}\mathbf{r}_y,\end{aligned}\tag{3.17}$$

and

$$\ddot{\mathbf{r}}_z = \frac{\partial\phi}{\partial r_z} = -\frac{\mu}{r^3}\mathbf{r}_z.$$

Unfortunately, the point-mass potential cannot accurately represent the gravity field of the Earth due to the non-spherical shape of the body. Instead, the potential function should be derived from a spheroid that closely represents the mass distribution of the Earth. Pines derives the gravity potential for a Cartesian position vector in terms of spherical coordinates [37],

$$\phi = \frac{\mu}{r} \left\{ 1 + \sum_{n=1}^{\infty} \left(\frac{a}{r}\right)^n \sum_{m=1}^n P_{n,m}(\sin \alpha) (C_{n,m} \cos m\lambda + S_{n,m} \sin m\lambda) \right\}.\tag{3.18}$$

This infinite series is the potential function of a spheroid with geopotential coefficients  $C_{n,m}$  and  $S_{n,m}$ . Further,  $a$  is the equatorial radius of the body,  $\alpha$  is the declination of the satellite,  $\lambda$  is the longitude of the satellite,  $n$  is the degree,  $m$  is the order, and  $P_{n,m}(u)$  is the Legendre polynomial defined by the indices  $n$  and  $m$  and the equation

$$P_{n,m}(\sin \alpha) = (1 - \sin^2 \alpha)^{\frac{m}{2}} \frac{1}{2^n!} \frac{d^{n+m}}{d \sin \alpha^{n+m}} (\sin^2 \alpha - 1)^n.\tag{3.19}$$

In this formulation, when  $|\alpha| \approx \frac{\pi}{2}$  the vectors that make up the partials of  $\phi$  involve numerical difficulty. Thus a change of coordinates is utilized to circumvent the non-

uniformity. Specifically, for  $r = (x^2 + y^2 + z^2)^{\frac{1}{2}}$ , one sets

$$\begin{aligned} s &= \frac{x}{r}, \\ t &= \frac{y}{r}, \end{aligned} \quad (3.20)$$

and

$$u = \frac{z}{r}$$

where  $\mathbf{R} = r[ \mathbf{i} \ s \ t \ u ]$ . Further, the Legendre polynomials,  $P_{n,m}(u)$  is replaced by the polynomial

$$A_{n,m} = \frac{1}{2^n n!} \frac{d^{n+m}}{du^{n+m}} (u^2 - 1)^n, \quad (3.21)$$

and the terms  $\sin m\lambda$  and  $\cos m\lambda$  are replaced by  $r_m(s, t)$  and  $i_m(s, t)$  which are the real and imaginary parts of  $(s + it)^m$ , respectively

$$\cos m\lambda \cos^m \alpha = r_m(s, t), \quad (3.22)$$

and

$$\sin m\lambda \cos^m \alpha = i_m(s, t). \quad (3.23)$$

Hence the gravitational potential can be written as

$$\phi = \frac{\mu}{r} \left[ 1 + \sum_{n=1}^{\infty} \left( \frac{a}{r} \right)^n \sum_{m=1}^n A_{n,m}(u) (C_{n,m} r_m(s, t) + S_{n,m} i_m(s, t)) \right]. \quad (3.24)$$

The partials of  $\phi$  with respect to  $\mathbf{R}$  are

$$\begin{aligned} \frac{\partial r}{\partial \mathbf{R}} &= \left( \frac{1}{r} \right) \mathbf{R} \\ \frac{\partial s}{\partial \mathbf{R}} &= \left( \frac{1}{r} \right) \mathbf{i} - \left( \frac{s}{r} \right) \mathbf{R} \\ \frac{\partial t}{\partial \mathbf{R}} &= \left( \frac{1}{r} \right) \mathbf{j} - \left( \frac{t}{r} \right) \mathbf{R} \\ \frac{\partial u}{\partial \mathbf{R}} &= \left( \frac{1}{r} \right) \mathbf{k} - \left( \frac{u}{r} \right) \mathbf{R}. \end{aligned} \quad (3.25)$$

Thus, the acceleration is

$$F = \left( \frac{\partial \phi}{\partial r} - \frac{s}{r} \frac{\partial \phi}{\partial s} - \frac{t}{r} \frac{\partial \phi}{\partial t} - \frac{u}{r} \frac{\partial \phi}{\partial u} \right) \mathbf{R} \\ + \frac{1}{r} \frac{\partial \phi}{\partial s} \mathbf{i} + \frac{1}{r} \frac{\partial \phi}{\partial t} \mathbf{j} + \frac{1}{r} \frac{\partial \phi}{\partial u} \mathbf{k}. \quad (3.26)$$

The Legendre polynomial described in Equation 3.21 satisfies the recursion equation

$$A_{n,m}(u) = \left[ \frac{1}{(n-m)} \right] (uA_{n,m+1} - A_{n-1,m+1}). \quad (3.27)$$

Further, the recursion relationships for  $r_m(s, t)$  and  $i_m(s, t)$  are

$$r_m(s, t) = sr_{m-1}(s, t) - ti_{m-1}(s, t) \quad (3.28)$$

and

$$i_m(s, t) = si_{m-1}(s, t) - tr_{m-1}(s, t). \quad (3.29)$$

Introducing the variable  $\rho = \frac{a}{r}$ , the recursion equations

$$\rho_0 = \frac{\mu}{r}, \\ \rho_1 = \rho \rho_0, \\ \rho_n = \rho \rho_{n-1}, \quad (3.30)$$

are derived for all  $n > 1$ . Also, the equation

$$\frac{\rho_n}{r} = \frac{\rho_{n+1}}{a} \quad (3.31)$$

holds. In this regard, the mass coefficients

$$D_{n,m}(s, t) = C_{n,m}r_m(s, t) + S_{n,m}i_m(s, t), \\ E_{n,m}(s, t) = C_{n,m}r_{m-1}(s, t) + S_{n,m}i_{m-1}(s, t), \quad (3.32)$$

and

$$F_{n,m}(s, t) = S_{n,m}r_{m-1}(s, t) + C_{n,m}i_{m-1}(s, t)$$

are introduced. Therefore the acceleration vector is given by the equation

$$F = a_1\mathbf{i} + a_2\mathbf{j} + a_3\mathbf{k} + a_4\mathbf{R}. \quad (3.33)$$

In this equation, the acceleration forces are defined as

$$\begin{aligned} a_1 &= \sum_{n=0}^{\infty} \frac{\rho_{n+1}}{a} \sum_{m=0}^n A_{n,m}(u)mE_{n,m}, \\ a_2 &= \sum_{n=0}^{\infty} \frac{\rho_{n+1}}{a} \sum_{m=0}^n A_{n,m+1}(u)mF_{n,m}, \\ a_3 &= \sum_{n=0}^{\infty} \frac{\rho_{n+1}}{a} \sum_{m=0}^n A_{n,m+1}(u)D_{n,m}, \end{aligned} \quad (3.34)$$

and

$$a_4 = - \sum_{n=0}^{\infty} \frac{\rho_{n+1}}{a} \sum_{m=0}^n A_{n+1,m+1}(u)D_{n,m}.$$

If the default gravity table is not utilized a suitably sized table must be provided with the required un-normalized coefficients. If only the normalized coefficient values,  $\bar{C}_{l,m}$  are known, the transformation can be introduced,

$$C_{l,m} = \frac{\bar{C}_{l,m}}{\prod_{l,m}} \quad (3.35)$$

where

$$\prod_{l,m} = \sqrt{\frac{(l+m)!}{(l-m)!k(2l+1)}} \quad (3.36)$$

and  $k = 1$  if  $m = 0$  and  $k = 2$  if  $m \neq 0$ . The gravity table is a square matrix with dimensions one greater than the highest degree (due to the necessity of zeroth order terms). For example, the default gravity table has coefficients up to the 9th degree thus the table is a  $10 \times 10$  matrix. The rows in the gravity table represent the degree

and the columns the order. The format for the gravity table is:

$$\begin{array}{cccccc}
 C_{0,0} & C_{0,1} & C_{0,2} & \cdots & C_{0,n} \\
 C_{1,0} & C_{1,1} & C_{1,2} & \cdots & C_{1,n} \\
 C_{2,0} & C_{2,1} & C_{2,2} & \cdots & C_{2,n} \\
 \vdots & \vdots & \vdots & \vdots & \vdots \\
 C_{n,0} & C_{n,1} & C_{n,2} & \cdots & C_{n,n}
 \end{array} \tag{3.37}$$

For clarity, the  $J_2$  coefficient value is represented by the  $-C_{2,0}$  coefficient in the table,  $J_3$  by  $-C_{3,0}$ ,  $J_4$  by  $-C_{4,0}$  and so forth.

### 3.3.2 High Order Gravity Moon

The High Order Gravity Moon model is identical to the Earth model except for a transformation that takes in the current position of the vehicle and converts the reference frame from Earth-centered to Moon-centered. Using Figure 3.4 the geocentric position vector is converted to a selenocentric position vector through simple vector subtraction

$$\mathbf{r}_{\odot sat} = \mathbf{r}_{\oplus sat} - \mathbf{r}_{\oplus \odot}, \tag{3.38}$$

where the subscript  $\oplus$  refers to the Earth,  $\odot$  to the Moon, and  $sat$  to the satellite.

The double subscripts are representative of the vectors

$$\mathbf{r}_{\odot sat} = \mathbf{r}_{sat} - \mathbf{r}_{\odot}, \tag{3.39}$$

$$\mathbf{r}_{\oplus sat} = \mathbf{r}_{sat} - \mathbf{r}_{\oplus},$$

and

$$\mathbf{r}_{\oplus \odot} = \mathbf{r}_{\odot} - \mathbf{r}_{\oplus}.$$

A similar transformation is done for the velocity vector as well. The planetary body reference is also switched from the Earth to the Moon to account for a different

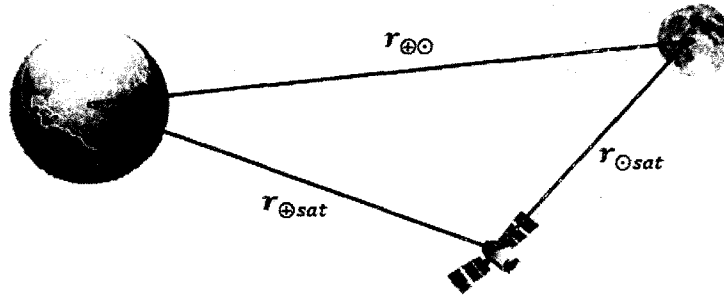


Figure 3.4: Three body configuration of position vectors between the Earth, Moon, and satellite

gravitational constant, planet radius, and gravity coefficient table [27].

### 3.3.3 Validation of Higher Order Gravity Model

#### Gravitation Perturbation as a Function of Latitude and Longitude

The first validation test of the High Order Gravity model is to develop a map of the Earth's gravity field to compare against established models. A Simulink/stateflow model is created to quickly run through 10,000 test cases of unique position vectors at a constant geocentric altitude above the surface of the Earth. The position vectors are calculated at a set altitude of 540 km with one hundred unique latitude values ranging from  $-90^\circ$  to  $90^\circ$  and one hundred unique longitude values between  $0^\circ$  and  $360^\circ$  using the equation

$$\mathbf{r} = R \begin{bmatrix} \cos(\phi_{gc}) \cos(\lambda) \\ \cos(\phi_{gc}) \sin(\lambda) \\ \sin(\phi_{gc}) \end{bmatrix}, \quad (3.40)$$

where  $\phi_{gc}$  is the geocentric latitude and  $\lambda$  is the longitude. The dominant effects of the central term  $J_0$ , and  $J_2$ , are removed to produce the gravity perturbation due to

just high order effects. That is,

$$\begin{aligned}\ddot{\mathbf{r}}_{J_2} &= -\frac{\mu}{r^3}\mathbf{r} + \mathbf{a}_{J_2} \\ \ddot{\mathbf{r}}_{J_{2-9}} &= -\frac{\mu}{r^3}\mathbf{r} + \mathbf{a}_{J_{2-9}} \\ \mathbf{a}_{J_{3-9}} &= \mathbf{a}_{J_{2-9}} - \mathbf{a}_{J_2}\end{aligned}$$

where  $\mathbf{a}_{J_{2-9}}$  is the acceleration due to higher order gravity as defined in Equation 3.33,  $\mathbf{a}_{J_2}$  is the acceleration due to  $J_2$  as defined in Equation 3.10, and  $\mathbf{a}_{J_{3-9}}$  is the acceleration due to high order gravity to include all coefficients up to degree 9 except  $J_2$ . To determine the radial component of the perturbation, the dot product is taken,

$$\mathbf{a}_{J_{3-9}} = -\mathbf{a}_{J_{3-9}} \cdot \hat{\mathbf{u}}_r \quad (3.41)$$

where  $\hat{\mathbf{u}}_r$  is the unit position vector

$$\hat{\mathbf{u}}_r = \frac{\mathbf{r}}{\|\mathbf{r}\|}. \quad (3.42)$$

The results are plotted on a topography map of the Earth as seen in Figure 3.5. The depiction illustrates how the Earth's gravity field differs from the gravity field of a uniform, featureless Earth surface. The different colors on the map highlight the relative strength of the gravitational force over the surface of the Earth (red representing the strongest effect, blue the weakest). The GRACE model (complete to 160 degrees) is shown in Figure 3.6 for comparison. Figure 3.6 is a map of Earth's gravity field as produced by the joint NASA-German Aerospace Center Gravity Recovery and Climate Experiment (GRACE) mission. The units in the map are in gals which is a unit of acceleration often used when studying gravity, defined as  $1 \frac{cm}{s^2}$ . Converting the units into  $\frac{m}{s^2}$ , the range of the radial perturbation acceleration magnitudes from Figure 3.6 is  $-6 \times 10^{-6} - 6 \times 10^{-6} \frac{m}{s^2}$ . This is comparable to the high order gravity model range of  $-5 \times 10^{-6} - 3 \times 10^{-6} \frac{m}{s^2}$ . The GRACE project has produced the most



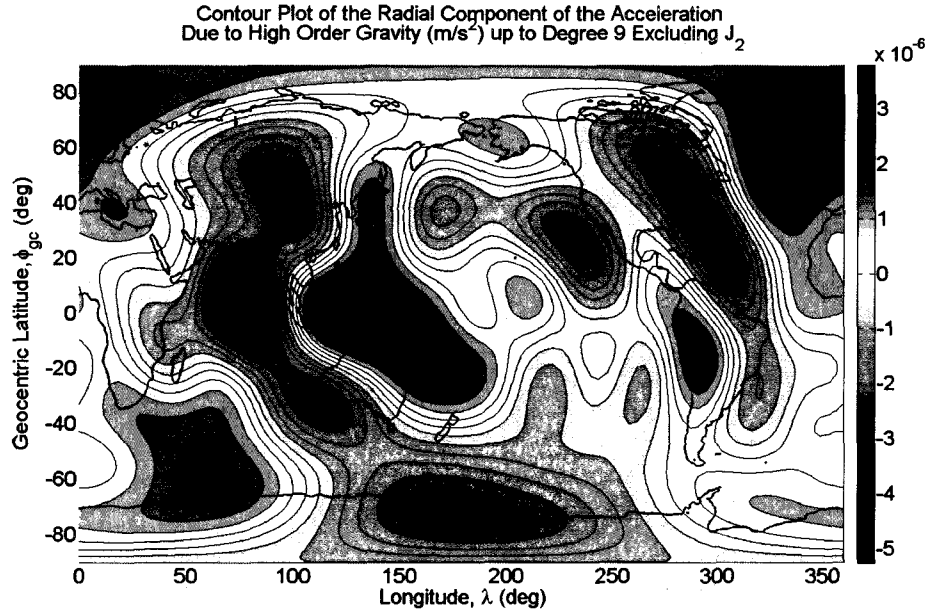


Figure 3.5: Radial component of the gravitational perturbation,  $\mathbf{a}_{J_{3-9}} \left( \frac{m}{s^2} \right)$ , due to higher order gravity up to degree 9 excluding  $J_2$  with respect to latitude/longitude

update data on the Earth's gravity field. A comparison of Figure 3.5 and Figure 3.6 show enough similarities to establish a foundation to validate the implementation of the High Order Gravity model. With the model validated, the effects of high order gravity on satellite propagation is illustrated in the following section. Emphasis is placed on the effects of higher order terms excluding  $J_2$  to depict the importance of applying high fidelity gravity models in accurate propagation tools.

### Effects of High Order Gravitational Coefficients on Satellite Propagation

The potential generated by a non-spherical Earth causes periodic variations in all the orbital elements. The largest perturbations, however, occur in the longitude of ascending node and argument of perigee. The Earth's equatorial bulge introduces a force component toward the equator which causes orbiting satellites to reach the ascending node short of the crossing point for a spherical Earth. This westward rotation is illustrated in Figure 3.7 which depicts a circular orbit with an altitude of 300 km propagated over 10 periods with only higher order gravity perturbing the

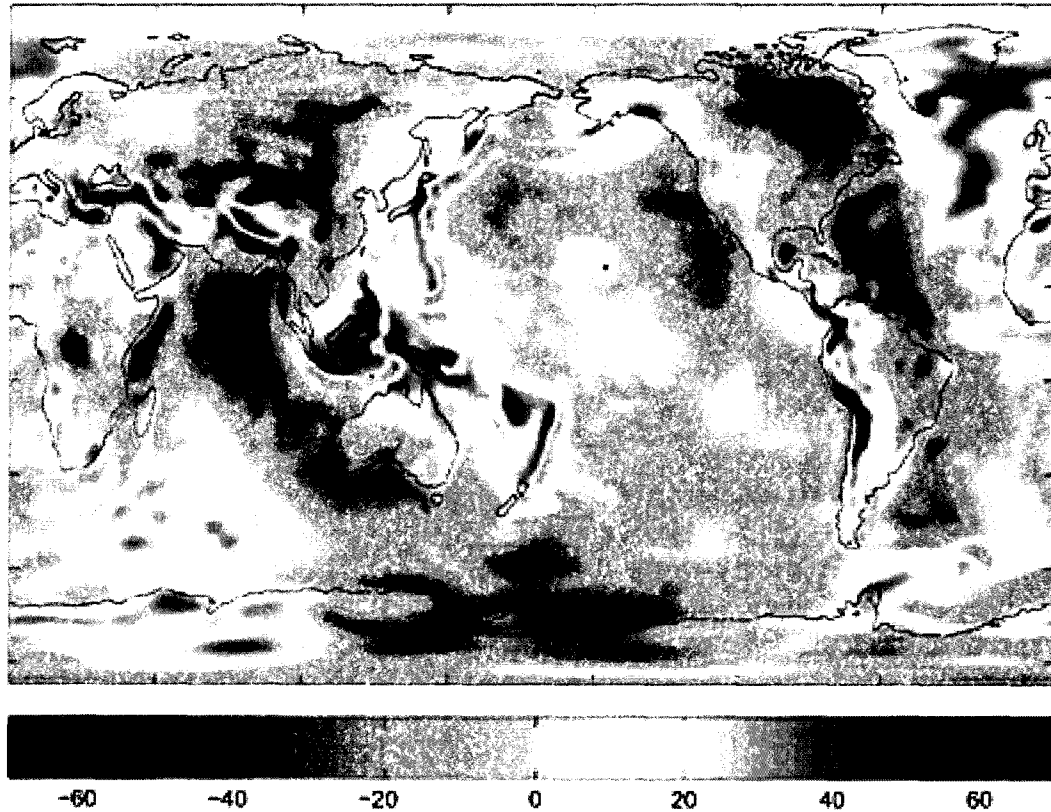


Figure 3.6: Earth's gravity field anomalies (mGal) as determined by GRACE [2]

motion. The rate of regression of the ascending node is numerically evaluated to the first order in the equation

$$\dot{\Omega}_{J_2} = -\frac{3}{2} J_2 \left( \frac{R_{\oplus}}{p} \right)^2 \mathbf{n} \cos i, \quad (3.43)$$

where  $p$  is the semiparameter defined by the equation

$$p = a_0 (1 - e^2), \quad (3.44)$$

and

$$\mathbf{n} = \sqrt{\frac{\mu}{a_0^3}} \left[ 1 + \frac{3}{2} \frac{J_2 R_{\oplus}^2}{p^2} \left( 1 - \frac{3}{2} \sin^2 i \right) (1 - e^2)^{\frac{1}{2}} \right] \quad (3.45)$$

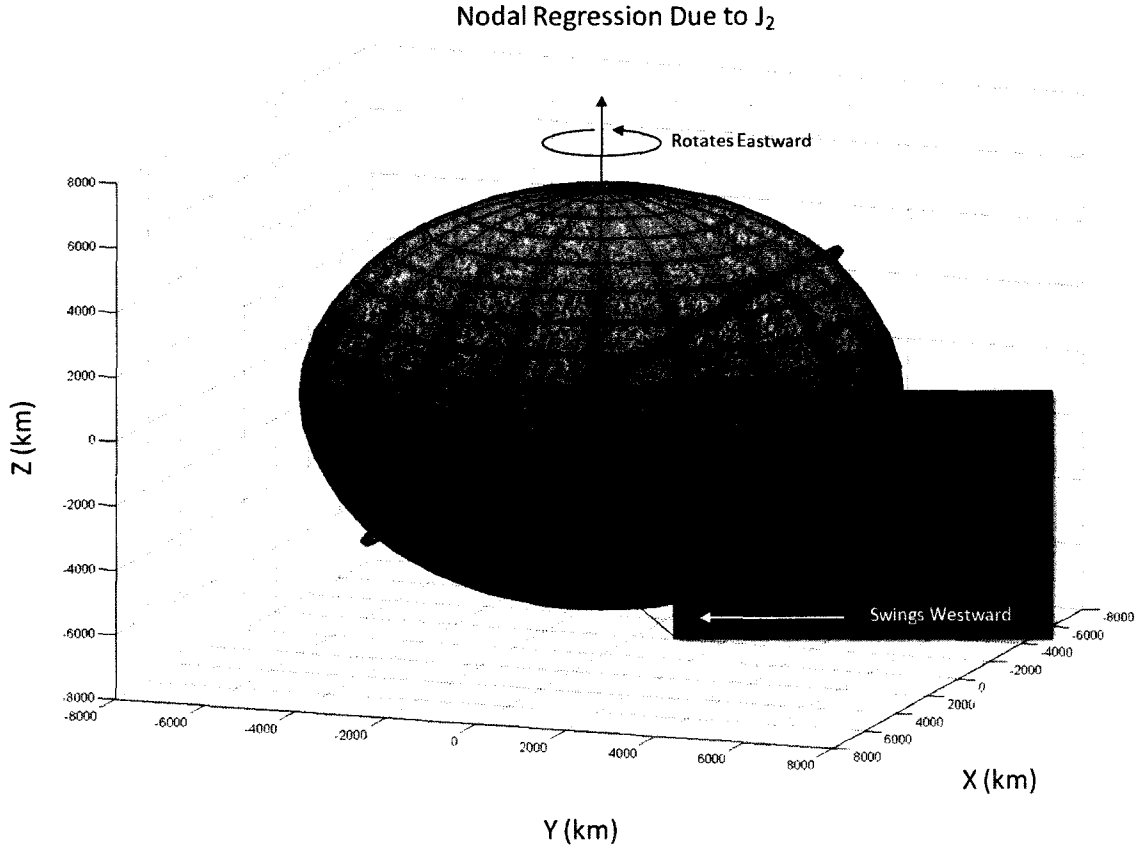


Figure 3.7: The gravitational pull of the Earth's equatorial bulge causes the orbital plane of an eastbound satellite to regress westward

where  $\mathbf{n}$  is the orbit mean motion with  $J_2$  correction. Further, it should be noted that the node regresses for direct orbits and advances for retrograde orbits. There is no nodal regression to first order for polar orbits. The secular motion of the perigee occurs because the perturbed force is no longer proportional to the inverse square radius and the orbit is consequently no longer a closed ellipse. The rate of change of  $\omega$  is

$$\dot{\omega}_{J_2} = \frac{3}{4} J_2 \left( \frac{R_{\oplus}}{p} \right)^2 \mathbf{n} (5 \cos^2 i - 1). \quad (3.46)$$

At the critical inclination of  $63.43^\circ$  or  $116.57^\circ$  the perturbation in the argument of perigee is zero. Equations 3.43 and 3.46 highlight the relationship between inclination, altitude and the rate of secular variation. For small values of inclination the cosine

function is driven to 1 increasing the rate. Likewise, for smaller values of altitude the ratio of  $\frac{R_{\oplus}}{p}$  becomes larger, also increasing the rate of perturbation. These trends are highlighted in Figure 3.8 which plots the final position error due to  $J_{2-9}$  for circular orbits with varying altitudes and inclinations propagated over one period. At an altitude of 100 km, the deviation difference between an orbit with  $i = 0^\circ$  and  $i = 90^\circ$  is 97 km after only one revolution. Further, at an inclination of  $0^\circ$  the deviation difference between an orbit at an altitude of 100 km and 1000 km is 16 km.

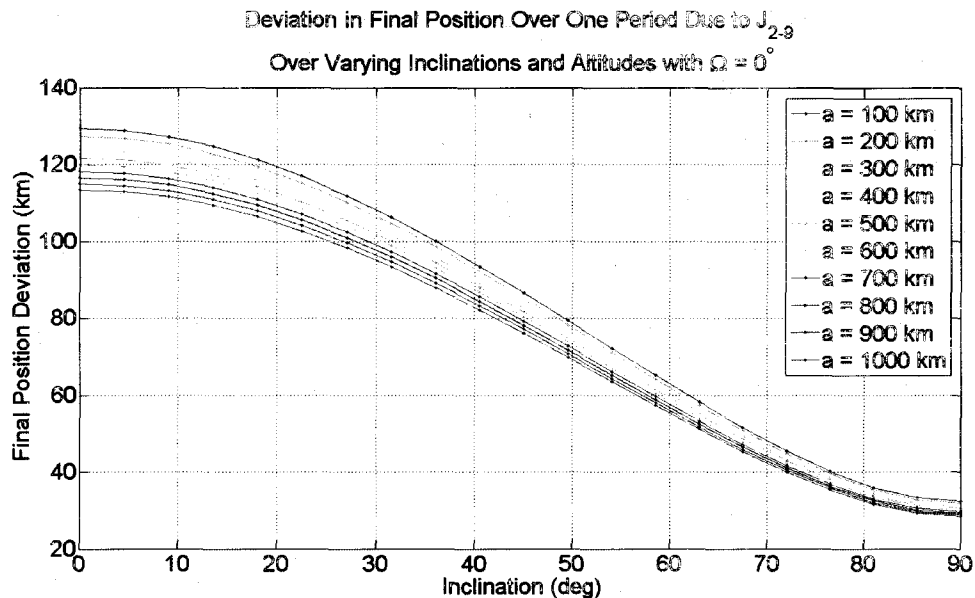


Figure 3.8: Deviation in final position (km) due to  $J_{2-9}$  for circular orbits with varying altitudes and inclinations propagated over one period

Even with the dominant  $J_2$  coefficient removed, the higher order gravity coefficients play a role in perturbing satellite motion. To illustrate this affect, the High Order Gravity model is used in conjunction with an Encke Nystrom propagator to test over 600 unique orbits. Each orbit has a distinct initial conic position and velocity calculated over varying inclinations and right ascension of ascending nodes. All cases are propagated over one Keplerian orbit. The perturbation error between the high order gravity model,  $J_{2-9}$ , and the lower order gravity coefficient models is computed by taking the magnitude difference in the initial and final position vectors

propagated over one period. That is,

$$\Delta \mathbf{x} = |\mathbf{r}_f - \mathbf{r}_0| \quad (3.47)$$

where  $\mathbf{r}_f$  is the position at the final time,  $t_f$ , is

$$t_f = t_0 + 2\pi\sqrt{\frac{a^3}{\mu}}. \quad (3.48)$$

The results are plotted in Figures 3.9 and 3.10. At an altitude of 100 km, removing the  $J_2$  coefficient decreases the position deviation after one orbit from 130 km to 1 km. Though this reduction is significant and highlights the dominant affect of  $J_2$ , it also illustrates the effect higher order gravity coefficients have on orbit perturbation. A 1 km deviation per revolution will quickly deteriorate an orbit from its intended path if corrections are not made. Using Equation 3.47, values are calculated for  $\Delta \mathbf{x}_{J_2}$ ,

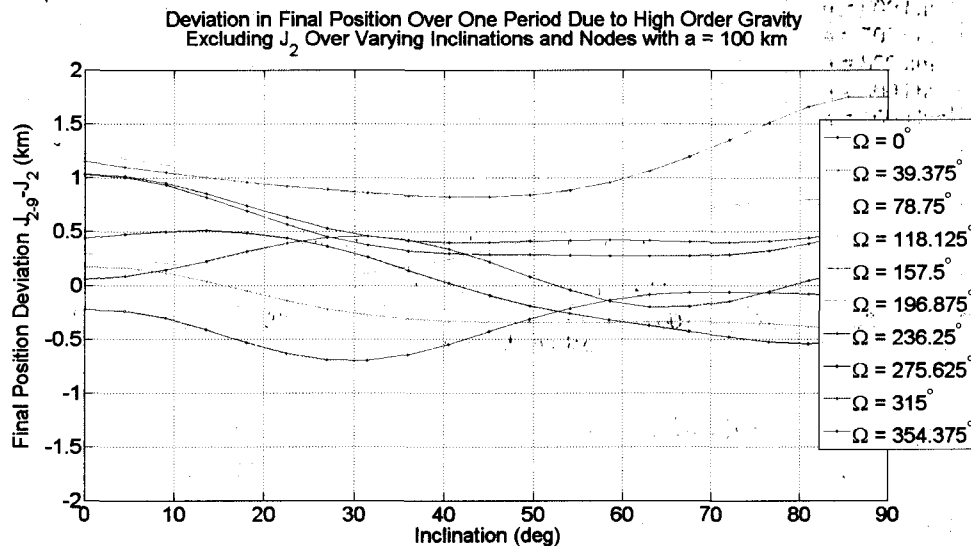


Figure 3.9: Deviation in final position (km) due to  $J_{3-9}$  for circular orbits with varying inclinations and ascending nodes at  $a = 100$  km propagated over one period

$\Delta \mathbf{x}_{J_{2-3}}$ ,  $\Delta \mathbf{x}_{J_{2-4}}$  and so forth until each successive gravity coefficient is tested. With these calculations the root mean square error is found between the high order gravity

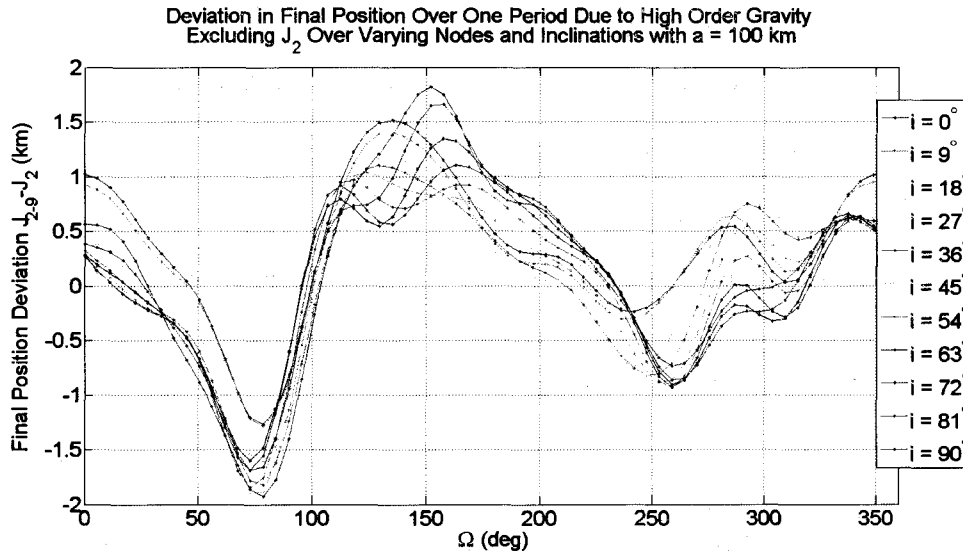


Figure 3.10: Deviation in final position (km) due to  $J_{3-9}$  for circular orbits with varying ascending nodes and inclinations at  $a = 100$  km propagated over one period

case,  $\Delta \mathbf{x}_{J_{2-9}}$  and all the other gravity coefficient cases. For instance, comparing  $J_{2-9}$  and  $J_2$ , one finds that

$$RMS(\Delta \mathbf{x}_{J_{2-9}}, \Delta \mathbf{x}_{J_2}) = \sqrt{\frac{\sum_{i=1}^n (x_{J_{2-9},i} - x_{J_2,i})^2}{n}} \quad (3.49)$$

where  $n$  is the number of elements in the vector  $\Delta \mathbf{x}$ .

The values produced in this case are compared to those produced in the NASA report, *The Gravitational Acceleration Equations* [41]. The parameters are 630 test cases with inclinations varying from  $0^\circ$  to  $90^\circ$  and the right ascension of ascending node varying from  $0^\circ$  to  $360^\circ$ . The results are given in Table 3.1.

In comparing the High Order Gravity model output with the NASA legacy data, two values were of interest: the ‘‘Truth Comparison’’, and the ‘‘Max Error’’. The ‘‘Truth Comparison’’ columns in the table represent how each gravitational model is compared against the ‘truth’, in this case the high order gravity model to the 9th order,  $J_{2-9}$ . The 9th order is selected as the truth since it is the highest order available at the time. Against itself, the  $J_{2-9}$  model has no error, thus the results

	NASA Model[41]			High Order Gravity Model		
Model Order	RMS Error	Truth Comparison	Max Error	RMS Error	Truth Comparison	Max Error
9	82	0	0	0	0	0
8	83	1	49	40	40	103
7	129	47	53	101	101	297
4	273	191	565	233	233	678
2	538	456	1130	444	444	1167
$J_2$ only	789	707	1810	701	701	1720

Table 3.1: Comparison of NASA and High Order Gravity model prediction position deviation

seen in the first row. The NASA model ‘truth’ values are smaller or very similar to the High Order Gravity model values for all orders, with the largest discrepancy between the 7th order models for the two, with a difference of only 54. Comparing the maximum error between the two models yields a greater error for all the high order cases produced by the High Order Gravity model, except  $J_2$  only. The information between the two models is similar enough to further validate the accuracy of the high order gravity model.

### 3.3.4 Model Configuration

As with all the perturbations modeled in this research, the High Order Gravity model can be turned “on” or “off” based upon a user specified flag, fHOG, in the initialization file. The default value ‘1’, turns the HOG model on, thus decomposing the model into harmonics using Legendre polynomials. The value ‘0’ for fHOG results in the computation of the low terms  $J_2$  and  $J_2J_3J_4$  if a low fidelity model is required.

The specific gravity coefficients used by the model depend upon the ‘degree’ specified by the user and the order of interest. See Table 3.2 for the effect of setting different values for these parameters.

The gravity model is designed as a general model that can be applied to any planetary body. For this reason the model must be initialized with values specific to

fHOG	degree	order	Description
0	0	0	Spherical Earth
0	2,4,9	0	Describes only the zonal harmonics (order = 0) where gravity field is reduced to bands of latitude, i.e. 2 refers to only $J_2$ coefficient
1	0-9	0-9	Describes zonal, sectoral (degree = order), and tesseral (degree $\neq$ order) harmonics. Takes into consideration mass distribution of the Earth in the latitudinal and longitudinal direction.

Table 3.2: Summary of effects for setting different parameters in the Higher Order Gravity model

the planet of interest. The required parameter definitions to utilize the High Order Gravity model are defined in Table 3.3.

Parameter	Units	Description
$\mu$	$\left(\frac{m^3}{s^2}\right)$	Gravitational parameter
rg	$(m)$	Radius of planet
degree	unitless	Order of perturbation: 0, 2, 4, or 9
fHOG	unitless	Flag for HOG model: 1 = on 0 = off
table	unitless	Harmonic coefficients (10x10)

Table 3.3: Required parameter definitions for higher order gravity model initialization

### 3.4 Atmospheric Drag

Spacecraft in near Earth orbit with altitudes less than 1000 km experience significant drag due to collisions with atmospheric particles. Dependent on velocity, drag is a non-conservative perturbation in that the total energy of the orbit is not conserved. Since drag is the greatest at perigee, it reduces the velocity at this point resulting in the degradation of the apogee height on successive revolutions. This reduces the orbit semimajor axis and eccentricity and tends to circularize the orbit. The acceleration due to aerodynamic drag is [44]:

$$\mathbf{a}_{drag} = -\frac{1}{2} \frac{c_D A}{m} \rho v_{rel}^2 \frac{\mathbf{v}_{rel}}{|\mathbf{v}_{rel}|} \quad (3.50)$$



The coefficient of drag,  $c_D$ , is a dimensionless quantity which reflects the vehicle's susceptibility to drag forces. Depending on the geometric form of the vehicle, the coefficient is a difficult value to estimate. The mass,  $m$ , is assumed to be constant. The cross-sectional area,  $A$ , normal to the velocity vector is difficult to accurately compute due to the changing orientation of the vehicle. For this reason the area is also approximated. Since Earth's atmosphere has a mean motion due to the Earth's rotation, the velocity in the drag calculation must be relative to the atmosphere. For simplicity, the program assumes no atmospheric rotation. The most challenging parameter to calculate is the atmospheric density,  $\rho$ , which indicates how dense the atmosphere is at a specific altitude.

The density distribution of a homogeneous, ideal gas with an altitude  $h$  is determined by the ideal gas law [34]

$$\rho = \frac{pM}{gRT}, \quad (3.51)$$

and by the equation of hydrostatic balance,

$$\Delta p = -\rho g \Delta h \quad (3.52)$$

where  $p$  is the gas pressure. In the preceding equations,  $M$  is the mean molecular mass of all atmospheric constituents,  $g$  is the acceleration due to gravity,  $R$  is the universal gas constant, and  $T$  is the absolute temperature measured in Kelvins. Substituting  $\rho$  from Equation 3.51 into Equation 3.52 and integrating Equation 3.52 from an initial altitude  $h_0$  to a final altitude,  $h$ ,

$$\rho = \rho_0 \frac{T_0 M}{T M_0} \exp\left(-\int_{h_0}^h \frac{gM}{RT} dh\right) \quad (3.53)$$

the formula for atmospheric pressure and density is determined. In general,  $g$ ,  $M$ , and  $T$  are functions of altitude and time. The most challenging aspect in modeling

atmospheric density involves the determination of the relationship between  $M$ ,  $T$ , and time which are of a quasi-cyclic nature. At altitudes between 120-600 km, a range known as the thermosphere, large temperature variations ranging from 800-1200 K occur over a typical solar cycle. The temperature fluctuations are a result of the local absorption of Extreme Ultraviolet Radiation. At altitudes between 500-800 km, the atmospheric density between solar maximum and solar minimum increases by approximately two orders of magnitude. Figure 3.11 depicts a general illustration of the properties of the Earth's atmosphere [34]. The variations are associated with

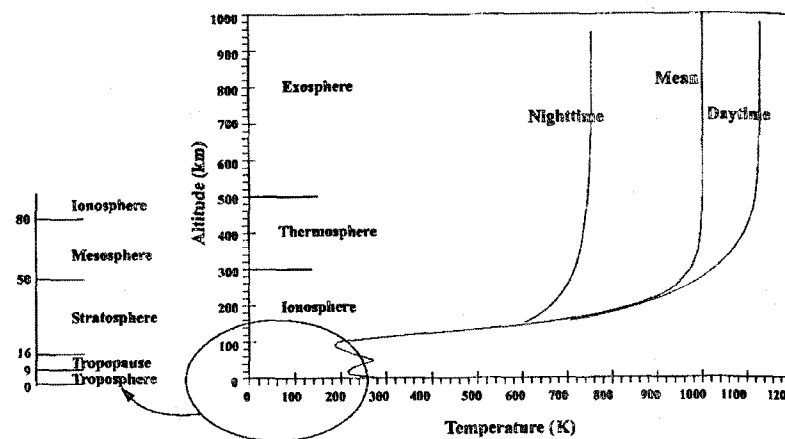


Figure 3.11: General illustration of the Earth's atmosphere with the bands representing areas of similar properties [49]

changes in the solar energy absorbed by the Earth's atmosphere which occur daily, seasonally, and half-yearly.

Daily, or diurnal variations arise as the Earth rotates. An atmospheric bulge, which represents a density maximum, lags the general direction of the Sun. It is centered on meridians where the local time is 2:00-2:30 P.M. A minimum value occurs opposite the bulge at 4:00 A.M. each day. The bulge is also centered at the equator on the equinoxes but moves to higher latitudes depending on the Sun's declination which varies throughout the year [49].

The seasonal and semi-annual variations last approximately six months and are

related to the varying distance of the Earth from the Sun as well as the Sun's declination. Density variations are also related to the 11 year solar cycle which strongly varies the amount of solar radiation that reaches the Earth.

For the calculation of Atmospheric Drag, a simplified static model of the atmosphere that only considers the altitude profile is employed. The model assumes the entire atmosphere is isothermal and the density of the atmosphere decays exponentially with increasing altitude. Thus, from Equation 3.53, assuming  $T = T_0 = const$  and  $M = M_0 = const$ , the density is calculated as

$$\rho = \rho_0 \exp\left(-\frac{h - h_0}{H}\right), \quad (3.54)$$

where  $\rho_0$  is the sea-level density, equal to  $1.225 \text{ kg/m}^3$ , and  $H = RT_0 / (gM_0) = const$  is the reciprocal of the atmospheric scale height set to  $8.434 \times 10^3 \text{ m}$  [40]. Though this model approximates much of the atmosphere, its simplifying assumptions induce a large uncertainty in the accuracy of the model.

### 3.5 Solar Radiation

Solar radiation pressure is a result of the impact of light photons emitted from the Sun on a vehicle's surface. Like drag, it is a non-conservative perturbation, but it has a more pronounced effect at higher orbits and during interplanetary missions. Solar radiation pressure is different from aerodynamic drag in that the force produced is in the antisolar direction, rather than always opposite the spacecraft's velocity vector. For this reason the effects of solar radiation may average close to zero for orbits which experience periods of solar occultation by the Earth [24]. The acceleration due to solar radiation is calculated by the equation

$$\mathbf{a}_{SR} = -\frac{p_{SR} C_R A_{\odot}}{m} \frac{\mathbf{r}_{sat\odot}}{|\mathbf{r}_{sat\odot}|}, \quad (3.55)$$

where  $p_{SR}$ , is the solar pressure per unit area, or the change in momentum defined as

$$p_{SR} = 4.57 \times 10^{-6} \frac{\text{N}}{\text{m}^2}. \quad (3.56)$$

The variable  $c_R$  is the reflectivity and can have a value between 0.0 and 2.0, indicating how the vehicle reflects incoming radiation. A value of 0.0 means the object is translucent to radiation, and thus no force is transmitted. A value of 1.0 indicates all the radiation is absorbed and all the force is transmitted. Finally, a value of 2.0 means all the radiation is reflected and twice the force is transmitted [49].  $A_{\odot}$  is the area of the spacecraft exposed to the Sun. Determining both  $c_R$  and  $A_{\odot}$  is difficult as the vehicle is often changing altitude. For this reason, an average value is selected for both based on the possible orientations of the vehicle throughout the flight. The variable  $m$  is the mass of the vehicle and, depending on the mission, may change drastically over time. For simplicity purposes the mass is assumed constant. However, if a thrust model were added the mass would be computed as an additional state. The symbol  $\mathbf{r}_{sat\odot}$  denotes the position vector from the vehicle to the Sun; because this vector always points away from the sun, a unit vector yields the appropriate sign. The SPICE ephemeris program is used to calculate the position of the Sun with respect to the vehicle.

Solar radiation pressure does not act on a spacecraft during periods of solar occultation by the Earth or other bodies. As a result a program such as *Shadow*, as defined in Vallado [49], can be utilized to determine whether or not the spacecraft is in complete sunlight, penumbra, or umbra.

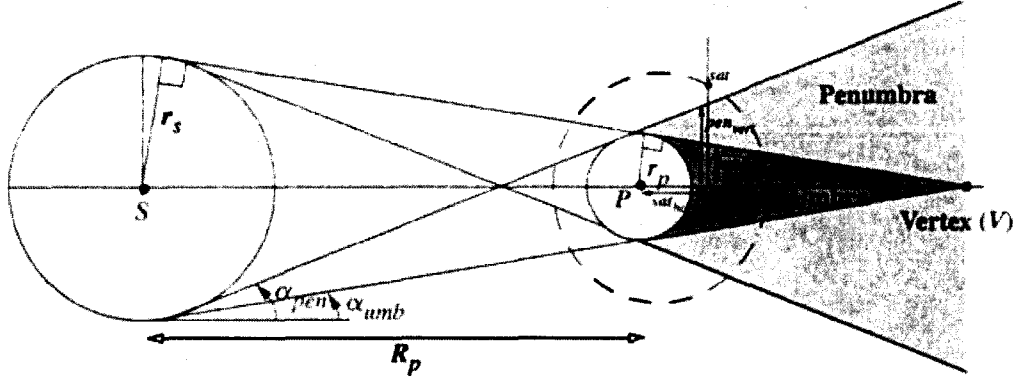


Figure 3.12: Geometry used by the program *Shadow* to calculate the regions of penumbra and umbra experienced by the vehicle [49]

*Shadow* utilizes the geometry in Figure 3.12 to determine if the vehicle is in an eclipsed region. An initial check,

$$\mathbf{r}_{\odot} \cdot \mathbf{r} < 0 \quad (3.57)$$

determines whether or not the vehicle is in sunlight or any form of shadow. If true, the angle,  $\zeta$ , between  $-\mathbf{r}_{\odot}$  and  $\mathbf{r}$  is calculated and used to determine the horizontal,  $sat_{horiz}$ , and vertical,  $sat_{vert}$ , components of the position vector,

$$sat_{horiz} = |\mathbf{r}| \cos(\zeta) \quad (3.58)$$

and

$$sat_{vert} = |\mathbf{r}| \sin(\zeta). \quad (3.59)$$

The vertical components of the penumbra and umbra region are found using the equations

$$PEN_{vert} = R_{\oplus} + \tan(\alpha_{pen}) sat_{horiz}, \quad (3.60)$$

and

$$UMB_{vert} = R_{\oplus} - \tan(\alpha_{umb})sat_{horiz} \quad (3.61)$$

where  $\alpha_{pen}$  and  $\alpha_{umb}$  are the angles for the Sun as defined in Figure 3.12. They are calculated using the right triangle relationships

$$\tan(\alpha_{pen}) = \frac{r_s + r_p}{R_p} = \frac{696,000 + 6,378}{149,599,870} = 0.26900424^\circ, \quad (3.62)$$

and

$$\tan(\alpha_{umb}) = \frac{r_s - r_p}{R_p} = \frac{696,000 - 6,378}{149,599,870} = 0.26411888^\circ \quad (3.63)$$

where  $r_s$  is the radius of the Sun,  $r_p$  is the radius of the planet which in this case is Earth, and  $R_p$  is the distance from the center of the Sun to the center of the Earth. The criterion to determine which type of eclipse the satellite is in is as follows: If  $sat_{vert} \leq PEN_{vert}$ , the satellite is in penumbra. If  $sat_{vert} \leq PEN_{vert}$  and  $sat_{vert} \leq UMB_{vert}$ , the satellite is in umbra. Finally, if neither of the previous statements is true, the satellite is not in any form of eclipse. The *Shadow* function is implemented in the *Solar Radiation* model by multiplying Equation 3.55 by the parameter  $\nu$  whose value is dependent on the eclipse type. The values of  $\nu$  used in this research are listed in Table 3.4. It is clear that the weight of  $\nu$  plays a large role in the magnitude of the perturbation caused by solar radiation.

Shadow	$\nu$
None	1
Penumbra	0.5
Umbra	0

Table 3.4: Value of the solar radiation parameter  $\nu$  based on the shadow type

Implemented with Cowell's method, the perturbation models in this chapter comprise the "predicting" portion of the predictor-corrector developed for this study. Since

the final propagated states will not always match up with the desired values, a means of correction to the initial states is implemented. The following chapter develops the corresponding “correcting” part of the process.

# Chapter 4

## State Transition Matrix

The following chapter describes the error state transition matrix that forms the basis for the “corrector” used in the predictor-corrector algorithm for this thesis. The state transition matrix linearizes the trajectory determination problem to further refine the initial velocity guess to produce a final high fidelity trajectory. The derivation of the partial derivatives of the perturbations discussed in the previous chapter are also considered. The accuracy of the matrix is demonstrated over varying times of flight and initial perturbation percentages to demonstrate the linear sensitivity region. Finally, the application of the matrix in a shooting method technique is demonstrated.

The derivative of the state transition matrix begins by assuming the existence of two close trajectories. Of the two trajectories, only one is known. To determine the unknown trajectory the difference between the two trajectories is computed. If the two trajectories are  $\mathbf{X}$  and  $\mathbf{Y}$ , the initial conditions and derivatives of the states are defined as [49]

$$\begin{aligned}\mathbf{X}(t_0) &= \mathbf{X}_0 & \text{and} & & \dot{\mathbf{X}} &= \vec{f}(\mathbf{X}), \\ \mathbf{Y}(t_0) &= \mathbf{Y}_0 & \text{and} & & \dot{\mathbf{Y}} &= \vec{f}(\mathbf{Y})\end{aligned}\tag{4.1}$$

where  $\vec{f}$  denotes a function of the state. If the difference between the two trajectories



is  $\delta\mathbf{x}$ , then

$$\mathbf{Y} = \mathbf{X} + \delta\mathbf{x}. \quad (4.2)$$

Substituting Equation 4.2 into Equation 4.1 results in

$$\dot{\mathbf{Y}} = \vec{f}(\mathbf{X} + \delta\mathbf{x}). \quad (4.3)$$

Since  $\vec{f}(\mathbf{X} + \delta\mathbf{x})$  is nonlinear, the function is expanded in a Taylor series about  $\mathbf{X}$ , ( $\delta\mathbf{x} = \mathbf{Y} - \mathbf{X}$ ),

$$\dot{\mathbf{Y}} = \vec{f}(\mathbf{X}) + \frac{\partial \vec{f}(\mathbf{X})}{\partial \mathbf{X}} \delta\mathbf{x} + \frac{\partial^2 \vec{f}(\mathbf{X})}{2! \partial \mathbf{X}^2} \delta\mathbf{x}^2 + \dots \quad (4.4)$$

where  $\vec{f}(\mathbf{X})$  is a time varying square matrix. The time derivative of Equation 4.2 is taken and substituted into the left-hand side of Equation 4.4

$$\dot{\mathbf{X}} + \delta\dot{\mathbf{x}} = \vec{f}(\mathbf{X}) + \frac{\partial \vec{f}(\mathbf{X})}{\partial \mathbf{X}} \delta\mathbf{x} + \frac{\partial^2 \vec{f}(\mathbf{X})}{2! \partial \mathbf{X}^2} \delta\mathbf{x}^2 + \dots \quad (4.5)$$

which using Equation 4.1 is reduced to the equation

$$\delta\dot{\mathbf{x}} = \frac{\partial \vec{f}(\mathbf{X})}{\partial \mathbf{X}} \delta\mathbf{x} + \mathbf{u} = \mathbf{G} \delta\mathbf{x} + \mathbf{u}. \quad (4.6)$$

Here  $\mathbf{u}$  represents the neglected higher order terms and  $\mathbf{G}$  is a matrix of partial derivatives known as the Jacobian matrix which represents the linearized dynamics. Its solution is the time-varying difference between the two neighboring trajectories.

A relationship for the  $\mathbf{G}$  matrix is found by assuming a solution to Equation 4.6 of the form

$$\delta\mathbf{x} = \Phi(t, t_0) \delta\mathbf{x}_0 \quad (4.7)$$

which is also written as

$$\begin{bmatrix} \delta\mathbf{r} \\ \delta\mathbf{v} \end{bmatrix} = \Phi(t, t_0) \begin{bmatrix} \delta\mathbf{r}_0 \\ \delta\mathbf{v}_0 \end{bmatrix}. \quad (4.8)$$

For these equations  $\mathbf{u} = 0$  and  $\Phi(t, t_0)$  is the state transition matrix which relates an initial set of perturbed state vectors to a final set of perturbed state vectors over a given period of time [48][5]. The components of the matrix are

$$\Phi(t, t_0) = \begin{bmatrix} \frac{\partial \mathbf{r}}{\partial \mathbf{r}_0} & \frac{\partial \mathbf{r}}{\partial \mathbf{v}_0} \\ \frac{\partial \mathbf{v}}{\partial \mathbf{r}_0} & \frac{\partial \mathbf{v}}{\partial \mathbf{v}_0} \end{bmatrix} = \begin{bmatrix} \Phi_{11} & \Phi_{12} \\ \Phi_{21} & \Phi_{22} \end{bmatrix}, \quad (4.9)$$

where

$$\Phi_{11} = \left[ \frac{\partial \mathbf{r}}{\partial \mathbf{r}_0} \right] = \begin{bmatrix} \frac{\partial x}{\partial x_0} & \frac{\partial x}{\partial y_0} & \frac{\partial x}{\partial z_0} \\ \frac{\partial y}{\partial x_0} & \frac{\partial y}{\partial y_0} & \frac{\partial y}{\partial z_0} \\ \frac{\partial z}{\partial x_0} & \frac{\partial z}{\partial y_0} & \frac{\partial z}{\partial z_0} \end{bmatrix}. \quad (4.10)$$

The state is numerically integrated using the matrix differential equation which is found by taking the derivative of Equation 4.7,

$$\delta \dot{\mathbf{x}} = \dot{\Phi} \delta \mathbf{x}_0 + \Phi \delta \dot{\mathbf{x}}_0 \quad (4.11)$$

where  $\delta \dot{\mathbf{x}}_0 = 0$ . Substituting Equation 4.6 into Equation 4.11 produces

$$\mathbf{G} \delta \mathbf{x} = \dot{\Phi} \delta \mathbf{x}_0. \quad (4.12)$$

Substituting the right side of Equation 4.7 back into Equation 4.12 produces

$$\mathbf{G} \Phi(t, t_0) \delta \mathbf{x}_0 = \dot{\Phi}(t, t_0) \delta \mathbf{x}_0 \quad (4.13)$$

which reduces to the first-order differential equation

$$\dot{\Phi}(t, t_0) = \mathbf{G} \Phi(t, t_0), \quad (4.14)$$

with the initial condition

$$\Phi(t, t_0) = \mathbf{I}_{6 \times 6}. \quad (4.15)$$

Note the dynamic coefficient matrix consists of nonlinear, time-varying terms  $G_1 = \frac{\partial \ddot{\mathbf{r}}}{\partial \mathbf{r}}$  and  $G_2 = \frac{\partial \ddot{\mathbf{v}}}{\partial \mathbf{v}}$ :

$$\mathbf{G} = \begin{bmatrix} \mathbf{0}_{3 \times 3} & \mathbf{I}_{3 \times 3} \\ G_1 & G_2 \end{bmatrix} \quad (4.16)$$

The following describes the development of the partials for each individual perturbation required by  $G_1$  and  $G_2$  in Equation 4.16.

## 4.1 N-Body Partial

The most basic state transition matrix consists of partials calculated from the two-body conic motion derived from Equation 2.10,

$$\ddot{\mathbf{r}}_{\oplus sat} = -\frac{\mu}{r_{\oplus sat}^3} \mathbf{r}_{\oplus sat}. \quad (4.17)$$

As previously mentioned, an analytic solution exists for conic motion. One derivation of the analytic Keplerian matrix is found in Reference [45]. The simplest partials to add to the conic state transition matrix are those resulting from three body acceleration. From Equation 3.1 one derives that

$$\ddot{\mathbf{r}}_{\oplus sat} = -\frac{\mu_{\oplus}}{r_{\oplus sat}^3} \mathbf{r}_{\oplus sat} + \frac{\mu_{\odot}}{r_{sat \odot}^3} \mathbf{r}_{sat \odot} - \frac{\mu_{\oplus}}{r_{\oplus \odot}^3} \mathbf{r}_{\oplus \odot}. \quad (4.18)$$

Thus,  $\frac{\partial \ddot{\mathbf{r}}}{\partial \mathbf{r}} = f_n(r, t)$ . The partials on the diagonal have the form

$$\frac{\partial \ddot{r}_i}{\partial r_i} = -\frac{\mu_{\oplus}}{r_{\oplus sat}^3} + \frac{3\mu_{\oplus} r_{\oplus sat, i}^2}{r_{\oplus sat}^5} - \frac{\mu_{\odot}}{r_{\odot sat}^3} + \frac{3\mu_{\odot} r_{\odot sat, i}^2}{r_{\odot sat}^5}. \quad (4.19)$$

All other sub-components of the matrix are defined as

$$\frac{\partial \ddot{r}_i}{\partial r_j} = \frac{3\mu_{\oplus} r_{\oplus sat, i} r_{\oplus sat, j}}{r_{\oplus sat}^5} + \frac{3\mu_{\odot} r_{\odot sat, i} r_{\odot sat, j}}{r_{\odot sat}^5}, \quad j \neq i \quad (4.20)$$

where  $i$  and  $j$  refer to any vector sub-components  $x$ ,  $y$ , or  $z$ . To add in a fourth body to the state transition matrix, such as the Sun, the last two terms of Equation 4.19 and the last term in Equation 4.20 are repeated with  $\mu$  and the position vectors updated so they are with respect to the fourth body. Thus, the updated Equations 4.19-4.20 are

$$\frac{\partial \ddot{r}_i}{\partial r_i} = -\frac{\mu_{\oplus}}{r_{\oplus sat}^3} + \frac{3\mu_{\oplus} r_{\oplus sat, i}^2}{r_{\oplus sat}^5} - \frac{\mu_{\odot}}{r_{\odot sat}^3} + \frac{3\mu_{\odot} r_{\odot sat, i}^2}{r_{\odot sat}^5} - \frac{\mu_{\otimes}}{r_{\otimes sat}^3} + \frac{3\mu_{\otimes} r_{\otimes sat, i}^2}{r_{\otimes sat}^5} \quad (4.21)$$

$$\frac{\partial \ddot{r}_i}{\partial r_j} = \frac{3\mu_{\oplus} r_{\oplus sat, i} r_{\oplus sat, j}}{r_{\oplus sat}^5} + \frac{3\mu_{\odot} r_{\odot sat, i} r_{\odot sat, j}}{r_{\odot sat}^5} + \frac{3\mu_{\otimes} r_{\otimes sat, i} r_{\otimes sat, j}}{r_{\otimes sat}^5}, \quad j \neq i \quad (4.22)$$

where the subscript  $\otimes$  refers to the Sun. The equations can be rewritten in a generalized form to include n-bodies:

$$\frac{\partial \ddot{r}_i}{\partial r_i} = G \sum_{j=3}^n m_j \left( -\frac{1}{r_{j sat}^3} + \frac{3r_{j sat, i}^2}{r_{j sat}^5} \right) \quad (4.23)$$

$$\frac{\partial \ddot{r}_i}{\partial r_i} = G \sum_{j=3}^n m_j \left( \frac{3r_{j sat, i} r_{j sat, j}}{r_{j sat}^5} \right), \quad j \neq i \quad (4.24)$$

Since for acceleration due to n-bodies,  $\ddot{r}$  is only a function of position, the dynamic coefficient matrix reduces to:

$$\mathbf{G} = \begin{bmatrix} \mathbf{0} & \mathbf{I} \\ G_1 & \mathbf{0} \end{bmatrix} \quad (4.25)$$

The state transition matrix is propagated forward in time using the variable step differential equation solvers discussed in Section 2.8.5. For each time step the SPICE

ephemeris program calculates the updated position vector of the Moon and or Sun as needed in Equations 4.19-4.20.

## 4.2 Gravity Potential Partialals

The state transition matrix can be updated to include more complex perturbations such as higher order gravity, drag, and solar radiation. Like the three-body equations of motion, the equations due to the non-spherical Earth depend only on the satellite's position,  $\frac{\partial \ddot{r}}{\partial r} = fn(r, t)$ , and thus no partials are taken with respect to velocity. The following derivation is based on Long's [25] calculations of the partials of the potential function as seen in Equation 3.18. To maintain conformity with Long's development, the potential function variable  $\phi$  is replaced by  $U$ . Thus, the acceleration due to high order gravity is the gradient of the potential function,  $\mathbf{a}_{J_{2-9}} = \frac{\partial U}{\partial \mathbf{r}}$ , which is transformed into spherical coordinates for simplicity. That is,

$$\mathbf{a}_{J_{2-9}} = \frac{\partial U}{\partial \mathbf{r}} = \frac{\partial U}{\partial r} \frac{\partial r}{\partial \mathbf{r}} + \frac{\partial U}{\partial \lambda} \frac{\partial \lambda}{\partial \mathbf{r}} + \frac{\partial U}{\partial \phi} \frac{\partial \phi}{\partial \mathbf{r}}. \quad (4.26)$$

The partial of  $\mathbf{a}_{J_{2-9}}$  with respect to  $\mathbf{r}$  is found by differentiating Equation 4.26. Specifically,

$$\begin{aligned} \frac{\partial \mathbf{a}_{J_{2-9}}}{\partial \mathbf{r}} &= \frac{\partial}{\partial \mathbf{r}} \left( \frac{\partial U}{\partial r} \right) \frac{\partial r}{\partial \mathbf{r}} + \frac{\partial}{\partial \mathbf{r}} \left( \frac{\partial U}{\partial \phi} \right) \frac{\partial \phi}{\partial \mathbf{r}} + \frac{\partial}{\partial \mathbf{r}} \left( \frac{\partial U}{\partial \lambda} \right) \frac{\partial \lambda}{\partial \mathbf{r}} \\ &\quad + \frac{\partial U}{\partial r} \frac{\partial^2 r}{\partial \mathbf{r}^2} + \frac{\partial U}{\partial \phi} \frac{\partial^2 \phi}{\partial \mathbf{r}^2} + \frac{\partial U}{\partial \lambda} \frac{\partial^2 \lambda}{\partial \mathbf{r}^2}, \end{aligned} \quad (4.27)$$

where the partial derivatives of  $\frac{\partial U}{\partial r}$ ,  $\frac{\partial U}{\partial \phi}$ , and  $\frac{\partial U}{\partial \lambda}$  with respect to  $\mathbf{r}$  are obtained using the following matrix

$$\frac{\partial}{\partial \mathbf{r}} \begin{bmatrix} \frac{\partial U}{\partial r} \\ \frac{\partial U}{\partial \phi} \\ \frac{\partial U}{\partial \lambda} \end{bmatrix} = \begin{bmatrix} \frac{\partial^2 U}{\partial r^2} & \frac{\partial^2 U}{\partial r \partial \phi} & \frac{\partial^2 U}{\partial r \partial \lambda} \\ \frac{\partial^2 U}{\partial \phi \partial r} & \frac{\partial^2 U}{\partial^2 \phi} & \frac{\partial^2 U}{\partial \phi \partial \lambda} \\ \frac{\partial^2 U}{\partial \lambda \partial r} & \frac{\partial^2 U}{\partial \lambda \partial \phi} & \frac{\partial^2 U}{\partial \lambda^2} \end{bmatrix} \begin{bmatrix} \frac{\partial r}{\partial \mathbf{r}} \\ \frac{\partial \phi}{\partial \mathbf{r}} \\ \frac{\partial \lambda}{\partial \mathbf{r}} \end{bmatrix}. \quad (4.28)$$

The second partial derivatives of the potential are

$$\begin{aligned} \frac{\partial^2 U}{\partial r^2} &= \frac{\mu}{r^3} \sum_{n=2}^{\infty} \left( \frac{R_{\oplus}}{r} \right)^n (n+2)(n+1) \\ &\times \sum_{m=0}^n (C_n^m \cos m\lambda + S_n^m \sin m\lambda) P_n^m(\sin \phi), \end{aligned} \quad (4.29)$$

$$\begin{aligned} \frac{\partial^2 U}{\partial r \partial \phi} &= \frac{\partial^2 U}{\partial \phi \partial r} = -\frac{\mu}{r^2} \sum_{n=2}^{\infty} \left( \frac{R_{\oplus}}{r} \right)^n (n+1) \\ &\times \sum_{m=0}^n (C_n^m \cos m\lambda + S_n^m \sin m\lambda) [P_n^{m+1}(\sin \phi) - m \tan \phi P_n^m(\sin \phi)], \end{aligned} \quad (4.30)$$

$$\begin{aligned} \frac{\partial^2 U}{\partial r \partial \lambda} &= \frac{\partial^2 U}{\partial \lambda \partial r} = -\frac{\mu}{r^3} \sum_{n=2}^{\infty} \left( \frac{R_{\oplus}}{r} \right)^n (n+1) \\ &\times \sum_{m=0}^n m (S_n^m \cos m\lambda - C_n^m \sin m\lambda) P_n^m(\sin \phi), \end{aligned} \quad (4.31)$$

$$\begin{aligned} \frac{\partial^2 U}{\partial \phi^2} &= \frac{\mu}{r} \sum_{n=2}^{\infty} \left( \frac{R_{\oplus}}{r} \right)^n \sum_{m=0}^n (C_n^m \cos m\lambda + S_n^m \sin m\lambda) [\tan \phi P_n^{m+1}(\sin \phi) \\ &+ [m^2 \sec^2 \phi - m \tan^2 \phi - n(n+1)] P_n^m(\sin \phi)], \end{aligned} \quad (4.32)$$

$$\begin{aligned} \frac{\partial^2 U}{\partial \phi \partial \lambda} &= \frac{\partial^2 U}{\partial \lambda \partial \phi} = \frac{\mu}{r} \sum_{n=2}^{\infty} \left( \frac{R_{\oplus}}{r} \right)^n \sum_{m=0}^n m (S_n^m \cos m\lambda - C_n^m \sin m\lambda) \\ &\times [P_n^{m+1}(\sin \phi) - m \tan \phi P_n^m(\sin \phi)], \end{aligned} \quad (4.33)$$

and

$$\frac{\partial^2 U}{\partial \lambda^2} = -\frac{\mu}{r} \sum_{n=2}^{\infty} \left( \frac{R_{\oplus}}{r} \right)^n \sum_{m=0}^n m^2 (C_n^m \cos m\lambda + S_n^m \sin m\lambda) P_n^m(\sin \phi). \quad (4.34)$$

The partial derivatives of  $r$ ,  $\phi$ , and  $\lambda$  with respect to  $\mathbf{r}$ , where  $\mathbf{r} = [r_x \ r_y \ r_z]$  are

$$\frac{\partial r}{\partial \mathbf{r}} = \frac{\mathbf{r}^T}{r}, \quad (4.35)$$

$$\frac{\partial \phi}{\partial \mathbf{r}} = \frac{1}{\sqrt{r_x^2 + r_y^2}} \left[ -\frac{r_z \mathbf{r}^T}{r^2} + \frac{\partial r_z}{\partial \mathbf{r}} \right], \quad (4.36)$$

and

$$\frac{\partial \lambda}{\partial \mathbf{r}} = \frac{1}{(r_x^2 + r_y^2)} \left[ r_x \frac{\partial r_y}{\partial \mathbf{r}} - r_y \frac{\partial r_x}{\partial \mathbf{r}} \right]. \quad (4.37)$$

The required second partial derivatives of  $r$ ,  $\phi$ , and  $\lambda$  in Equation 4.27 are found by differentiating Equations 4.35-4.37 with respect to  $\mathbf{r}$ . That is,

$$\frac{\partial^2 r}{\partial \mathbf{r}^2} = \frac{1}{r} \left[ \mathbf{I} - \frac{\mathbf{r}\mathbf{r}^T}{r^2} \right], \quad (4.38)$$

$$\begin{aligned} \frac{\partial^2 \phi}{\partial \mathbf{r}^2} = & -\frac{1}{(r_x^2 + r_y^2)^{\frac{3}{2}}} \left[ \left( \frac{\partial r_z}{\partial \mathbf{r}} \right)^T - \frac{r_z \mathbf{r}}{r^2} \right] \left[ r_x \left( \frac{\partial r_x}{\partial \mathbf{r}} \right) + r_y \left( \frac{\partial r_y}{\partial \mathbf{r}} \right) \right] \\ & - \frac{1}{r^2 \sqrt{r_x^2 + r_y^2}} \left[ \mathbf{r} \left( \frac{\partial r_z}{\partial \mathbf{r}} \right) + r_z \mathbf{I} - \frac{2r_z}{r^2} \mathbf{r}\mathbf{r}^T \right], \end{aligned} \quad (4.39)$$

and

$$\frac{\partial^2 \lambda}{\partial \mathbf{r}^2} = -\frac{2}{(r_x^2 + r_y^2)} \begin{bmatrix} -r_y \\ r_x \\ 0 \end{bmatrix} \left[ r_x \left( \frac{\partial r_x}{\partial \mathbf{r}} \right) + r_y \left( \frac{\partial r_y}{\partial \mathbf{r}} \right) \right] + \frac{1}{(r_x^2 + r_y^2)} \begin{bmatrix} 0 & -1 & 0 \\ 1 & 0 & 0 \\ 0 & 0 & 0 \end{bmatrix} \quad (4.40)$$

where  $\frac{\partial r_x}{\partial \mathbf{r}} = (1, 0, 0)$ ,  $\frac{\partial r_y}{\partial \mathbf{r}} = (0, 1, 0)$ , and  $\frac{\partial r_z}{\partial \mathbf{r}} = (0, 0, 1)$ . To reduce the analytical computations necessary for taking the partial derivatives of a high order gravity model, the partials for only  $J_2$ ,  $J_3$ , and  $J_4$  are considered.

When taking the partials of Equation 3.10, consider first the partials with respect to the  $x$  and  $y$  components of both the acceleration and position vectors. The partial on the diagonal is

$$\frac{\partial a_{J_2,i}}{\partial r_i} = -\frac{3J_2\mu R_\oplus^2}{2\mathbf{r}^5} + \frac{15J_2\mu R_\oplus^2 r_i^2}{2\mathbf{r}^7} + \frac{15J_2\mu R_\oplus^2 r_z^2}{2\mathbf{r}^7} - \frac{105J_2\mu R_\oplus^2 r_i^2 r_z^2}{2\mathbf{r}^9}, \quad (4.41)$$

and the partial on the off diagonals is

$$\frac{\partial a_{J_2,i}}{\partial r_j} = \frac{15J_2\mu R_\oplus^2 r_i r_j}{2\mathbf{r}^7} - \frac{105J_2\mu R_\oplus^2 r_i r_j r_z^2}{2\mathbf{r}^9} \quad i \neq j. \quad (4.42)$$

The partial of the  $z$  component of the acceleration vector on the diagonal is

$$\frac{\partial a_{J_2,z}}{\partial r_z} = -\frac{9J_2\mu R_\oplus^2}{2\mathbf{r}^5} + \frac{45J_2\mu R_\oplus^2 r_z^2}{\mathbf{r}^7} - \frac{105J_2\mu R_\oplus^2 r_z^4}{2\mathbf{r}^9}, \quad (4.43)$$

and the partial on the off diagonals for the  $z$  component is

$$\frac{\partial a_{J_2,z}}{\partial r_i} = \frac{45J_2\mu R_\oplus^2 r_i r_z}{2\mathbf{r}^7} - \frac{105J_2\mu R_\oplus^2 r_i r_z^3}{2\mathbf{r}^9}. \quad (4.44)$$

Similar equations exist for the partials of the acceleration due to  $J_3$  and  $J_4$  (Equations 3.12-3.13). Again, considering the partials just with respect to the  $x$  and  $y$  components, the diagonal term is

$$\frac{\partial a_{J_3,i}}{\partial r_i} = -\frac{15J_3\mu R_\oplus^3 r_z}{2\mathbf{r}^7} + \frac{105J_3\mu R_\oplus^3 r_i^2 r_z}{2\mathbf{r}^9} + \frac{35J_3\mu R_\oplus^3 r_z^3}{2\mathbf{r}^9} - \frac{315J_3\mu R_\oplus^3 r_i^2 r_z^3}{2\mathbf{r}^{11}}, \quad (4.45)$$

and

$$\begin{aligned} \frac{\partial a_{J_4,i}}{\partial r_i} = & -\frac{15J_4\mu R_\oplus^4}{8\mathbf{r}^7} + \frac{105J_4\mu R_\oplus^4 r_i^2}{8\mathbf{r}^9} + \frac{105J_4\mu R_\oplus^4 r_z^3}{4\mathbf{r}^9} - \frac{945J_4\mu R_\oplus^4 r_i^2 r_z^2}{4\mathbf{r}^{11}} \\ & - \frac{315J_4\mu R_\oplus^4 r_z^4}{8\mathbf{r}^{11}} + \frac{3465J_4\mu R_\oplus^4 r_i^2 r_z^2}{8\mathbf{r}^{13}}. \end{aligned} \quad (4.46)$$

The off diagonal equations are

$$\frac{\partial a_{J_3,i}}{\partial r_j} = \frac{105J_3\mu R_\oplus^3 r_i r_j r_z}{2\mathbf{r}^9} - \frac{315J_3\mu R_\oplus^3 r_i r_j r_z^3}{2\mathbf{r}^{11}} \quad i \neq j, \quad (4.47)$$

and

$$\frac{\partial a_{J_4,i}}{\partial r_j} = \frac{105J_4\mu R_\oplus^4 r_i r_j}{8\mathbf{r}^9} - \frac{945J_4\mu R_\oplus^4 r_i r_j r_z^2}{4\mathbf{r}^{11}} + \frac{3465J_4\mu R_\oplus^4 r_i r_j r_z^4}{8\mathbf{r}^{13}} \quad i \neq j. \quad (4.48)$$

The partial of the  $z$  component of the  $J_3$  and  $J_4$  acceleration vectors on the diagonal are

$$\frac{\partial a_{J_3,z}}{\partial r_z} = -\frac{75J_3\mu R_\oplus^3 r_z}{2\mathbf{r}^7} + \frac{175J_3\mu R_\oplus^3 r_z^3}{\mathbf{r}^9} - \frac{315J_3\mu R_\oplus^3 r_z^5}{2\mathbf{r}^{11}}, \quad (4.49)$$



and

$$\frac{\partial a_{J_4,z}}{\partial r_z} = -\frac{75J_4\mu R_\oplus^4}{8\mathbf{r}^7} + \frac{1575J_4\mu R_\oplus^4 r_z^2}{8\mathbf{r}^9} - \frac{4725J_4\mu R_\oplus^4 r_z^4}{8\mathbf{r}^{11}} + \frac{3465J_4\mu R_\oplus^4 r_z^6}{8\mathbf{r}^{13}}. \quad (4.50)$$

Further, the partials on the off diagonal for the  $z$  component of the  $J_3$  and  $J_4$  acceleration vectors are

$$\frac{\partial a_{J_3,z}}{\partial r_i} = \frac{105J_3\mu R_\oplus^3 r_i r_z^2}{\mathbf{r}^9} - \frac{315J_3\mu R_\oplus^3 r_i r_z^4}{2\mathbf{r}^{11}} - \frac{15J_3\mu R_\oplus^3 r_i}{2\mathbf{r}^7}, \quad (4.51)$$

and

$$\frac{\partial a_{J_4,z}}{\partial r_i} = \frac{525J_4\mu R_\oplus^4 r_i r_z}{8\mathbf{r}^9} - \frac{1575J_4\mu R_\oplus^4 r_i r_z^3}{4\mathbf{r}^{11}} + \frac{3465J_4\mu R_\oplus^4 r_i r_z^5}{8\mathbf{r}^{13}}. \quad (4.52)$$

Again, because  $\frac{\partial a_{J_2-4}}{\partial r} = fn(r, t)$ , the dynamics coefficient matrix is

$$\mathbf{G} = \begin{bmatrix} \mathbf{0} & \mathbf{I} \\ G_1 & \mathbf{0} \end{bmatrix} \quad (4.53)$$

where  $G_1$  is rewritten as

$$G_1 = \begin{bmatrix} \frac{\partial a_{J_2,x}}{\partial r_x} + \frac{\partial a_{J_3,x}}{\partial r_x} + \frac{\partial a_{J_4,x}}{\partial r_x} & \frac{\partial a_{J_2,x}}{\partial r_y} + \frac{\partial a_{J_3,x}}{\partial r_y} + \frac{\partial a_{J_4,x}}{\partial r_y} & \frac{\partial a_{J_2,x}}{\partial r_z} + \frac{\partial a_{J_3,x}}{\partial r_z} + \frac{\partial a_{J_4,x}}{\partial r_z} \\ \frac{\partial a_{J_2,y}}{\partial r_x} + \frac{\partial a_{J_3,y}}{\partial r_x} + \frac{\partial a_{J_4,y}}{\partial r_x} & \frac{\partial a_{J_2,y}}{\partial r_y} + \frac{\partial a_{J_3,y}}{\partial r_y} + \frac{\partial a_{J_4,y}}{\partial r_y} & \frac{\partial a_{J_2,y}}{\partial r_z} + \frac{\partial a_{J_3,y}}{\partial r_z} + \frac{\partial a_{J_4,y}}{\partial r_z} \\ \frac{\partial a_{J_2,z}}{\partial r_x} + \frac{\partial a_{J_3,z}}{\partial r_x} + \frac{\partial a_{J_4,z}}{\partial r_x} & \frac{\partial a_{J_2,z}}{\partial r_y} + \frac{\partial a_{J_3,z}}{\partial r_y} + \frac{\partial a_{J_4,z}}{\partial r_y} & \frac{\partial a_{J_2,z}}{\partial r_z} + \frac{\partial a_{J_3,z}}{\partial r_z} + \frac{\partial a_{J_4,z}}{\partial r_z} \end{bmatrix}. \quad (4.54)$$

### 4.3 Atmospheric Drag Partialals

From Equation 3.50 it is clear that to incorporate drag into the state transition matrix the partials due to both position and velocity are required. The partial

with respect to the position vector is

$$\frac{\partial a_{drag,i}}{\partial r_j} = -\frac{C_D A \rho_0}{2m} \frac{r_j}{H} (r_x^2 + r_y^2 + r_z^2)^{-\frac{1}{2}} \exp\left(\frac{(r_x^2 + r_y^2 + r_z^2)^{\frac{1}{2}} - R_{\oplus}}{H}\right) (v_x^2 + v_y^2 + v_z^2)^{\frac{1}{2}} v_i. \quad (4.55)$$

The partial with respect to velocity on the diagonal is

$$\frac{\partial a_{drag,i}}{\partial v_i} = -\frac{C_D A \rho_0}{2m} \left[ \left( v_i^2 (v_x^2 + v_y^2 + v_z^2)^{-\frac{1}{2}} + (v_x^2 + v_y^2 + v_z^2)^{\frac{1}{2}} \right) \exp\left(\frac{(r_x^2 + r_y^2 + r_z^2)^{\frac{1}{2}} - R_{\oplus}}{H}\right) \right], \quad (4.56)$$

and the partial with respect to velocity on the off diagonal is

$$\frac{\partial a_{drag,i}}{\partial v_j} = -\frac{C_D A \rho_0}{2m} \left[ (v_x^2 + v_y^2 + v_z^2)^{-\frac{1}{2}} v_i v_j \exp\left(\frac{(r_x^2 + r_y^2 + r_z^2)^{\frac{1}{2}} - R_{\oplus}}{H}\right) \right]. \quad (4.57)$$

Since  $\frac{\partial a_{drag}}{\partial r} = fn(r, v, t)$ , the dynamics coefficient matrix is

$$\mathbf{G} = \begin{bmatrix} \mathbf{0} & \mathbf{I} \\ G_1 & G_2 \end{bmatrix}. \quad (4.58)$$

Summarizing, the  $G_1$  sub-component of the dynamics coefficients matrix can be written as

$$G_1 = \begin{bmatrix} \frac{\partial a_{drag,x}}{\partial r_x} & \frac{\partial a_{drag,x}}{\partial r_y} & \frac{\partial a_{drag,x}}{\partial r_z} \\ \frac{\partial a_{drag,y}}{\partial r_x} & \frac{\partial a_{drag,y}}{\partial r_y} & \frac{\partial a_{drag,y}}{\partial r_z} \\ \frac{\partial a_{drag,z}}{\partial r_x} & \frac{\partial a_{drag,z}}{\partial r_y} & \frac{\partial a_{drag,z}}{\partial r_z} \end{bmatrix}, \quad (4.59)$$

and similarly the  $G_2$  component can be written as

$$G_2 = \begin{bmatrix} \frac{\partial a_{drag,x}}{\partial v_x} & \frac{\partial a_{drag,x}}{\partial v_y} & \frac{\partial a_{drag,x}}{\partial v_z} \\ \frac{\partial a_{drag,y}}{\partial v_x} & \frac{\partial a_{drag,y}}{\partial v_y} & \frac{\partial a_{drag,y}}{\partial v_z} \\ \frac{\partial a_{drag,z}}{\partial v_x} & \frac{\partial a_{drag,z}}{\partial v_y} & \frac{\partial a_{drag,z}}{\partial v_z} \end{bmatrix}. \quad (4.60)$$

## 4.4 Accuracy of Error State Transition Matrix

In addition to the partials previously discussed, perturbation partials for solar radiation and higher order gravity can be added to the state transition matrix to ensure the greatest accuracy. However, as additional terms are included in the matrix it becomes computationally more costly to integrate. A motivating factor for the development of the Cowell-STM predictor-corrector is the option of generating solutions efficiently. Thus, finding the balance between accuracy and computation time is critical.

A number of state transition matrices are calculated with varying levels of fidelity. The matrices tested are listed in Table 4.1. Each is put through two main tests to

STM Label	Perturbations Included
2-Body	2-Body (Earth)
3-Body	3-Body (Earth and Moon)
4-Body	4-Body (Earth, Moon, and Sun)
4-Body $J_2$	4-Body (Earth, Moon, and Sun), $J_2$ gravity coefficient (Earth)
4-Body $J_2J_3$	4-Body (Earth, Moon, and Sun), $J_2$ and $J_3$ gravity coefficients (Earth)
4-Body $J_2$ Drag	4-Body (Earth, Moon, and Sun), $J_2$ gravity coefficient (Earth), and drag

Table 4.1: List of varying fidelity state transition matrices tested for selection purposes determine the relative accuracy and sensitivity of the matrix. The first test varies the transfer time for one set of initial states. Since the STM is numerically integrated, longer propagation times will inherently accumulate more error. The test illustrates the rate of the increasing error as well as compares the relative accuracy of each state transition matrix.

The transfer time test consists of selecting initial states  $(\mathbf{r}_0, \mathbf{v}_0, t_0)$  which remain constant as the value for  $t_f$  varies in small increments up to the total transfer time. Using the initial states and transfer time, the Cowell propagator calculates the final states using

$$\dot{\mathbf{X}} = f(\mathbf{X}, t) \quad (4.61)$$

with the initial condition,

$$\mathbf{X}_0 = \begin{bmatrix} \mathbf{r}_0 \\ \mathbf{v}_0 \end{bmatrix}, \quad (4.62)$$

thus,

$$\mathbf{X}_f = \int_{t_0}^{t_f} \dot{\mathbf{X}} dt. \quad (4.63)$$

Along with the dynamics coefficient matrix the state transition matrix is computed as,

$$\dot{\Phi}(t_t, t_0) = \mathbf{G}\Phi(t_f, t_0), \quad (4.64)$$

with the initial condition

$$\Phi_0 = \mathbf{I}_{6 \times 6}. \quad (4.65)$$

Next an initial perturbation of 0.01% involves adding to the radial component of the position vector

$$\mathbf{r}_{pert} = \mathbf{r}_0 + \delta\mathbf{r}, \quad (4.66)$$

where

$$\delta\mathbf{r} = 0.001 \frac{\mathbf{r}_0}{|\mathbf{r}_0|}. \quad (4.67)$$

Using  $\mathbf{r}_{pert}$  as the initial position, the Cowell propagator calculates the final states again using Equation 4.61 and Equation 4.63,

$$\dot{\mathbf{X}}_{fpert} = \int_{t_0}^{t_f} \dot{\mathbf{X}} dt \quad (4.68)$$

with the new initial condition,

$$\mathbf{X}_{0pert} = \mathbf{X}_0 + \delta\mathbf{X}_0, \quad (4.69)$$

where  $\delta\mathbf{X}_0 = \begin{bmatrix} \delta\mathbf{r} \\ 0 \end{bmatrix}$ . The difference between the two Cowell propagations is the expected error in the final states due to the initial perturbation

$$\Delta\mathbf{X}_{Cowell}(t_f, t_0) = \mathbf{X}_{fpert} - \mathbf{X}_f. \quad (4.70)$$

The expected error is also calculated using the state transition matrix

$$\Delta\mathbf{X}_{STM}(t_f, t_0) = \Phi \begin{bmatrix} \delta\mathbf{r} \\ 0 \end{bmatrix}. \quad (4.71)$$

The magnitude difference between the Cowell and STM prediction is the error for state transition matrix for that transfer time. That is,

$$Error = |\Delta\mathbf{X}_{Cowell}(t_f, t_0) - \Delta\mathbf{X}_{STM}(t_f, t_0)|. \quad (4.72)$$

The second test varies the initial perturbation percentage for the same initial state with a constant transfer time. Since the analytic state transition matrix is derived from linear approximations along the Keplerian trajectory, the perturbations must remain small. This characteristic is true for all state transition matrices. If the deviations are too large the problem becomes nonlinear and the state transition matrix cannot predict an accurate resultant error. By varying the initial perturbations, the point at which the perturbations become too large for the matrix to accurately handle is identified, illustrating the limitations of the STM. Furthermore, the test highlights which matrices are least sensitive to varying perturbations.

The initial perturbation percentages range from 0.001% - 9%. The test is performed using the exact algorithm as the time test to determine the error in the individual state transition matrices. Since this research focuses on both low Earth orbit and translunar trajectories a general case from each category is selected for the

transfer time test and perturbation percentage test. The results are presented in the following section.

#### 4.4.1 Low Earth Orbit Transfer Test Results

The initial conditions for the low Earth orbit transfer case are listed in Table 4.2.

Parameter	Initial Orbit	Final Orbit
$a$	100 km	400 km
$e$	0.1	0.1
$i$	$0^\circ$	$0^\circ$
$\Omega$	$0^\circ$	$0^\circ$
$\omega$	$0^\circ$	$0^\circ$
$\nu$	$0^\circ$	$180^\circ$
$r_0$	[6.478 0 0] km	
$v_0$	[0 8.226 0] km/s	
$t_0$	0 sec	
$t_f$	100-3200 sec	

Table 4.2: Initial conditions for low Earth orbit state transition matrix time accuracy test

Figure 4.1 illustrates the orbit propagated over the complete 3,200 second transfer time. During this propagation the individual perturbation magnitudes are recorded and plotted in Figure 4.2. The acceleration of the non-conic Earth gravity remains large throughout the trajectory due to the effect of  $J_2$  on equatorial orbits. As expected, the acceleration due to the Earth's gravitational pull decreases and the three-body effects of the Earth, Sun, and Moon increase as the vehicle moves towards the apogee of its final orbit. Due to the large distance between the vehicle and the Moon for the entirety of the transfer, the acceleration due to lunar gravity remains small. At the perigee of the orbit drag plays a significant role, however it quickly diminishes as the vehicle travels out of the Earth's dense atmosphere. Finally, solar radiation remains small, on the magnitude of  $10^{-11}$ , and at one point drops to zero as the satellite enters the Earth's shadow. Figure 4.2 highlights both dominating and insignificant perturbations to the vehicle in low Earth orbit transfers. However it is

LEO 180° Transfer Trajectory Between Orbits  
with  $i = 0^\circ$  and  $e = 0.1$

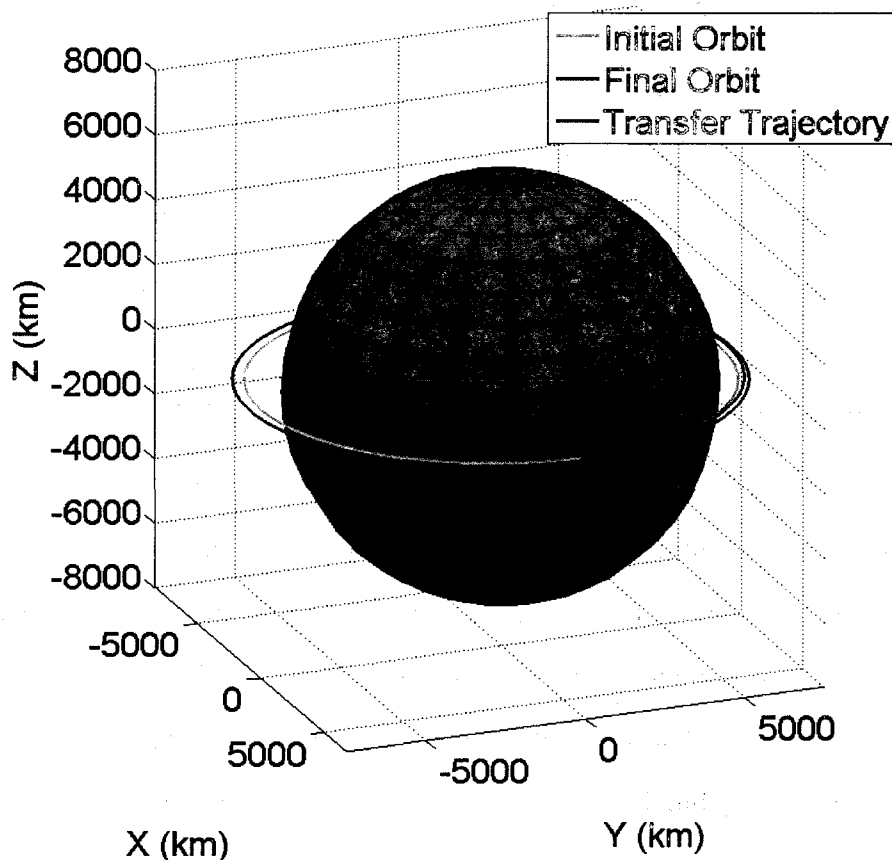


Figure 4.1: Illustration of 180° low Earth orbit transfer between two orbits with  $i = 0^\circ$  and  $e = 0.1$

unclear what fidelity models should be included in the state transition matrix. The results from the varying time and perturbation tests, which are found in Figures 4.3 and 4.4, help to clarify that particular dilemma.

For both tests, the 2-Body, 3-Body, and 4-Body state transition matrices perform almost identically, as do the 4-Body $J_2$  and 4-Body $J_2J_3$  matrices. For this reason only one line is plotted to represent multiple matrices in these cases. As expected, Figure 4.3 illustrates an increase in the error at relatively the same rate for all matrices as the transfer time increases. Upon closer inspection, the 4-Body $J_2$ Drag matrix performs slightly more accurately than the other matrices. After 3,200 seconds, the

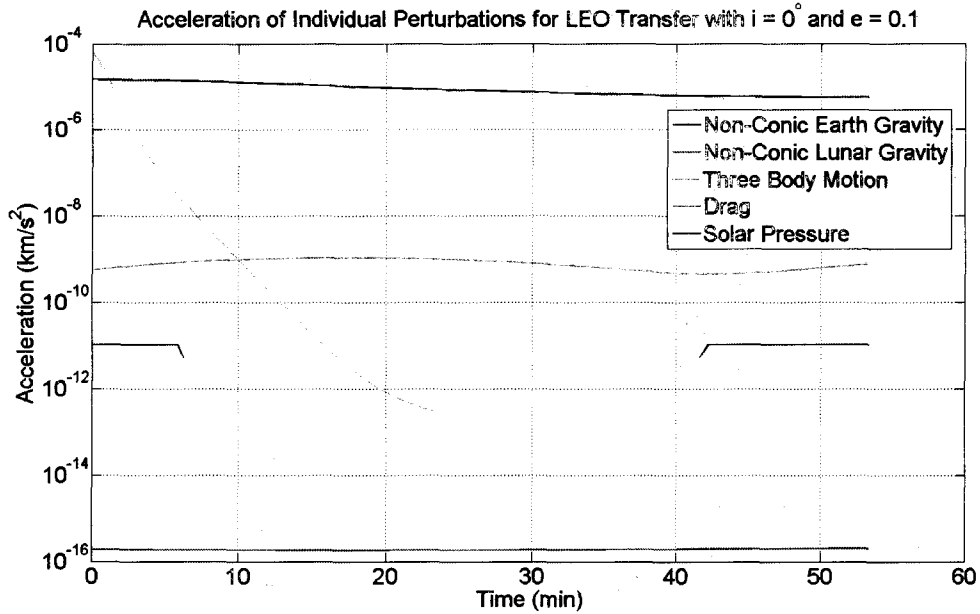


Figure 4.2: Individual perturbation magnitudes for  $180^\circ$  low Earth orbit transfer between two orbits with  $i = 0^\circ$  and  $e = 0.1$

4-Body  $J_2$  Drag matrix is 40 meters more accurate than any other matrix.

The perturbation test and Figure 4.4 illustrates that all the matrices are quite sensitive to initial perturbations. A perturbation percentage of only 0.3% in the radial direction of the position vector results in an error of 1,200 km after 3,200 seconds. As the perturbation percentages increases the non-linearity of the drag model results in the matrix producing the greatest error. Closer inspection reveals that to maintain an error under 12 km for a 3,200 second propagation, the maximum deviation the STMs can handle is 0.001%. A more detailed analysis again illustrates the accuracy of the 4-Body  $J_2$  Drag matrix over the other matrices. At an initial perturbation percentage of 0.0018%, the 4-Body  $J_2$  Drag matrix is 70 meters more accurate than the 4-Body  $J_2$  or 4-Body  $J_2 J_2$  STMs and 80 meters more accurate than the n-body matrices (2-Body, 3-Body, 4-Body).



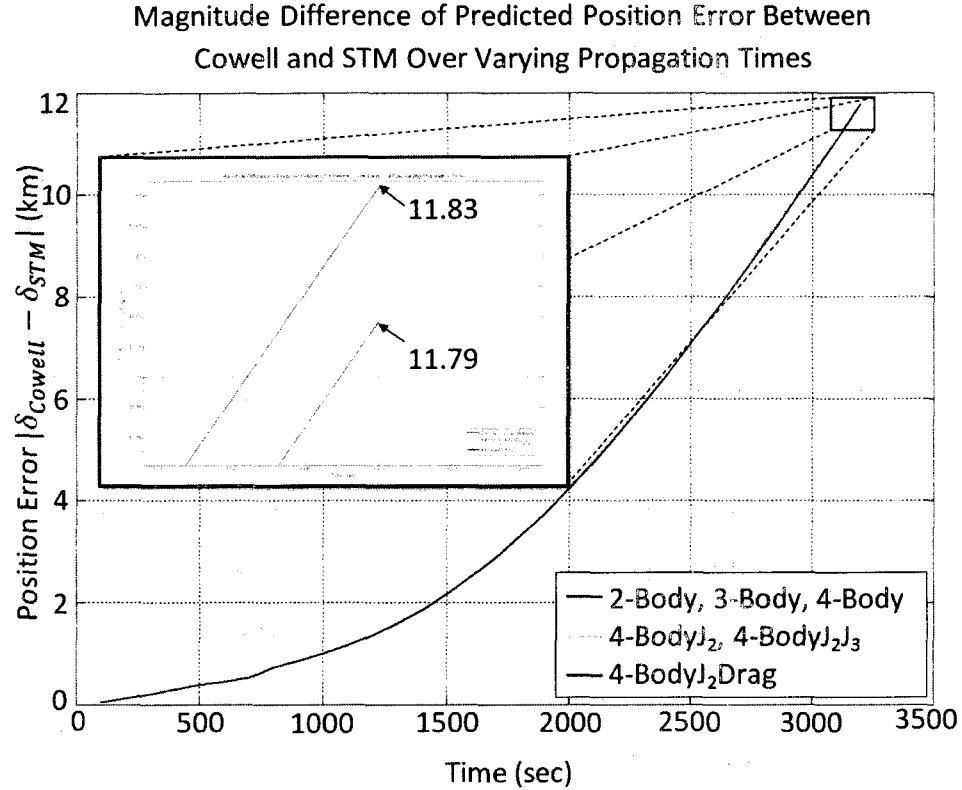


Figure 4.3: Magnitude difference in predicted position error between Cowell and the state transition matrix for a LEO transfer over varying transfer times

#### 4.4.2 Translunar Transfer Test Results

The initial conditions for the translunar test are listed in Table 4.3.

Parameter	Initial Earth Orbit	Final Lunar Orbit
$a$	170 km	200 km
$e$	0	0
$i$	$16^\circ$	$15^\circ$
$\Omega$	$71^\circ$	$100^\circ$
$\omega$	not specified	
$\nu$	not specified	
$r_{0-TLI}$	[-2343 -6113 76.57] km	
$v_{0-TLI}$	[7.146 -7.907 2.497] km/s	
$t_0$	383,013,000 sec (Feb 20, 2012 12:00:00)	
$t_f$	383,443,200 sec (Feb 25, 2012 12:00:00)	

Table 4.3: Initial conditions for translunar state transition matrix time accuracy test

Figure 4.5 illustrates the propagation of the orbit over the 5 day transfer time.

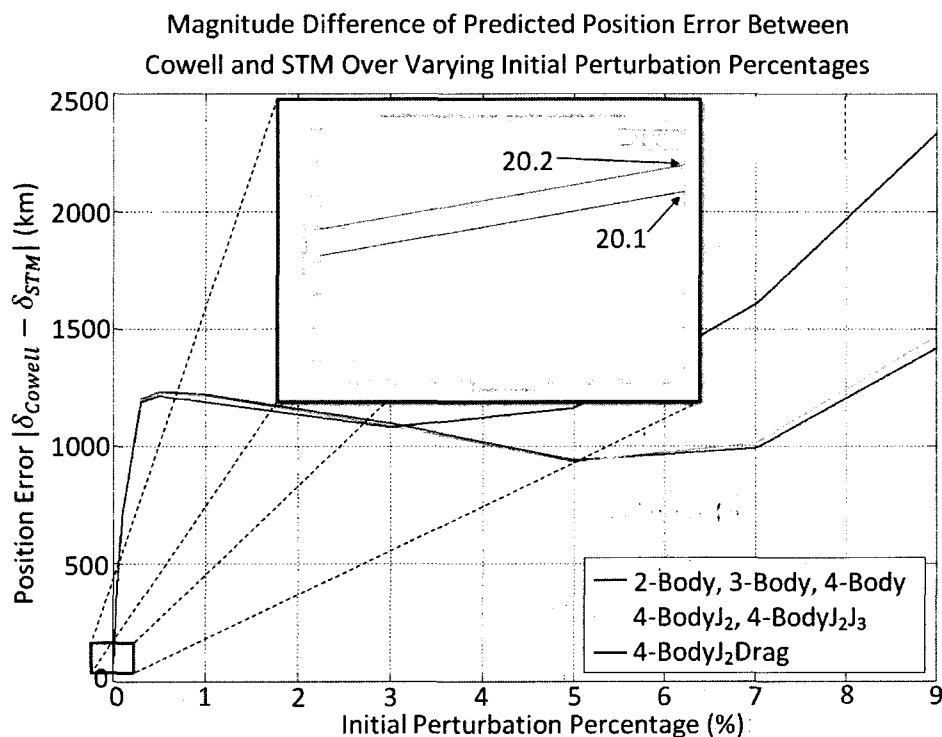


Figure 4.4: Magnitude difference in predicted position error between Cowell and the state transition matrix for a LEO transfer over varying initial perturbation percentages

During this propagation, as with the low Earth orbit test, the individual perturbation magnitudes are recorded and plotted in Figure 4.6.

Foreseeably, as the vehicle travels away from the Earth and towards the Moon the gravitational acceleration due to the Earth decreases and the acceleration due to lunar gravity increases. In a similar manner, the lunisolar three-body acceleration increases as well. Since the translunar orbit begins at a relatively high Earth altitude, the effects of drag are small and last for a very short period of time before Earth's atmosphere no longer has an effect on the trajectory. Finally, solar pressure remains small and constant throughout the transfer.

Figures 4.7 and 4.8 show the results for the varying transfer times and initial perturbation percentage tests for the translunar case. Figure 4.7 illustrates the relative accuracy of the 4-Body $J_2$ , 4-Body $J_2J_3$ , and 4-Body $J_2$ Drag matrices as compared to

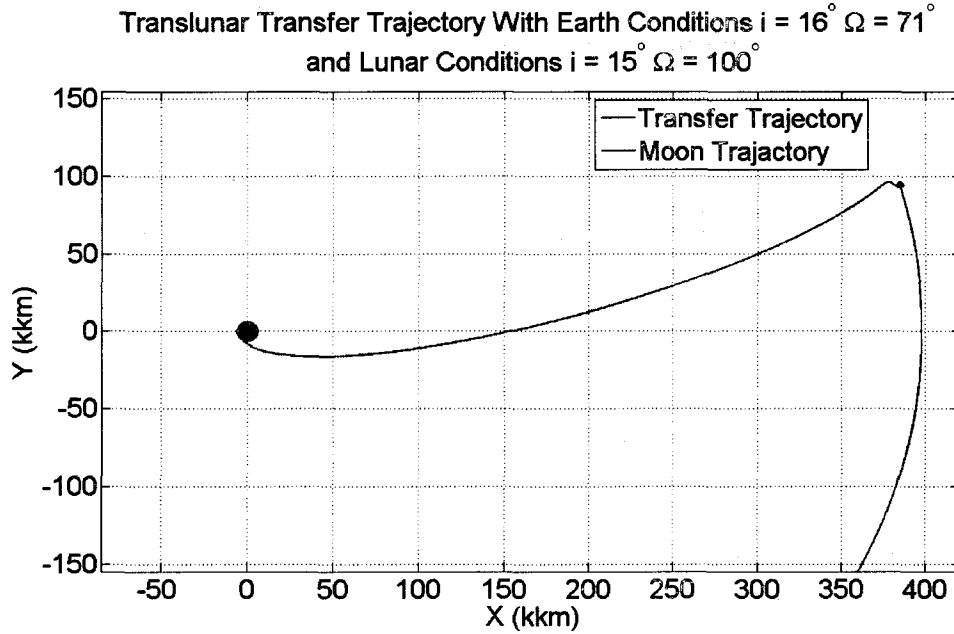


Figure 4.5: Illustration of a 5 day translunar transfer with conditions  $i_{\oplus} = 16^\circ$   $\Omega_{\oplus} = 71^\circ$  and  $i_{\ominus} = 15^\circ$   $\Omega_{\ominus} = 100^\circ$

the n-body matrices for majority of the transfer times. However, as the trajectory nears the Moon all the matrices become highly inaccurate when compared to the propagated Cowell states. This is because none of the matrices model the gravitational pull of the Moon, which as illustrated in Figure 4.6, becomes a dominating force at the end of the transfer period.

The results highlighted in Figure 4.8 show a similar trend as those for the LEO case in Figure 4.4. All of the matrices are extremely sensitive to initial perturbations. Depending on the matrix, an initial perturbation of only 1% in the position vector can lead to an error of 500,000 km over the 5 day translunar transfer. Again, the higher fidelity matrices, such as those including additional gravity coefficients and drag produce the worse results for the larger perturbation percentages. However, closer analysis reveals that at perturbation percentages less than 0.009%, the same models perform much more accurately (under 1000 km error).

After analyzing the cumulative results of the varying time and initial perturba-

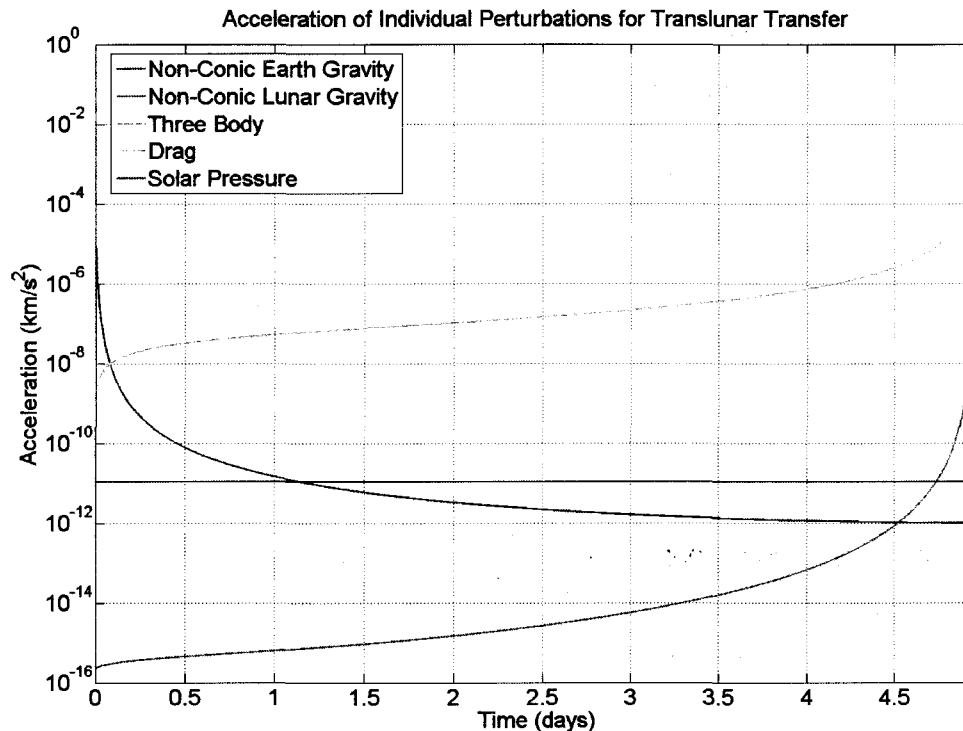


Figure 4.6: Individual perturbation magnitudes for translunar transfer between a low Earth orbit with  $i = 16^\circ$   $\Omega = 71^\circ$  and a low lunar orbit with  $i = 15^\circ$   $\Omega = 100^\circ$

tion tests for a general low Earth orbit and translunar transfer, specific matrices are selected for use in the Cowell-STM predictor-corrector method. For low Earth orbits the 4-Body  $J_2$  Drag matrix is selected due to the magnitude of drag perturbation low orbits experience. Further, the overall performance of the 4-Body  $J_2$  Drag matrix exceeds that of any other matrix for the tests performed. For translunar transfers, the 4-Body  $J_2$  matrix was selected. Since the the transfers begin at high Earth altitudes, the effect of drag is negligible and thus not necessary to include in the matrix. Excluding drag also reduces the computational time of the STM. Since the performance of the 4-Body  $J_2$  and 4-Body  $J_2 J_3$  matrices is almost identical, for reduced computational time, the 4-Body  $J_2$  matrix is selected over the 4-Body  $J_2 J_3$  matrix.

Through its application in an iterative shooting method procedure, the state transition matrix forms the basis for the correction portion of the predictor-corrector method.

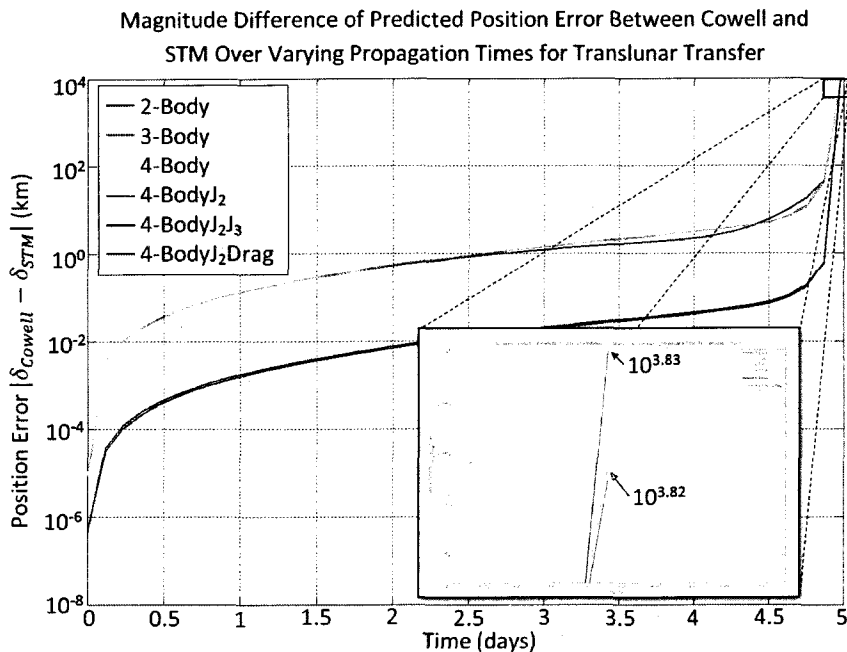


Figure 4.7: Magnitude difference in predicted position error between Cowell and the state transition matrix for a translunar transfer over varying times

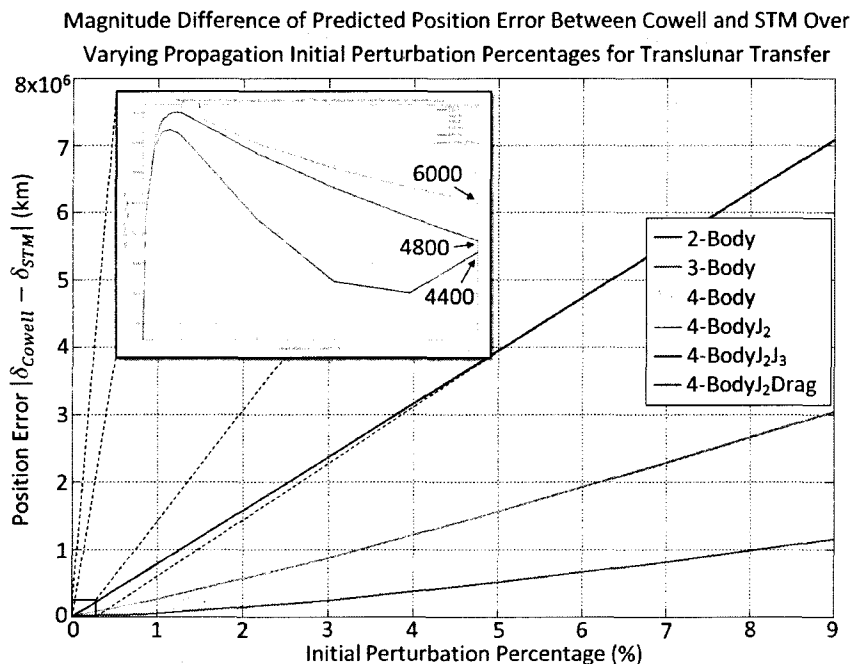


Figure 4.8: Magnitude difference in predicted position error between Cowell and the state transition matrix for a translunar transfer over varying initial perturbation percentages

## 4.5 Shooting Method

The shooting method is a technique which numerically solves a two-point boundary value problem by reducing it to the solution of an initial value problem. For this research, the boundary value problem focuses on determining the transfer trajectory between two orbits subject to initial and final constraints. Given an initial state,  $(\mathbf{r}_1, \mathbf{v}_1)$  and time of flight,  $t_2$ , the state transition matrix is calculated, and the Cowell propagator integrates the states forward in time  $(\mathbf{r}_{2int}, \mathbf{v}_{2int})$ .

Assuming the error in the final position is the only concern, the difference between the integrated position vector,  $\mathbf{r}_{2int}$ , and the desired position vector,  $\mathbf{r}_2$ , is the error

$$\delta\mathbf{r}_2 = \mathbf{r}_2 - \mathbf{r}_{2int}. \quad (4.73)$$

To reduce this error, the initial velocity,  $\mathbf{v}_1$ , must be updated. From Equations 4.8 and 4.9 one finds

$$\Phi_{11}\delta\mathbf{r}_1 + \Phi_{12}\delta\mathbf{v}_1 = \delta\mathbf{r}_2 \quad (4.74)$$

and

$$\Phi_{21}\delta\mathbf{r}_1 + \Phi_{22}\delta\mathbf{v}_1 = \delta\mathbf{v}_2. \quad (4.75)$$

Again, because the goal is to only reduce the error in the final position,  $\delta\mathbf{v}_2$  and Equation 4.75 are of no consequence. Furthermore, it is assumed that the initial position vector cannot change, thus  $\delta\mathbf{r}_1 = 0$ . As a result, Equation 4.74 reduces to

$$\Phi_{12}\delta\mathbf{v}_1 = \delta\mathbf{r}_2. \quad (4.76)$$

Solving for  $\delta\mathbf{v}_1$  yields

$$\delta\mathbf{v}_1 = [\Phi_{12}]^{-1} \delta\mathbf{r}_2. \quad (4.77)$$

Thus, at each iteration the new initial delta velocity is updated as

$$\mathbf{v}_{1,(i+1)} = \mathbf{v}_{1,i} + \delta\mathbf{v}_{1,i}, \quad (4.78)$$

where  $i$  represents the iteration number. The process iterates until  $|\delta\mathbf{r}_2| < 1 \times 10^{-6}$ , or the process has exceeded a number, say forty iterations, in which case the shooting method has failed to converge. See Figure 4.9 for an illustration of the shooting method. Figure 4.10 summarizes the shooting method as it applies specifically to

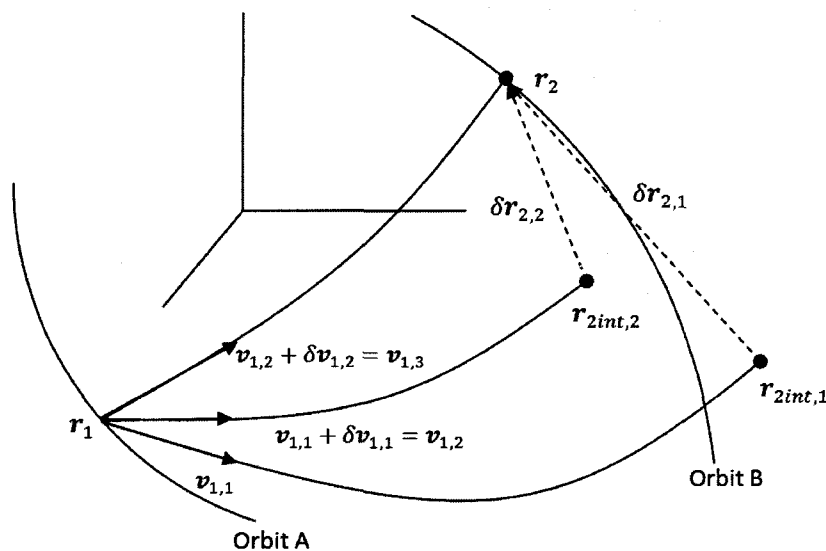


Figure 4.9: Illustration of Lambert shooting method

the translunar and low Earth orbit transfer applications. With the development of the Cowell-STM predictor-corrector complete, the next two chapters detail the performance of the tool as applied to these two applications.

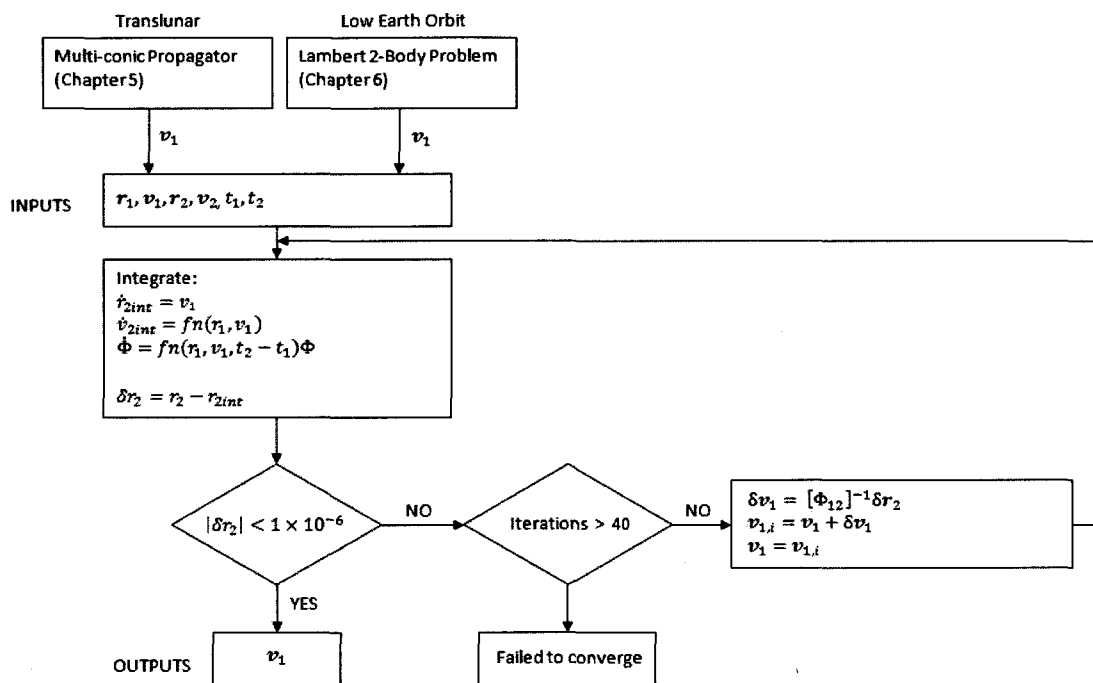


Figure 4.10: Flow chart summary of the higher order Lambert method formulation



# Chapter 5

## Translunar Application

The objective of testing translunar transfers is to develop a feasible trajectory between low Earth orbits (LEO) and low lunar orbits (LLO). The following chapter begins with an overview of pseudostate theory and its use in approximating three body trajectories. The next section provides details on JSC's trajectory propagator "EXLX" that interfaces with the user through an Excel mapping function. The interface enables the user to select viable transfer parameters based on the initial desired conditions. The parameters are input into the multi-conic propagator and are used to acquire an initial guess for the transfer velocity between a low Earth orbit and the first lunar orbit insertion burn to enter into a circular low lunar orbit, known as the Translunar Injection (TLI) and Lunar Orbit Insertion (LOI) burns respectively (see Figure 5.1). Utilizing the shooting method discussed in Section 4.5, the initial transfer velocity guess is updated to include higher order perturbations. Figure 5.2 summarizes the development of acquiring the final transfer velocity. The remainder of the chapter discusses the process of selecting the translunar test cases as well as assesses the performance of the method in generating feasible solutions.

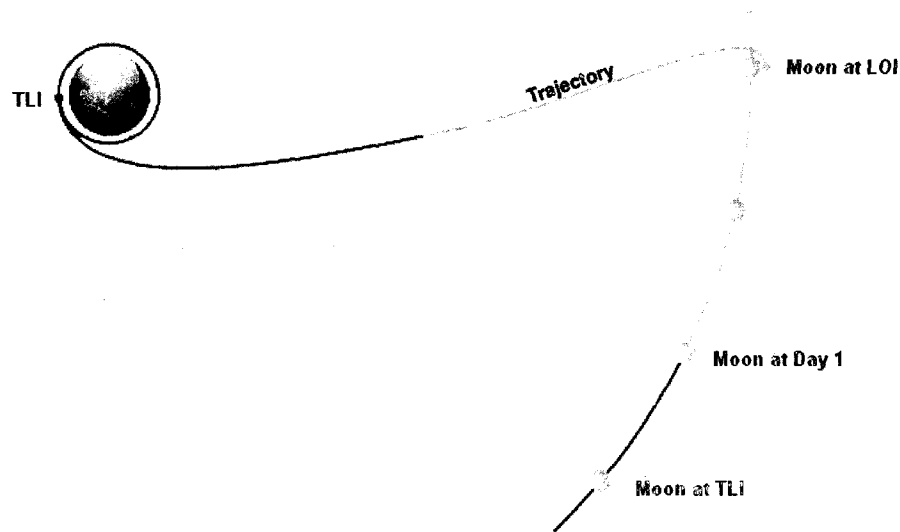


Figure 5.1: General illustration of translunar transfer between TLI and LOI

## 5.1 Pseudostate Theory for Approximating Three-Body Trajectories

EXLX is an operations planning tool used to approximate low Earth orbit to low lunar orbit trajectories. The purpose of the program is to produce a variety of viable translunar transfers so that a trade study can be performed between the cost and time required to reach the Moon. EXLX uses the three-body pseudostate theory to compute overlapped conic transfer trajectories between the Earth and Moon [16][30][29]. Wilson developed the original EXLX program and describes the fundamentals of these concepts in the paper “A Pseudostate Theory for the Approximation of Three-Body Trajectories” [47]. The following summarizes the findings of this reference.

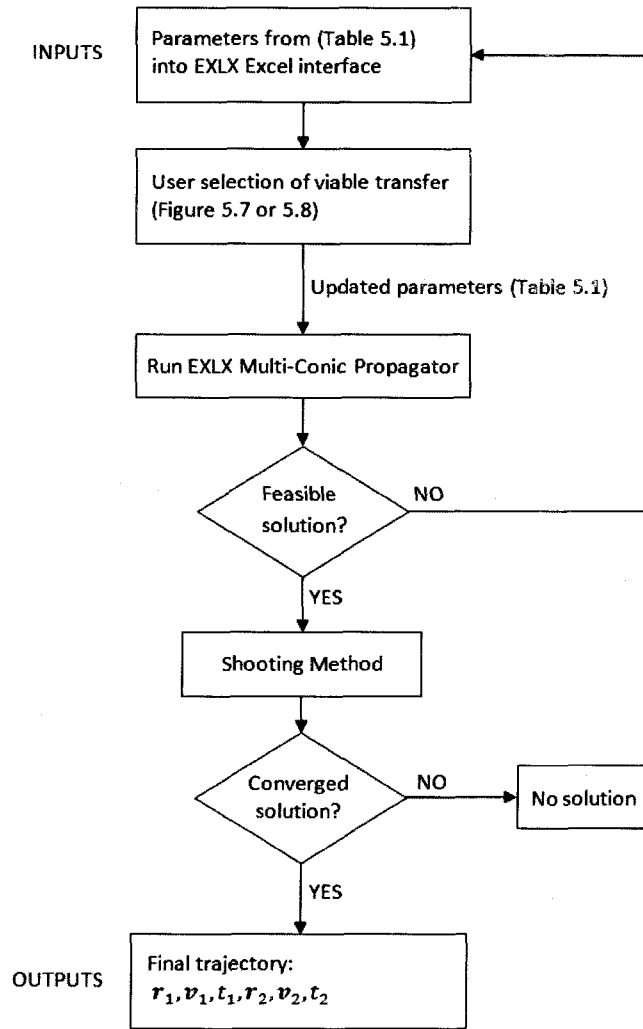


Figure 5.2: Summary of translunar transfer velocity computation and shooting method application

### 5.1.1 Conic Approximations

Using the three-body geometry illustrated in Figure 3.4 and defined in Equation 3.39, the vectors

$$\begin{aligned}
 \boldsymbol{\rho} &= \mathbf{r}_{\oplus\ominus} \\
 \mathbf{r} &= \mathbf{r}_{\ominus sat} \\
 \mathbf{R} &= \mathbf{r}_{\oplus sat}
 \end{aligned} \tag{5.1}$$

are introduced to reduce the complexity of multi-subscripts. For any time  $t_J$ , the vectors are related by the equations

$$\mathbf{R}_J = \boldsymbol{\rho}_J + \mathbf{r}_J, \quad (5.2)$$

and

$$\dot{\mathbf{R}}_J = \dot{\boldsymbol{\rho}}_J + \dot{\mathbf{r}}_J. \quad (5.3)$$

Assuming the mass of the spacecraft is negligible, the acceleration due to three-body motion (Equation 3.1) for each vector is

$$\ddot{\boldsymbol{\rho}}_J = -(\mu_{\oplus} + \mu_{\odot}) \frac{\boldsymbol{\rho}_J}{\rho_J^3}, \quad (5.4)$$

$$\ddot{\mathbf{r}}_J = -\mu_{\odot} \frac{\mathbf{r}_J}{r_J^3} + \mu_{\oplus} \frac{\boldsymbol{\rho}_J}{\rho_J^3} - \mu_{\oplus} \frac{\mathbf{R}_J}{R_J^3}, \quad (5.5)$$

and

$$\ddot{\mathbf{R}}_J = -\mu_{\oplus} \frac{\mathbf{R}_J}{R_J^3} + \mu_{\odot} \frac{\mathbf{r}_J}{r_J^3} - \mu_{\odot} \frac{\boldsymbol{\rho}_J}{\rho_J^3}. \quad (5.6)$$

The velocity vectors at two different times,  $t_I$  and  $t_E$ , are related by the equations

$$\dot{\boldsymbol{\rho}}_E - \dot{\boldsymbol{\rho}}_I = -(\mu_{\oplus} + \mu_{\odot}) \int_{t_I}^{t_E} \left( \frac{\boldsymbol{\rho}_J}{\rho_J^3} \right) dt_J, \quad (5.7)$$

$$\dot{\mathbf{r}}_E - \dot{\mathbf{r}}_I = -\mu_{\odot} \int_{t_I}^{t_E} \left( \frac{\mathbf{r}_J}{r_J^3} \right) dt_J + \mu_{\oplus} \int_{t_I}^{t_E} \left( \frac{\boldsymbol{\rho}_J}{\rho_J^3} \right) dt_J - \mu_{\oplus} \int_{t_I}^{t_E} \left( \frac{\mathbf{R}_J}{R_J^3} \right) dt_J, \quad (5.8)$$

and

$$\dot{\mathbf{R}}_E - \dot{\mathbf{R}}_I = -\mu_{\oplus} \int_{t_I}^{t_E} \left( \frac{\mathbf{R}_J}{R_J^3} \right) dt_J + \mu_{\odot} \int_{t_I}^{t_E} \left( \frac{\mathbf{r}_J}{r_J^3} \right) dt_J - \mu_{\odot} \int_{t_I}^{t_E} \left( \frac{\boldsymbol{\rho}_J}{\rho_J^3} \right) dt_J. \quad (5.9)$$

The position vectors are related by the equations

$$\boldsymbol{\rho}_E - \boldsymbol{\rho}_I = (t_E - t_I) \dot{\boldsymbol{\rho}}_I - (\mu_{\oplus} + \mu_{\odot}) \int_{t_I}^{t_E} \int_{t_I}^{t_K} \left( \frac{\boldsymbol{\rho}_J}{\rho_J^3} \right) dt_J dt_K, \quad (5.10)$$

$$\begin{aligned} \mathbf{r}_E - \mathbf{r}_I = & (t_E - t_I) \dot{\mathbf{r}}_I - \mu_{\odot} \int_{t_I}^{t_E} \int_{t_I}^{t_K} \left( \frac{\mathbf{r}_J}{r_J^3} \right) dt_J dt_K + \\ & \mu_{\oplus} \int_{t_I}^{t_E} \int_{t_I}^{t_K} \left( \frac{\boldsymbol{\rho}_J}{\rho_J^3} \right) dt_J dt_K - \mu_{\oplus} \int_{t_I}^{t_E} \int_{t_I}^{t_K} \left( \frac{\mathbf{R}_J}{R_J^3} \right) dt dt_K, \end{aligned} \quad (5.11)$$

and

$$\begin{aligned} \mathbf{R}_E - \mathbf{R}_I = & (t_E - t_I) \dot{\mathbf{R}}_I - \mu_{\oplus} \int_{t_I}^{t_E} \int_{t_I}^{t_K} \left( \frac{\mathbf{R}_J}{R_J^3} \right) dt_J dt_K + \\ & \mu_{\odot} \int_{t_I}^{t_E} \int_{t_I}^{t_K} \left( \frac{\mathbf{r}_J}{r_J^3} \right) dt_J dt_K - \mu_{\odot} \int_{t_I}^{t_E} \int_{t_I}^{t_K} \left( \frac{\boldsymbol{\rho}_J}{\rho_J^3} \right) dt_J dt_K, \end{aligned} \quad (5.12)$$

where  $J$  and  $K$  are intermediate variables of integration. There are no known closed form solutions to Equations 5.8, 5.9, 5.11, or 5.12. However Equations 5.7 and 5.10 can be solved using two-body conic equations. Equation 5.7 results in dual definitions

$$\dot{\boldsymbol{\rho}}_E - \dot{\boldsymbol{\rho}}_I = \dot{\boldsymbol{\rho}}_{I(\mu_{\oplus} + \mu_{\odot})E} - \dot{\boldsymbol{\rho}}_I, \quad (5.13)$$

and

$$\dot{\boldsymbol{\rho}}_E - \dot{\boldsymbol{\rho}}_I = \dot{\boldsymbol{\rho}}_E - \dot{\boldsymbol{\rho}}_{E(\mu_{\oplus} + \mu_{\odot})I}.$$

Similarly Equation 5.10 yields

$$\boldsymbol{\rho}_E - \boldsymbol{\rho}_I = \boldsymbol{\rho}_{I(\mu_{\oplus} + \mu_{\odot})E} - \boldsymbol{\rho}_I, \quad (5.14)$$

and

$$\boldsymbol{\rho}_E - \boldsymbol{\rho}_I = \boldsymbol{\rho}_E - \boldsymbol{\rho}_{E(\mu_{\oplus} + \mu_{\odot})I}.$$

Here the compound subscripts refer to a vector resulting from the conic propagation of a base-point state vector. The first element of the subscript identifies the base-point vector, the second element describes the gravitational constant used in the conic

propagation, and the third element is the time component of the conically propagated state vector. Thus, in Equation 5.13, the term  $\dot{\boldsymbol{\rho}}_{I(\mu_{\oplus}+\mu_{\odot})E}$  refers to the velocity vector found by propagating the base-point state vector from time  $t_I$ ,  $(\boldsymbol{\rho}_I, \dot{\boldsymbol{\rho}}_I)$ , along a conic trajectory to time  $t_E$  using the combined Earth-Moon gravitational parameter  $\mu_{\oplus} + \mu_{\odot}$ .

When the spacecraft is very close to the Moon the sum of the last two terms in Equation 5.5 is close to zero. By removing these two terms Equation 5.5 has the same form as Equation 5.4 and thus the two-body conic approximations in Equations 5.13 and 5.14 can be applied to  $\mathbf{r}$  as well. The selenocentric conic approximations for velocity are then

$$\dot{\mathbf{r}}_E - \dot{\mathbf{r}}_I \cong \dot{\mathbf{r}}_{I\mu_{\odot}E} - \dot{\mathbf{r}}_I = -\mu_{\odot} \int_{t_I}^{t_E} \left( \frac{\mathbf{r}_{I\mu_{\odot}J}}{r_{I\mu_{\odot}J}^3} \right) dt_J, \quad (5.15)$$

and

$$\dot{\mathbf{r}}_E - \dot{\mathbf{r}}_I \cong \dot{\mathbf{r}}_E - \dot{\mathbf{r}}_{E\mu_{\odot}I} = -\mu_{\odot} \int_{t_I}^{t_E} \left( \frac{\mathbf{r}_{E\mu_{\odot}J}}{r_{E\mu_{\odot}J}^3} \right) dt_J. \quad (5.16)$$

The approximations for position are

$$\mathbf{r}_E - \mathbf{r}_I \cong \mathbf{r}_{I\mu_{\odot}E} - \mathbf{r}_I = (t_E - t_I) \dot{\mathbf{r}}_I - \mu_{\odot} \int_{t_I}^{t_E} \int_{t_I}^{t_K} \left( \frac{\mathbf{r}_{I\mu_{\odot}J}}{r_{I\mu_{\odot}J}^3} \right) dt_J dt_K, \quad (5.17)$$

and

$$\mathbf{r}_E - \mathbf{r}_I \cong \mathbf{r}_E - \mathbf{r}_{E\mu_{\odot}I} = (t_E - t_I) \dot{\mathbf{r}}_{E\mu_{\odot}I} - \mu_{\odot} \int_{t_I}^{t_E} \int_{t_I}^{t_K} \left( \frac{\mathbf{r}_{E\mu_{\odot}J}}{r_{E\mu_{\odot}J}^3} \right) dt_J dt_K. \quad (5.18)$$

The selenocentric conic approximations can be used whenever the spacecraft is close to the Moon within the time interval  $(t_I, t_E)$ .

A similar set of approximations can be made when the spacecraft is near the Earth. With this condition the sum of the last two terms in Equation 5.6 are close to zero and thus can be omitted to estimate the geocentric conic approximations. For

velocity these equations are

$$\dot{\mathbf{R}}_E - \dot{\mathbf{R}}_I \cong \dot{\mathbf{R}}_{I\mu_\oplus E} - \dot{\mathbf{R}}_I = -\mu_\oplus \int_{t_I}^{t_E} \left( \frac{\mathbf{R}_{I\mu_\oplus J}}{R_{I\mu_\oplus J}^3} \right) dt_J, \quad (5.19)$$

and

$$\dot{\mathbf{R}}_E - \dot{\mathbf{R}}_I \cong \dot{\mathbf{R}}_E - \dot{\mathbf{R}}_{E\mu_\oplus I} = -\mu_\oplus \int_{t_I}^{t_E} \left( \frac{\mathbf{R}_{E\mu_\oplus J}}{R_{E\mu_\oplus J}^3} \right) dt_J; \quad (5.20)$$

and for the position vectors the associated equations are

$$\mathbf{R}_E - \mathbf{R}_I \cong \mathbf{R}_{I\mu_\oplus E} - \mathbf{R}_I = (t_E - t_I) \dot{\mathbf{R}}_I - \mu_\oplus \int_{t_I}^{t_E} \int_{t_I}^{t_K} \left( \frac{\mathbf{R}_{I\mu_\oplus J}}{R_{I\mu_\oplus J}^3} \right) dt_J dt_K, \quad (5.21)$$

and

$$\mathbf{R}_E - \mathbf{R}_I \cong \mathbf{R}_E - \mathbf{R}_{E\mu_\oplus I} = (t_E - t_I) \dot{\mathbf{R}}_{E\mu_\oplus I} - \mu_\oplus \int_{t_I}^{t_E} \int_{t_I}^{t_K} \left( \frac{\mathbf{R}_{E\mu_\oplus J}}{R_{E\mu_\oplus J}^3} \right) dt_J dt_K. \quad (5.22)$$

Again, the geocentric conic approximations can only be made when the spacecraft is near the Earth within the time interval  $(t_I, t_E)$ .

Distances representative of “near the Moon” and “near the Earth” are a function of each body’s respective sphere of influence (SOI) [7]. The Moon’s sphere of influence is usually defined as some value between 9 and 14 Earth radii from the center of the Moon. The number is based on the observations of when selenocentric conic approximations more accurately define spacecraft motion than geocentric conic approximations. The classical method of patched conics as developed by Egorov [21] assumes that selenocentric conic approximations are used when the spacecraft is within the sphere of influence of the Moon, and geocentric conic approximations are used to describe motion outside of the lunar sphere of influence. On the Earth to Moon transfer, the spacecraft is initially propagated along the geocentric conic trajectory until it reaches the Moon’s sphere of influence. At this point the state vector is transformed from geocentric coordinates to selenocentric coordinates (see Section

3.3.2) and the propagation continues along the selenocentric conic trajectory until the desired terminal point is reached.

### 5.1.2 Overlapped Conic Approximation

The disadvantage of the classic patched conic technique is that the omitted terms in Equations 5.5 and 5.6 can possess large values in the region near the Moon's sphere of influence. In this case, significant errors result from the conic approximation technique. The overlapped conic approximation is an alternative method that does not neglect the final terms from Equations 5.5 and 5.6 but still retains the simplicity of the classic two-body approach [39].

To set up the problem assume an interior point  $I$  that is located within the Moon's sphere of influence and an exterior point  $E$  that is located within the vicinity of the Moon but outside of the sphere of influence as depicted in Figure 5.3. For this reason the interior point is defined with respect to selenocentric coordinates, denoted by the symbol  $\sigma$

$$\sigma_I = (t_I, \mathbf{r}_I, \dot{\mathbf{r}}_I), \quad (5.23)$$

and the exterior point is defined with respect to geocentric coordinates, denoted by the symbol  $\xi$

$$\xi_E = (t_E, \mathbf{R}_E, \dot{\mathbf{R}}_E). \quad (5.24)$$

A relationship is needed between Equations 5.23 and 5.24 where  $t_{p\oplus} \leq t_I \leq t_E \leq t_{p\ominus}$  or  $t_{p\oplus} \geq t_I \geq t_E \geq t_{p\ominus}$ . Here  $t_{p\oplus}$  refers to the perigee passage time and  $t_{p\ominus}$  refers to pericyynthion, or the time of periapse passage for the lunar orbit. This restriction requires no periapse passage between the terminal points, ensuring that the conic approximations remain valid. At periapse points the propagation must be switched from exterior-to-interior to interior-to-exterior or vice versa depending on the direction of the transfer. The periapse restriction does not mean the overlapped conic approach



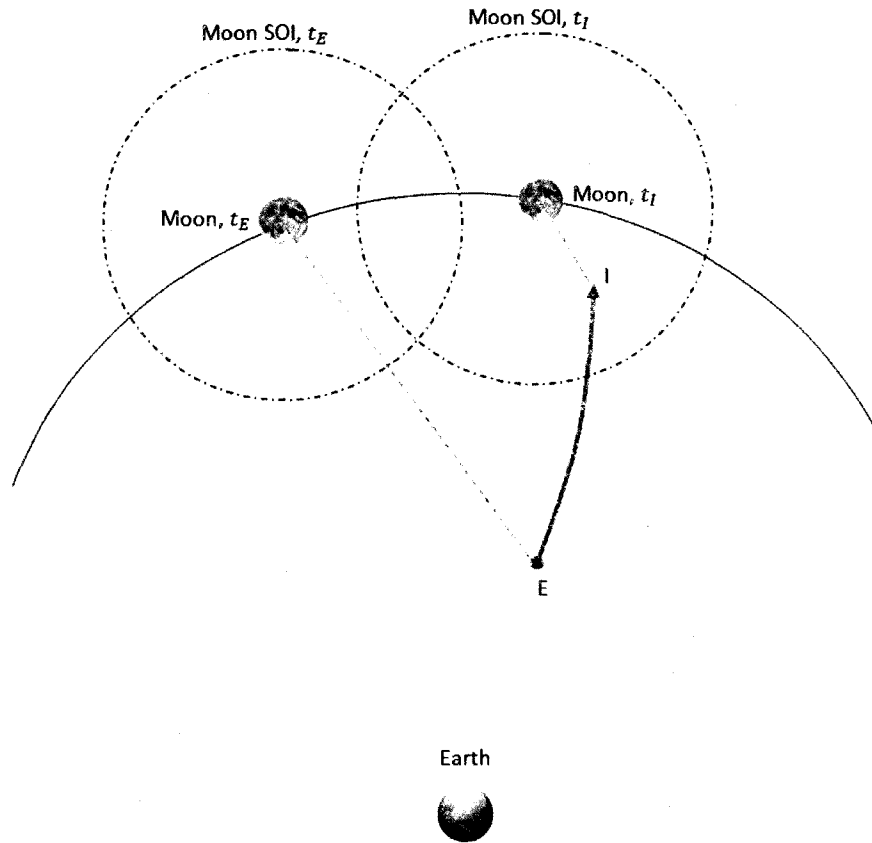


Figure 5.3: Definition of interior and exterior points for overlapped conic approximation

cannot be utilized for transfers that pass through periapse points, only that such transfers require more than one step.

The first step in determining a relationship between the selenocentric interior point and the geocentric exterior point begins with finding approximate solutions for Equations 5.9 and 5.12 which have no known closed-form solutions. For the integral of  $\left(\frac{\mathbf{R}_J}{R_J^3}\right)$  it is expected that the geocentric conic approximation of  $\mathbf{R}_J$  will be reasonably accurate with a proper selection of the base-point vector. Since the exterior point is closer to the Earth than the interior point, it makes sense that  $\mathbf{R}_J \cong \mathbf{R}_{E\mu_\oplus J}$  is a better approximation than  $\mathbf{R}_J \cong \mathbf{R}_{I\mu_\oplus J}$ . Substituting this value in and using the

relationship found in Equation 5.20, the first single integral in Equation 5.9 becomes

$$-\mu_{\oplus} \int_{t_I}^{t_E} \left( \frac{\mathbf{R}_J}{R_J^3} \right) dt_J \cong -\mu_{\oplus} \int_{t_I}^{t_E} \left( \frac{\mathbf{R}_{E\mu_{\oplus}J}}{R_{E\mu_{\oplus}J}^3} \right) dt_J = \dot{\mathbf{R}}_E - \dot{\mathbf{R}}_{E\mu_{\oplus}I}. \quad (5.25)$$

Using Equation 5.22, the double integral in Equation 5.12 becomes

$$-\mu_{\oplus} \int_{t_I}^{t_E} \int_{t_I}^{t_K} \left( \frac{\mathbf{R}_J}{R_J^3} \right) dt_J dt_K \cong -\mu_{\oplus} \int_{t_I}^{t_E} \int_{t_I}^{t_K} \left( \frac{\mathbf{R}_{E\mu_{\oplus}J}}{R_{E\mu_{\oplus}J}^3} \right) dt_J dt_K \cong \mathbf{R}_E - \mathbf{R}_{E\mu_{\oplus}I} - \Delta t_{IE} \dot{\mathbf{R}}_{E\mu_{\oplus}I}, \quad (5.26)$$

where  $\Delta t_{IE} = t_E - t_I$ . A similar approximation is made for the integral of  $\left( \frac{\mathbf{r}_J}{r_J^3} \right)$ . Since the interior point is closer to the Moon the following selenocentric conic approximation is made  $\mathbf{r}_J \cong \mathbf{r}_{I\mu_{\odot}J}$ . Substituting this value in and using the relationship found in Equation 5.15, the single integral in Equation 5.9 becomes

$$-\mu_{\odot} \int_{t_I}^{t_E} \left( \frac{\mathbf{r}_J}{r_J^3} \right) dt_J \cong -\mu_{\odot} \int_{t_I}^{t_E} \left( \frac{\mathbf{r}_{I\mu_{\odot}J}}{r_{I\mu_{\odot}J}^3} \right) dt_J = \dot{\mathbf{r}}_{I\mu_{\odot}E} - \dot{\mathbf{r}}_I. \quad (5.27)$$

Using Equation 5.17, the double integral in Equation 5.12 becomes

$$-\mu_{\odot} \int_{t_I}^{t_E} \int_{t_I}^{t_K} \left( \frac{\mathbf{r}_J}{r_J^3} \right) dt_J dt_K \cong -\mu_{\odot} \int_{t_I}^{t_E} \int_{t_I}^{t_K} \left( \frac{\mathbf{r}_{I\mu_{\odot}J}}{r_{I\mu_{\odot}J}^3} \right) dt_J dt_K \cong \mathbf{r}_{I\mu_{\odot}E} - \mathbf{r}_I - \Delta t_{IE} \dot{\mathbf{r}}_I. \quad (5.28)$$

The integral for  $\left( \frac{\rho}{\rho_J^3} \right)$  is found from Equations 5.7 and 5.10 where

$$-\mu_{\odot} \int_{t_I}^{t_E} \left( \frac{\rho_J}{\rho_J^3} \right) dt_J = \epsilon \Delta \dot{\rho}_{IE}, \quad (5.29)$$

and

$$-\mu_{\odot} \int_{t_I}^{t_E} \int_{t_I}^{t_K} \left( \frac{\rho_J}{\rho_J^3} \right) dt_J dt_K = \epsilon [\Delta \rho_{IE} - \Delta t_{IE} \dot{\rho}_I] \quad (5.30)$$

with  $\Delta\dot{\boldsymbol{\rho}}_{IE} = \dot{\boldsymbol{\rho}}_E - \dot{\boldsymbol{\rho}}_I$ ,  $\Delta\boldsymbol{\rho}_{IE} = \boldsymbol{\rho}_E - \boldsymbol{\rho}_I$ , and  $\epsilon$  is the constant

$$\epsilon = \frac{\mu_{\odot}}{\mu_{\odot} + \mu_{\oplus}}. \quad (5.31)$$

Substituting Equations 5.5, 5.25, 5.27, and 5.29 into Equation 5.9 yields

$$\dot{\mathbf{R}}_{E\mu_{\oplus}I} \cong \dot{\boldsymbol{\rho}}_I + \dot{\mathbf{r}}_{I\mu_{\odot}E} + \epsilon\dot{\boldsymbol{\rho}}_{IE}. \quad (5.32)$$

Further, substituting Equations 5.2, 5.3, 5.26, 5.28, 5.30, and 5.32 into Equation 5.12 yields

$$\mathbf{R}_{E\mu_{\oplus}I} \cong \boldsymbol{\rho}_I + \mathbf{r}_{I\mu_{\odot}E} - \Delta t_{IE}\dot{\mathbf{r}}_{I\mu_{\odot}E} - \epsilon\{\boldsymbol{\rho}_I - [\boldsymbol{\rho}_E - \Delta t_{IE}\dot{\boldsymbol{\rho}}_E]\}. \quad (5.33)$$

Equations 5.32 and 5.33 can be rearranged to derive

$$\dot{\mathbf{r}}_{I\mu_{\odot}E} \cong \dot{\mathbf{R}}_{E\mu_{\oplus}I} - \dot{\boldsymbol{\rho}}_I - \epsilon\Delta\dot{\boldsymbol{\rho}}_{IE}, \quad (5.34)$$

and

$$\mathbf{r}_{I\mu_{\odot}E} \cong \mathbf{R}_{E\mu_{\oplus}I} - \boldsymbol{\rho}_I + \Delta t_{IE}\dot{\mathbf{r}}_{I\mu_{\odot}E} + \epsilon\{\boldsymbol{\rho}_I - [\boldsymbol{\rho}_E - \Delta t_{IE}\dot{\boldsymbol{\rho}}_E]\}. \quad (5.35)$$

If the interior state vector,  $\sigma_I$  from Equation 5.23, is known, then  $\mathbf{r}_{I\mu_{\odot}E}$  and  $\dot{\mathbf{r}}_{I\mu_{\odot}E}$  can be calculated by selenocentric conic propagation to time  $t_E$ . The lunar positions and velocities at the two terminal points,  $\boldsymbol{\rho}_I$ ,  $\dot{\boldsymbol{\rho}}_I$ ,  $\boldsymbol{\rho}_E$ , and  $\dot{\boldsymbol{\rho}}_E$  can be found through an ephemeris program such as SPICE (Section 3.2) or by conic propagation (Section 2.2). Thus Equations 5.32 and 5.33 are used to find the state vector in closed-form,

$$\xi_{E\mu_{\oplus}I} = (t_I, \mathbf{R}_{E\mu_{\oplus}I}, \dot{\mathbf{R}}_{E\mu_{\oplus}I}). \quad (5.36)$$

Since conic propagation is reversible, the following equation

$$\dot{\mathbf{R}}_{(E\mu_{\oplus}I)\mu_{\oplus}E} = \dot{\mathbf{R}}_E \quad (5.37)$$

holds. Hence the closed-form approximate solution of  $\xi_E$  is found by propagating  $\xi_{E\mu_{\oplus}I}$  along a geocentric conic to time  $t_E$ .

Conversely, if the exterior state vector,  $\xi_E$ , is known, then  $\mathbf{R}_{E\mu_{\oplus}I}$  and  $\dot{\mathbf{R}}_{E\mu_{\oplus}I}$  can be computed using geocentric conic propagation to time  $t_I$ . In this case, Equations 5.34 and 5.35 are applied to find the state vector

$$\sigma_{I\mu_{\odot}E} = (t_E, \mathbf{r}_{I\mu_{\odot}E}, \dot{\mathbf{r}}_{I\mu_{\odot}E}). \quad (5.38)$$

The closed-form approximate solution of  $\sigma_I$  is then found by propagating  $\sigma_{I\mu_{\odot}E}$  along a selenocentric conic to time  $t_I$ .

If the interval between  $t_I$  and  $t_E$  is broken into many segments, Equations 5.32 and 5.33 can be applied in each subsequent interval. This develops an approximate numerical integration algorithm which enables both large integration steps and maintains good accuracy. The terms in Equations 5.32 and 5.33 multiplied by the factor  $\epsilon$  are integrals of the three-body perturbing acceleration and thus provide a first order rectification to the conic orbits between propagation steps. Additional rectification terms are added to Equations 5.32 and 5.33 to account for  $J_2$  and solar perturbations as shown in Reference [13].

For preliminary translunar mission trade studies, the ability to take large integration steps, such as perigee to pericyynthion, is desired so that many trajectories may be evaluated. For these problems, perturbations due to the sun and an oblate Earth are ignored. Without these major perturbations the rectification terms in Equations 5.32 and 5.33 can be omitted without significantly increasing the error of the approximation. The error remains small as long as the definition of the lunar vicinity

remains within a selenocentric “pseudostate transformation sphere” (PTS) having a radius of 20 to 40 Earth radii. Here the word “pseudostate” derives from the phrase “pseudo target aiming point” which refers to a point a translunar transfer trajectory approximated as an ellipse would pass through [38]. The pseudostate transformation sphere is centered on and moves with the Moon. With a radius larger than that defined by the Moon’s sphere of influence, the PTS expands into Earth’s sphere of influence, allowing the selenocentric conic to overlap a portion of the geocentric conic. Outside of this sphere, only geocentric conic propagation is used to define the motion of the spacecraft.

The simplified overlapped conic equations form the basis for the pseudostate theory discussed next.

### 5.1.3 Pseudostate Theory

When the rectification terms are removed from Equations 5.32 and 5.33 the equations

$$\dot{\mathbf{R}}_{E\mu\oplus I} = \dot{\boldsymbol{\rho}}_I + \dot{\mathbf{r}}_{I\mu\odot E}, \quad (5.39)$$

and

$$\mathbf{R}_{E\mu\oplus I} = \boldsymbol{\rho}_I + \mathbf{r}_{I\mu\odot E} - \Delta t_{IE} \dot{\mathbf{r}}_{I\mu\odot E} \quad (5.40)$$

are returned. In addition to its use as an algorithm for propagating known state vectors, the pseudostate theory provides the most value in applying the overlapped conic approximation to boundary value problems using procedures that do not require a first-guess state vector.

Pseudostate terminals are points on the trajectory at which the overlapped conic segments begin and end. Each segment has an interior and exterior terminal. Interior terminals may be the initial or final point in the trajectory as illustrated in Figure 5.4, or a pericynthion point as illustrated in Figure 5.5. Exterior terminals may be

the initial or final point of a trajectory, Figure 5.4 or point  $e$  in Figure 5.5, or the point at which the trajectory passes through the pseudostate transformation sphere, point  $E$  in Figure 5.5.

Associated with each terminal is a real state vector and a pseudostate vector, denoted using the  $(*)$  symbol. Relative to the geocentric frame, the interior pseudostate vector is defined by the equation

$$\xi_I^* = \left( t_I, \mathbf{R}_I^*, \dot{\mathbf{R}}_I^* \right), \quad (5.41)$$

where  $\mathbf{R}_I^* = \mathbf{R}_{E\mu_{\oplus}I}$  and  $\dot{\mathbf{R}}_I^* = \dot{\mathbf{R}}_{E\mu_{\oplus}I}$ . The same vector in selenocentric coordinates is

$$\sigma_I^* = (t_I, \mathbf{r}_I^*, \dot{\mathbf{r}}_I^*). \quad (5.42)$$

Relative to the selenocentric frame, the exterior pseudostate is written as

$$\sigma_E^* = (t_E, \mathbf{r}_E^*, \dot{\mathbf{r}}_E^*), \quad (5.43)$$

where  $\mathbf{r}_E^* = \mathbf{r}_{I\mu_{\odot}E}$  and  $\dot{\mathbf{r}}_E^* = \dot{\mathbf{r}}_{I\mu_{\odot}E}$ . Again, a similar method is used to find the exterior geocentric pseudostate, specifically,

$$\xi_E^* = \left( t_E, \mathbf{R}_E^*, \dot{\mathbf{R}}_E^* \right). \quad (5.44)$$

The time component of an interior or exterior pseudostate is equal to the time component of the corresponding interior or exterior real state vector. Within the pseudostate transformation sphere (PTS) the real states are connected indirectly through the pseudostate as follows (Figure 5.4). The exterior real state,  $E$ , and the interior pseudostate,  $I^*$  are propagated through a geocentric conic trajectory, the interior and exterior pseudostate,  $I^*$  and  $E^*$ , are propagated through a selenocentric linear trajectory, and the exterior pseudostate,  $E^*$ , and the interior real state,  $I$ , are propagated

through a selenocentric conic trajectory.

When the exterior pseudostate terminal is a PTS pierce point, the interior pseudostate is connected by a geocentric conic to the real PTS pierce state, point  $E$  in Figure 5.5, and to any real state outside the sphere, such as point  $M$  in Figure 5.5. For this reason, it is not necessary to evaluate the geocentric conic state vector at the pierce point for trajectories passing through the sphere.

If the perigee is passed between the initial and final points of a trajectory, the transfer must be divided into two separate segments in order to apply the overlapped conic method. As shown in Figure 5.5, the pericynthion and post-pericynthion segments share a common interior real state,  $i = I$ . Ideally, the time component of the interior state should equal the pericynthion passage time,  $t_i = t_{p_\odot}$ , but can differ by as much as two hours and still maintain accuracy of the solution.

Further, it should be noted that the exterior states of the pericynthion and post-pericynthion segments are connected by a selenocentric conic trajectory. Hence the segments can be connected without evaluating the interior real state vector.

#### 5.1.4 Translunar Targeting

Perhaps the most useful application of the pseudostate method is in the solution of split boundary problems. Combined with an iterative procedure, the pseudostate method can match two or more conic segments so that they satisfy specified boundary conditions [12]. One such example involves calculating the geocentric translunar injection state vector  $\xi_{p_\oplus}$ , and the selenocentric lunar orbit insertion state vector  $\sigma_{p_\odot}$  for an impulsive transfer between low Earth orbit and low lunar orbit. This problem, illustrated in Figure 5.6, is the foundation of the EXLX multi-conic propagator discussed in Section 5.2. The boundary conditions at the Earth end of the trajectory include the perigee radius  $R_{p_\oplus}$ , the translunar injection speed  $V_{p_\oplus} = \left| \dot{\mathbf{R}}_{p_\oplus} \right|$ , and the inclination of the geocentric transfer trajectory. At the lunar end of the transfer the

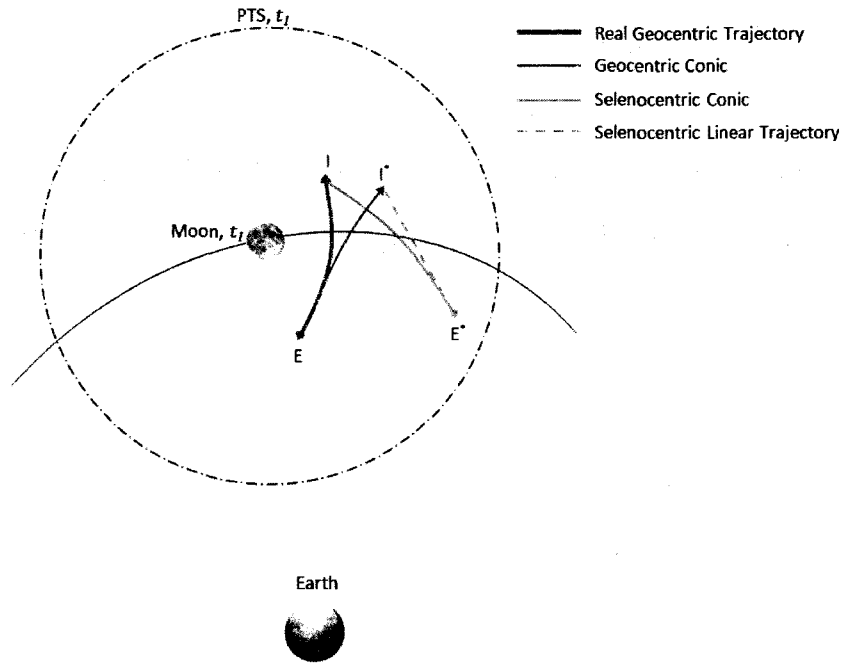


Figure 5.4: Pseudostate terminals for a short segment of a translunar trajectory

boundary conditions include the time of orbit insertion  $t_{p_\odot} = t_i$ , the pericyynthion radius  $r_{p_\odot} = |\mathbf{r}_i|$ , and the restriction that the lunar orbit plane contain a given vector  $r_L$ . The problem is solved by iterating on  $\mathbf{R}_i^*$ , the geocentric interior pseudostate position vector. For the first iteration  $\mathbf{R}_i^* = \boldsymbol{\rho}_i$  which can be found from an ephemeris program.

If  $V_{p_\oplus}^2 < \frac{2\mu_\oplus}{R_{p_\oplus}}$ , the geocentric conic is elliptical and has an apogee distance of  $R_A$ . In this case it is assumed that  $|\mathbf{R}_i^*| = R_i^* < R_A$  for any value of  $\mathbf{R}_i^*$  used in the iterative process. It is also assumed that the declination of  $\mathbf{R}_i^*$  is never greater than the geocentric orbit inclination. If these requirements are met, there exist geocentric conics that pass through  $\mathbf{R}_i^*$  which satisfy the initial boundary conditions on  $R_{p_\oplus}$ ,  $V_{p_\oplus}$ , and inclination. For each possible conic the quantities for  $\dot{\mathbf{R}}_i^*$ ,  $t_{p_\oplus}$ ,  $R_{p_\oplus}$ , and  $\dot{\mathbf{R}}_{p_\oplus}$  are computed explicitly. It is assumed selection criteria are specified, such as the azimuth angle sign, to determine which of the possible conics is the unique solution.

Having calculated  $\dot{\mathbf{R}}_i^*$ , Equation 5.3 is used to find  $\dot{\mathbf{r}}_i^*$ . Based on the earlier



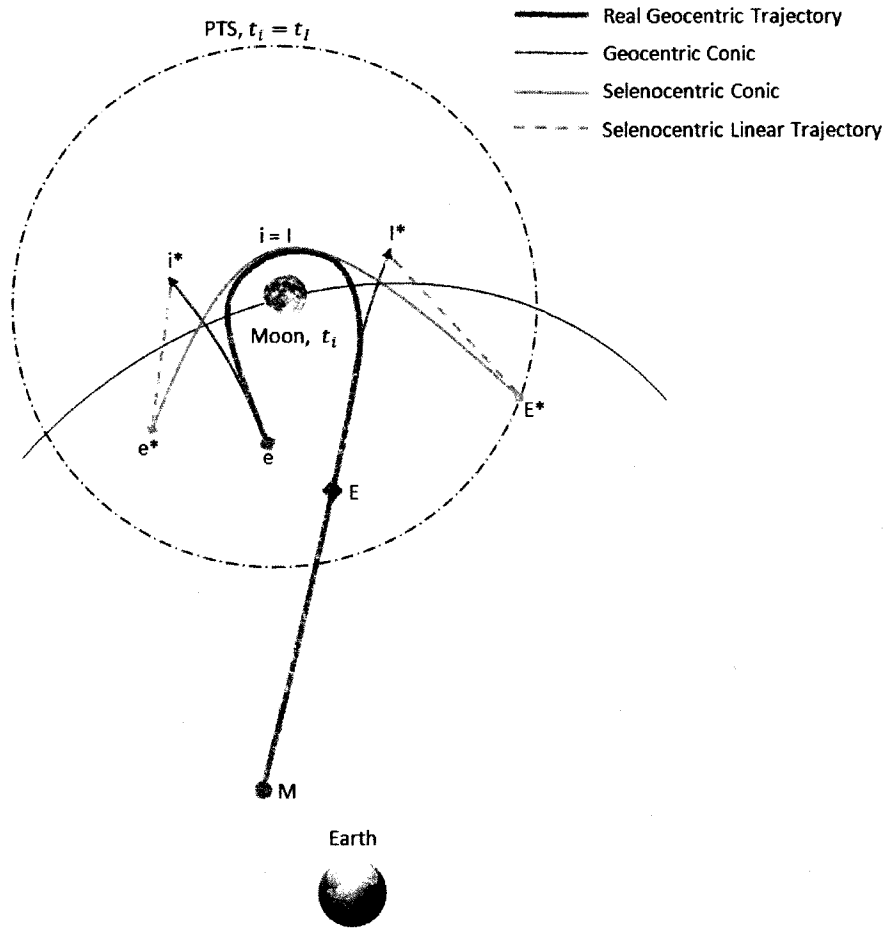


Figure 5.5: Pseudostate terminals for a circumlunar segment of a translunar trajectory  
 assumption that  $\mathbf{R}_i^* = \boldsymbol{\rho}_i$ , on the first iteration  $\mathbf{r}_i^*$  is not exact. However, the assumption is accurate enough to compute a new estimate  $\mathbf{R}_i^{*'} for the interior pseudostate position using the following equations.$

The linear relationship between interior and exterior pseudostates mentioned earlier defines  $\mathbf{r}_e^* = \mathbf{r}_i^*$ . The remaining components of the exterior pseudostate,  $t_e$  and  $\mathbf{r}_e^*$  are found by applying the lunar boundary conditions. For this case, the magnitude of  $\mathbf{r}_e^*$  is equal to the pseudostate transformation sphere radius,  $r_s$ . The equation for specific mechanical energy gives

$$v_{p\odot} = \left[ (v_e^*)^2 - \frac{2\mu_{\odot}}{r_s} + \frac{2\mu_{\odot}}{r_{p\odot}} \right], \quad (5.45)$$

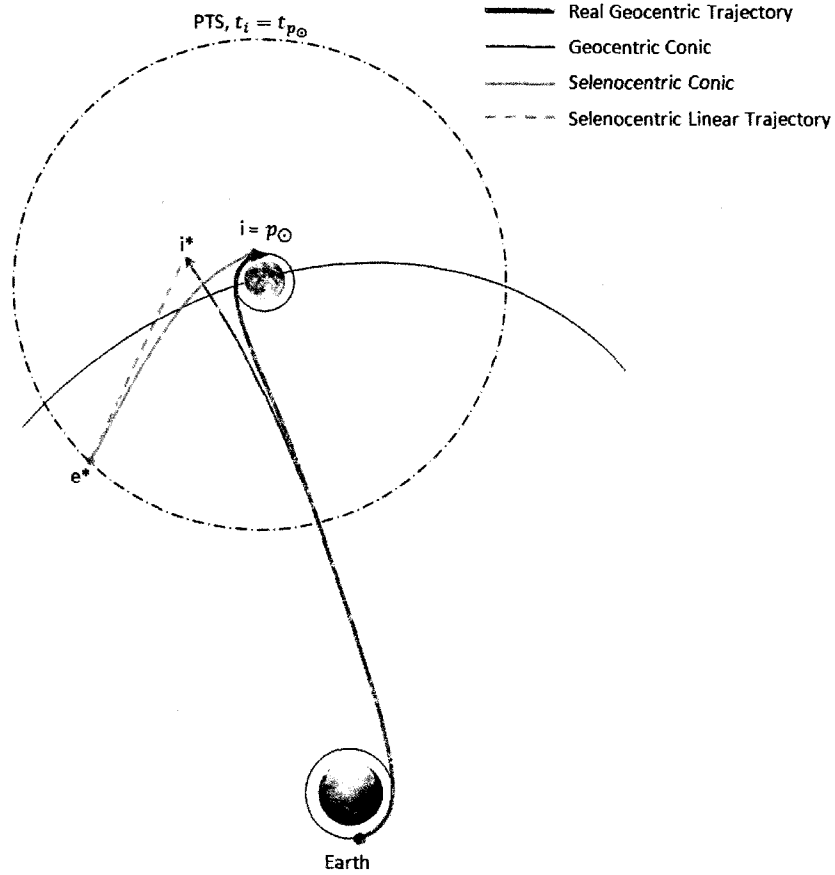


Figure 5.6: Pseudostate terminal geometry for translunar targeting problem

where  $v_{p_\odot} = |\dot{\mathbf{r}}_{p_\odot}|$  and  $v_e^* = |\dot{\mathbf{r}}_e^*|$ . The requirement that  $r_L$  lie in the selenocentric orbit plane leads to

$$\hat{\mathbf{h}} = \frac{\mathbf{r}_L \times \dot{\mathbf{r}}_e^*}{|\mathbf{r}_L \times \dot{\mathbf{r}}_e^*|}, \quad (5.46)$$

where  $\hat{\mathbf{h}}$  is the unit vector in the direction of the selenocentric angular momentum.

Next the other unit vectors

$$\hat{\mathbf{v}}_e^* = \frac{\dot{\mathbf{r}}_e^*}{v_e^*}, \quad (5.47)$$

and

$$\hat{\mathbf{b}} = \hat{\mathbf{v}}_e^* \times \hat{\mathbf{h}} \quad (5.48)$$

are computed. From the definition of a cross product  $\hat{\mathbf{b}}$  is normal to  $\hat{\mathbf{v}}_e^*$ , and both

of these unit vectors lie in the selenocentric orbit plane. The exterior pseudostate position vector can then be written as

$$\mathbf{r}_e^* = X\hat{\mathbf{b}} - Y\hat{\mathbf{v}}_e^*, \quad (5.49)$$

where  $X$  and  $Y$  are defined as

$$X = \frac{r_{p_\odot} v_{p_\odot}}{v_e^*}, \quad (5.50)$$

and

$$Y = (r_s^2 - X^2)^{\frac{1}{2}}. \quad (5.51)$$

With  $\mathbf{r}_e^*$ ,  $\dot{\mathbf{r}}_e^*$ , and  $t_{p_\odot}$ , the exterior pseudostate time  $t_e$  and the pericyynthion state vector components  $\mathbf{r}_{p_\odot}$  and  $\dot{\mathbf{r}}_{p_\odot}$  are computed explicitly. The new geocentric interior pseudostate position is then calculated from the equation

$$\mathbf{R}_i^{*'} = \boldsymbol{\rho}_i + \mathbf{r}_e^* + (t_i - t_e)\dot{\mathbf{r}}_e^*. \quad (5.52)$$

If  $|R_i^* - R_i^{*'}|$  is less than a set tolerance value, the solution converges and the values for  $\xi_{p_\oplus}$  and  $\sigma_{p_\odot}$  are correct. If this is not the case,  $\mathbf{R}_i^*$  is replaced by  $\mathbf{R}_i^{*'}$  and the computations are repeated until the tolerance criterion is met.

The following section characterizes the user interface to EXLX as well as the steps required to achieve a realistic translunar trajectory for specified boundary conditions.

## 5.2 EXLX Configuration

### 5.2.1 Parameter Selection User Interface

EXLX includes an Excel interface to aid in the selection of transfer trajectories between circular Earth and lunar orbits. The user interacts with the interface by selecting a variety of desired parameters which are found in Table 5.1.

Parameter	Units
Date of MET Zero (origin of Mission Elapsed Time scale)	Year\Month\d\hh:mm
Altitude of Earth circular parking orbit	km
Inclination of Earth orbit ( $i_{\oplus}$ )	deg
Right ascension of ascending node ( $\Omega_{\oplus}$ )	deg
Time of Earth orbit ascending node definition wrt MET Zero	d\hh:mm
Time of Earth orbit departure wrt MET Zero	d\hh:mm
Time of lunar orbit insertion wrt MET Zero	d\hh:mm
Perisel altitude of plane change ellipse	km
Orbit period of plane-change ellipse	d\hh:mm
Altitude of lunar circular parking orbit	km
Selenographic inclination of lunar orbit ( $i_{\odot}$ )	deg
Selenographic longitude of lunar orbit ascending node ( $\Omega_{\odot}$ )	deg
Time of lunar orbit ascending node definition wrt MET Zero	d\hh:mm

Table 5.1: User selected parameters for EXLX Excel interface for three-burn sequence

In addition to the parameters just listed, the user has the option of “flying out” single or triple impulse maneuvers. For three-impulse cases, the lunar orbit insertion time is considered the first impulse which establishes a selenocentric plane-change ellipse. The parameters in Table 5.1 refer to a three-impulse burn. In the case of a single impulse transfer, the “perisel altitude of plane-change ellipse” and “orbit-period of plane change ellipse” parameters no longer exist and instead are replaced with a “low limit on perisel altitude of approach hyperbola” option. EXLX also has the option to constrain any output variable with lower and upper bounds. For example, the user may put restrictions on the impulsive translunar injection azimuth angle or the time between the translunar injection and the lunar orbit insertion.

After the setup parameters are selected, the interface maps the resulting data. The mapping takes the form of a two dimensional scan space represented by a matrix. Though EXLX can handle a variety of scan types, for this research the scans were limited to lunar parking orbit accessibility scans and timetable scans. Lunar parking orbit accessibility scans have axes which represent various longitude of the ascending nodes,  $\Omega_{\odot}$ , and orbit inclinations,  $i_{\odot}$ , for possible lunar parking orbits. Timetable

scans have axes representing times of departure from Earth and arrival at the Moon. The scans permit effective optimization of the LOI  $\Delta V$  and the time of flight trade to be performed. Figure 5.7 is an example of a lunar parking orbit accessibility scan, and Figure 5.8 demonstrates a timetable output scan matrix after a run. For this research, the only constraint placed on the trajectory is that the magnitude of the lunar orbit insertion burn must be less than 840 m/s. This is a realistic value for Crew Exploration Vehicle missions. Though delta velocities greater than this restriction are feasible, the EXLX multi-conic propagator discussed next only implements burns with this maximum magnitude, thus the interface trajectory selection is restricted. The scan matrix highlights those cases which conform with the velocity restriction. The user can select a highlighted cell and generate the initialization parameters for use by the multi-conic propagator. These parameters include all those listed in Table 5.1 and any restrictions placed on the transfer by the user. The feasible conditions selected through the Excel interface are utilized by the EXLX multi-conic propagator to integrate the entire translunar trajectory.

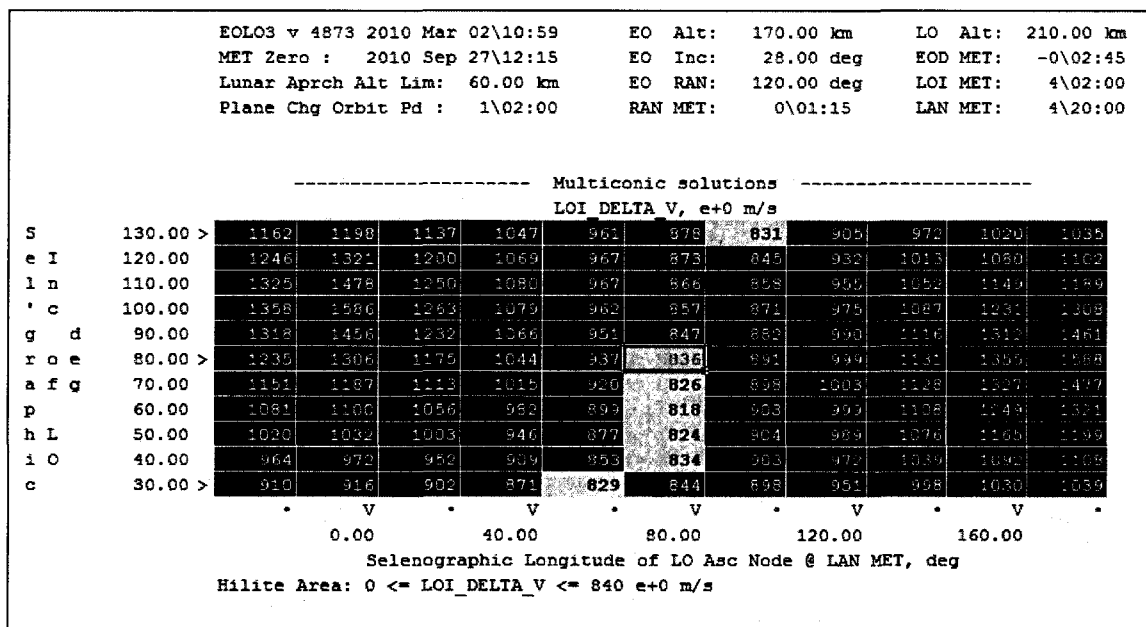


Figure 5.7: Example of EXLX Excel lunar parking orbit accessibility scan matrix

		EOLOS v 4873 2010 Feb 04\08:35				EO Alt: 170.00 km				LO Alt: 210.00 km		
		MET Zero : 2010 Sep 27\12:15				EO Inc: 28.00 deg				LO Inc: 80.00 deg		
		Lunar Aprch Alt Lim: 60.00 km				EO RAN: 120.00 deg				LO LAN: 80.00 deg		
		Plane Chg Orbit Pd : 1\02:00				RAN MET: 0\01:15				LAN MET: 4\20:00		
----- Multiconic solutions -----												
LOI_DELTA_V, e+0 m/s												
	4\12:00 >	816	816	818	820	823	826	829	832	836	839	843
	4\10:00	817	817	819	821	824	827	830	834	837	841	845
L d	4\08:00	816	817	819	822	825	828	832	836	840	844	848
O \	4\06:00	816	818	820	823	827	831	834	839	843	847	852
I h	4\04:00	817	819	822	826	829	833	837	842	846	851	856
h	4\02:00 >	818	821	824	828	832	836	841	846	850	855	860
M :	3\00:00	820	823	827	831	836	840	845	850	855	860	866
E m	3\22:00	822	826	831	835	840	845	850	855	860	866	872
T m	3\20:00	826	830	835	839	844	850	855	861	866	872	878
	3\18:00	830	834	839	844	850	855	861	867	873	879	886
	3\16:00 >	834	839	845	850	856	862	868	874	881	887	894
		.	V	.	V	.	V	.	V	.	V	.
		-0\06:45		-0\04:45		-0\02:45		-0\00:45		0\01:15		
		EOD MET, d\hh:mm										
		Hilite Area: 0 <= LOI_DELTA_V <= 840 e+0 m/s										

Figure 5.8: Example of EXLX Excel timetable scan matrix

## 5.2.2 EXLX Multi-Conic Propagator

The EXLX multi-conic propagator models the translunar trajectory using the three-body pseudostate theory to compute overlapped conic transfer trajectories between the Earth and Moon. The original model for the lunar ephemeris calculations is replaced to match the current SPICE ephemeris model used in this research (Section 3.2.1). The purpose of this replacement is to ensure consistency between the ephemeris programs used in EXLX and the predictor-corrector scheme. During the multi-conic trajectory propagation, perturbations due to both solar effects and the oblateness of the Earth are accounted for. The circular Earth and lunar parking orbits precess under the influence of  $J_2$  and 4-body motion to include the Moon and the Sun. During the transfer period between the two orbits, EXLX again accounts for 4-body motion but does not consider the acceleration due to gravity. For three-burn cases,  $J_2$  is ignored in the plane-change ellipse. Unlike the Cowell propagator, the EXLX propagator does not implement higher order gravity coefficients, drag, or solar pressure in any phase of its modeling. Figure 5.9 shows the difference in perturbation

approximations of each flight phase for the EXLX and Cowell propagators.

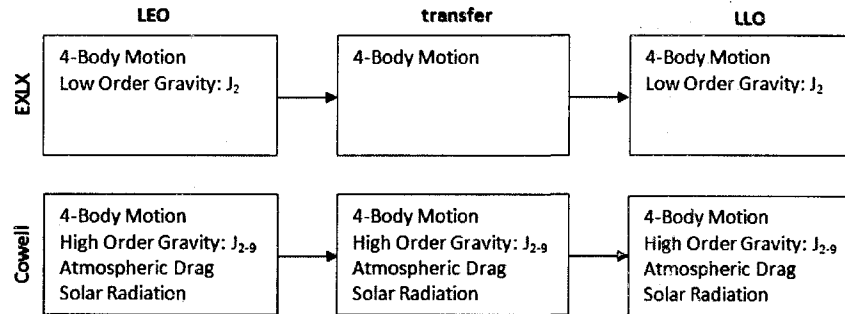


Figure 5.9: Perturbation dynamics applied in each flight phase for the EXLX and Cowell propagators over a translunar trajectory

In calculating the impulsive translunar injection burn, EXLX solves Lambert's problem (Section 6.1) with the position in the lunar parking orbit optimized for minimum delta velocity.

Using the viable parameters selected from the Excel interface, the EXLX multi-conic propagator applies an overlapped conic approximation to determine a feasible trajectory for a translunar mission. The final trajectory output from EXLX includes the states from the Mean Epoch Time through the third lunar insertion burn (LOI3). Avoiding the complexity of adding thrust acceleration to the Cowell propagator, the initial position and velocity of the vehicle is set to the states produced by EXLX at the translunar insertion (TLI) burn. The final states are taken as those at the first lunar orbit insertion burn (LOI1). When the EXLX trajectory is flown out using the high fidelity Cowell propagator, the integrated states miss the desired final position due to the limited accuracy of the perturbation models utilized by the EXLX multi-conic propagator. To produce a more accurate final state, assuming the initial position is fixed, the initial velocity must be updated. The velocity correction is computed through the error state transition matrix and the updated states are flown out with the Cowell propagator again. This iterative shooting method process continues until

the integrated position value comes within a set tolerance of the desired final position.

The method just described summarizes the process of acquiring the most accurate translunar transfer velocities given the perturbation models applied in the Cowell-STM predictor-corrector. The following section details the process of selecting translunar test cases.

### 5.3 Test Case Selection

The process in selecting the translunar test cases begins with choosing which parameters to hold constant and which to vary for each case. Preliminary testing illustrates that holding the Earth and Moon orbits constant and changing the date does not vary the transfer orbit enough to thoroughly test a variety of possible cases. This is because the geometry of the Moon with respect to the Earth stays relatively the same over the period of a year. Although the Moon's declination will change from  $\pm 28.5^\circ$  as a result of the tilt of the Earth ( $23.5^\circ$ ) and Moon ( $5^\circ$ ) with respect to the ecliptic plane (Figure 5.10), the variation is not enough to greatly change the transfer trajectory between two constant Earth and lunar orbits. Hence it is not the position of the

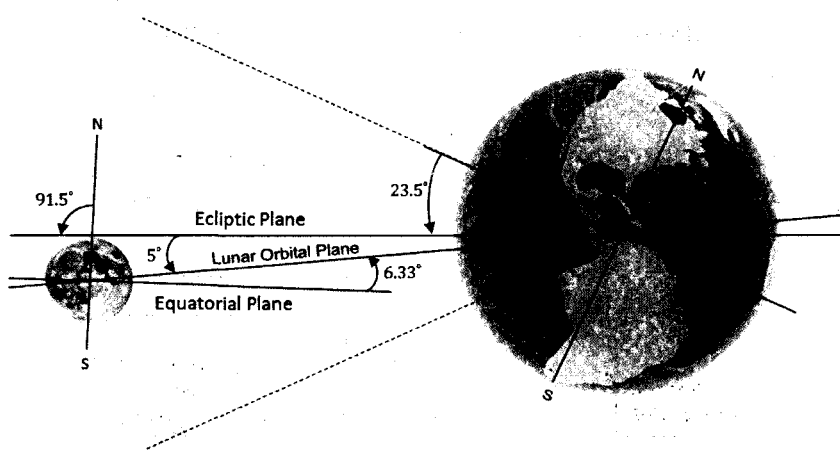


Figure 5.10: Tilt of the Earth and Moon with respect to the ecliptic plane



Moon that greatly affects the transfer trajectory but the characteristics of the Earth and lunar parking orbits. As a result, from Table 5.1 the Earth orbit inclination,  $i_{\oplus}$ , and right ascension of ascending node,  $\Omega_{\oplus}$ , as well as the lunar orbit inclination,  $i_{\odot}$ , and longitude of ascending node,  $\Omega_{\odot}$ , were the four parameters selected to independently vary. The remainder of the parameters from Table 5.1 were set to the values in Table 5.2 for all test cases.

Parameter	Value
Date of MET Zero (origin of Mission Elapsed Time scale)	February 20, 2012 12:00
Altitude of Earth circular parking orbit	170 km
Inclination of Earth orbit ( $i_{\oplus}$ )	$0^{\circ} - 360^{\circ}$ (deg)
Right ascension of ascending node ( $\Omega_{\oplus}$ )	$0^{\circ} - 360^{\circ}$ (deg)
Time of Earth orbit ascending node definition wrt MET Zero	0\01:30
Time of Earth orbit departure wrt MET Zero	0\00:30
Time of lunar orbit insertion wrt MET Zero	5\00:00
Perisel altitude of plane change ellipse	50 km
Orbit period of plane-change ellipse	1\00:00
Altitude of lunar circular parking orbit	200 km
Selenographic inclination of lunar orbit ( $i_{\odot}$ )	$0^{\circ} - 360^{\circ}$ (deg)
Selenographic longitude of lunar orbit ascending node ( $\Omega_{\odot}$ )	$0^{\circ} - 360^{\circ}$ (deg)
Time of lunar orbit ascending node definition wrt MET Zero	4\20:00

Table 5.2: Selected parameter values for translunar test cases

Though the translunar cases were selected for triple impulse maneuvers, only the first burn, LOI1, is considered. Since integrating multiple burns into the predictor-corrector algorithm would require multi-level targeting, for simplicity only the first burn is calculated. Due to the fact that the Excel interface to EXLX does not support changing any other orbital elements, such as eccentricity or true anomaly, these values remain constant throughout the test cases. For the set time of flight of 5 days and the maximum velocity constraint of 840 m/s on the LOI  $\Delta V$ , not all combinations of geocentric and selenocentric inclinations and nodes are possible. To develop an initial idea of the parameter ranges that are feasible, multiple scans are performed across lunar inclinations from  $0^{\circ} - 360^{\circ}$  and ascending nodes from  $0^{\circ} - 360^{\circ}$  for a variety of initial Earth orbits. Each scan produces a  $360^{\circ} \times 360^{\circ}$  matrix of LOI  $\Delta V$ 's

which are plotted as contours. Figure 5.11 is an example of one scan for an initial Earth orbit with  $i_{\oplus} = 0^{\circ}$  and  $\Omega_{\oplus} = 0^{\circ}$ . The white contour line plotted on the figure represents the isoline ranging from 0-840 m/s. These lines mark the boundaries of feasible lunar parameter regions for the particular Earth orbit tested. Thus, for this specific initial Earth orbit, the only feasible lunar orbits are near equatorial ( $i_{\odot} = 0^{\circ} = 360^{\circ}$  or  $180^{\circ}$ ) at any node, or any inclination at either the ascending or descending node ( $\Omega_{\odot} = 90^{\circ}$  or  $270^{\circ}$ ). Due to the difficulty of analyzing multiple

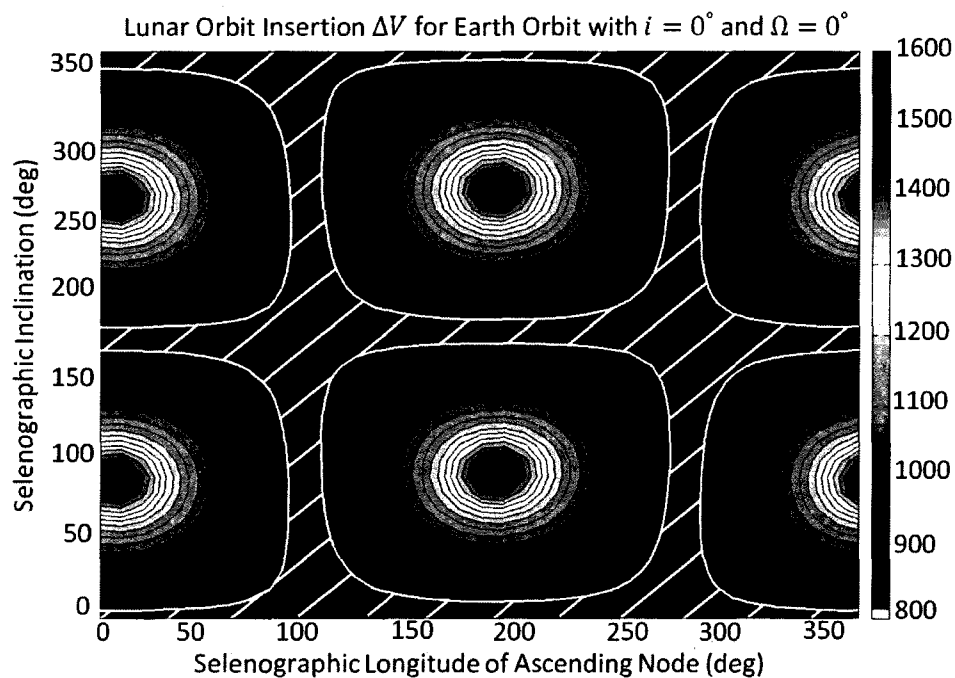


Figure 5.11: Contour plot of lunar orbit insertion  $\Delta V$  for an initial Earth orbit with  $i_{\oplus} = 0^{\circ}$  and  $\Omega_{\oplus} = 0^{\circ}$ . The white lines represent lunar orbit parameter regions that meet the constraint of  $\Delta V_{max} = 840$  km/s

contour plots on one figure, for comparison purposes only the isoline at 840 m/s is plotted over the varying initial Earth orbits. Figure 5.12 shows the results for a few of the initial Earth orbits tested, with the first data set representing the information plotted in Figure 5.11. It is clear that the trend of feasible lunar parameters from Figure 5.11 is carried over to some degree for each initial Earth orbit tested. Where some initial Earth orbits lend themselves to a variety of possible final lunar orbits, such

as those with initial condition combinations of  $i_{\oplus} = 45^{\circ}$  and  $\Omega_{\oplus} = 45^{\circ}$  or  $i_{\oplus} = 315^{\circ}$  and  $\Omega_{\oplus} = 135^{\circ}$ , others require very specific lunar conditions to result in a feasible trajectory. The small contour regions representative of an Earth orbit with  $i_{\oplus} = 90^{\circ}$  and  $\Omega_{\oplus} = 315^{\circ}$  is one example in Figure 5.12. To see the results broken down by each Earth orbit analyzed refer to Appendix A. The trends highlighted in Figure 5.12 and

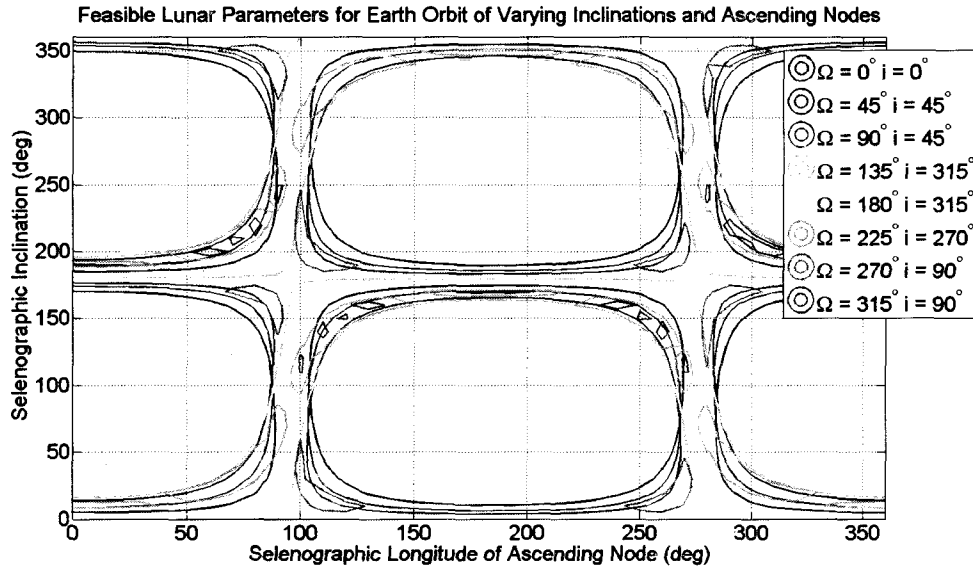


Figure 5.12: Contour plot of feasible lunar orbit parameters for varying initial Earth orbit parameters

more specifically in Appendix Figures A.1-A.8 provide guidelines for selecting Earth and lunar parameters for each test case. Once a feasible combination of parameters is selected, the values are utilized by the EXLX multi-conic process to propagate the trajectory. For a few set of feasible Earth and lunar conditions selected from the Excel interface, the multi-conic propagator does not converge. This is a result of an iteration number limitation on solving the procedure described in Section 5.1.4. In trying to propagate the conic with a  $J_2$  correction, the value  $|R_i^* - R_i^{*'}|$  does not reduce below the set tolerance of  $1 \times 10^{-8}$  before the maximum number of iterations, 29, is reached. Theorizing that convergence is within a few iterations and that the parameters only need slight adjustments, the lunar parameters are run through the

multi-conic method again with a change of  $\pm 3^\circ$ . This simple correction addresses the convergence issue. For those solutions that do converge, the final state vector is checked for any large discontinuities by visually inspecting the plotted trajectory. For a few cases, the outputted trajectories contain discontinuities that force the states to change unrealistically in short periods of time. Cases such as these are eliminated as infeasible.

The user interface for EXLX preclude a large number of Monte Carlo runs. For this reason only 110 cases are tested. See Appendix B for how this sample size is selected. The distribution of the feasible parameters selected for the 110 Earth and Moon orbits (see Appendix C for the details of each test case) is plotted in Figure 5.13. Also plotted on the figure is the most encompassing boundary line from Figure 5.12. Clearly, most of the lunar parameters are within the plotted contour lines. Those that are outside of the isolines in Figure 5.13 are not necessarily in the “infeasible” region, since the plot is only a generalized representation of what the exact contour may look like.

From the trends discussed earlier, it is deduced most of the Earth inclinations are restricted to prograde orbits as delineated by the horizontal lines in Figure 5.13. Prograde and retrograde orbits are distinguished by the direction of their rotation about the central body. In a prograde orbit, the vehicle rotates counterclockwise around the central body as viewed from the north pole, thus the orbits have inclinations between  $0^\circ - 90^\circ$ . Retrograde orbits on the other hand, rotate clockwise around the central body as viewed from the north pole, thus they have inclinations between  $90^\circ - 180^\circ$  [10]. Though the inclination ranges just described are the most common for prograde/retrograde motion, inclinations can exist between  $180^\circ - 360^\circ$ . Orbits with inclinations between  $180^\circ - 270^\circ$  are the same as the prograde orbits between  $0^\circ - 90^\circ$  except they have retrograde motion. Likewise, orbits with inclinations between  $270^\circ - 360^\circ$  are the same as orbits between  $90^\circ - 180^\circ$  except with prograde

motion.

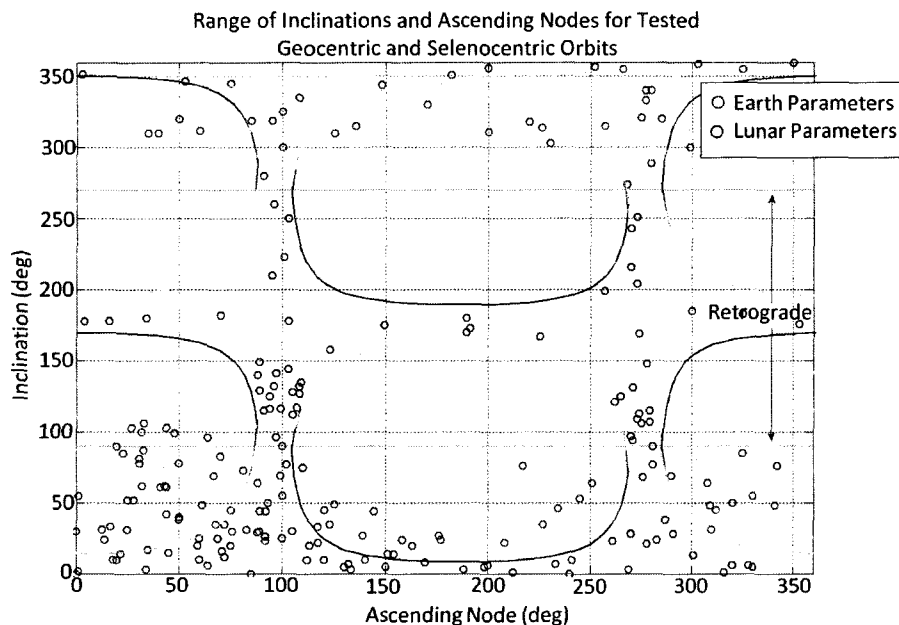


Figure 5.13: Distribution of Earth and lunar orbital elements for 110 test cases

## 5.4 Results and Analysis

All 110 translunar test cases converge using the Cowell-STM predictor-corrector method. A histogram of the results is found in Figure 5.14. Only three cases are outside the 1.5 interquartile range and they have iteration counts of 30, 31, and 34 respectively. The convergence trend of a number of the cases as well as the outlier cases is highlighted in Figure 5.15. Two trends appear to cause a larger than average number of iterations. It seems that the quicker the shooting method drops  $|\Delta R|$  below 100 km, the quicker the case converges. Those cases that bounce back and forth, oscillating between 1,000-10,000 km have the most difficulty converging. Though this trend occurs frequently, it is not always the case. As seen in Figure 5.15 with the outlier case that requires 30 iterations,  $|\Delta R|$  drops below 100 km at 7 iterations but then proceeds to take 23 very small steps until it converges (the last 20 steps have magnitudes less than 100 m). Hence, cases which have oscillating trends or multiple

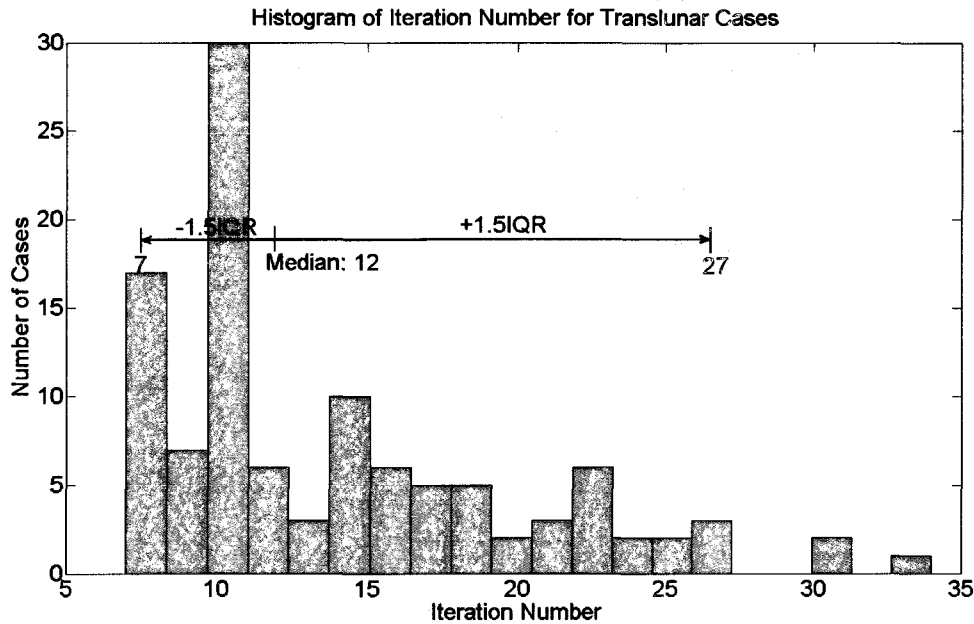


Figure 5.14: Histogram of the iteration number for the 110 translunar test cases

small steps result in the largest number of iterations. The cause of these trends is discussed next.

Figure 5.16 shows a plot of a variety of trajectories within the  $\pm 1.5\text{IQR}$  as well as the outlier cases at the the first LOI burn. Each trajectory is for a different lunar orbit insertion. It is clear that those trajectories that require more iterations follow a slightly different trajectory path then those with fewer iterations. The distinction is between whether the final lunar orbit is prograde or retrograde.

Those transfers that require more iterations enter into prograde lunar orbits while those with fewer iterations go into retrograde orbits. An example of both types of transfers is illustrated in Figures 5.17 and 5.18.

One point of interest is the change in velocity from the initial EXLX guess the predictor-corrector determines is necessary to hit the desired final location in the lunar orbit. Figure 5.19 is a histogram showing the number of cases that fell into each range of  $|\Delta V|$  with the statistical data labeled as well. Four outlier points exist with velocities of 0.05375 km/s, 0.06284 km/s, 0.09125 km/s, and 0.1424 km/s re-

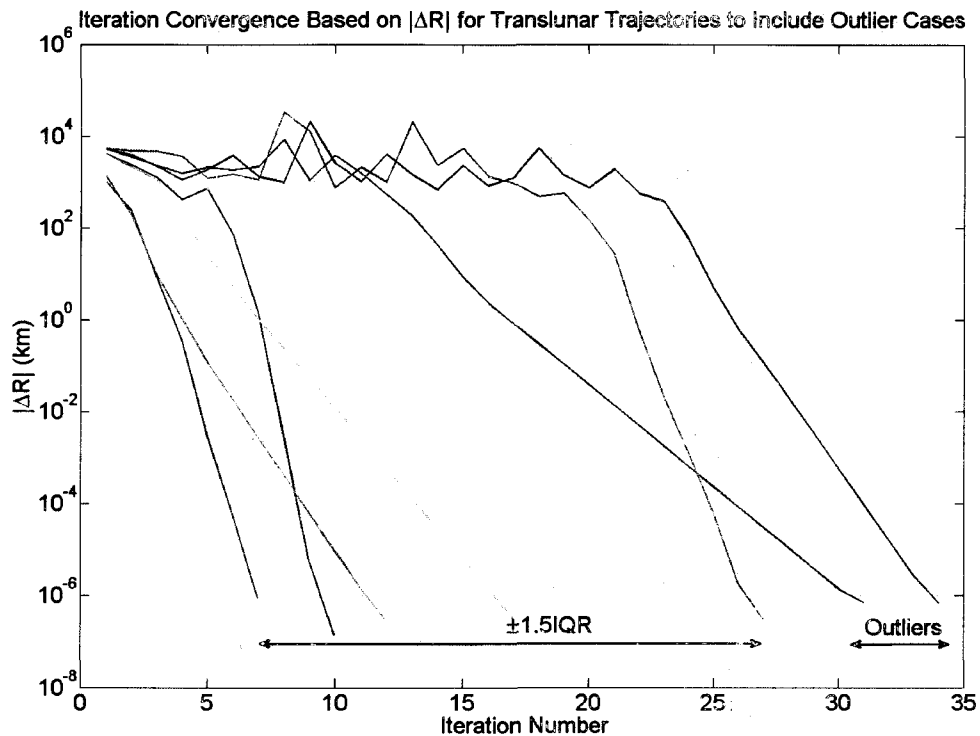


Figure 5.15: Convergence rate for a range of translunar cases with iteration numbers within 1.5IQR as well as the rate for the three outlier cases

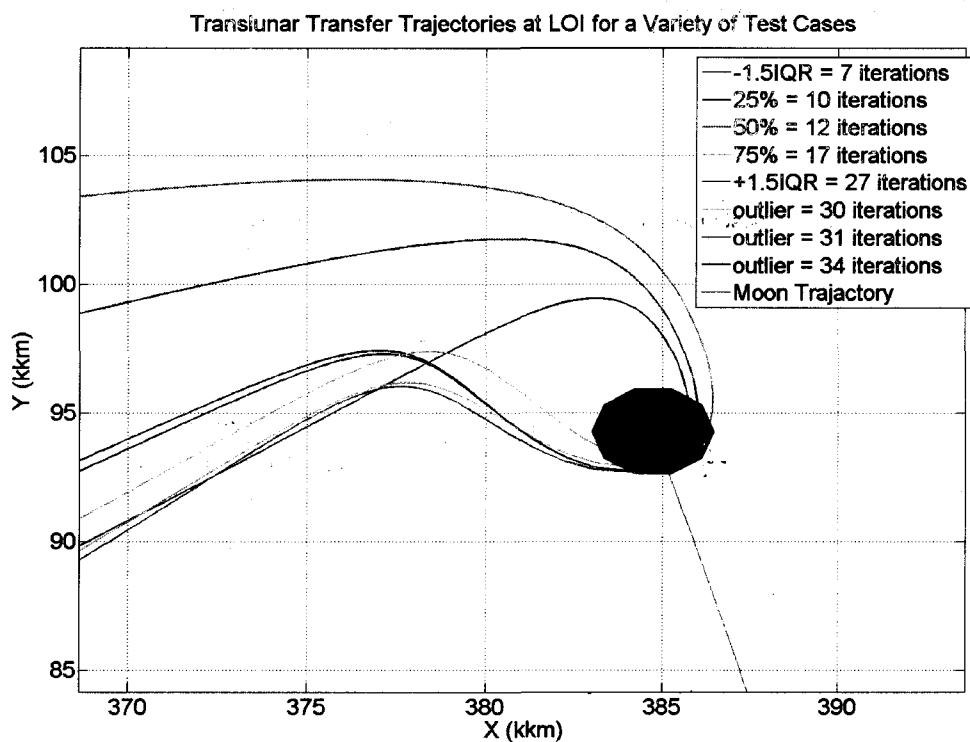


Figure 5.16: Translunar trajectories at LOI1 for a variety of test cases

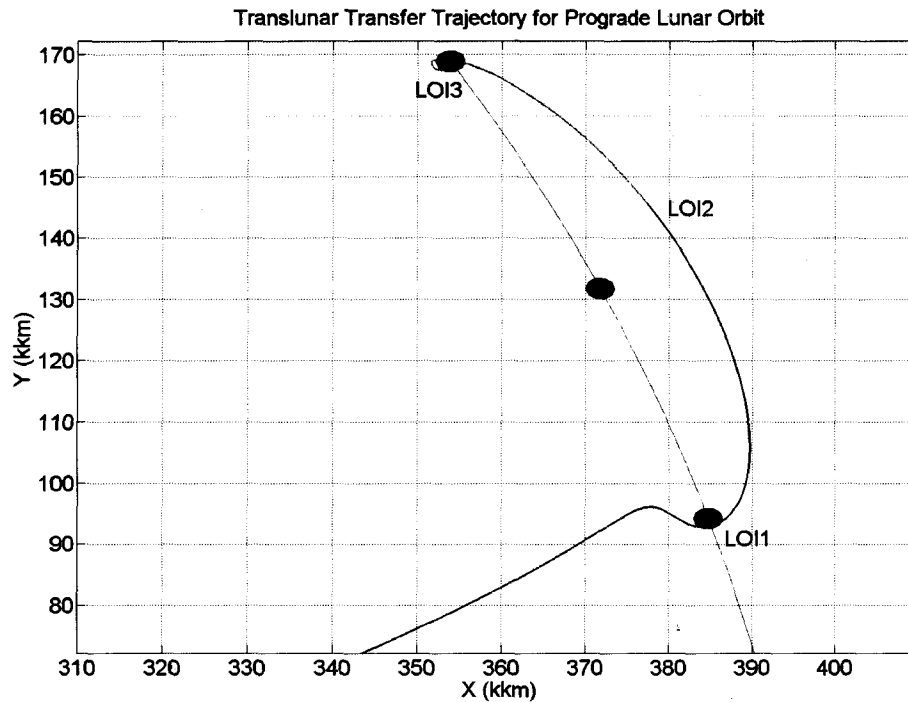


Figure 5.17: Example of a translunar transfer into a lunar prograde orbit (Test Case #77)

spectively. To determine if there is a correlation between the lunar orbit inclination and the  $\Delta V$  change required, the information from Figure 5.19 is separated by inclination and plotted as a stem plot in Figure 5.20. As with cases that require more iterations, cases with prograde lunar orbits are more likely to require a larger change in velocity from the initial EXLX guess. This is highlighted in Figure 5.20 where the two dotted horizontal lines represent the cutoff points for the 50th percentile and the 75th percentile of the data respectively. All four outlier cases have prograde lunar orbits as well.

#### 5.4.1 Translunar Shooting Method Sensitivity

The translunar cases are tested in a similar manner to the STM in Section 4.4. An initial perturbation is applied one at a time to the radial, tangential, and normal components of the position and velocity vector to determine the effects on the shoot-



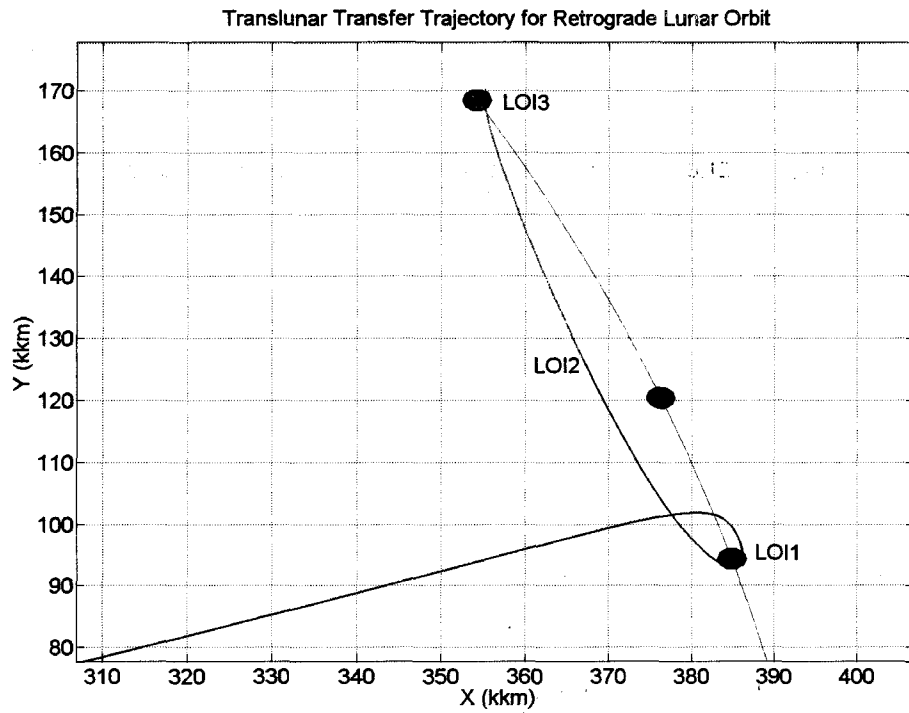


Figure 5.18: Example of a translunar transfer into a lunar retrograde orbit (Test Case #71)

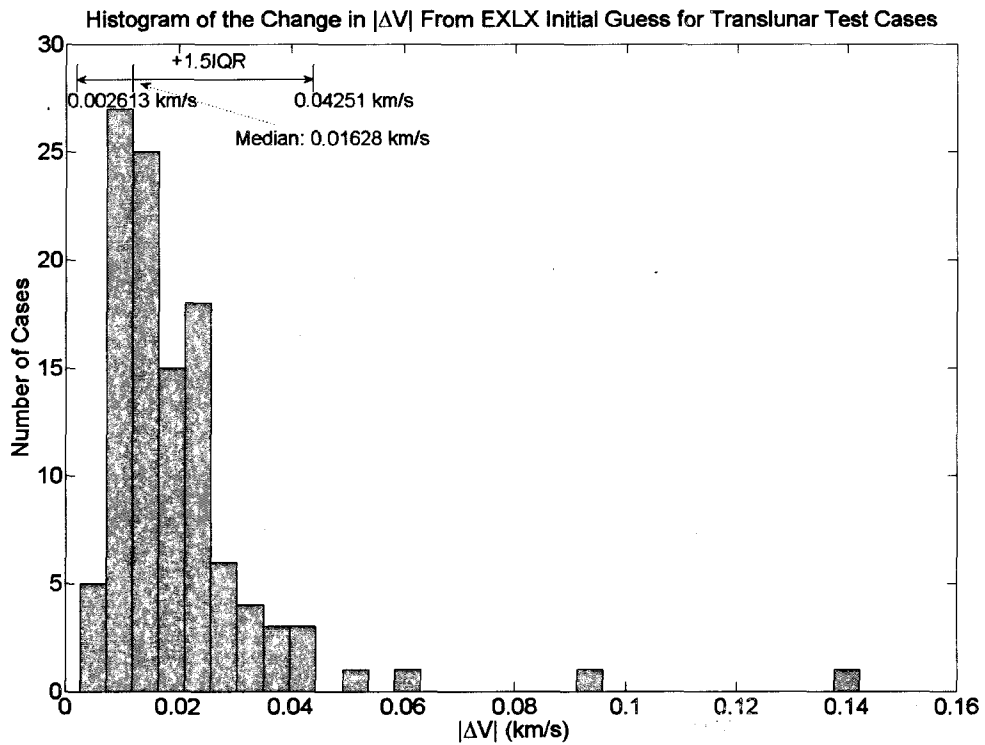


Figure 5.19: Histogram of the change in  $|\Delta V|$  required for the translunar test cases

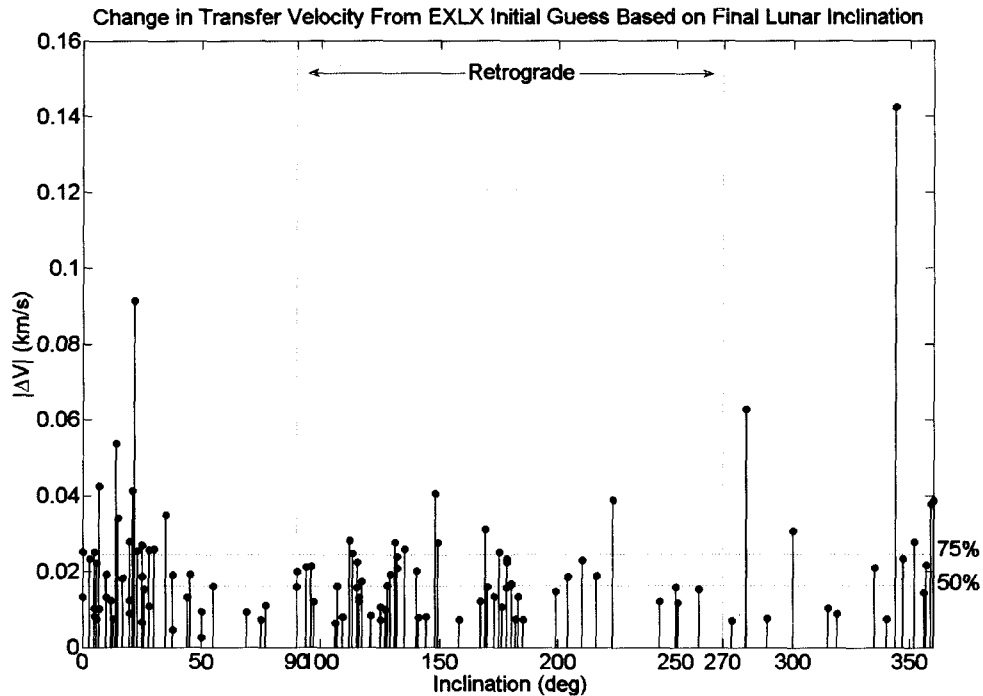


Figure 5.20: Stem plot of  $|\Delta V|$  based on the final lunar orbit inclination

ing method convergence. The purpose is to obtain a grasp of the sensitivity of the prediction-correction process to the initial guess. For Earth to Moon transfers one expects the sensitivities to be high because the region of “linearity” for the trajectory is correspondingly small. By adding perturbations, the ability of the state transition matrix to represent the transfer trajectory is tested.

The perturbation percentages range from 0-4% and are tested on all 110 cases. The results for the position perturbations are shown in Figure 5.21 and the results for the velocity perturbations are shown in Figure 5.22. For illustrative purposes a red dotted line is plotted to mark the cut off point of 40 iterations. Any data plotted above this line failed to converge under the maximum number of iterations. Note that a convergence failure represents the need for a more accurate initial guess, in this case, one that falls within the linear region assumed by the state transition matrix.

The first three columns of both plots highlight the convergence of all test cases with zero perturbation. Increasing the perturbation error to 0.001%, plotted as the second

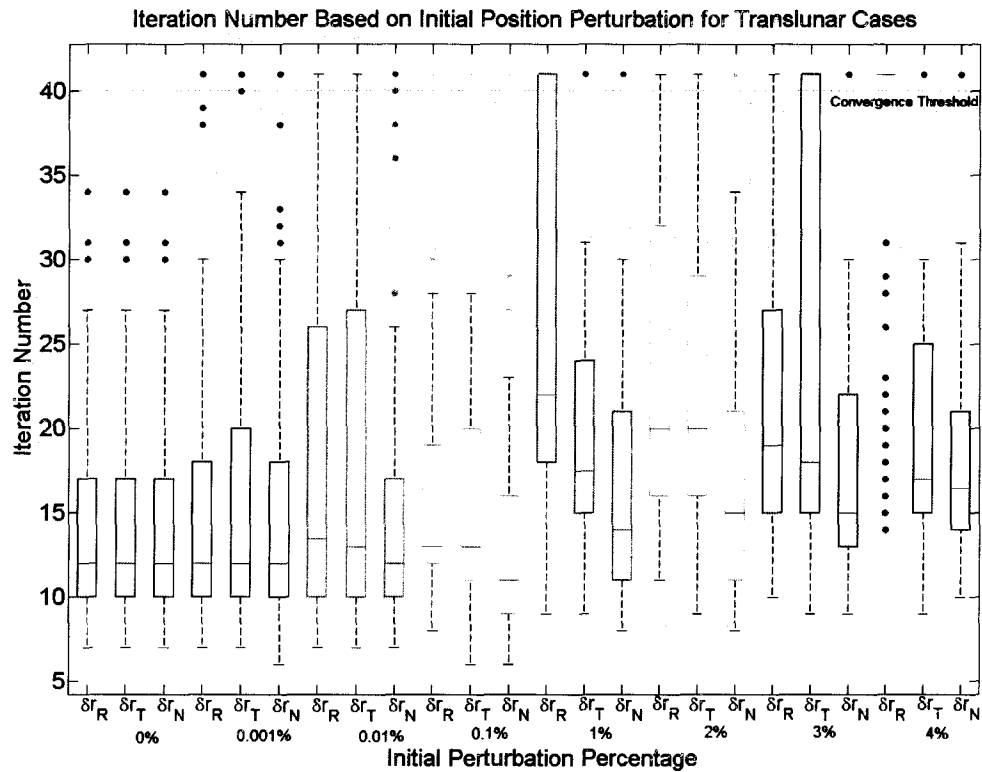


Figure 5.21: Number of iterations based on initial position perturbation percentage for the translunar test cases

set of three columns, results in a few non-converging solutions, however majority converge under 40 iterations. As the perturbation percentage increases, the number of cases failing to converge increases as well. Errors in the radial direction of the position perturbation plots and tangential direction of the velocity perturbation plots result in far more non-converging solutions due to the direction of motion. With a 4% error in the initial radial direction of the position perturbation or 2% error in the initial tangential direction of the velocity perturbation all but a few outlier cases fail.

Further work is conducted on the test cases that result in non-convergent solutions after a certain perturbation to determine if a particular value or range of values for individual parameters produce these results. Observations show that the inclination of the final lunar orbit has the largest effect on whether or not a test case produces a non-convergent solution for initial perturbations between 0.001%-4%. Figure 5.23

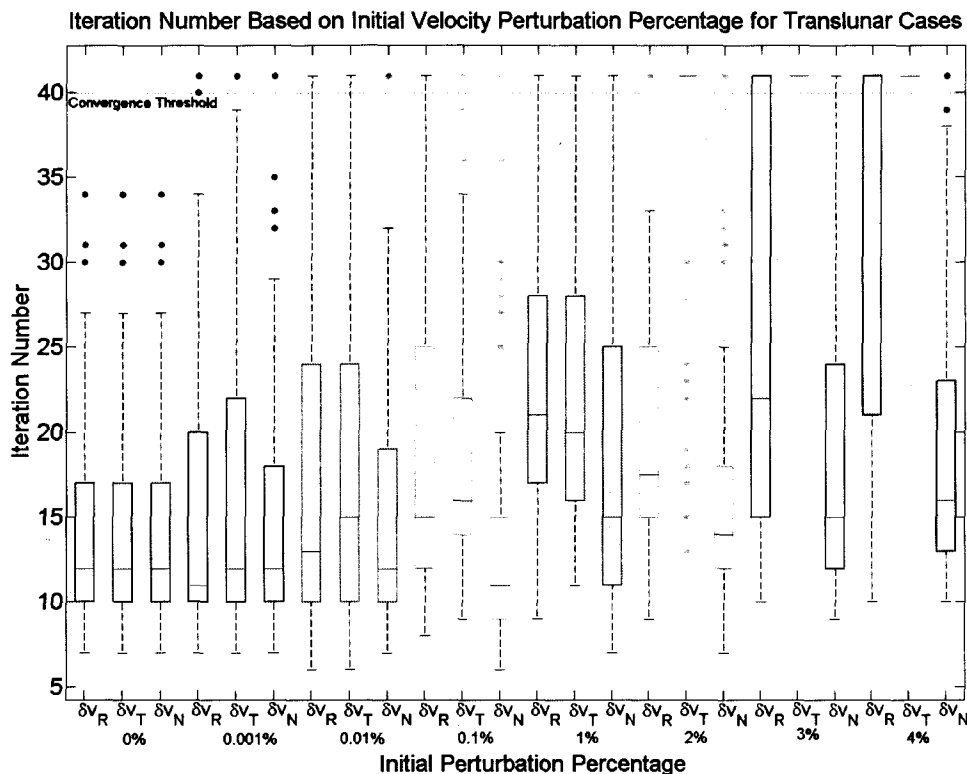


Figure 5.22: Number of iterations based on initial velocity perturbation percentage for the translunar test cases

provides a closer examination of the lunar orbit inclinations in question. The figure shows a tendency for lunar orbits with low prograde inclinations, particularly those between  $\pm 30$  degrees, to have the most difficulty in converging when a perturbation of 0.001% is added. As the perturbation increases, the range of lunar inclinations that result in failing cases increases as well. Eventually, a perturbation of 3% ensures all cases fail. Having already shown that prograde orbits require more iterations, it makes sense that these same orbits would be more likely to fail if perturbations were added further increasing the iteration number. However, what is interesting is that adding very small perturbations, such as 0.001%, only affects the small inclinations. Of the 24 cases that fail with a perturbation of 0.001% in the initial velocity, 21 of the cases have inclinations less than  $28^\circ$ . A possible explanation for the sensitivity of these particular orbits is the effect of the Moon's gravity potential.

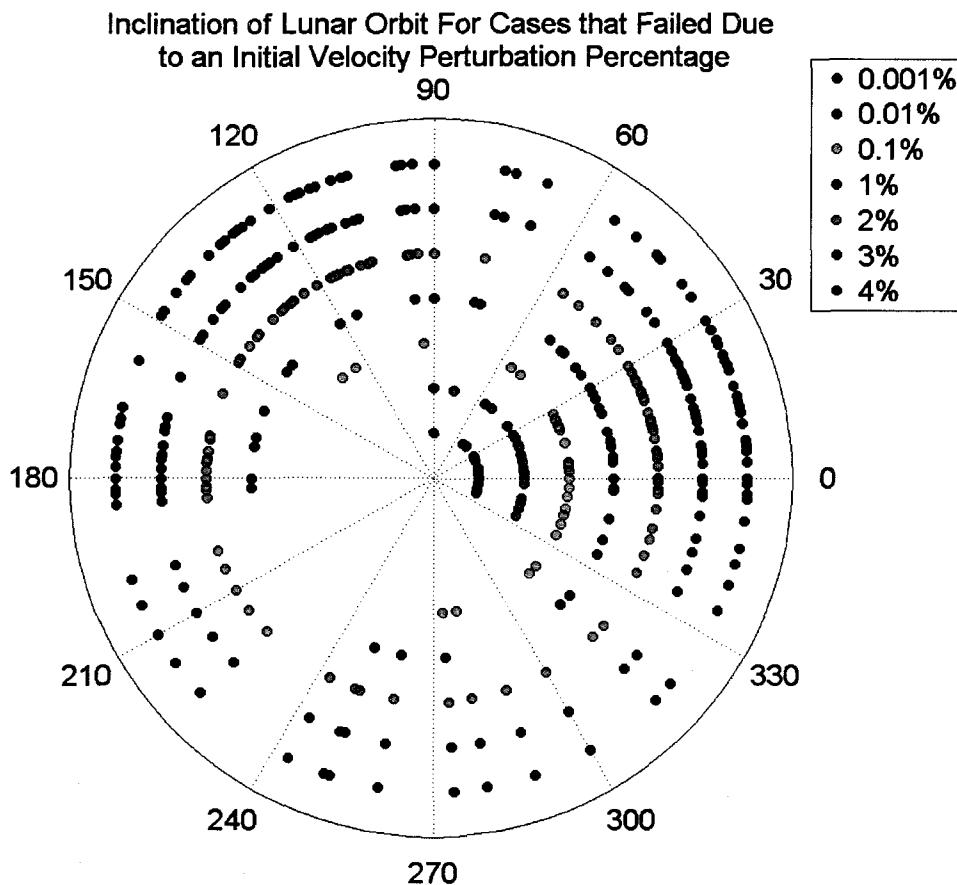


Figure 5.23: Inclinations of lunar orbits that resulted in non-convergent solutions for varying initial velocity perturbation percentages

Like the Earth, the Moon's gravity field is strongest near the equator as a result of  $J_2$ . Figure 5.24 shows the Moon's gravity field up to degree 9 and is created using the same method as Figure 3.5 in Chapter 3. For comparison Figure 5.25 shows the radial gravity field of the Moon expanded to 150 degree order. The figures do not share the same axes thus it is easiest to just compare the relative latitude of the strongest gravity anomalies. The  $J_2$  term in both figures is removed to illustrate the presence of lower order harmonics, however, if  $J_2$  were graphed it would be the strongest force. Even without the dominating force, orbits in low inclinations will be influenced by large gravitational perturbations. Though strong gravity anomalies exist outside of low latitudes on the Moon, the equatorial bulge has the largest continuous cluster of

anomalies. Thus, low inclination orbits that spend the majority of the time over the equator will perturb more than higher inclined orbits. Since the gravity model for EXLX only includes low order gravity coefficients its predicted trajectories will not take into account the anomalies shown in Figure 5.24. The trajectories propagated with the Cowell propagator, however, include the gravity model up to degree 9 and thus will reflect all the anomalies seen in Figure 5.24.

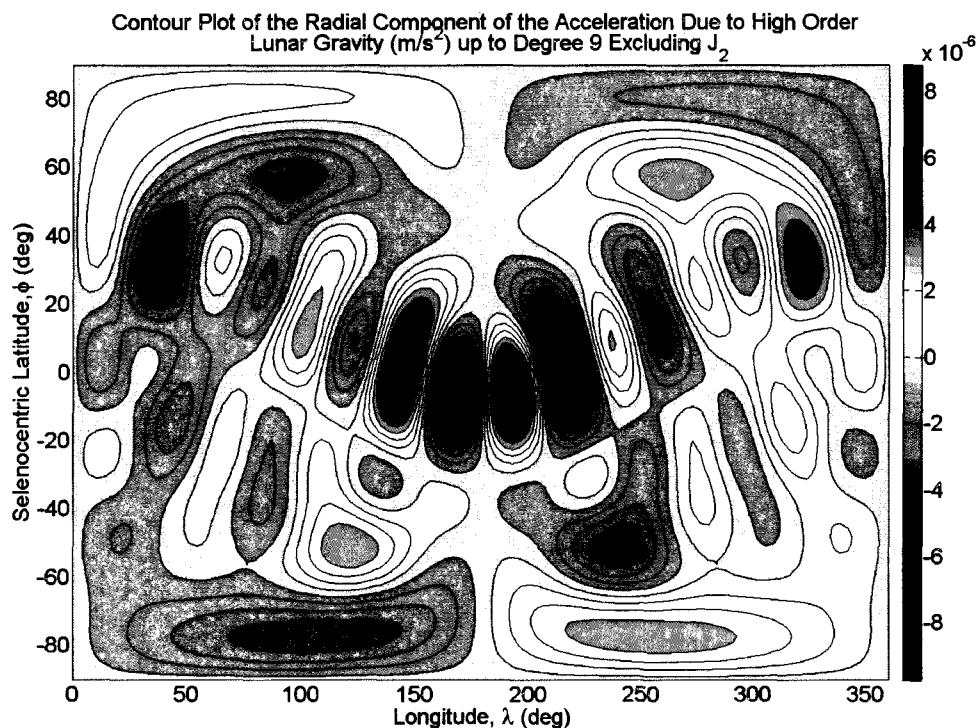


Figure 5.24: Radial component of the gravitational perturbation,  $\mathbf{a}_{J_{3-9}}$  ( $\frac{m}{s^2}$ ), due to lunar higher order gravity up to degree 9 excluding  $J_2$  with respect to latitude/longitude

For situations in which the EXLX trajectory flew through a large gravitational anomaly and the Cowell propagator flew around, it would be difficult, if not impossible to converge in most cases. This is the case with two of the outlier cases, Case #98 and Case #99, with near equatorial final lunar orbits at  $i = 359^\circ$  and  $i = 360^\circ$  respectively. Figure 5.26 and Figure 5.27 highlight the results of the shooting method at the first LOI. The blue line on the plots represent the trajectory of the Moon and the red line is the predicted trajectory output from EXLX. The green lines represent the multiple

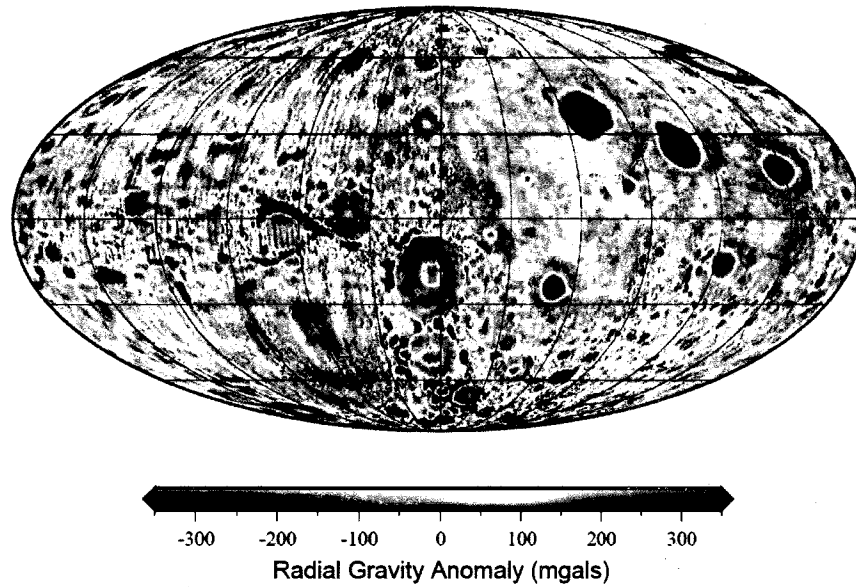


Figure 5.25: Radial gravity field (mGal) of the Moon expanded to degree 150 with the  $J_2$  term removed [51]

attempt trajectories the predictor-corrector tries until it converges within  $1 \times 10^{-6}$  km of the desired final position. The axes are with respect to an Earth centered at (0,0) coordinates. Observing the propagated trajectories near the path of the Moon, it is clear the Cowell propagator is influenced by an acceleration which makes it difficult to follow the predicted EXLX trajectory. In fact, despite both cases having initially prograde final orbits, the converged solution at the first lunar orbit insertion burn puts the vehicle on a retrograde path. This is possible because the shooting method targets a final position vector and not a final velocity vector which would determine the direction of the orbit and whether or not its motion is direct or retrograde.

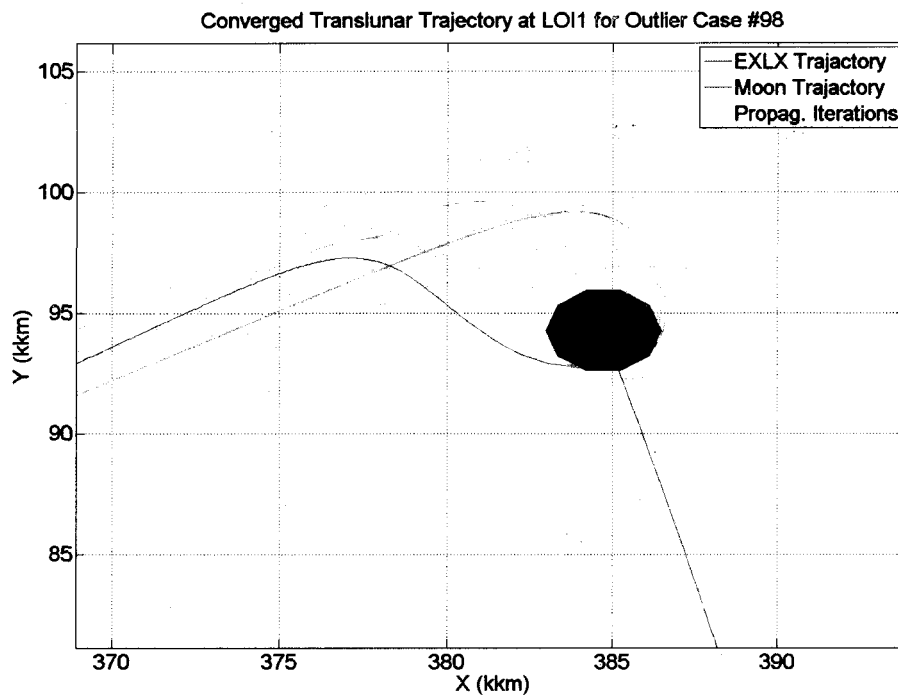


Figure 5.26: Convergence of translunar test Case #98 ,  $i = 359^\circ$ , at LOI1 with 31 iterations

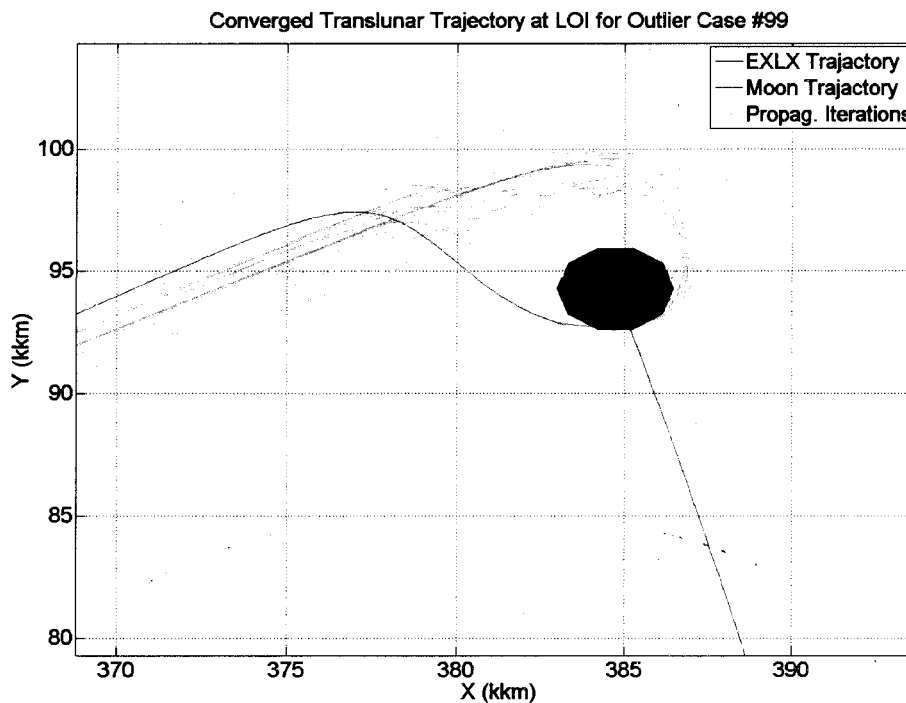


Figure 5.27: Convergence of translunar test Case #99 ,  $i = 360^\circ$ , at LOI1 with 34 iterations



To test the theory that higher order gravity influences the large number of iterations for both cases, 31 and 34 respectively, Case #98 and Case #99 are run through the predictor-corrector again with only the lunar gravity coefficients utilized by EXLX:  $J_{2-4}$  included. The results are seen Figure 5.28 and Figure 5.29. In both cases the iteration number decreases drastically. For Case #98 the number decreases from 31 to 20, for Case #99 from 34 to 18 iterations. The figures also illustrate that removing the higher order lunar gravity coefficients alleviates the issue of the orbit path switching from prograde to retrograde. The remainder of the test cases with final lunar orbit inclinations less than  $25^\circ$  but greater than  $335^\circ$  were run through the same test. A comparison of the iteration number statistics between these cases with and without HOG applied is plotted in a histogram in Figure 5.30. The median value of iterations drops from 18 to 16 with the range for the middle 50% of the data dropping from between 14-22 iterations to between 13.25-18 iterations when HOG is removed. Further, the  $\pm 1.5\text{IQR}$  decreases from 8-34 iterations to 8-21 iterations. This information illustrates the contribution of high order gravity to the sensitivity of the Cowell predictor-tool for final lunar orbits with low inclinations.

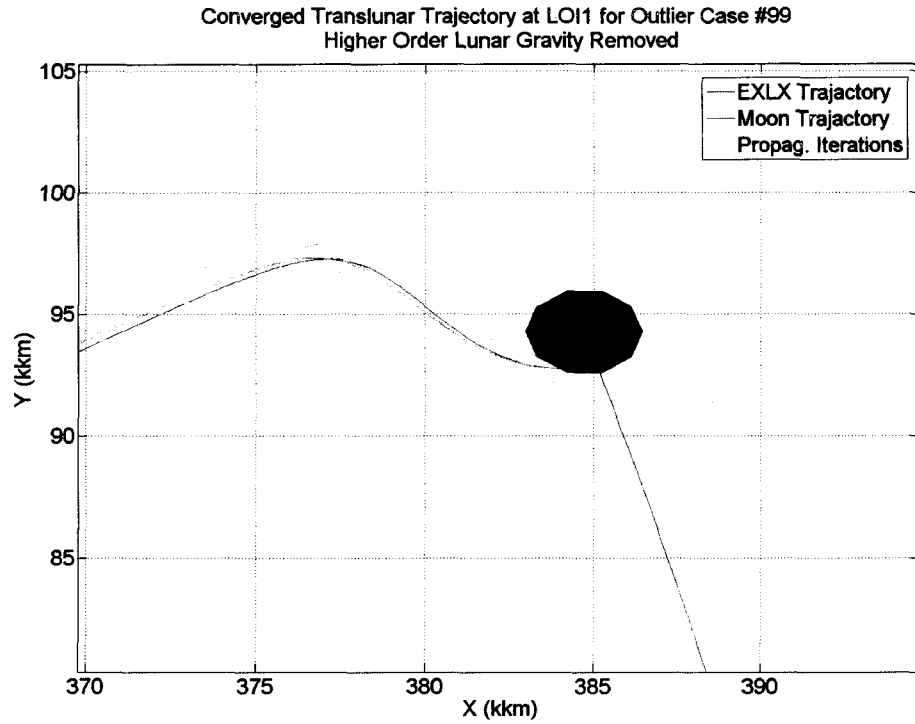


Figure 5.28: Convergence of translunar test Case #98 ,  $i = 359^\circ$ , at LOI1 with 20 iterations after lunar higher order gravity is removed

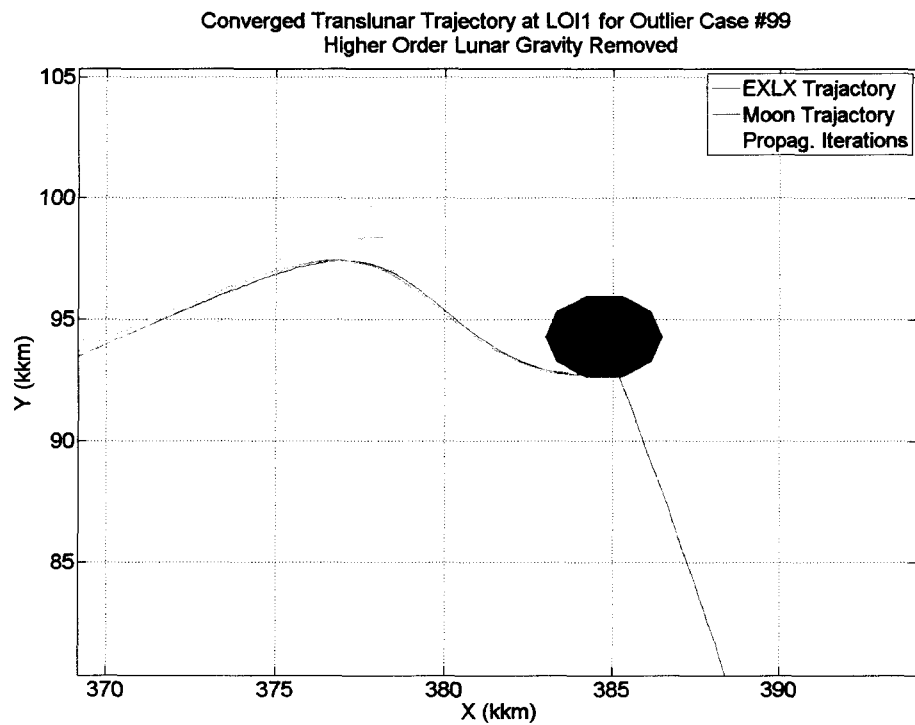


Figure 5.29: Convergence of translunar test Case #99 ,  $i = 360^\circ$ , at LOI1 with 18 iterations after lunar higher order gravity is removed

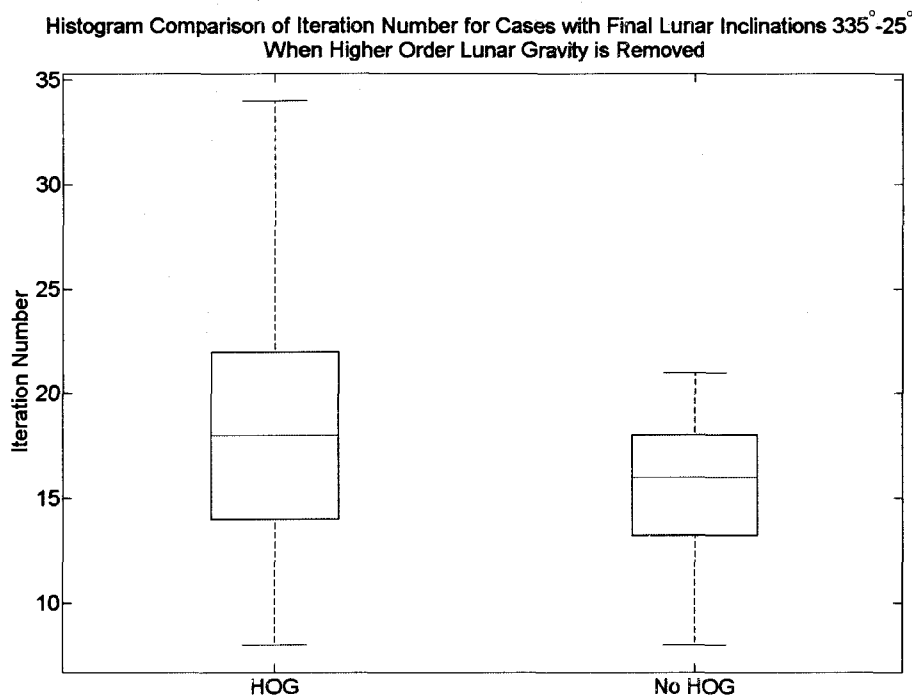


Figure 5.30: Histogram comparing iteration number for test cases with lunar inclinations  $\pm 25^{\circ}$  with and without higher order lunar gravity coefficients applied

## 5.5 Conclusion

The following section details the limitations of the Cowell-STM method for translunar applications as well as summarizes the findings from the test cases.

### 5.5.1 Method Limitations

The Cowell-STM method has two main limitations. The first is that the process does not consider varying time of flight. In searching for the correct transfer velocity to reach a desired location, the process assumes the time of flight is set to the value produced by EXLX and varies the initial velocity accordingly. As a result, feasible but sometimes unrealistic transfers are calculated. This dilemma could be circumvented, and more optimal solutions calculated, if the transfer time were computed as a dynamic parameter.

An additional limitation is that the predictor-corrector method only calculates the transfer velocity for the first LOI burn even though all the transfers tested were three burn maneuvers. In an ideal situation the method would determine the transfer velocity needed for the first burn and using the Cowell propagator compute the final states at LOI1. The states at LOI1 then become the initial conditions to determine the transfer velocity needed to reach LOI2 as predicted by the EXLX multi-conic propagator. This process would continue through LOI3 putting the vehicle in its final lunar orbit. The difficulty in such a method is that any change required in one burn's initial conditions would cause a chain reaction changing the initial conditions of any previous burns. For example, consider the situation in which the TLI transfer velocity to reach LOI1 is calculated and the states are propagated forward in time. From here a second shooting method calculates the transfer velocity from LOI1 to LOI2. However, if the "shoot out" between LOI1 and LOI2 does not place the final position at LOI2 within tolerance, the initial velocity for the LOI1 transfer must be updated. Back propagating the change in velocity from LOI1 to TLI results in a different position and initial velocity. Since the position at TLI cannot change this will require an additional "shoot out" between TLI and LOI1. This iterative process of dealing with more than one transfer burn is known as two-level targeting. One way to alleviate some of the obstacles faced with the complexity of multi-level targeting is to allow the time of flight to vary from the values determined by EXLX. Both the time constraint and multi-level targeting process should be considered for future updates on the Cowell-STM predictor-corrector method.

### 5.5.2 Summary of Test Results

Updating the initial transfer velocity produced by the EXLX multi-conic propagator with the Cowell-STM method identifies a number of sensitivities in the test case selection. Here "sensitivities" are defined as cases that result in a larger than average

number of iterations to converge. The first is the sensitivity of the process to transfers entering into lunar orbits with low inclinations. For many of these cases, low lunar inclinations lead to converged trajectories with retrograde orbits. Inherently, retrograde orbits are not more difficult to transfer into than prograde orbits, hence the sensitivity is linked to the perturbation that causes the transfer to switch from a prograde to retrograde orbit. As is shown, higher order gravity coefficients in the Cowell model result in perturbations close to the Moon that are not predicted by the EXLX multi-conic propagator. As a result, certain trajectories become difficult to follow as the Moon's gravitational pull affects the vehicle motion. In some cases, the converged solution has to switch from a prograde to retrograde orbit in order to meet the final position tolerance. Cases that require a switch in orbit type from the initial guess require a larger iteration number. The removal of higher order gravity from the Cowell method alleviates the high iteration number problem. An additional improvement to the predictor-corrector method to help reduce this sensitivity would be to include some of the lunar low order gravity partials in the state transition matrix. The closer the STM mirrors the Cowell propagator in terms of perturbation models, the less deviation between the two methods and the fewer iterations needed for convergence.

The initial perturbation percentage test illustrates that by perturbing the initial guess provided by EXLX by only 4%, all translunar test cases fail to converge. The fact that such a small perturbation could result in complete failure illustrates how sensitive the predictor-corrector is to the initial guess.

Having tested and validated the performance of the Cowell-STM tool in translunar conditions, the functionality of the predictor-corrector is substantiated by testing low Earth orbit transfer situations.

# Chapter 6

## Low Earth Orbit Application

The higher order propagator is tested on low Earth orbit applications by utilizing the Cowell-STM predictor-corrector method to determine the appropriate delta velocities to transfer from one LEO orbit to another. These cases differ from the translunar cases in two major aspects. The first is the lack of a robust program such as EXLX to predict initial transfer velocities and flight times. The second is the much stronger influence of drag on the vehicle's motion. Chapter 6 begins with a discussion of Lambert's problem and the use of its solution as an initial guess for the transfer velocity between two low Earth orbits. Section 6.2 details the test case selection process, and the final section discusses the performance of the predictor-corrector process as applied to LEO scenarios.

### 6.1 Lambert's Method

Lambert's method forms the basis of the prediction algorithm for low Earth orbit problems. It is an orbit determination technique that given two position vectors and the time of flight, calculates the unknown transfer orbit [22][23],

$$[\mathbf{v}_1, \mathbf{v}_2] = \text{lambert}(\mathbf{r}_1, \mathbf{r}_2, \Delta t). \quad (6.1)$$

Battin derives a formulation for the Lambert problem combining Lagrange's equations from his proof of Lambert's theorem and Gauss's equations from the *Theoria Motus* [7].

### 6.1.1 Lagrange's Equations

Lagrange's form of the transfer-time equation for elliptical orbits is

$$\sqrt{\mu} (t_2 - t_1) = a^{\frac{3}{2}} [(\alpha - \sin \alpha) - (\beta - \sin \beta)], \quad (6.2)$$

with  $\alpha = \phi + \psi$  and  $\beta = \phi - \psi$ . The variables  $\phi$  and  $\psi$  are defined with respect to the eccentric anomalies of the two orbits,  $E_1$  and  $E_2$ , by the equations

$$\cos \phi = e \cos \frac{1}{2} (E_2 - E_1) , \quad (6.3)$$

and

$$\psi = \frac{1}{2} (E_2 - E_1) . \quad (6.4)$$

For fixed geometry, Lagrange's transfer-time equation is a function only of the semi-major axis. However, this poses a problem in that the transfer time is a double-valued function of  $a$ : each pair of conjugate orbits has the same semimajor axis and the derivative of the transfer time with respect to  $a$  is infinite for that value of  $a = a_m$ . Here  $a_m$  is the semimajor axis of the minimum energy orbit. Thus for convenience Equation 6.2 is recast in the form

$$\sqrt{\frac{\mu}{a_m^3}} (t_2 - t_1) = \frac{\alpha - \sin \alpha}{\sin^3 \frac{1}{2} \alpha} - \lambda^3 \frac{\beta - \sin \beta}{\sin^3 \frac{1}{2} \beta}, \quad (6.5)$$

where

$$\lambda = \left( \frac{s - c}{s} \right)^{\frac{1}{2}}, \quad (6.6)$$

and  $c$  is the chord such that

$$c = 2a \sin \psi \sin \phi, \quad (6.7)$$

with

$$\lambda s = a (\cos \psi - \cos \phi). \quad (6.8)$$

A similar transformation for hyperbolic orbits (see Reference [7] for details of the transformation process) exists, specifically

$$\sqrt{\frac{\mu}{a_m^3}} (t_2 - t_1) = \frac{\sinh \alpha - \alpha}{\sinh^3 \frac{1}{2} \alpha} - \lambda^3 \frac{\sinh \beta - \beta}{\sinh^3 \frac{1}{2} \beta}. \quad (6.9)$$

By defining the hypergeometric function  $Q_\alpha$  as

$$Q_\alpha = \begin{cases} \frac{\alpha - \sin \alpha}{\sin^3 \frac{1}{2} \alpha} \\ \frac{\sinh \alpha - \alpha}{\sinh^3 \frac{1}{2} \alpha} \end{cases} \quad (6.10)$$

for elliptic orbits, Equations 6.5 and 6.9 become identical. Thus,

$$\sqrt{\frac{\mu}{a_m^3}} (t_2 - t_1) = Q_\alpha - \lambda^3 Q_\beta \quad (6.11)$$

where  $Q_\alpha$  is a hypergeometric function such that:

$$Q_\alpha = \begin{cases} \frac{4}{3} F\left(3, 1; \frac{5}{2}; \sin^2 \frac{1}{4} \alpha\right) \\ \frac{4}{3} F\left(3, 1; \frac{5}{2}; -\sinh^2 \frac{1}{4} \alpha\right) \end{cases} \quad (6.12)$$

Here the notation refers to that of hypergeometric series:

$$F(\alpha, \beta; \gamma; x) = 1 + \frac{\alpha\beta}{\gamma} \frac{x}{1!} + \frac{\alpha(\alpha+1)\beta(\beta+1)}{\gamma(\gamma+1)} \frac{x^2}{2!} + \frac{\alpha(\alpha+1)(\alpha+2)\beta(\beta+1)(\beta+2)}{\gamma(\gamma+1)(\gamma+2)} \frac{x^3}{3!} + \dots \quad (6.13)$$



If  $x$  and  $y$  are two variables defined as

$$x = \begin{cases} \cos \frac{1}{2}\alpha \\ \cosh \frac{1}{2}\alpha \end{cases} \quad \text{and} \quad y = \begin{cases} \cos \frac{1}{2}\beta \\ \cosh \frac{1}{2}\beta \end{cases}, \quad (6.14)$$

Equation 6.11 becomes

$$\sqrt{\frac{\mu}{a_m^3}}(t_2 - t_1) = \frac{4}{3}F \left[ 3, 1; \frac{5}{2}; \frac{1}{2}(1 - x) \right] - \frac{4}{3}\lambda^3 F \left[ 3, 1; \frac{5}{2}; \frac{1}{2}(1 - y) \right] \quad (6.15)$$

where  $y$  is related to  $x$  by the equation

$$y = \sqrt{1 - \lambda^2(1 - x^2)}. \quad (6.16)$$

The advantage of defining the transfer time as a function of  $x$  is that the problems previously mentioned concerning the definition with respect to the semimajor axis no longer apply. Furthermore, as Figure 6.1 illustrates, the graph of the transfer time as a function of  $x$  for various values of  $\lambda$  is single-valued, monotonic, and adaptable to iterative solutions. Note the value of  $x$  has the following significance:  $-1 < x < 1$  for elliptical orbits;  $x = 1$  for parabolic orbits; and  $1 < x < \infty$  for hyperbolic orbits.

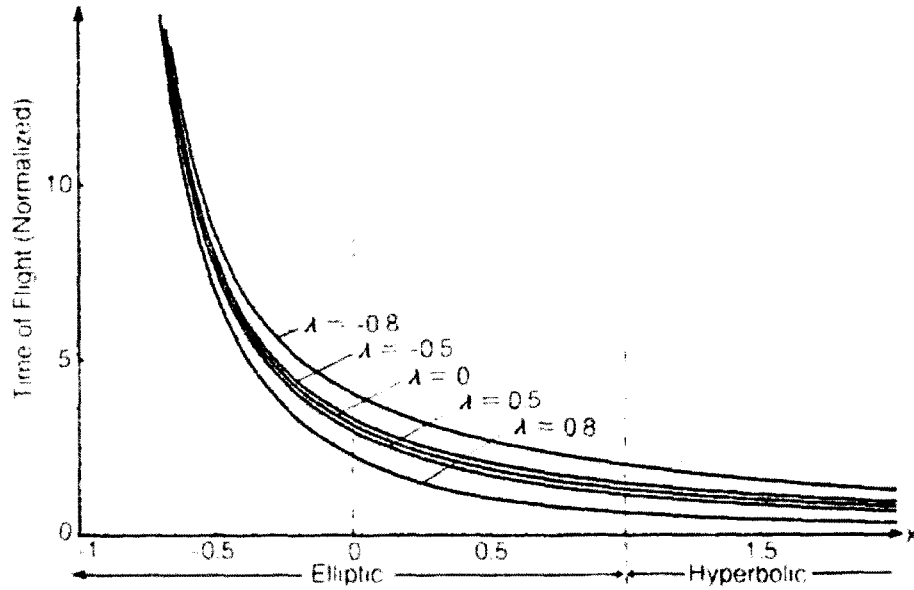


Figure 6.1: Transfer time as a function of  $x$  using Lagrange's equations for the Lambert problem solution [7]

### 6.1.2 Gauss's Formulation

Gauss defined the transfer-time equation for an elliptic orbit as

$$\sqrt{\mu}(t_2 - t_1) = a^{\frac{3}{2}}(2\psi - \sin 2\psi) + 2\lambda s a^{\frac{1}{2}} \sin \psi, \quad (6.17)$$

and for a hyperbolic orbit as

$$\sqrt{\mu}(t_2 - t_1) = (-a)^{\frac{3}{2}}(\sinh 2\psi - 2\psi) + 2\lambda s (-a)^{\frac{1}{2}} \sinh \psi. \quad (6.18)$$

Defining a positive quantity  $\eta$  by the equation

$$s\eta^2 = \begin{cases} 2a \sin^2 \psi \\ -2a \sinh^2 \psi \end{cases}, \quad (6.19)$$

the transfer-time equation is rewritten in the form

$$\sqrt{\frac{\mu}{a_m^3}}(t_2 - t_1) = \eta^3 Q_{2\psi} + 4\lambda\eta. \quad (6.20)$$

With additional transformations

$$\eta^2 = \begin{cases} (1 - \lambda)^2 + 4\lambda \sin^2 \frac{1}{2}\psi \\ (1 - \lambda)^2 - 4\lambda \sinh^2 \frac{1}{2}\psi \end{cases}, \quad (6.21)$$

and the hyperbolic function, one can write

$$Q_{2\psi} = \begin{cases} \frac{4}{3}F\left(3, 1; \frac{5}{2}; \sin^2 \frac{1}{2}\psi\right) \\ \frac{4}{3}F\left(3, 1; \frac{5}{2}; -\sinh^2 \frac{1}{2}\psi\right) \end{cases}. \quad (6.22)$$

Introducing the symbol

$$S_1 = \begin{cases} \sin^2 \frac{1}{2}\psi \\ -\sinh^2 \frac{1}{2}\psi \end{cases}, \quad (6.23)$$

Equation 6.20 can be rewritten as

$$\sqrt{\frac{\mu}{a_m^3}}(t_2 - t_1) = \frac{4}{3}\eta^3 F\left(3, 1; \frac{5}{2}; S_1\right) + 4\lambda\eta, \quad (6.24)$$

where

$$\eta^2 = (1 - \lambda)^2 + 4\lambda S_1 \quad \eta \geq 0 \quad (6.25)$$

and  $0 < S_1 < 1$  for elliptical orbits;  $S_1 = 0$  for parabolic orbits; and  $-\infty < S_1 < 0$  hyperbolic orbits.

Figure 6.2 is a graph of the transfer time as a function of  $-S_1$  for various values of  $\lambda$ . Like Figure 6.1, the curves are monotonic but they are not conducive to iterative solutions as evident in the crossing curves.

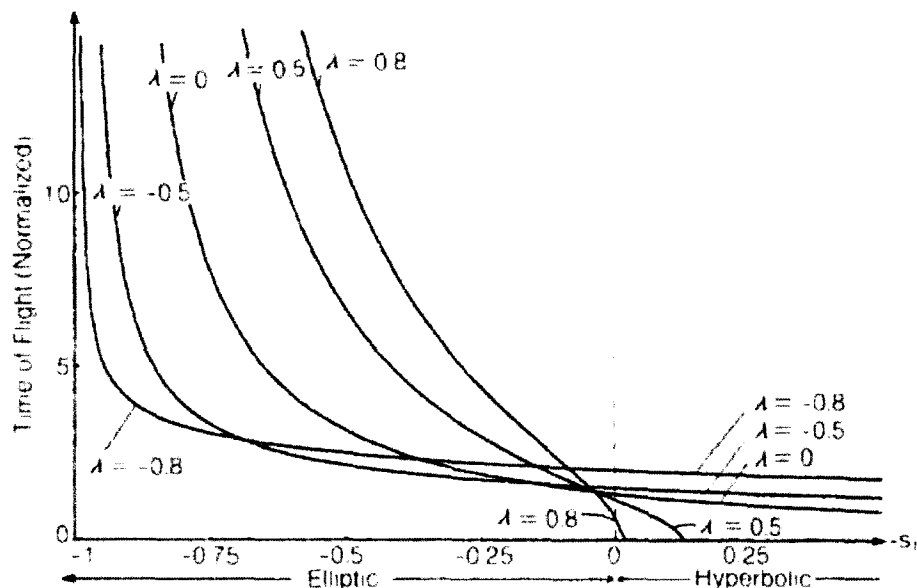


Figure 6.2: Transfer time as a function of  $-S_1$  using Gauss's equations for the Lambert problem solution [7]

### 6.1.3 Battin's Combined Equation

Battin compares both transfer-time formulations by highlighting the benefit of Lagrange's equations for use in iterative schemes, but also the advantage of Gauss's equations in computation efficiency with the calculation of only one hyperbolic function required. By relating  $S_1$  and  $x$  so the advantages of both formulations are realized, Battin concludes his discussion with the following algorithm. The geometry of the Lambert problems leads to the calculation of the parameters

$$2a_m = s = \frac{1}{2}(r_1 + r_2 + c), \quad (6.26)$$

and

$$\lambda s = \sqrt{r_1 r_2} \cos \frac{1}{2} \theta \quad (6.27)$$

where  $c$  is the chord length between the two magnitude position vectors  $r_1$  and  $r_2$ ,

$$c = \sqrt{r_1^2 + r_2^2 - 2r_1r_2 \cos(\theta)} \quad (6.28)$$

and  $\theta$  is the transfer angle between the two position vectors. With an initial guess for  $x$ , as defined in Lagrange's formulation, the following,

$$\begin{aligned} y &= \sqrt{1 - \lambda^2(1 - x^2)}, \\ \eta &= y - \lambda x, \\ S_1 &= \frac{1}{2}(1 - \lambda - x\eta), \end{aligned} \quad (6.29)$$

and

$$Q = \frac{4}{3}F\left(3, 1; \frac{5}{2}; S_1\right) \quad (6.30)$$

are computed where  $F\left(3, 1; \frac{5}{2}; S_1\right)$  is a hypergeometric function which may be evaluated by continued fractions. These values are utilized to find the transfer time from

$$\sqrt{\frac{\mu}{a_m^3}}(t_2 - t_1) = \eta^3 Q + 4\lambda\eta. \quad (6.31)$$

The algorithm is iterated upon using Newton's method (see Reference [7]) until a desired convergence is acquired. The velocity vector at the initial position in terms of the value  $x$  found is

$$\mathbf{v}_1 = \frac{1}{\eta} \sqrt{\frac{\mu}{a_m}} \left\{ \left[ 2\lambda \frac{a_m}{r_1} - (\lambda + x\eta) \right] \mathbf{i}_{r_1} + \sqrt{\frac{r_2}{r_1}} \sin \frac{1}{2}\theta \mathbf{i}_h \times \mathbf{i}_{r_1} \right\}, \quad (6.32)$$

where  $\mathbf{i}_{r_1}$  is the unit vector in the direction of  $\mathbf{r}_1$  and  $\mathbf{i}_h$  is the unit vector normal to the orbital plane. Figure 6.3 summarizes the Lambert 2-body dynamic formulation in an algorithm flow chart. The output of the formulation is used as the initial transfer velocity guess for low Earth orbit calculations.

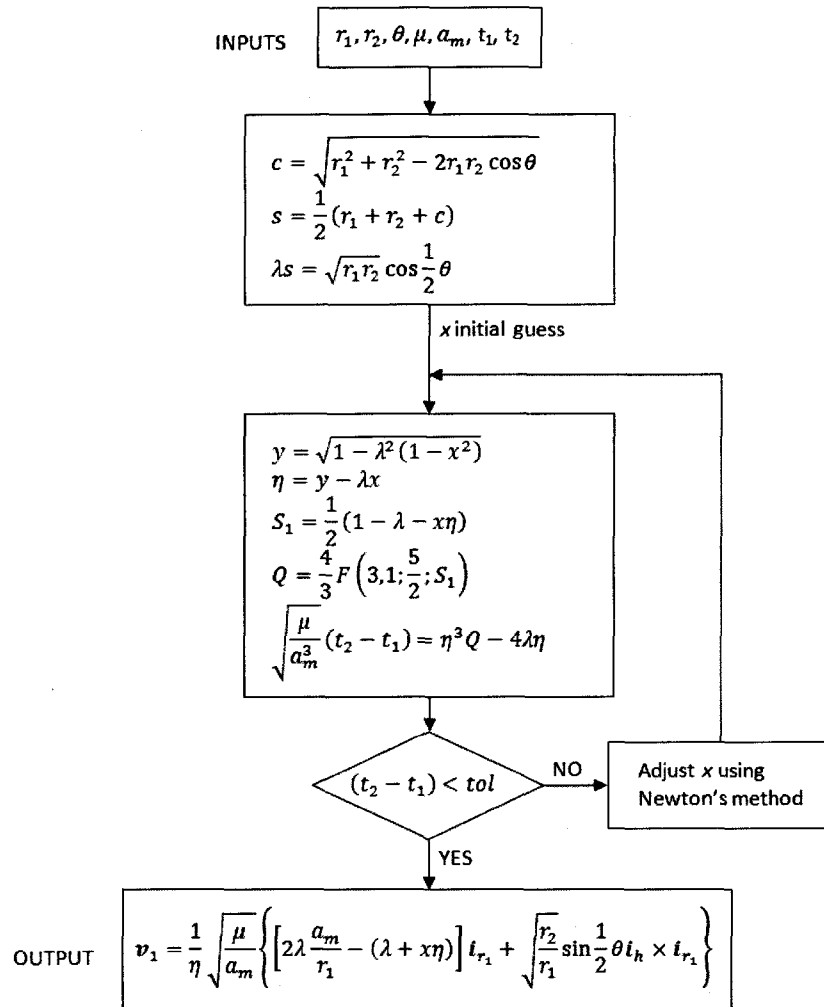


Figure 6.3: Flow chart summary of Lambert 2-body dynamic formulation

## 6.2 Test Case Selection

The test cases are selected over a variety of low Earth orbits. Unlike the translunar test cases which restrict varying only the inclination and the ascending node of the orbits, the low Earth orbit cases give leeway to vary any of the orbital elements. The parameters of the initial and final orbit are varied as highlighted in Table 6.1.

Parameter	Initial Orbit	Final Orbit
altitude	100 km	300-500 km
$e$	0-0.9	0-0.9
$i$	$0^\circ - 90^\circ$	$0^\circ - 90^\circ$
$\Omega$	$0^\circ$	$0^\circ$
$\omega$	$0^\circ$	$0^\circ$
$\nu$	$135^\circ - 225^\circ$	$0^\circ$

Table 6.1: Variation in initial and final orbit parameters for testing LEO cases

Realistically, low Earth orbit transfers occur between similar orbits with differing altitudes and phasing angles. As a result, no cases with drastically different initial and final orbits, such as a transfer between a polar and equatorial orbit, are tested. Transfers such as these are also not tested because they are prohibitively expensive to achieve with a single burn and only 2-burn sequences were tested in this thesis. Instead, the altitude of the initial orbit is set at 100 km with the final altitude varying as defined in Table 6.1. The eccentricities and inclinations of both orbits are set equal. The right ascension of the ascending node is set to  $0^\circ$  for both orbits and the true anomaly of the initial orbit is varied to ensure a realistic transfer angle. The true anomaly angle is varied  $\pm 45^\circ$  off the basic Hohmann transfer angle of  $180^\circ$ . Preliminary testing highlights a convergence issue with transfer angles of exactly  $180^\circ$ , thus angles of  $180^\circ \pm 2$  but never exactly  $180^\circ$  are tested. A discussion of this limitation is in Section 6.4.1. The two-body Lambert formulation as discussed in Section 6.1.1 is used to calculate the initial delta velocity. Examples of the low Earth initial and final orbits for a variety of inclinations and eccentricities tested are illustrated in Figure 6.4. Figure 6.5 depicts a range of transfer angles tested as well.

Lambert calculations require orbit transfer times and though determining the time of flight (TOF) is not central to this research, a feasible value is required to test low Earth orbit cases. The time of flight is found using a rudimentary guess and check iterative procedure. The time of flight is initially set to a number with a large enough value so to provide enough time to transfer between the two orbits,

Example of Tested LEO Orbits Over a Variety of Eccentricities and Inclinations

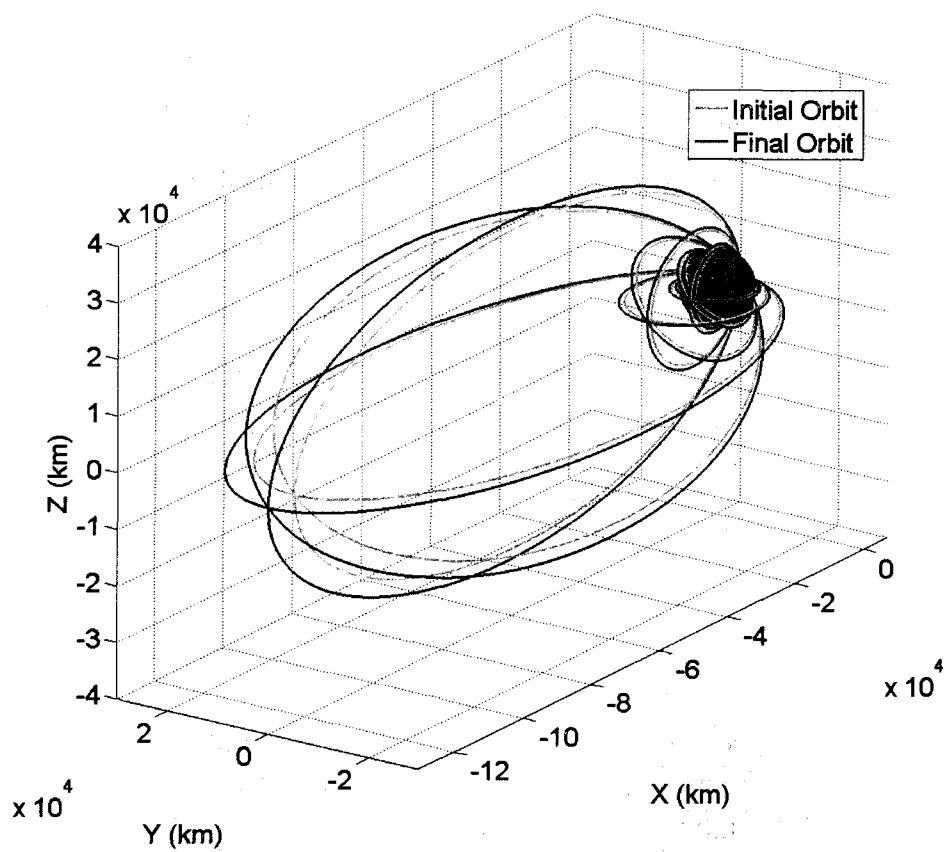


Figure 6.4: Example of low Earth initial and final orbits for a variety of eccentricities and inclinations



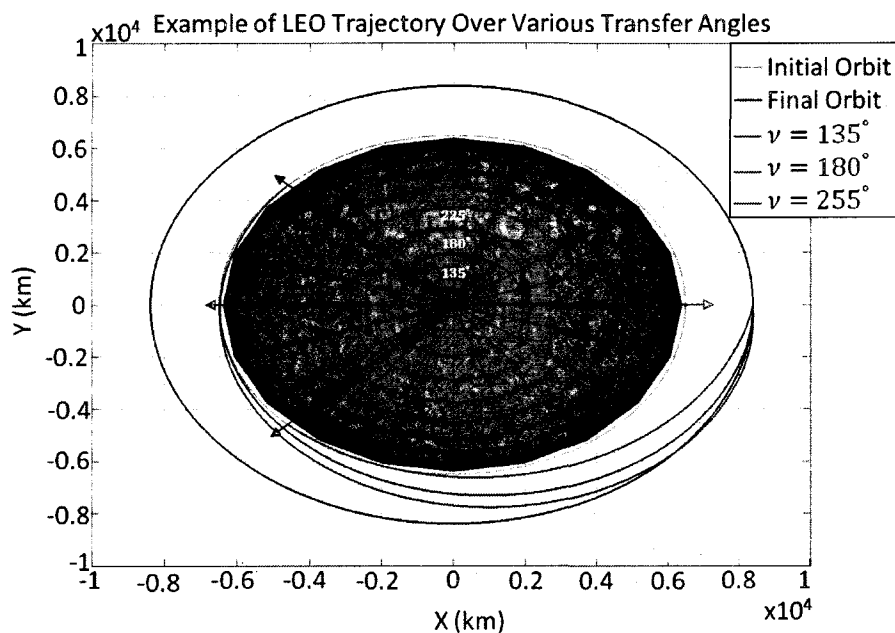


Figure 6.5: Example of the range of transfer angles tested for low Earth orbit trajectories

but realistically would never be flown. The trajectory is then flown out with the delta velocity predicted by Lambert using the Cowell propagator. If the trajectory is feasible, the time is decreased and flown out again. This process is repeated until a time of flight is tested that could not be flown out by the propagator due to the infeasibility of reaching a desired location in a short amount of time. In cases such as these the trajectory would tend to fly through the Earth instead of around it. The time prior to the infeasible test is selected as the transfer time. This process can be summarized as a linear search. Due to the large variety of orbit types, a range of transfer times is selected. The variation in time between each orbit is based on the eccentricity and true anomaly. Table 6.2 lists the time of flight selected for orbits that fell within the parameters highlighted. Note that the TOFs selected are not necessarily optimal but provide a feasible value for the Lambert routine given that all perturbations to include higher order gravity, n-body motion, drag, and solar radiation pressure are included.

<b>e</b>	<b><math>\nu</math></b>	<b>TOF</b>
0-0.01	135°	4,000 sec
	155°	3,625 sec
	175° – 185°	3,250 sec
	205°	2,875 sec
	225°	2,500 sec
0.1	135°	5,000 sec
	155°	4,625 sec
	175° – 185°	3,850 sec
	205°	3,075 sec
	225°	2,700 sec
0.5	135°	13,000 sec
	155°	10,000 sec
	175°	9,000 sec
	178° – 179°	8,500 sec
	181° – 182°	8,000 sec
	185°	7,500 sec
	205°	6,000 sec
	225°	4,000 sec
0.9	135°	200,000 sec
	155°	160,000 sec
	175°	104,000 sec
	178°	91,000 sec
	179°	90,500 sec
	181°	80,500 sec
	182°	80,000 sec
	185°	70,000 sec
	205°	25,000 sec
	225°	10,000 sec

Table 6.2: List of time of flights used for Lambert routine based on orbital elements

### 6.3 Results and Analysis

Using the same MATLAB ODE solvers as for the translunar test cases, 1050 low Earth orbit cases are tested using the Cowell predictor-corrector. All of the cases except 53 converge. A histogram of the iteration numbers plus statistical data for the test cases is plotted in Figure 6.6. There are 46 outlier cases not including the failed cases. Of the outlier cases 35 are within a range of 10-15 iterations. The maximum iteration number for all cases tested, excluding the failed cases is 32 iterations.

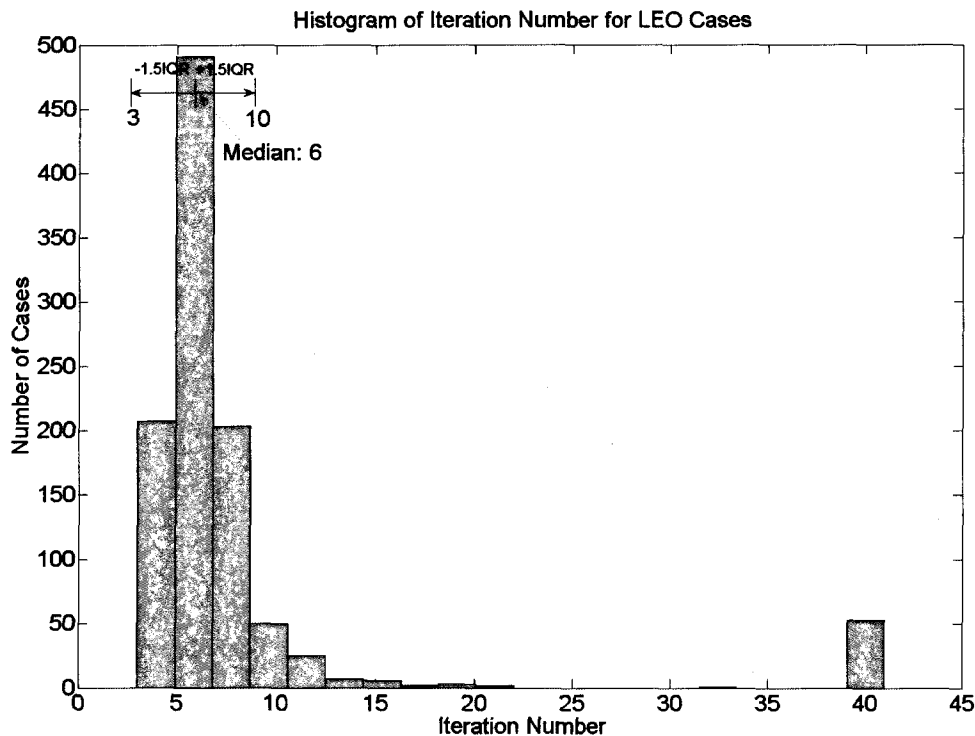


Figure 6.6: Histogram of the iteration number for the 1050 low Earth orbit test cases

The convergence trend of a number of the cases as well as the range of outlier cases is highlighted in Figure 6.7. Similar to the trend seen with the translunar convergence rates, those cases that require more iterations were a result of early oscillating values of  $|\Delta R|$  or iterative procedures that took multiple very small tests. For example, the oscillating case requiring 22 iterations began with a  $|\Delta R|$  of 44 km on the first attempt but on the second iteration produced a  $|\Delta R|$  of 327 km. The oscillations continued for 17 iterations until the magnitude of the position vector became small enough for the STM corrector to calculate a velocity that would put the final position vector in a much closer range to the desired location. Likewise, the case that has the largest number of iterations outside of failing cases at 32, drops to below 1 km after 4 iterations but then proceeds to take 28 very small steps until it converges. The cases that produce these difficult convergence trends are analyzed next.

To determine which test case parameters have the greatest effect on producing

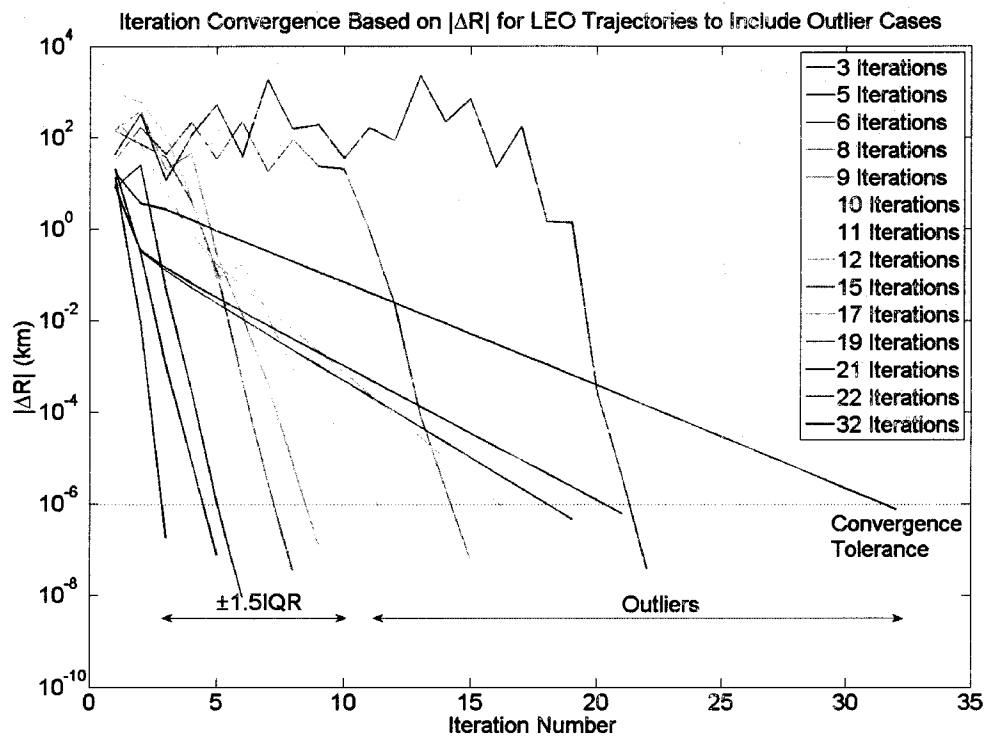


Figure 6.7: Convergence rate for a range of LEO cases with iteration numbers within 1.5IQR as well as the range of the outlier cases

outlier and failing solutions, histograms of individual parameter data are plotted. The results are found in Figures 6.8-6.11. Figure 6.8 illustrates no correlation between iteration number and altitude in that an almost equal number of all three altitudes tested fall into the outlier and failing category. In looking at the effects of eccentricity, Figure 6.9 highlights that cases with the largest eccentricity of 0.9, produce the most outlier and failing cases. This seems to be a result of the large transfer time. As the error in the state transition matrix increases over time it becomes more difficult to accurately update the velocity on each “shoot out” attempt resulting in more iterations. From Figure 6.10, the ease in which equatorial and polar orbits quickly converge is highlighted. From the 150 cases tested for each inclination, only 7 cases with an inclination of  $0^\circ$  and 4 cases with an inclination of  $90^\circ$  result in outlier or failing cases. This is because orbits with motion in only two planes tend to stay in those planes during convergence attempts, thus reducing the complexity of the

problem. This topic is discussed in more detail in Section 6.4.1. Finally, Figure 6.11 re-illustrates the issue with  $180^\circ$  transfers in that of the 99 outlier and failing cases 83 were from transfer angles of  $180^\circ \pm 2^\circ$ .

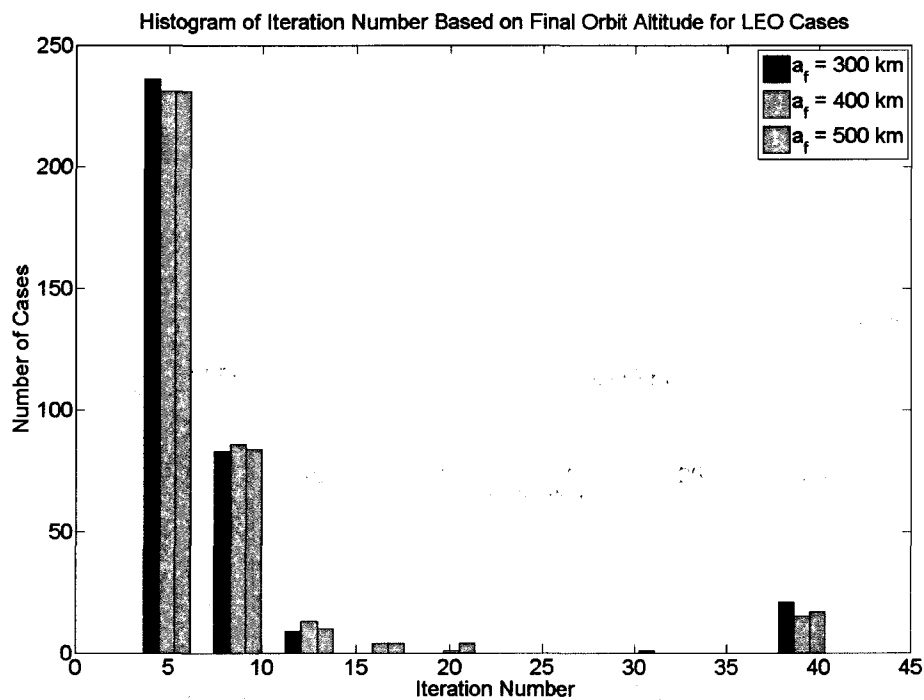


Figure 6.8: Histogram of iteration numbers based on final low Earth orbit altitude

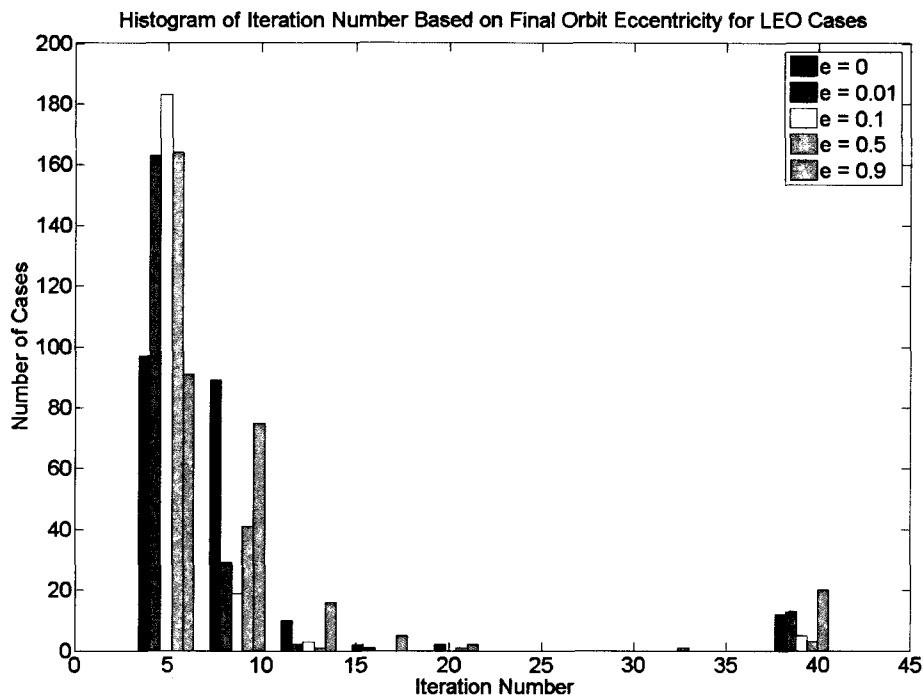


Figure 6.9: Histogram of iteration numbers based on initial/final low Earth orbit eccentricity

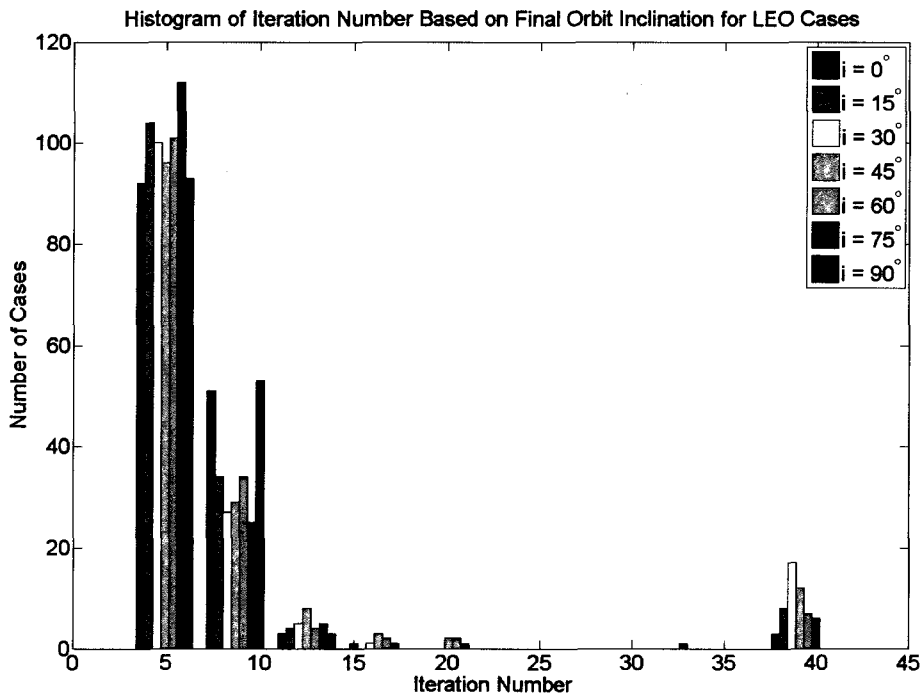


Figure 6.10: Histogram of iteration numbers based on initial/final low Earth orbit inclinations

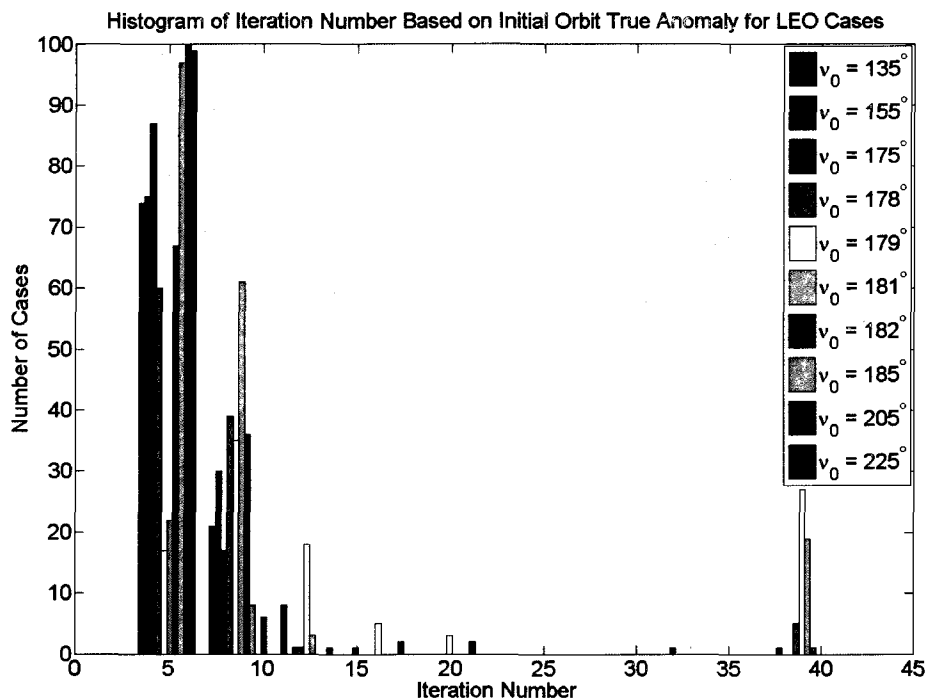


Figure 6.11: Histogram of iteration numbers based on initial low Earth orbit true anomalies

As with the translunar test cases, a point of interest is the change in velocity from the initial Lambert two-body guess the predictor-corrector determines is necessary to hit the desired final location in low Earth orbit. Figure 5.19 is a histogram showing the number of cases that fall into each range of  $|\Delta V|$ . All cases that fail to converge are given a velocity value of 1 km/s for plotting purposes. 156 outlier points exist outside the 53 failing cases, which is over three times the number of outlier cases produced when just looking at the iteration number. An interesting fact to note is how much larger the  $|\Delta V|$ s for the LEO cases are compared to the translunar cases. This underscores the higher fidelity of EXLX as a transfer velocity predictor compared to the Lambert routine for their respective transfer missions. This observation is not a surprise since EXLX includes 4-body motion and  $J_2$ - $J_4$  gravity coefficients whereas Lambert only assumes two-body motion with no perturbations.

In Figures 6.13-6.16 histograms illustrate the effect varying parameters have on the change in velocity. Figure 6.13 shows there is no correlation between the change in

velocity and the final altitude in that all altitudes tested produce the relatively same number of outliers. The trend in eccentricity changes in Figure 6.9 in that the three smallest eccentricities result in the largest velocity change. This is due to the fact that drag has the strongest effect at low altitudes which orbits with low eccentricities will maintain the longest. Since the Lambert transfer velocity does not consider drag in its calculations, a much stronger thrust is necessary to counter the perturbation. In observing how inclination played a role in effecting the  $|\Delta V|$  it is apparent that the Lambert routine calculates the most accurate transfer velocities for equatorial and polar orbits in that only 3 cases with an inclination of  $0^\circ$  and no cases with an inclination of  $90^\circ$  produce outlier or failing results. Figure 6.16 reiterates the point that transferring  $180^\circ$  is the most difficult transfer angle. All but one case with an initial true anomaly of  $\pm 2^\circ$  off a perfect Hohmann  $180^\circ$  transfer results in outlier or failing cases.

Comparing Figures 6.8-6.16, it is seen that higher iteration numbers do not necessarily equate to higher delta velocities. For the 103 outlier velocity cases that do not include failing cases only 20 have iteration numbers greater than 10. The case with the highest number of iterations, 32, has only a velocity change requirement of 0.00409 km/s where one case that converges in 8 iterations has a velocity change of 0.6249 km/s. Thus orbits with high velocity changes do not necessarily indicate difficult transfers for the Cowell predictor-corrector method. Instead, orbits with large velocity changes are those that the Lambert routine has difficulty predicting accurate initial transfer velocities for.

As with the translunar test cases, the low Earth orbit cases are tested over a range of initial perturbation percentages to determine the sensitivity of the initial guess. These results are plotted in Figure 6.17 for the position perturbations and Figure 6.18 for the velocity perturbations. For perturbations below 1% the position and velocity perturbations results are very similar in that around the same number of



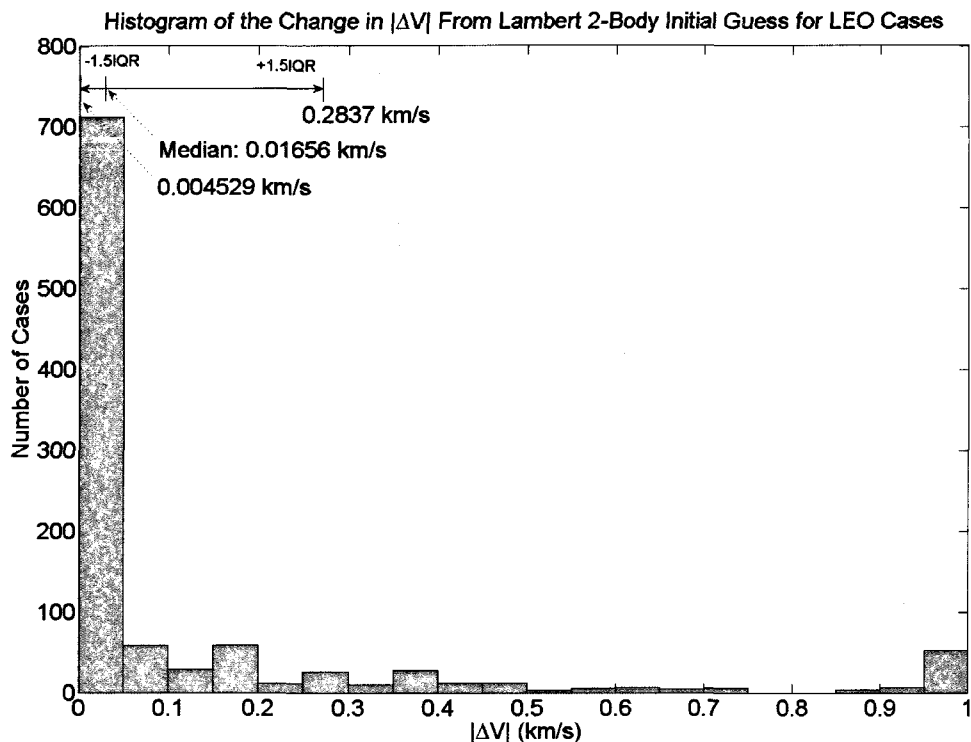


Figure 6.12: Histogram of the change in  $|\Delta V|$  required for the low Earth orbit test cases

cases fail for each. For example, at 0.01% 26 cases fail due to an initial perturbation in the position and 31 fail due to a perturbation in the velocity. At 0.1% these numbers are 30 and 37 respectively. The lower perturbation percentages also underscore the trend of inclination and true anomaly having the largest impact on the convergence of cases. Below 0.1% no equatorial or polar cases fail and only those with true anomalies of  $179^\circ$  or  $181^\circ$  fail. As the perturbations grow larger it becomes apparent that perturbations in the initial position vector result in more failing cases than those with perturbations in the initial velocity vector. At 1% error the number of failing cases for the position perturbation is 149 compared to only 61 with the velocity error. For 3% the number of failing cases is 266 and 119 for an initial position and velocity error respectively.

Also interesting to note is that it takes a 3% error in the initial velocity vector to cause orbits with inclinations of  $0^\circ$  or  $90^\circ$  to fail, where a perturbation of only 0.1%

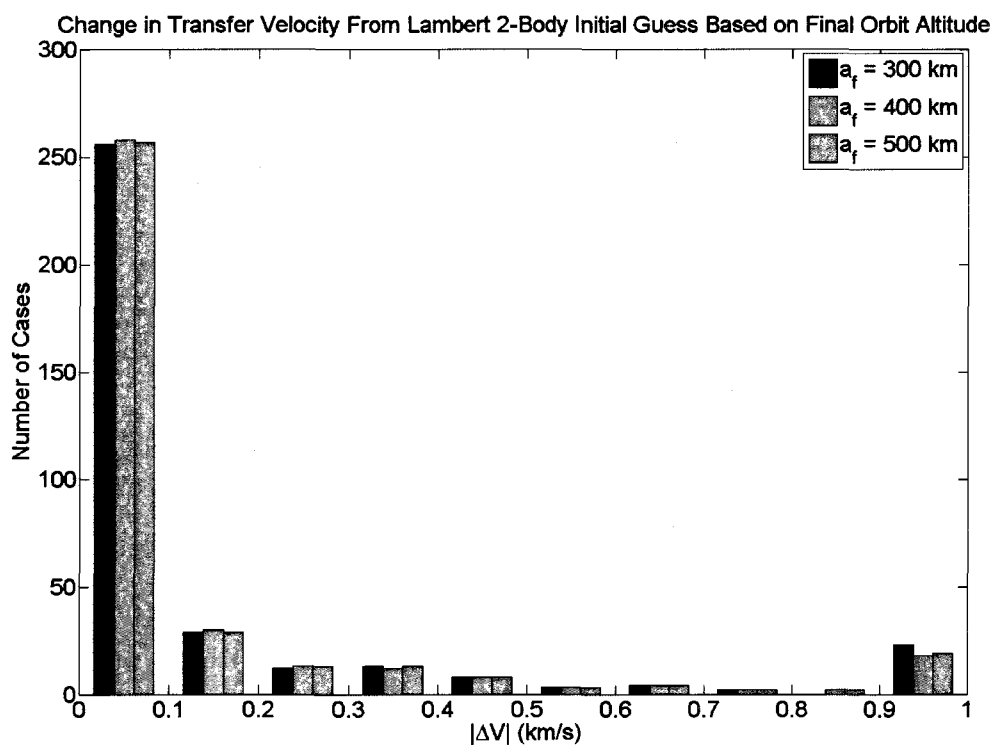


Figure 6.13: Histogram of LEO cases comparing change in transfer velocity from two-body Lambert initial guess based on final orbit altitude

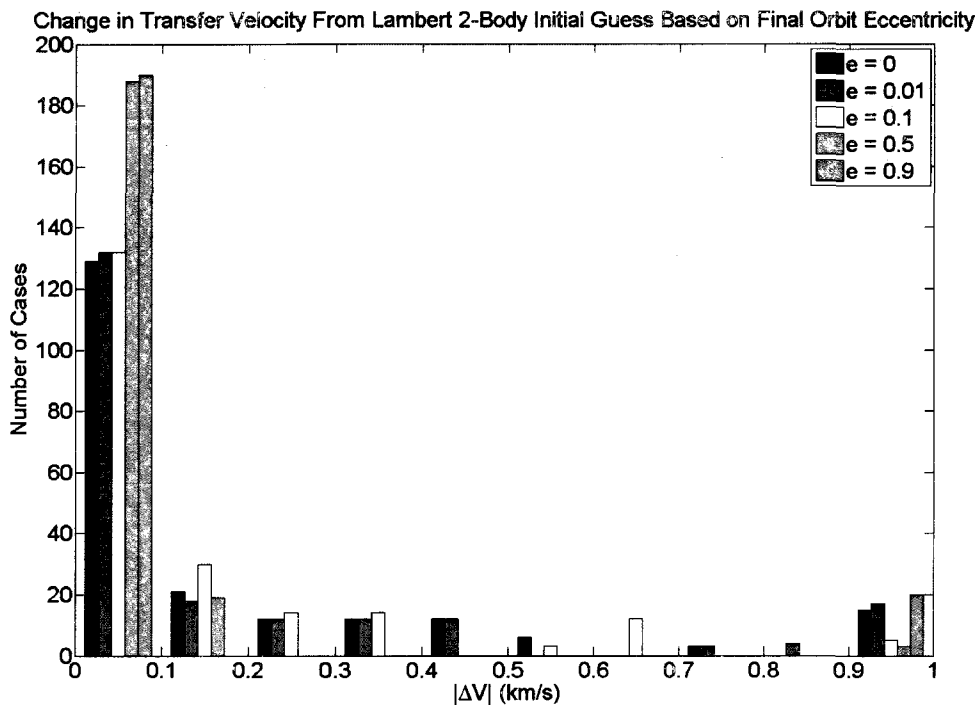


Figure 6.14: Histogram of LEO cases comparing change in transfer velocity from two-body Lambert initial guess based on initial/final orbit eccentricity

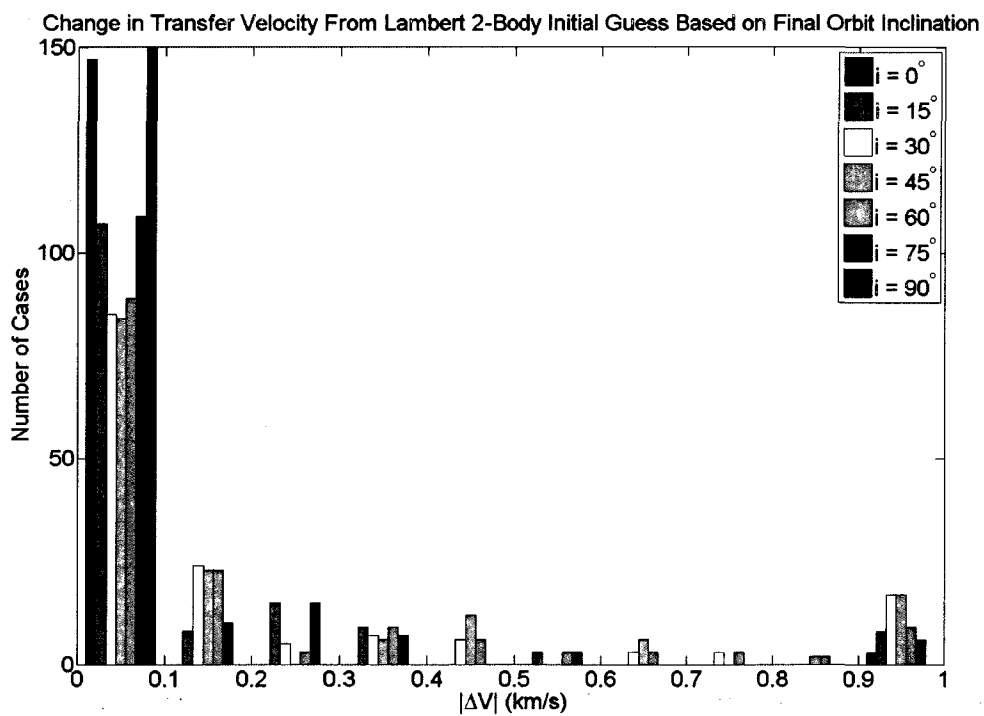


Figure 6.15: Histogram of LEO cases comparing change in transfer velocity from two-body Lambert initial guess based on initial/final orbit inclination

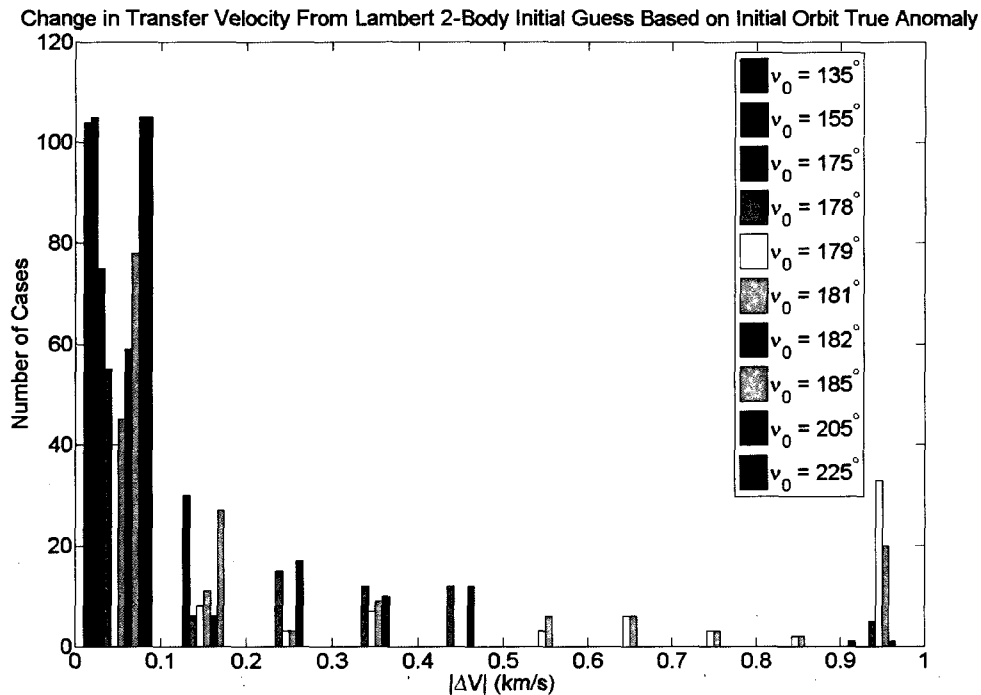


Figure 6.16: Histogram of LEO cases comparing change in transfer velocity from two-body Lambert initial guess based on initial orbit true anomaly

in the position vector results in 6 failing cases with equatorial orbits and 6 failing cases with polar orbits. The sensitivity to perturbations in the position vector may be explained by the fact that the predictor-corrector method can make updates to the initial velocity for each iteration but not the initial position as it is assumed constant. Thus, the initial transfer velocity computed by Lambert is based on the assumption that  $\mathbf{r}_0$  does not change. Even with a slightly inaccurate velocity guess, the Cowell-STM algorithm can correct and update the initial velocity in order to reach the final desired position. However, a perturbation in the initial position can only be corrected to a certain degree by changing the velocity before the deviation becomes too large to reach a converged solution. Again this illustrates that a better initial guess results in better convergence due to the linear assumptions of the state transition matrix.

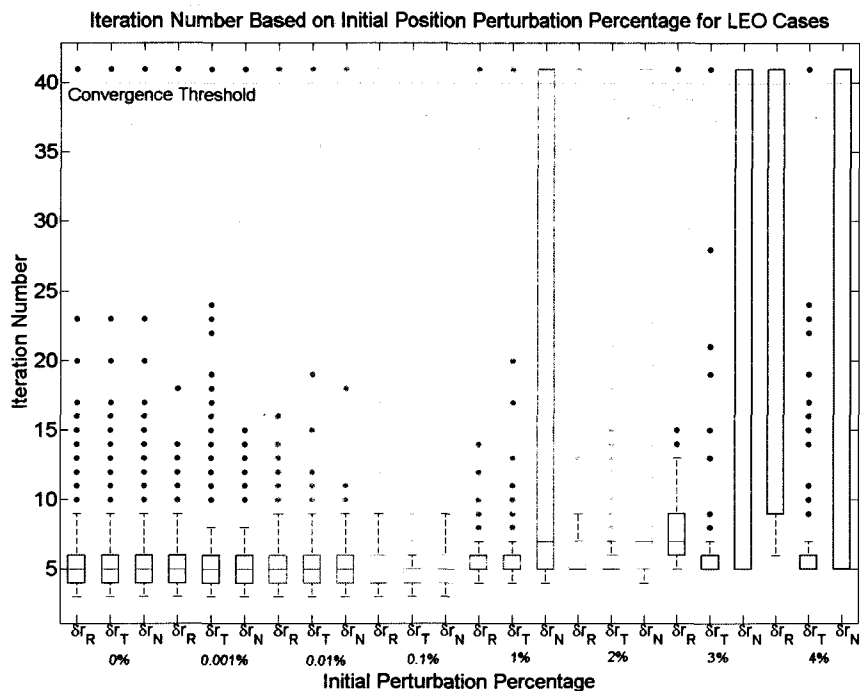


Figure 6.17: Number of iterations based on initial position perturbation percentage for the LEO test cases

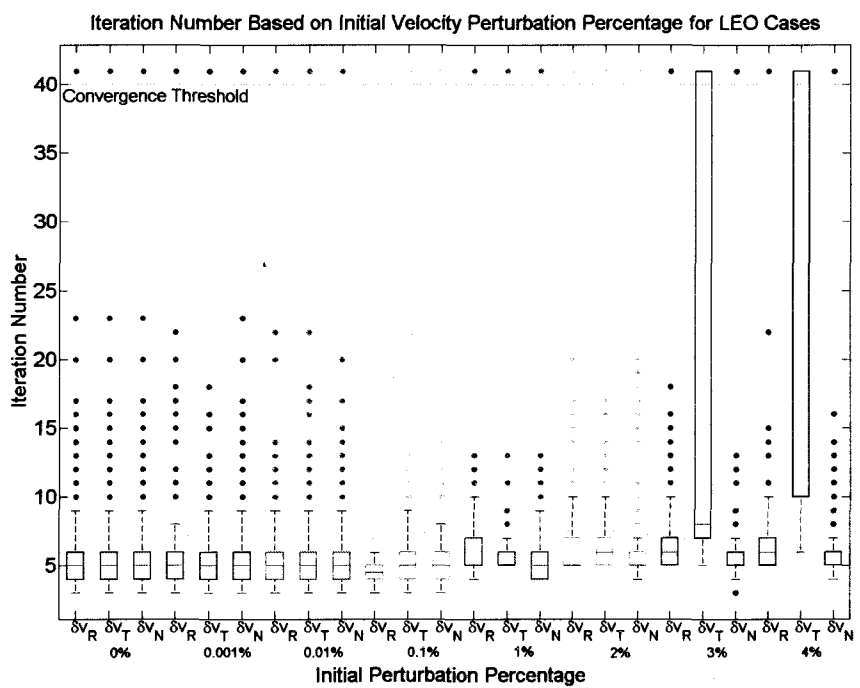


Figure 6.18: Number of iterations based on initial velocity perturbation percentage for the LEO test cases

## 6.4 Conclusions

The following section details the limitations of the Cowell-STM method for low Earth orbit transfer applications as well as summarizes the findings from the test cases.

### 6.4.1 Method Limitations

One major limitation on the predictor-corrector method for low Earth orbits is its inability to handle perfect  $180^\circ$  transfers. For orbits with  $\Delta\nu = 180^\circ$ , a transfer solution is difficult to determine because multiple answers produce the same final position vector. Furthermore, the plane of the transfer orbit is not uniquely determined and thus an infinite number of paths are feasible. Figure 6.19 shows an example of an attempt to transfer  $180^\circ$  between two circular orbits at an inclination of  $30^\circ$ . The predictor-corrector attempts multiple trajectory paths over a range of planes before hitting the maximum number of iterations. The initial trajectories are those plotted in blue which each successive attempt plotted in a warmer color with the last iteration in red. The trend of the 40 trajectories illustrates the corrector attempting trajectories further out of plane from the initial guess each try. By the last failing correction, the trajectory is over  $90^\circ$  out of plane compared to the initial Lambert 2-body guess. For two unique orbits the predictor-corrector can handle  $180^\circ$  transfers. These transfers are for equatorial ( $i = 0^\circ$ ) or polar ( $i = 90^\circ$ ) orbits. Orbits with these characteristics have motion in only two planes: an equatorial orbit has no motion in the z-plane and a polar orbit has no motion in the x-plane. As the Cowell method makes corrections to the initial velocity it does so keeping each propagation within the correct two planes. Hence, unlike the case illustrated in Figure 6.19 where the predictor-corrector guesses trajectories outside of the initial orbit plane, guesses made for equatorial or polar orbits stay in plane. Reducing the extra complexity in motion, the tool is able to converge at a much quicker rate. This is not the case for

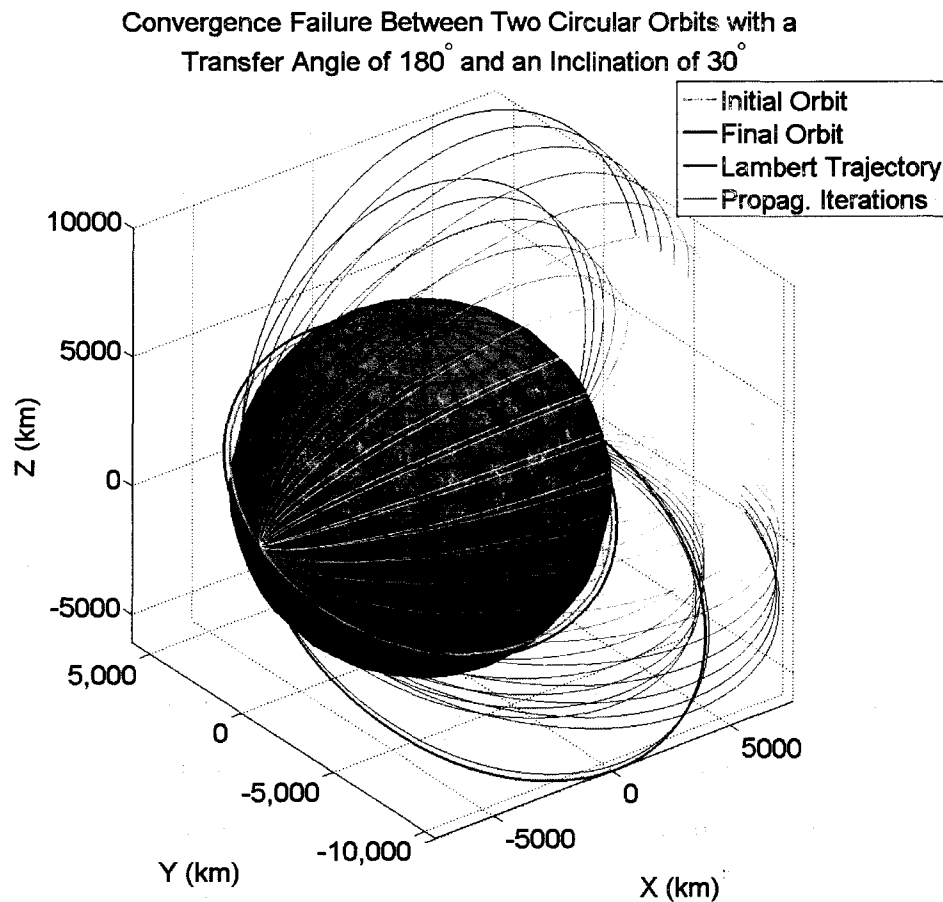


Figure 6.19: Convergence failure for a LEO trajectory between two circular orbits with a transfer angle of  $180^\circ$  and an inclination of  $30^\circ$

any inclined orbits in which every test with a  $180^\circ$  transfer angle fails to converge.

Further analysis on this issue shows that cases with a transfer angle of  $180^\circ$  produce results similar to Rosenbrock's banana function. Rosenbrock's function is a classic optimization problem whose global optimum is inside a long, narrow, parabolic-shaped flat valley. To find the valley is not difficult, however to converge to the global optimum in the valley is far more complex. As a result, Rosenbrock's function is often used to assess the performance of optimization algorithms [11]. Figure 6.20 depicts the evaluation of Rosenbrock's banana function plotted over two variables  $(x, y)$ .

Selecting an initial velocity based on converged solutions of orbits with transfer angles of  $179^\circ - 181^\circ$ , a  $180^\circ$  transfer with an inclination of  $45^\circ$  is propagated out

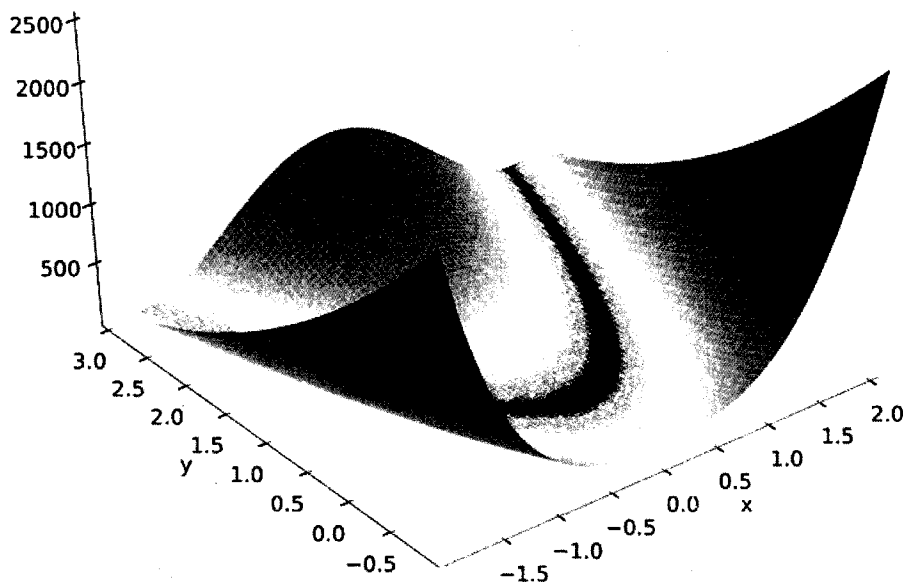


Figure 6.20: Illustration of Rosenbrock's function plotted over two variables [52]

using Cowell's method. The initial velocity is perturbed in small increments in all three planes to produce a contour plot of the error in the final position vector. The results in the  $y$ - $z$  plane are mapped in Figure 6.21. For clarification, Figure 6.22 is identical to Figure 6.21 with all but the contour representing  $|\Delta R| < 200$  km shaded out.

Figure 6.22 clearly shows a similar shaped contour as that produced by Rosenbrock's banana function. For this reason, the predictor-corrector method has no problem finding the valley of minimum values, but due to the large number of possible delta velocities that will put the vehicle in the correct range of position error, the corrector bounces along the curve until the maximum iteration limited is reached.



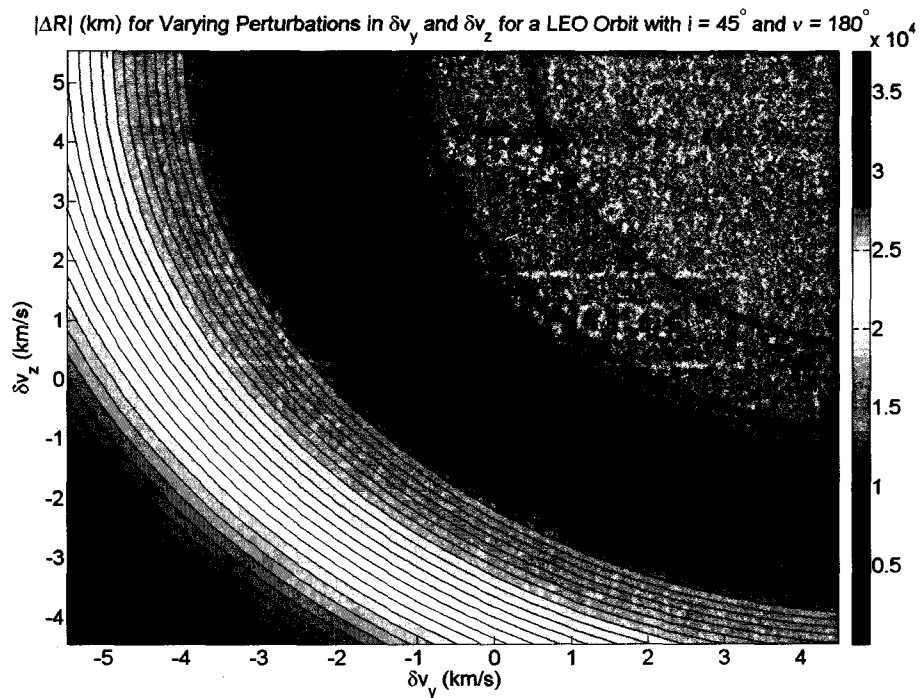


Figure 6.21: Contour plot illustrating the position error (km) in the y-z plane due to an initial velocity perturbation (km/s) for an orbit with  $\nu = 180^\circ$  and  $i = 45^\circ$

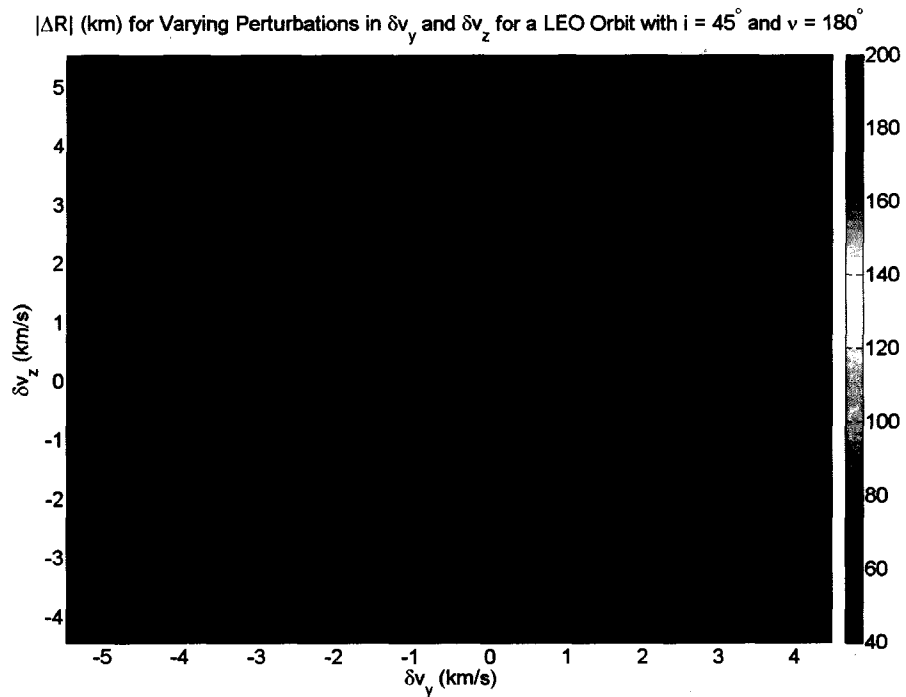


Figure 6.22: Contour plot illustrating position error (km) less than 200 km in the y-z plane due to an initial velocity perturbation (km/s) for an orbit with  $\nu = 180^\circ$  and  $i = 45^\circ$

Further, by re-examining Figure 6.21 it is easy to see why cases have issues converging in these situations: a guess of even 0.5 km/s in the wrong direction and the  $|\Delta R|$  jumps to over 1,000 km. For comparison, similar plots are produced for a transfer angle of  $160^\circ$  and an inclination of  $45^\circ$  which easily converged on a solution. Figure 6.23 is the contour plot and Figure 6.24 is the same plot with only the contours representing  $|\Delta R| < 200$  km highlighted. For the  $160^\circ$  transfer angle the range of possible velocities that results in low position errors is very small. Since the shooting method has so few velocities to attempt, it not only can find a solution, but in cases such as these in which the possible velocities are very limited, convergence occurs much more quickly as well. For the contour plots in the remaining planes (x-y and x-z) please refer to Appendix D. These plots highlight that majority of the velocity complexity occurs in the y-z plane.

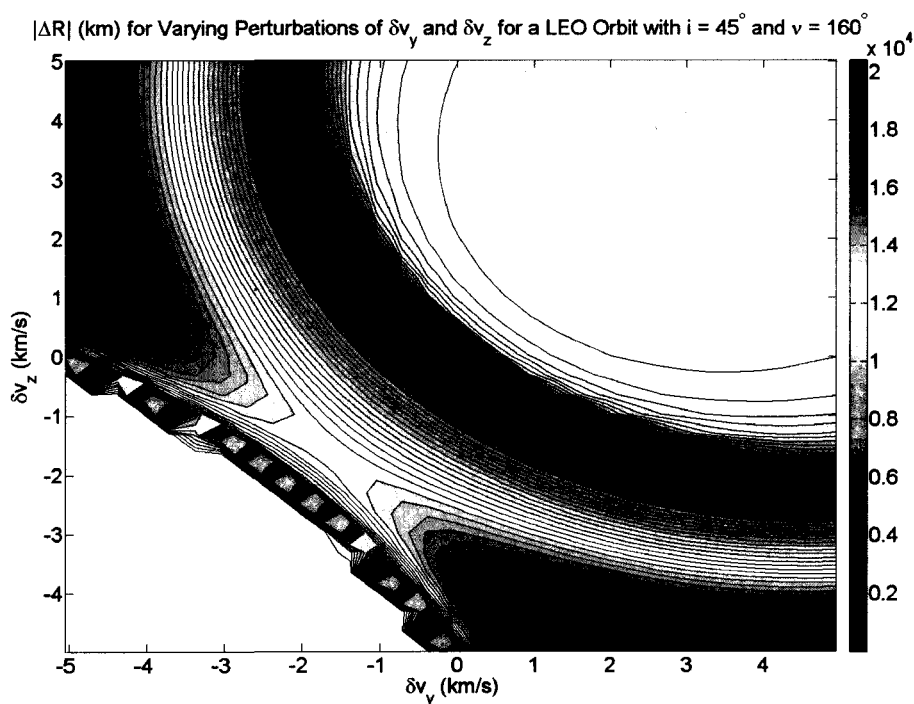


Figure 6.23: Contour plot illustrating the position error (km) in the y-z plane due to an initial velocity perturbation (km/s) for an orbit with  $\nu = 160^\circ$  and  $i = 45^\circ$

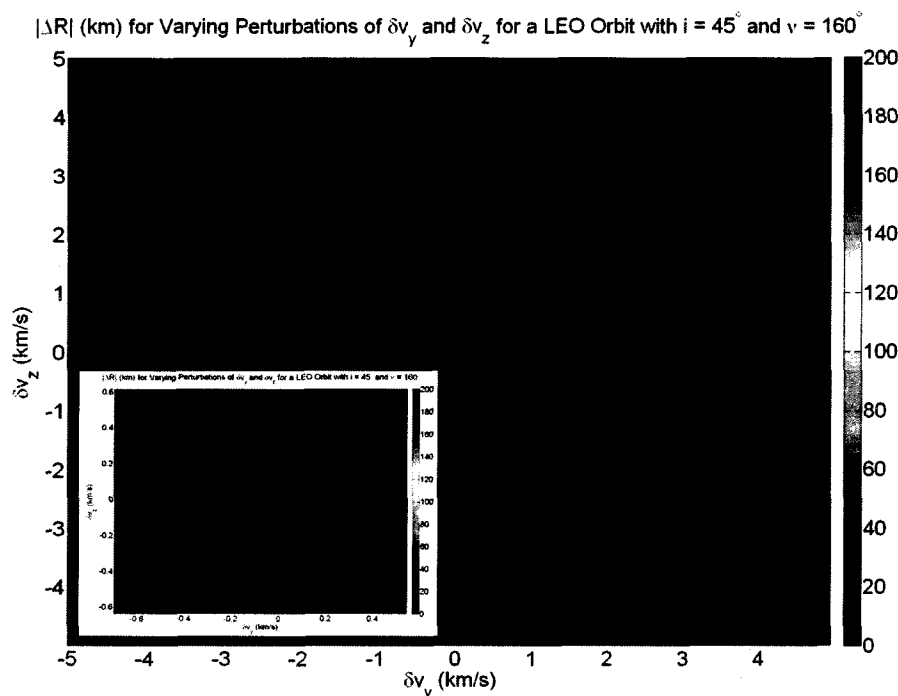


Figure 6.24: Contour plot illustrating position error (km) less than 200 km in the  $y$ - $z$  plane due to an initial velocity perturbation (km/s) for an orbit with  $\nu = 160^\circ$  and  $i = 45^\circ$

### 6.4.2 Summary of Test Results

Utilizing the Cowell-STM algorithm to correct the transfer velocities produced by Lambert 2-body dynamics points out a number of sensitivities to the method. Larger iteration numbers are indicative of sensitivities to the predictor-corrector method, whereas larger changes in velocity highlight weaknesses in the Lambert routine to calculate accurate transfer velocities.

The altitude of the final orbit plays little role in the number of iterations required to reach a converged solution. Analyzing the effects of eccentricity, orbits with eccentricities of 0.9 require the largest number of iterations. This is due to the longer time of flight required to transfer to highly elliptical orbits, 200,000 seconds as compared to 4,000 seconds for circular orbits. Since the STM is numerically integrated, the longer the matrix is propagated, the more inaccurate it becomes. As the matrix deviates

further from an accurate prediction, it becomes more difficult for the predictor-corrector to converge and thus the iteration number increases. In terms of velocity, orbits with the lowest altitudes and lowest range of eccentricities, 0-0.1 require the largest change in velocity. This is due to the strong effect of drag at low altitudes which orbits with low eccentricities maintain the longest. Since Lambert dynamics do not account for perturbations due to drag, the predicted transfer velocities are smaller than those required to overcome the perturbing force.

Results illustrate that orbits with equatorial or polar orbits require the least number of iterations and the least amount of velocity change. With respect to iteration number, the ease of convergence is due to the two-planar motion of these specific types of orbits. Since the initial velocity is in two planes, the STM corrector only makes changes to the velocity in these two planes. Removing the third dimension reduces the complexity of the possible transfer velocities and enables the tool to converge quickly. The small change required in the transfer velocity calculated from Lambert highlights the accuracy with which Lambert predicts polar and equatorial orbits. Those orbits that required the most iterations and velocity change have inclinations furthest from the equatorial and polar extremes.

As mentioned in the method limitations of the Cowell-STM algorithm, testing of orbits with transfer angles close to  $180^\circ$  result in the largest number of iterations and change in velocity required from the Lambert initial prediction. Regarding the iteration number, a few cases with true anomaly angles of  $135^\circ$ ,  $175^\circ$  and  $205^\circ$  result in iteration numbers greater than  $+1.5\text{IQR}$ , however majority are the result of transfer angles between  $178^\circ - 182^\circ$ . For change in velocity, all cases but one requiring a  $\Delta V$  greater than  $+1.5\text{IQR}$  are due to cases with true anomaly angles between  $178^\circ - 182^\circ$ .

Initial perturbation tests illustrate that the predictor-corrector process is sensitive to initial perturbations in the position vector. This may be due to the fact that the algorithm can correct for slight deviations in the initial velocity but because it assumes

the initial position is constant, no corrections can be made to the position vector. Since the transfer velocity predicted by Lambert is based on the same assumption that  $\mathbf{r}_0$  is constant, the perturbations to this vector can become only so large before the velocity corrections become too non-linear for the state transition matrix to correct.

# Chapter 7

## Closure

The following chapter summarizes the results of applying the Cowell-STM algorithm to translunar and low Earth orbit applications. It concludes with a look at potential future work to improve the method.

In order to more accurately predict the transfer velocities required for translunar and low Earth orbit transfers and produce realistic reference trajectories, a predictor-corrector method was developed to qualify the velocities determined by low fidelity models. The Cowell-STM method has real world application in navigation performance, delta velocity trade studies, and mission planning. The algorithm is significant in that the more accurate the transfer velocities are known prior to mission fly out, the less navigation correction is required resulting in a more cost-effective mission.

The method utilizes Cowell's method with high order perturbation models as the predicting propagator and a state transition matrix with lower order perturbation models as the corrector. The perturbation accelerations implemented in Cowell's method include solar and lunar correction terms, higher order Earth and lunar gravity up to degree 9, atmospheric drag, and solar radiation pressure. The state transition matrix used for the translunar cases implemented 4-body motion and the  $J_2$

gravity coefficient. The STM used in the low Earth orbit cases included the same perturbations as those for the translunar case, however drag was added as well. The selection of these particular low order models was based on a study between computation time and accuracy of the matrix. By reducing the matrix to include only those models listed, the predictor-corrector could calculate converged solutions in a reasonable amount of computational time. If higher order terms are needed, the same methodology presented in Chapter 4 may be followed to implement these terms.

For translunar cases, the Cowell predictor-corrector refined transfer velocities produced by the multi-conic propagator EXLX. EXLX approximates translunar trajectories using the three-body pseudostate theory to compute overlapped conic transfer trajectories between the Earth and Moon. All parameters of the test cases were held constant except the Earth and lunar inclinations and ascending nodes. Only those cases that met the  $\Delta V$  maximum constraint reasonable for a Crew Exploration Vehicle type mission were tested.

Of the 110 cases tested all converged using the predictor-corrector tool. Those cases that required a larger number of iterations were found to switch between prograde and retrograde orbits. This change in direction also required a larger change in transfer velocity from the initial value produced by EXLX. The reversal of lunar orbit direction was a result of higher order gravity perturbations near the Moon. Due to the fact that EXLX does not model high order lunar gravity, its predicted transfer trajectories took paths that were not feasible with the Cowell propagator. In these cases, only by switching the direction of the final orbit motion could the predictor-corrector converge on a solution.

Testing on initial orbit perturbations illustrated that all cases failed to converge if a perturbation of only 4% was applied to the initial states. This illustrates how sensitive the process is to the relative accuracy of the initial guess.

For low Earth orbit cases, Lambert's method was used to produce initial trans-

fer velocity guesses for the Cowell-STM method. The altitude, eccentricity, inclination, and true anomaly of the orbits varied for each test case. Testing was done to illustrate the effect of different orbit transfers on iteration number and change in predicted transfer velocity. Higher iteration numbers were indicative of sensitivities towards particular orbital parameters in the predictor-corrector process, whereas high velocity changes pointed to a weakness in the Lambert method for calculating accurate velocities. Concerning altitude, results highlighted little correlation between the initial altitude of the orbit and iteration number or change in velocity.

Results illustrated that orbits with the highest eccentricity of 0.9 required the most iterations, but orbits with low eccentricities of 0-0.1 required the most change in velocity. The first observation is a result of highly elliptical orbits requiring longer transfer times. The longer the STM is propagated for, the more inaccurate it becomes due to numerical roundoff making it more difficult for the predictor-corrector to converge on a solution. The second observation is due to the large effect of drag on vehicles orbiting at low altitudes. Lambert's method assumes no drag in its calculations thus for situations in which drag is present a much larger transfer velocity is required to reach the desired final position in the given transfer time.

Concerning inclination, testing showed that polar and equatorial orbits converged the most quickly. Since these orbits are defined in two planes, the Lambert shooting method makes velocity corrections in only two of the possible three directions. Due to this decrease in complexity, equatorial and polar orbits are more likely to converge in the fewest number of iterations.

With respect to true anomaly, preliminary testing showed the predictor-corrector algorithm could not handle transfer angles of exactly  $180^\circ$  for inclined orbits due to the difficulty of the solution space. For situations in which the transfer angle was  $180^\circ$  the allowable deviation in initial transfer velocity to produce a viable final position error becomes much tighter. Consequently, the algorithm makes multiple attempts



to find a solution utilizing velocities that are close to the solution but not accurate enough to converge. As a result of this restriction, Hohmann transfers were tested with transfer angles ranging between  $178^\circ - 182^\circ$  but never exactly  $180^\circ$ . Of the cases that failed, all but one were a result of transfer angles between  $178^\circ - 182^\circ$ . These angles resulted in the largest change in velocity as well.

An initial perturbation test also illustrated that the low Earth orbit cases were more sensitive to perturbations in the position vector than the velocity vector. This is mostly likely due to the Cowell-STM process which allows for correction of the initial velocity but not the initial position.

The results of the low Earth orbit test cases could be improved drastically if a higher fidelity tool for predicting transfer velocities was available. Additionally, the development of a tool to help calculate the most optimal transfer times for low Earth orbit transfers would produce more accurate solutions.

Additional work on the Cowell propagator predictor and state transition matrix corrector should focus on producing more accurate results. With respect to the propagator, more robust models can be applied to more closely mirror real world scenarios. For translunar or interplanetary missions the use of reference frame switching to reduce truncation error is one option that was not tested in this thesis. For low Earth orbits which are largely effected by drag, more sophisticated atmospheric models that reflect a dynamic atmosphere should be tested. As highlighted in previous chapters, numerical integration of the state transition matrix produces accumulated error over longer periods of transfer time. Further research into more sophisticated calculations of the matrix could reduce this error, reducing the convergence time as well as the sensitivity to the initial guesses. Finally, the predictor-corrector process would produce more realistic transfer velocities if finite burns were implemented.

One method of increasing the accuracy of the propagator would be to incorporate additional or higher fidelity perturbation models into the system. Cowell's method

relies on the calculation of a vehicle's state around a primary body. However, studies show that in transplanetary missions there is a point at which the Earth is no longer the primary body and the reference frame should switch to reduce round off error [50]. Reference frame switching, which is also used by the pseudostate method applied in EXLX, has the benefit of utilizing smaller state vectors to reduce round-off errors in calculations. This switch is dictated by the location of the vehicle with respect to the sphere of influence of each respective planet. The frame switch issue is best understood when viewing the spheres of influence of different planets as nested spheres all within the greater sphere of the sun. Figure 7.1 illustrates this concept.

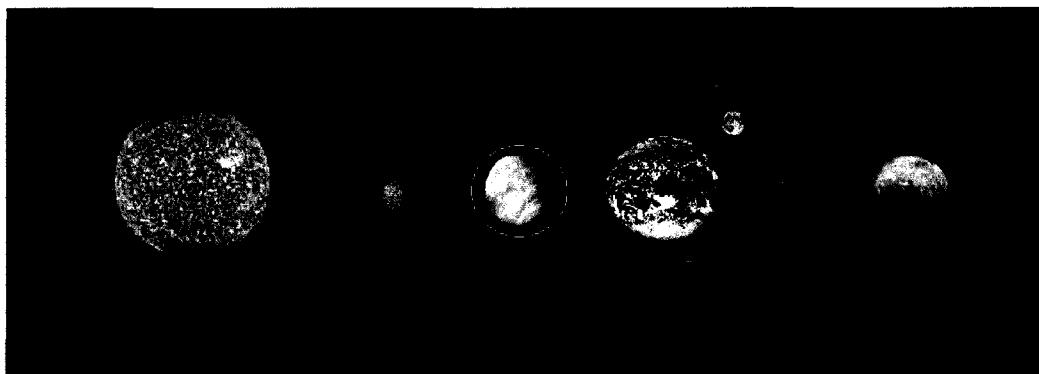


Figure 7.1: Spheres of influence for the Sun, Mercury, Venus, Earth, Moon, and Mars.

If frame switching logic were implemented, additional bodies should be added to the model to enable interplanetary missions. Information on the planet structure as well as any known gravity coefficients should be included as well.

With respect to low Earth orbits, higher fidelity atmospheric models should be implemented. The simplistic model applied in this research assumed many atmospheric parameters remained constant and thus does not accurately reflect real world effects. Unlike the static model used in this research, time varying models can take into consideration diurnal variations, the solar rotation cycle, seasonal variations, magnetic storm variations, and the rotating atmosphere to name a few. One of the most complete time-varying models is the Jaccia-Roberts atmosphere which contains

analytical expressions for calculating exospheric temperature as a function of position, time, solar activity, and geomagnetic activity. Density is determined from the exospheric temperature using temperature profiles or from the diffusion equation. However, as the most high fidelity model, the Jaccia-Roberts atmosphere also requires the most computational time [49]. If the computational cost of time-varying models is too great, high order static models such as the Harris-Priester model should be considered.

One of the major factors contributing to the iteration number in the predictor-corrector process is the level of accuracy of the state transition matrix. Even with no perturbations, the matrix produces errors that only increase as the time of flight increases. A more accurate state transition matrix would reduce the number of iterations required for convergence. One such method is the sensitivity matrix algorithm developed by Bryson and Ho and discussed by Der and Danchick [26] [18, 19] .

Finally, note that all burns calculated and implemented in this work were assumed to be purely impulsive burns. Realistically, burns occur over a finite period of time and modeling them in this way would provide more accurate initial burn velocities. For simplicity, the burn acceleration could be modeled assuming a constant acceleration,  $a_{max}$ . The total burn time could then be calculated using  $t_{burn} = \frac{\Delta V}{a_{max}}$ , where  $\Delta V$  is the burn velocity provided by EXLX or Lambert. The start time for the burn must occur earlier now due to its finite nature. Assuming  $t^*$  represents the burn start time for the impulsive case, one definition of the start time for the finite burn could be  $t_{burn0} = t^* - \frac{1}{2}t_{burn}$ . Using this as the start time, the states are propagated forward using the Cowell method to  $t^*$ , however, because of the perturbations applied in the model the final states at  $t^*$  will not match those used by EXLX or Lambert to calculate the transfer velocity. Thus a shooting method is required to determine the initial velocity that when propagated over a finite period of time results in final states at  $t^*$  that are within some tolerance of the initial states used by the impulsive burn.

From here an additional level of targeting is used to determine the transfer velocity from  $t^*$  to  $t_f$ . This targeting is the premise behind the research in this thesis. Each time the second level updates its initial conditions at  $t^*$  the conditions at  $t_{burn0}$  must be updated as well. Thus two-level targeting is required to implement finite burns into the predictor-corrector method.

As with any addition of a more complex algorithm, adding finite burns into the process will increase the require computational time. A trade study between accuracy and computation time must be made prior to implementing any of the future work just described.

# Appendix A

## Feasible Translunar Trajectories

The following contour plots (Figure A.1-A.8) represent the feasible lunar orbital element ranges for initial Earth orbits with varying inclinations and ascending nodes. The information was collected from a number of multi-conic runs produced by EXLX scans. The plots highlight a tendency for certain values of the Earth and lunar parameters to produce infeasible translunar transfers as determined by the maximum lunar orbit insertion velocity constraint placed on EXLX. The contour lines are indicative of the Moon's geometry for the transfer date selected. Note for cases in which the Earth orbit is equatorial,  $i_{\oplus} = 0^{\circ}$ , the horizontal asymptotic bands around  $i_{\odot} = 0^{\circ}$  and  $i_{\odot} = 180^{\circ}$  and the vertical bands around  $\Omega_{\odot} = 90^{\circ}$  and  $\Omega_{\odot} = 270$  indicate the largest regions of feasibility. For an initial equatorial Earth orbit the vehicle will always be able to enter into an equatorial lunar orbit. From the orientation of the Moon compared to the Earth, the vehicle will expend the least amount of velocity entering a lunar equatorial orbit at the nodes, either  $\Omega_{\odot} = 90^{\circ}$  or  $\Omega_{\odot} = 270^{\circ}$  depending on the direction of motion. The contour lines place boundaries on how the orbital elements were selected for testing of the translunar cases.

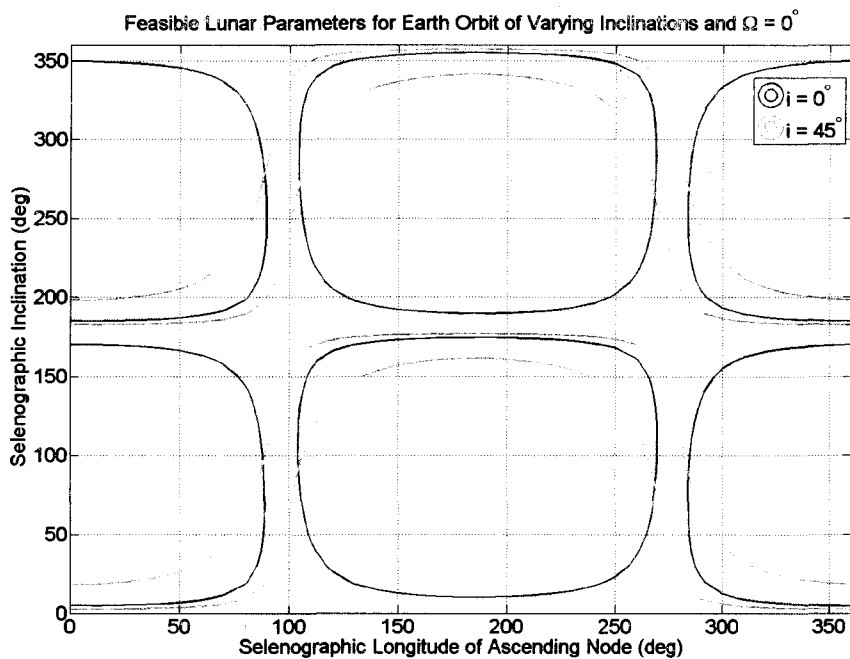


Figure A.1: Feasible lunar orbit parameters for an initial Earth orbit with varying inclinations and  $\Omega_{\oplus} = 0^\circ$

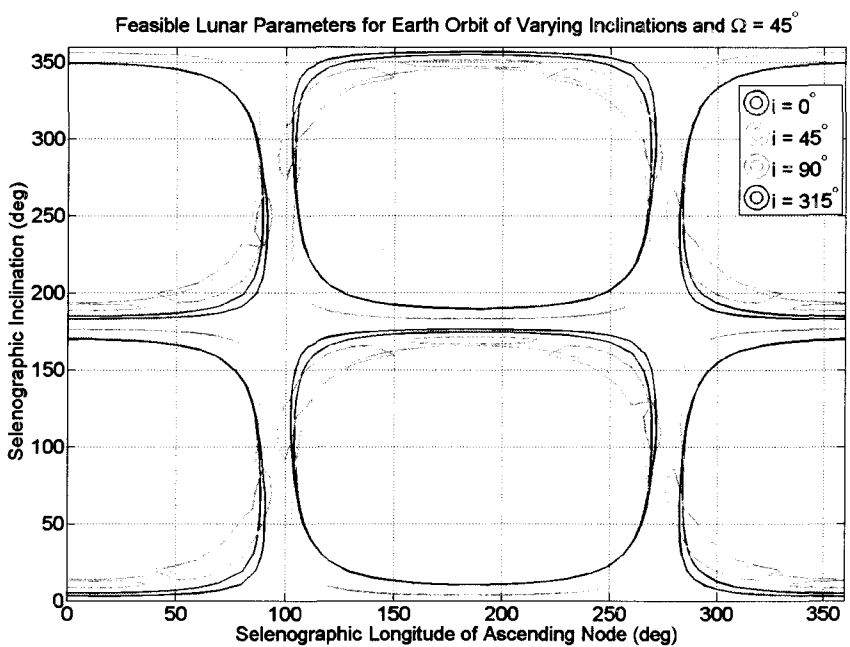


Figure A.2: Feasible lunar orbit parameters for an initial Earth orbit with varying inclinations and  $\Omega_{\oplus} = 45^\circ$

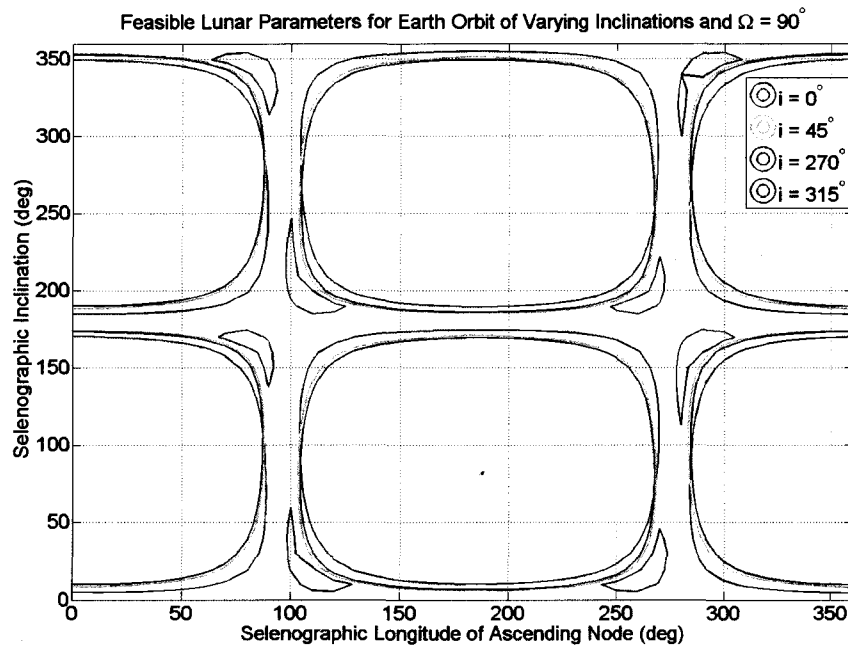


Figure A.3: Feasible lunar orbit parameters for an initial Earth orbit with varying inclinations and  $\Omega_{\oplus} = 90^\circ$

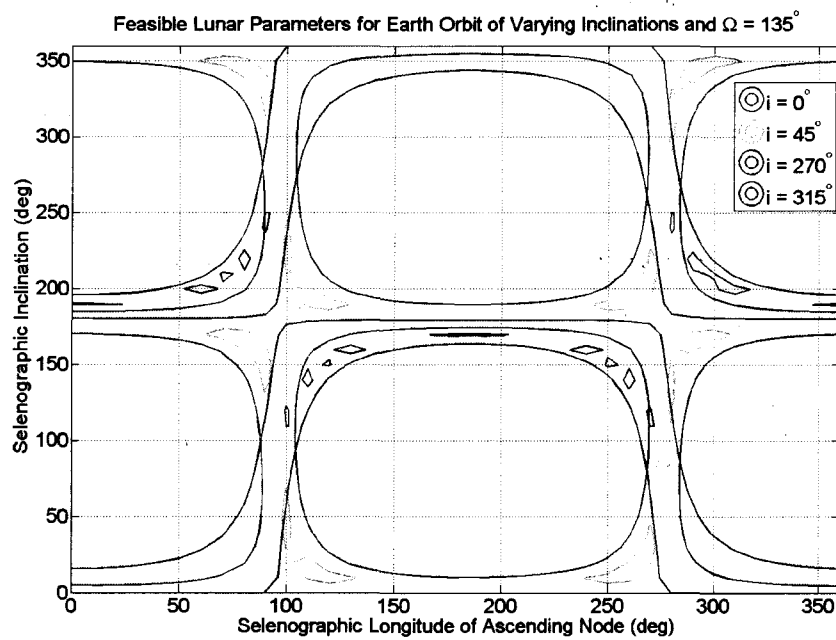


Figure A.4: Feasible lunar orbit parameters for an initial Earth orbit with varying inclinations and  $\Omega_{\oplus} = 135^\circ$

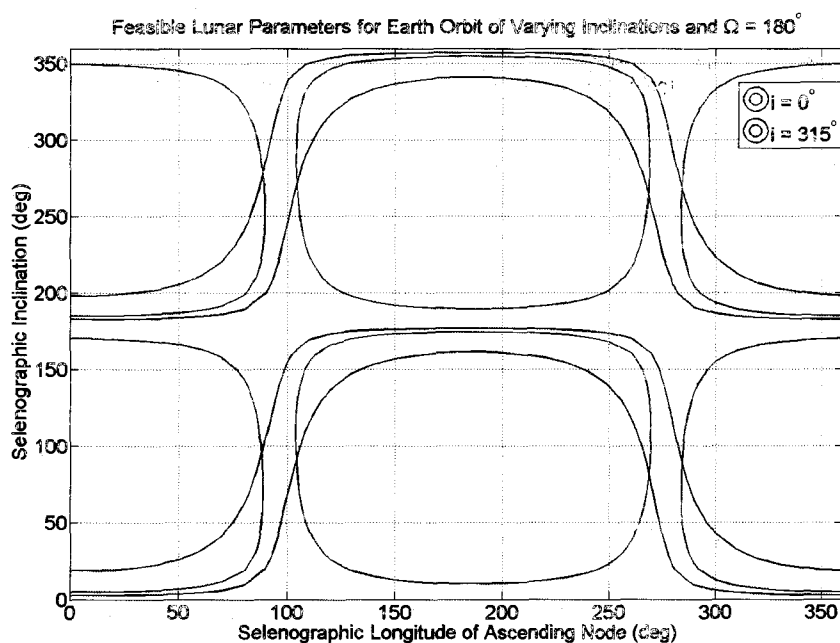


Figure A.5: Feasible lunar orbit parameters for an initial Earth orbit with varying inclinations and  $\Omega_{\oplus} = 180^\circ$

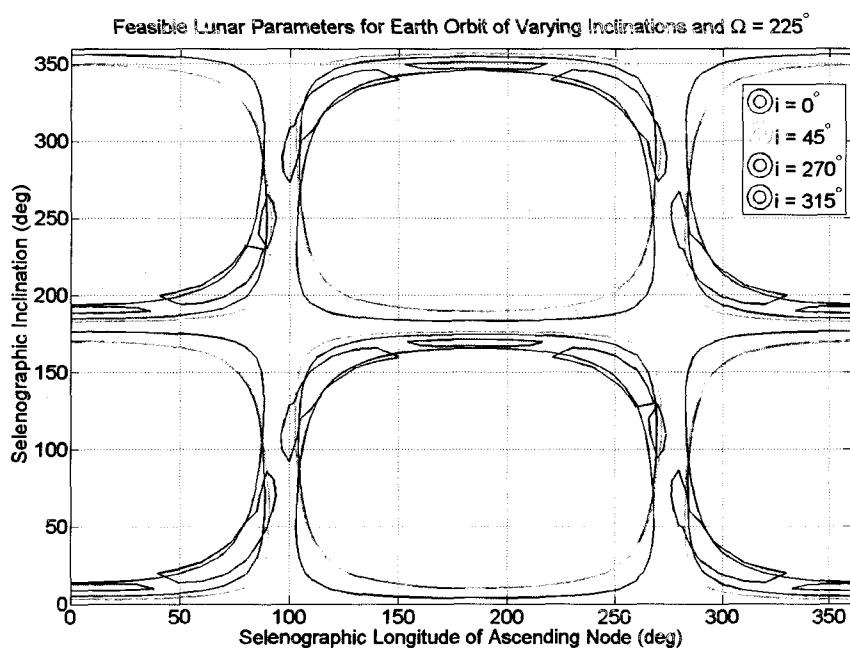


Figure A.6: Feasible lunar orbit parameters for an initial Earth orbit with varying inclinations and  $\Omega_{\oplus} = 225^\circ$



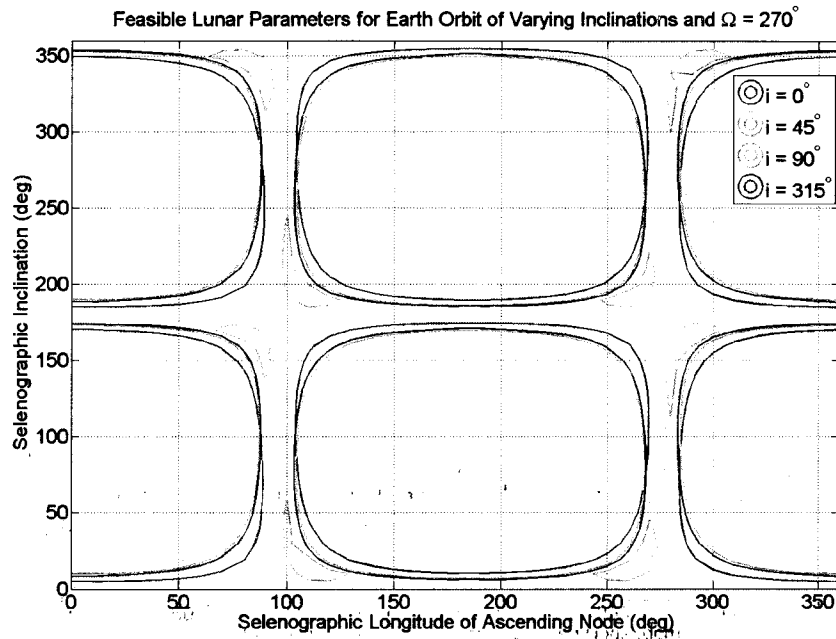


Figure A.7: Feasible lunar orbit parameters for an initial Earth orbit with varying inclinations and  $\Omega_{\oplus} = 270^\circ$

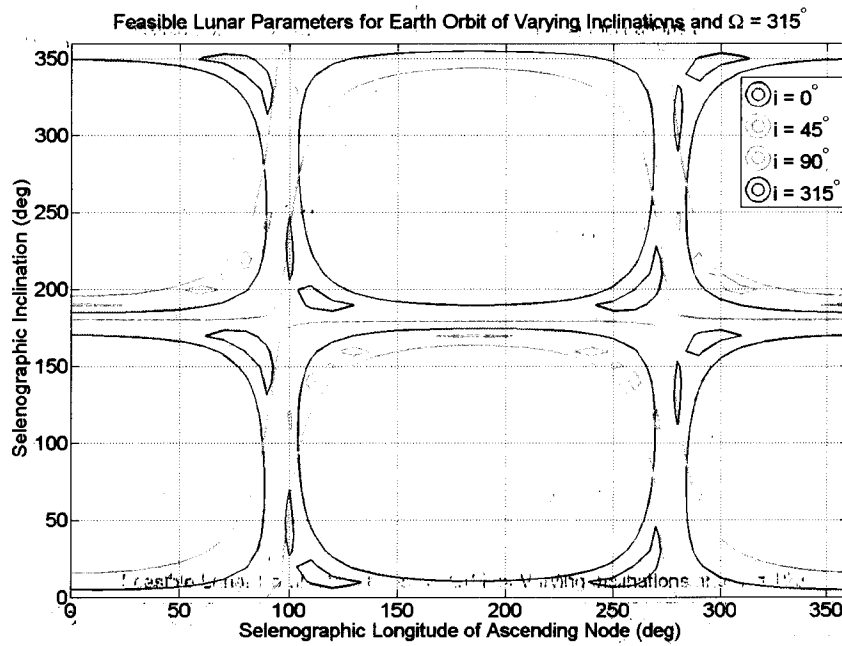


Figure A.8: Feasible lunar orbit parameters for an initial Earth orbit with varying inclinations and  $\Omega_{\oplus} = 315^\circ$

# Appendix B

## Monte Carlo Sample Size

Due to the time consuming manual process required to run multiple EXLX trajectories a reasonable minimum number of test cases was desired for Monte Carlo runs [36][35][46]. Preliminary testing illustrated all initial test cases converged (i.e. applying the shooting method with the Cowell propagator resulted in a converged solution under 40 iterations each time). With a probability of success close to 1 the following process was utilized to determine the minimal sample size.

A one-sided confidence interval with the probability of success,  $p$  is defined as:

$$100(1 - \alpha)\% \tag{B.1}$$

For a Monte Carlo sample size,  $n$ , the probability of obtaining  $n$  successes is  $p^n$ . Solving for  $p_L$  from the equation  $p_L^n = \alpha$  results in the lower bound on the probability of success with  $100(1 - \alpha)\%$  confidence. The value of  $n$  is thus:

$$n = \frac{\log \alpha}{\log p_L} \tag{B.2}$$

For a probability of success of 0.95 with a 95% confidence level, the minimum required number of samples is 59. As aforementioned, this number only holds up if the

probability of success is very close to 1 in reality. The final number of translunar test cases selected for testing was 110. As discussed in Chapter 5, all cases converged. Because the probability of success is so high the confidence level for the tool remains above 95% despite the small number of runs performed.

# Appendix C

## List of Test Cases

The following table details the parameters selected for each translunar test case:

Case #	Earth $i_{\oplus}^{\circ}$	Earth $\Omega_{\oplus}^{\circ}$	Moon $i_{\odot}^{\circ}$	Moon $\Omega_{\odot}^{\circ}$	Iterations
1	30	0	5	330	8
2	40	50	15	45	27
3	40	50	25	100	10
4	90	20	25	60	22
5	5	130	45	120	13
6	10	20	10	120	14
7	2	1	0	240	12
8	55	1	50	320	10
9	78	50	69	290	11
10	45	75	75	110	10
11	62	32	38	50	17
12	0	0	0	85	17
13	0	0	30	105	20
14	100	32	90	100	10
15	33	17	127	108	9
16	64	308	20	59	14
17	52	28	109	273	11
18	69	67	125	94	11
19	14	151	132	96	11
20	10	18	6	328	22
21	24	177	149	89	15

Case #	Earth $i_{\oplus}^{\circ}$	Earth $\Omega_{\oplus}^{\circ}$	Moon $i_{\ominus}^{\circ}$	Moon $\Omega_{\ominus}^{\circ}$	Iterations
22	85	325	170	189	11
23	3	133	5	198	20
24	61	41	50	93	11
25	106	33	135	109	11
26	99	48	25	69	19
27	52	25	14	22	22
28	69	99	141	97	7
29	103	27	35	72	21
30	14	154	178	16	10
31	10	112	140	88	8
32	96	64	128	105	12
33	24	14	26	92	19
34	103	44	132	108	16
35	85	23	112	105	7
36	3	34	178	103	8
37	61	44	144	103	8
38	30	76	116	94	10
39	30	89	44	89	30
40	48	61	158	123	7
41	16	71	55	100	17
42	42	44	125	265	10
43	64	88	289	280	11
44	73	81	315	257	27
45	44	92	176	353	8
46	23	92	199	257	9
47	44	144	216	270	11
48	10	241	148	278	8
49	49	125	107	279	9
50	77	281	5	150	15
51	76	217	20	113	18
52	55	330	97	270	16
53	33	117	115	279	8
54	24	283	7	233	26
55	31	13	28	291	17
56	6	64	96	97	25
57	35	123	180	189	14
58	83	70	116	99	8
59	29	88	10	60	18
60	68	276	77	102	11

Case #	Earth $i_{\oplus}^{\circ}$	Earth $\Omega_{\oplus}^{\circ}$	Moon $i_{\odot}^{\circ}$	Moon $\Omega_{\odot}^{\circ}$	Iterations
61	35	68	7	132	17
62	87	33	38	287	14
63	22	208	21	278	10
64	46	234	94	271	14
65	53	245	180	34	8
66	48	341	173	191	10
67	62	43	121	262	8
68	20	163	3	188	21
69	78	50	20	75	12
70	48	309	6	320	21
71	27	139	129	89	11
72	64	251	178	4	11
73	35	227	169	274	7
74	76	342	17	35	11
75	81	31	117	107	8
76	1	212	23	261	14
77	1	316	113	274	9
78	8	169	22	117	25
79	24	158	115	91	14
80	3	269	131	271	8
81	31	310	106	275	13
82	27	176	28	270	16
83	31	83	12	72	16
84	78	31	90	281	23
85	31	25	13	301	8
86	310	40	300	100	12
87	355	266	335	108	26
88	340	280	250	103	9
89	355	325	210	95	13
90	300	299	260	96	11
91	345	75	280	91	12
92	45	312	182	70	10
93	333	277	356	200	14
94	6	200	352	3	16
95	351	182	347	53	23
96	311	200	344	148	22
97	10	140	357	252	24
98	310	125	359	303	31
99	315	135	360	350	34
100	319	85	251	273	11

Case #	Earth $i_{\oplus}^{\circ}$	Earth $\Omega_{\oplus}^{\circ}$	Moon $i_{\ominus}^{\circ}$	Moon $\Omega_{\ominus}^{\circ}$	Iterations
101	320	50	175	149	10
102	330	170	167	225	9
103	303	230	185	300	12
104	320	285	183	325	10
105	321	275	243	270	11
106	312	60	204	273	11
107	314	226	274	268	11
108	310	35	223	101	9
109	325	100	319	95	16
110	318	220	340	277	18

Table C.1: List of parameters for translunar test cases

# Appendix D

## LEO Contour Maps

The following contour plots depict the error in position due to velocity perturbations in the x-z and x-y planes for transfer angles of  $180^\circ$  and  $160^\circ$  with orbit inclinations of  $45^\circ$ . Each two plots is a set with the first plot depicting the entire range of position errors and the second plot focused on just the contours that produce position errors less than 200 km. Compared to the plots in Section 6.4.1, it is clear that most of the error complexity comes from perturbations in the y-z plane. Velocity perturbations in the x-z and x-y planes highlight very specific regions of acceptable velocities thus a converged solution is much easier to achieve.



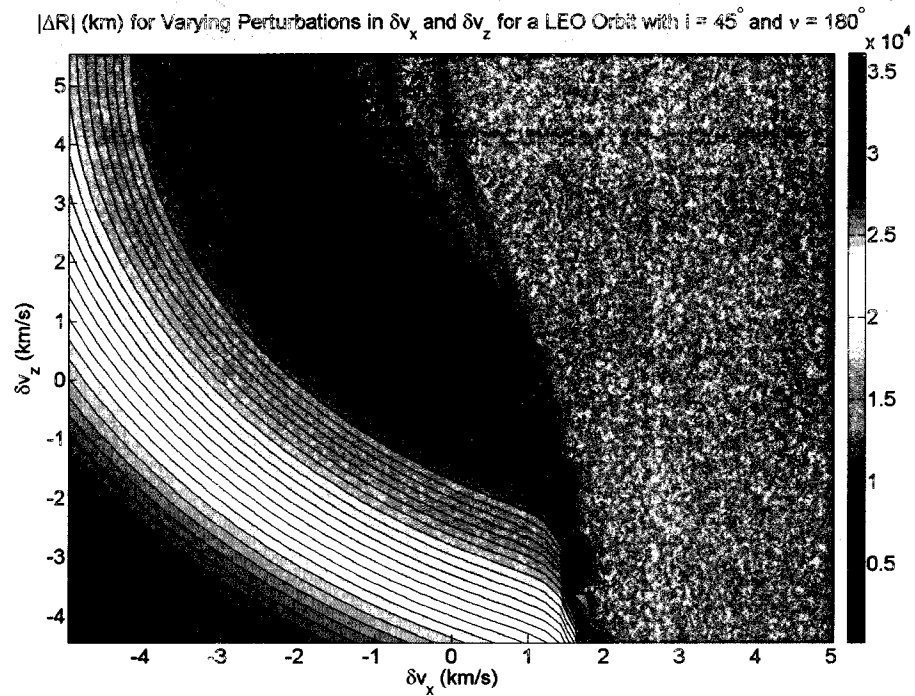


Figure D.1: Contour plot illustrating the position error (km) in the x-z plane due to an initial velocity perturbation (km/s) for an orbit with  $\nu = 180^\circ$  and  $i = 45^\circ$

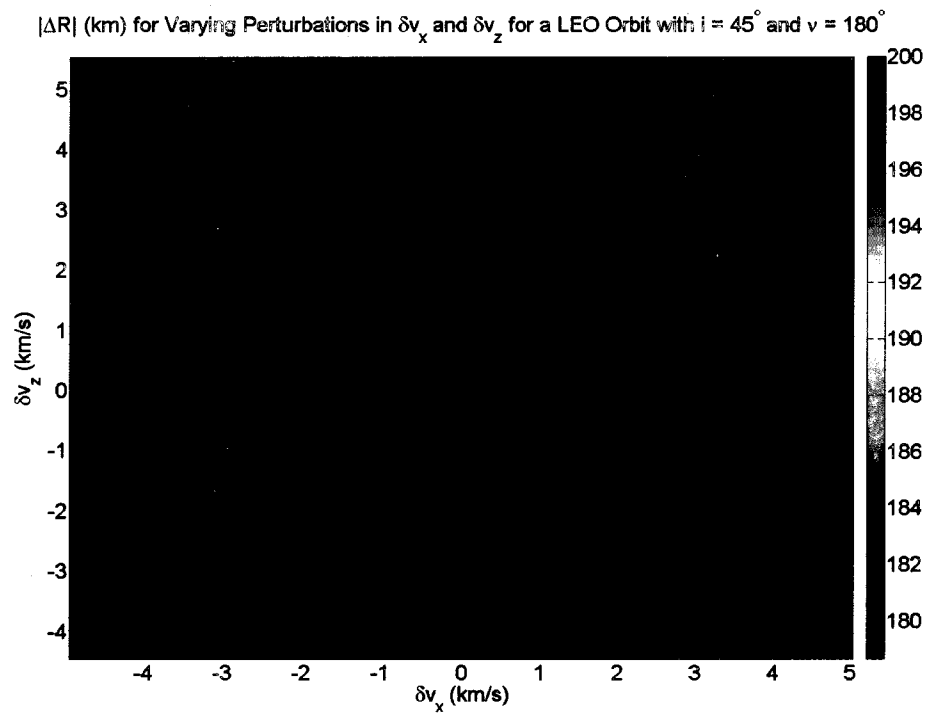


Figure D.2: Contour plot illustrating position error (km) less than 200 km in the x-z plane due to an initial velocity perturbation (km/s) for an orbit with  $\nu = 180^\circ$  and  $i = 45^\circ$

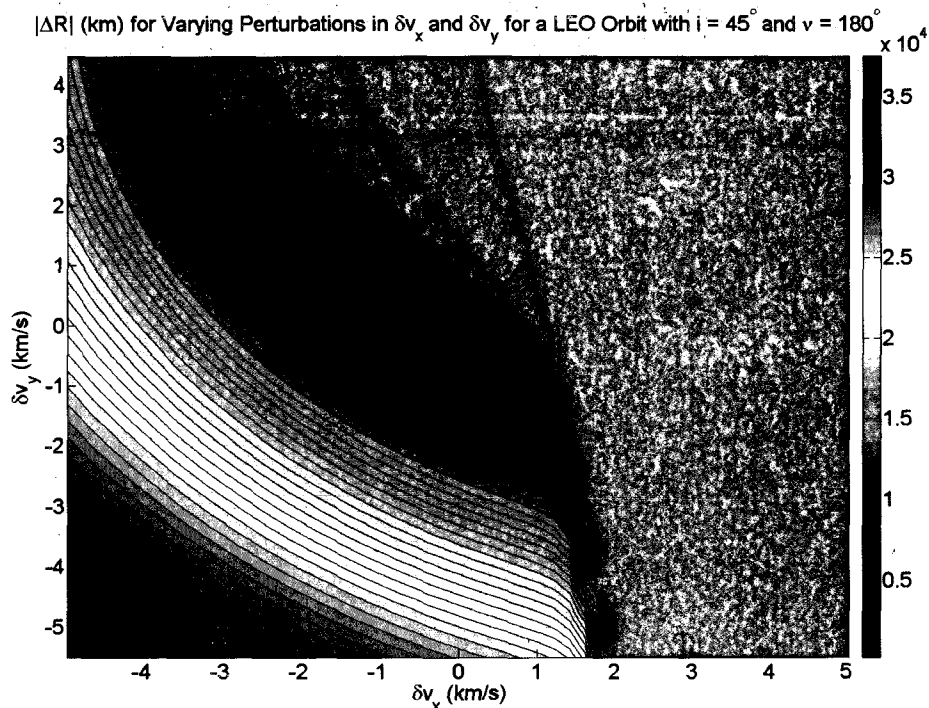


Figure D.3: Contour plot illustrating the position error (km) in the x-y plane due to an initial velocity perturbation (km/s) for an orbit with  $\nu = 180^\circ$  and  $i = 45^\circ$

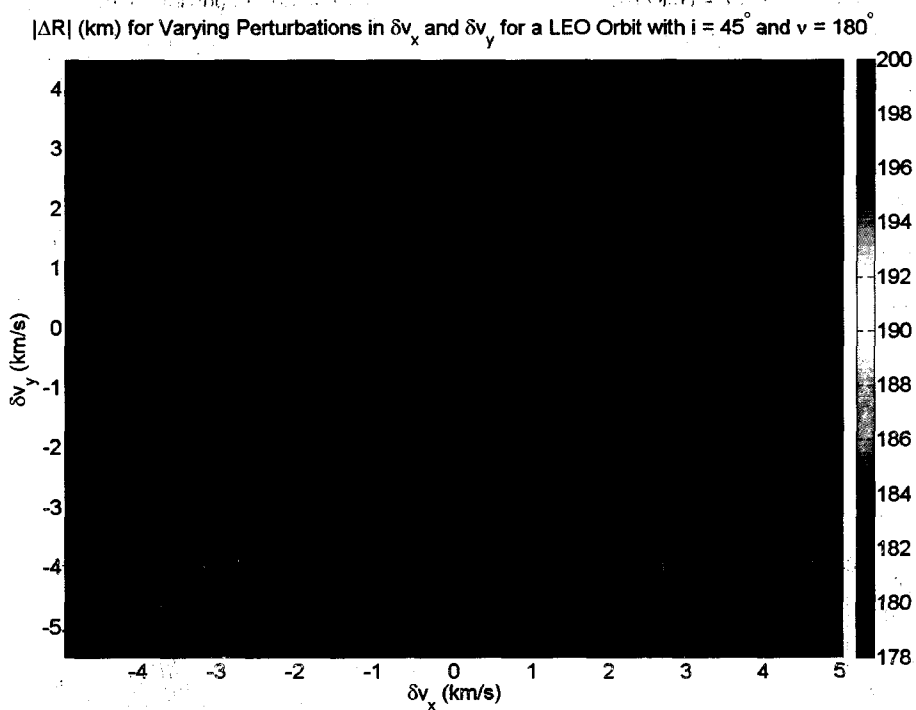


Figure D.4: Contour plot illustrating position error (km) less than 200 km in the x-y plane due to an initial velocity perturbation (km/s) for an orbit with  $\nu = 180^\circ$  and  $i = 45^\circ$

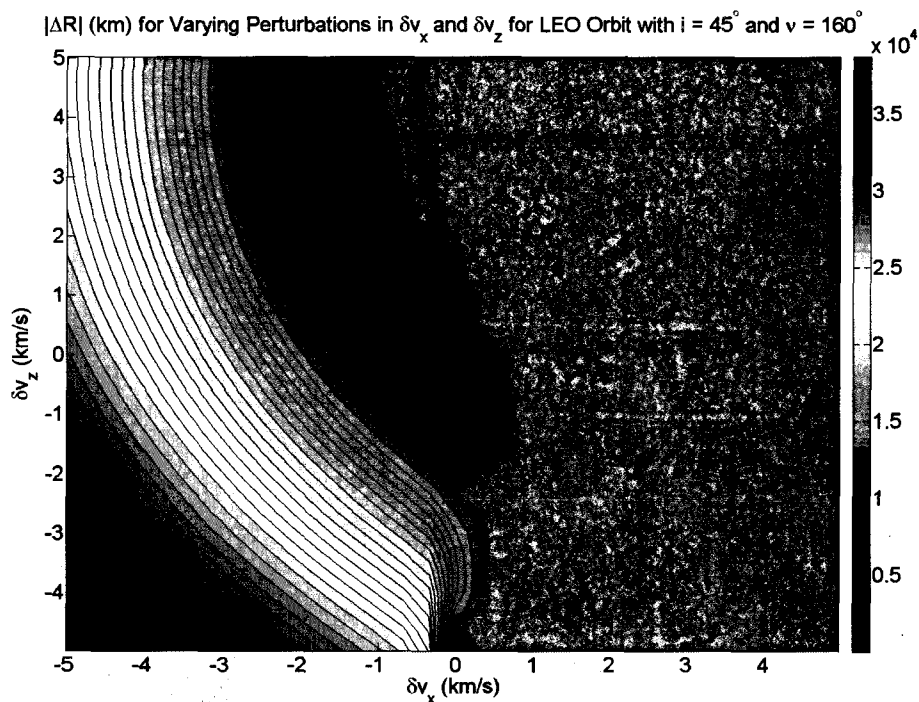


Figure D.5: Contour plot illustrating the position error (km) in the x-z plane due to an initial velocity perturbation (km/s) for an orbit with  $\nu = 160^\circ$  and  $i = 45^\circ$

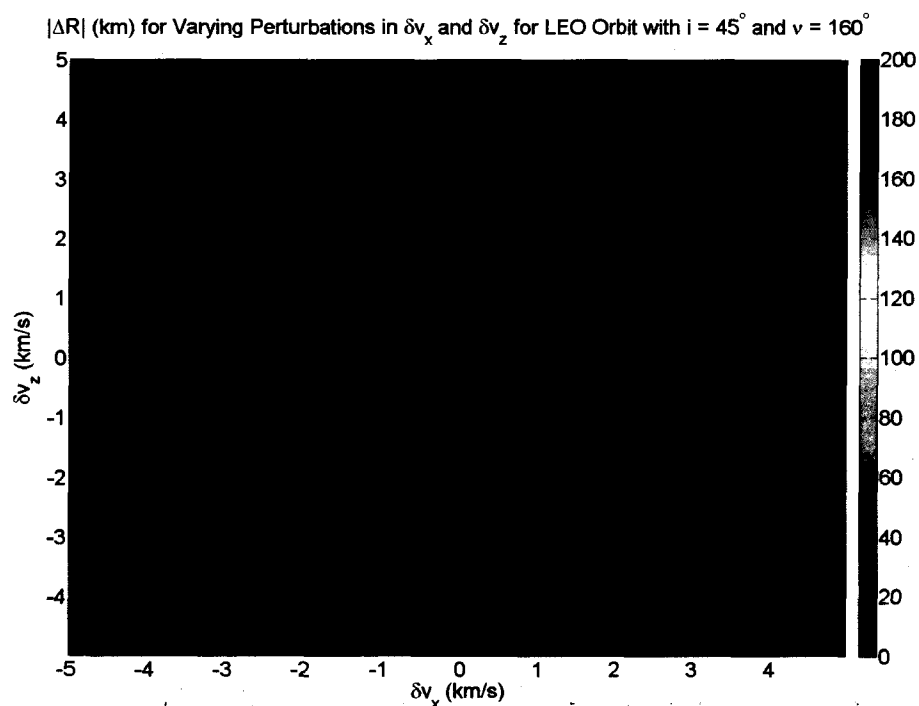


Figure D.6: Contour plot illustrating position error (km) less than 200 km in the x-z plane due to an initial velocity perturbation (km/s) for an orbit with  $\nu = 160^\circ$  and  $i = 45^\circ$

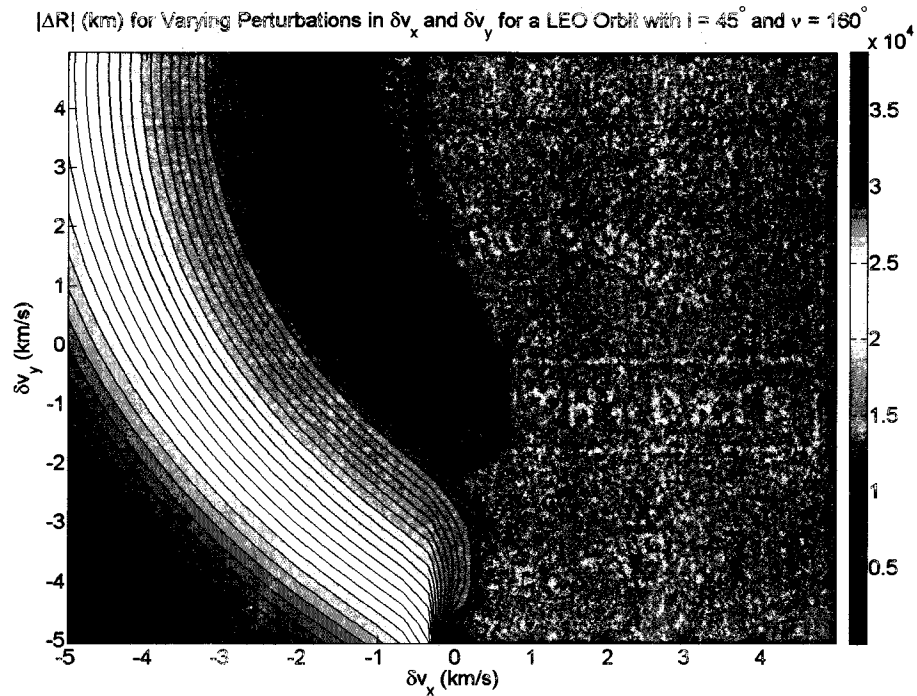


Figure D.7: Contour plot illustrating the position error (km) in the x-y plane due to an initial velocity perturbation (km/s) for an orbit with  $\nu = 160^\circ$  and  $i = 45^\circ$

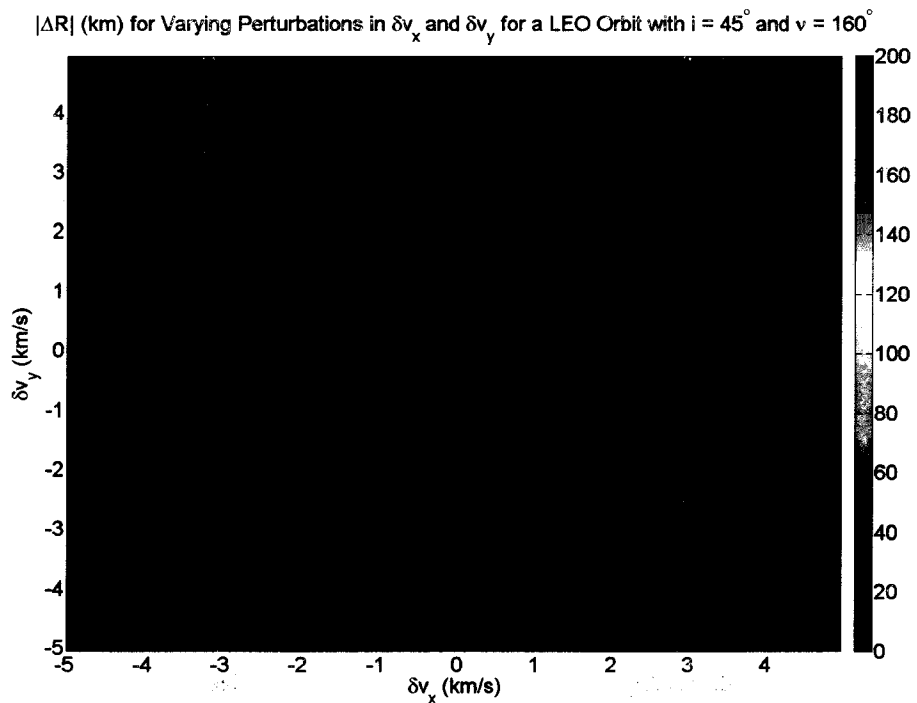


Figure D.8: Contour plot illustrating position error (km) less than 200 km in the x-y plane due to an initial velocity perturbation (km/s) for an orbit with  $\nu = 160^\circ$  and  $i = 45^\circ$

# Bibliography

- [1] *MATLAB 7.6.0 (R2008a) Help Manual*.
- [2] Oceanographers catch first wave of gravity mission's success. Jet Propulsion Laboratory: [www.jpl.nasa.gov/news/news.cfm?release=2003-103](http://www.jpl.nasa.gov/news/news.cfm?release=2003-103), July 2003.
- [3] Naif planetary data system navigation node. NASA: [naif.jpl.nasa.gov/naif/index.html](http://naif.jpl.nasa.gov/naif/index.html), Nov 2009.
- [4] R. L. Alford and J. J. F. Liu. Application of encke's method for low-earth orbit determination. *American Astronomical Society*, (No. 85-354).
- [5] F. Amato. *Robust Control of Linear Systems Subject to Time-Varying Parameters*. Springer-Verlag, Berlin, Germany, 2006.
- [6] R. R. Bate, D. D. Mueller, and J. E. White. *Fundamentals of Astrodynamics*. Dover Publications, Inc., 1971.
- [7] R. H. Battin. *An Introduction to the Mathematics and Methods of Astrodynamics*. American Institute of Aeronautics and Astronautics, Reston, VA, revised edition, 1999.
- [8] J. T. Betts. *Practical Method for Optimal Control Using Nonlinear Programming*. Society for Industrial and Applied Mathematics, Philadelphia, PA, 2001.
- [9] D. Brouwer and G.M. Clemence. *Methods of Celestial Mechanics*. Academic Press Inc., 1961.

- [10] C. D. Brown. *Spacecraft Mission Design*. American Institute of Aeronautics and Astronautics, Reston, VA, 2nd edition, 1998.
- [11] G. Buttazzo and A. Frediani, editors. *Variational Analysis and Aerospace Engineering*. Springer Science+Business Media, New York, NY, 2000.
- [12] D. V. Byrnes. Application of the pseudostate theory to the three-body lambert problem. *The Journal of the Astronautical Sciences*, Vol. 37(No. 3):221–232, July-September 1989.
- [13] D. V. Byrnes and H. L. Hooper. Multi-conic: A fast and accurate methode of computing space flight trajectories. *American Institute of Aeronautics and Astronautics*, (No. 70-1062), August 1970.
- [14] V. A. Chobotov, editor. *Orbital Mechanics*. American Institute of Aeronautics and Astronautics, 2002.
- [15] G. L. Condon. Lunar orbit insertion targeting and associated outbound mission design for lunar sortie missions. Hilton Head, South Carolina, 20-23 August 2007. AIAA Guidance, Navigation and Control Conference and Exhibit.
- [16] L. D’Amario and T.N. Edelbaum. Minimum impulse three-body trajectories. *American Institute of Aeronautics and Astronautics*, (Paper 73-145), Feb 1973.
- [17] J. M. A. Danby. *Fundamentals of Celestial Mechanics*. Willmann-Bell, Inc., Richmond, VA, 2nd edition, 1988.
- [18] G. J. Der. An elegant state transition matrix. *American Institute of Aeronautics and Astronautics*, (A9634790):776–791, July 1996.
- [19] G. J. Der and R. Danchick. Analytical and numerical error covariance matrix propagation (for spacecraft in earth orbital environments). *American Institute of Aeronautics and Astronautics*, (A9634798):854–878, July 1996.

- [20] C. D'Souza. The mathematical foundations and framework for the orion high-accuracy encke-nystrom trajectory integrator. Unpublished manuscript, June 2008.
- [21] V.A. Egorov. Certain problems of moon flight dynamics. *Russian Literature of Satellites, Part I*, International Physical Index, Inc., 1958.
- [22] P. R. Escobal. *Methods of Orbit Determination*. R. E. Krieger Publishing Company, 1965.
- [23] G. S. Gideon. A practical note on the use of lambert's equation. *American Institute of Aeronautics and Astronautics*, Vol. 3(No. 1), January 1965.
- [24] Michael Douglas Griffin and James R. French. *Space Vehicle Design*. American Institute of Aeronautics and Astronautics, 2nd edition, 2004.
- [25] C. E. Velez J. O. Cappellari and A. J. Fuchs. Mathematical theory of the goddard trajectory determination system. Technical Report X-582-76-77, Goddard Space Flight Center: National Aeronautics and Space Administration, Greenbelt, Maryland, April 1976.
- [26] A. E. Bryson Jr. and Y. Ho. *Applied Optimal Control*. Hemisphere Publishing Corporation, Washington, D.C., 1975.
- [27] W. H. Michael Jr. and W. T. Blackshear. Recent results on the mass, gravitational field and moments of inertia of the moon. *Earth, Moon, and Planets*, Vol. 3(No. 4):388–402, March 1972.
- [28] A. Kharab and R. B. Guenther. *An Introduction to Numerical Methods: A MATLAB Approach*. Chapman and Hall, 2nd edition, 2006.

- [29] K. Kledron and T.H. Sweetser. A comparison of onestep and other multiconic trajectory propagation methods. *American Institute of Aeronautics and Astronautics*, (Paper 88-4286), August 1988.
- [30] D. V. Brynes L. A. D'Amario and R. H. Stanford. Interplanetary trajectory optimization with application to galileo. *American Institute of Aeronautics and Astronautics*, Vol. 5(Paper 82-4248), Sept-Oct 1982.
- [31] E. R. Lancaster and R. C. Blanchard. A unified form of lambert's theorem. NASA Technical Note TN D-5368, National Aeronautics and Space Administration, 1969.
- [32] C. R. McInnes. *Solar Sailing: Technology, Dynamics and Mission Applications*. Springer-Verlag, 1999.
- [33] C. B. Moler. *Numerical Computing with MATLAB*. Society for Industrial and Applied Mathematics, Philadelphia, PA, 2004.
- [34] B. R. Rauschenbakh M. Y. Ovchinnikov and S. McKenna-Lawlor. *Essential Spaceflight Dynamics and Magnetospherics*. Kluwer Academic Publishers, Dordrecht, The Netherlands, 2003.
- [35] D. A. Nelson P. D. Spanos, L. J. Mushung and D. A. Hamilton. Spectral representation of high-frequency space shuttle flight data. *Journal of Aerospace Engineering*, 7(3), July 1994.
- [36] D.A. Nelson P. D. Spanos, L. J. Mushung and D.A. Hamilton. Low frequency spectral representation of space shuttle flight data. *Journal of Aerospace Engineering*, 3(2), April 1990.
- [37] S. Pines. Uniform representation of the gravitational potential and its derivatives. *AIAA*, Vol. 2(No.2), November 1973.



- [38] Jr. R. Y. Roth R. J. Richard, V. C. Clarke and W. E. Kirhofer. Earth-moon trajectories, 1965-70. Technical Report No. 32-503, National Aeronautics and Space Administration, Jet Propulsion Laboratory. Pasadena, CA., November 1965.
- [39] R.V. Ramanan and V. Adimurthy. Nonimpact lunar transfer trajectories using the pseudostate technique. *Journal of Guidance, Control, and Dynamics*, Vol. 28(No. 2), March-April 2005.
- [40] F. J. Regan and S. M. Anandakrishnan. *Dynamics of Atmospheric Re-Entry*. American Institute of Aeronautics and Astronautics, 1993.
- [41] C. Roithmayr. Contributions of spherical harmonics to magnetic and gravitational fields. Technical Report NASA/TM-2004-213007, National Aeronautics and Space Administration, Langley Research Center, Hampton, Virginia, March 2004.
- [42] A. E. Roy. *Orbital Motion*. Institute of Physics Publishing, 4th edition, 1978.
- [43] H. Schaub and J. L. Junkins. *Analytical Mechanics of Space Systems*. American Institute of Aeronautics and Astronautics, 2003.
- [44] B. D. Tapley B. E. Schutz and G. H. Born. *Statistical Orbit Determination*. Elsevier Academic Press, 2004.
- [45] S. W. Shepperd. Universal keplerian state transition matrix. *Celestial Mechanics*, Vol. 35, 1985.
- [46] I.M. Sobol. *A Primer for the Monte Carlo Method*. CRC Press, Boca Raton, FL, 1994.

- [47] Jr. S.W. Wilson. A pseudostate theory for the approximation of three-body trajectories. Number AIAA Paper No. 70-1061. AAS/AIAA Astrodynamics Conference, Santa Barbara, California, 19-21 August 1970.
- [48] The Analytic Sciences Corporation Technical Staff. *Applied Optimal Control*. The MIT Press, 1974.
- [49] D. A. Vallado. *Fundamentals of Astrodynamics and Applications*. Microcosm Press and Springer, 3rd edition, 2007.
- [50] M. P. Vautier and A. J. Sinclair. Effect of coordinate switching on translunar trajectory simulation accuracy. Honolulu, HI, 18-21 August 2008. AIAA Guidance, Navigation and Control Conference and Exhibit.
- [51] M. Wieczorek. Spherical harmonic models of planetary topography. <http://www.ipgp.fr/~wieczor/CrustalThicknessArchive/CrustalThickness.html>. Institut de Physique du Globe de Paris.
- [52] Wikipedia. Rosenbrock function. <http://en.wikipedia.org/wiki/Rosenbrockfunction.svg>.
- [53] D. Zwillinger. *CRC Standard Mathematical Tables and Formulae*. CRC Press, 1995.